Elucidating membrane disruption mechanisms of peptide antibiotics

Katharine Alexandra Hammond

A dissertation submitted in partial fulfilment of the requirements for the degree of

Doctor of Philosophy

at

University College London

Department of Physics & Astronomy

University College London

January 2021

I, Katharine Alexandra Hammond, confirm that the work presented in this thesis is my own. Where information has been derived from other sources, I confirm that this has been indicated in the thesis.

Abstract

Antimicrobial peptides and proteins hold promise as a next generation of antibiotics. Whilst conventional antibiotics must cross the microbial membrane to target intracellular processes, many of these agents act by disrupting microbial lipid bilayers. This alternative mode of action attacks a conserved structural component of the cell and offers a promising alternative for treating infections caused by multi-resistant pathogens.

To facilitate the translational development of antimicrobial peptides, it is beneficial to develop a fundamental understanding of their behaviour. However, resolving the interactions between antimicrobial peptides and lipid bilayers is challenging. Disruption to the lipid packing occurs at the nanoscale, is often dynamic and adapts under different environment conditions. Consequently, the rules linking peptide sequence to mechanisms of membrane disruption and biological activity remain largely unknown.

The work presented here directly addresses this challenge. AFM imaging of model membrane systems is used to visualise disruption mechanisms with high temporal and spatial resolution. The findings are then compared to biological assays, and reveal new sequence-function relationships. Starting with a simplified α-helical template, we demonstrate that both the mode of lipid disruption and the biological selectivity of a sequence can be controlled at the single amino acid level. Next, we demonstrate that incorporating motifs from membrane-active but non-lytic peptide sequences into an α-helical design can confer auxiliary lipid interactions. Moving on from single α-helices, we provide the first evidence of membrane disruption by multi-helix bacteriocins, resolving a hitherto unknown multimodal mechanism. In addition we resolve the membrane interactions of supramolecular peptide structures, confirming that self-assembly can offer mechanistic advantage. Finally, preliminary data is presented that improves on the chemical and structural specificity of AFM, and therefore the insights into peptide-lipid interactions that it can provide.

Impact Statement

The focus of this research is on resolving fundamental interactions between antimicrobial peptide sequences and their lipid bilayer targets. Antimicrobial peptides have the potential to be developed into a new generation of antibiotics, but a better understanding of the relationship between sequence, mode of action and biological activity is needed to enable rational design of more promising sequences.

The findings presented here will aid other researchers designing peptide sequences, by providing possible optimisation strategies. For example, our results indicate that more complex, multimodal mechanisms of membrane disruption induced by multi-helix bacteriocins can produce more potent antimicrobial responses. Furthermore, our results in both Chapter 3 and Chapter 5 show a loss of haemolytic activity when peptide-induced membrane defects are restricted to the upper leaflet of the lipid bilayer. This suggests that the design of sequences that do not induce transmembrane defects is a possible avenue for improving the therapeutic index.

In addition, the here revealed sequence-function relationships may motivate more studies to be conducted via the same approach, i.e., high-resolution imaging of model membrane systems treated with closely related peptide sequences under otherwise identical conditions. Looking ahead, significant progress would be made in the field if nanoscale AFM imaging could be bestowed with chemical specificity. The final chapter describes proof-of-concept methodologies that advance towards this goal, highlighting current progress (charge-mapping and chemical-tagging) and the need for further pursuit.

The research described in this thesis has led to one review, one book chapter and four research papers, all published in peer-reviewed journals. In addition, a second review has been submitted, and a fourth research paper is now ready for submission (see page 5 for details).

List of publications

The following manuscripts have been published in peer review journals and books:

Hammond, K.; Benn, G.; Bennett, I.; Parsons, E. S.; Ryadnov, M. G.; Hoogenboom, B. W.; Pyne, A. L. B. Imaging the Effects of Peptide Materials on Phospholipid Membranes by Atomic Force Microscopy. In *Polypeptide Materials. Methods in Molecular Biology*; Ryadnov, M. G., Ed.; Humana, New York, NY, **2021**; Vol. 2208, pp 225–235.

Hammond, K.; Ryadnov, M. G.; Hoogenboom, B. W. Atomic Force Microscopy to Elucidate How Peptides Disrupt Membranes. *Biochim. Biophys. Acta - Biomembr*. **2021**, *1863* (1), 183447.

Hammond, K.; Lewis, H.; Halliwell, S.; Desriac, F.; Nardone, B.; Ravi, J.; Hoogenboom, B. W.; Upton, M.; Derrick, J. P.; Ryadnov, M. G. Flowering Poration—A Synergistic Multi-Mode Antibacterial Mechanism by a Bacteriocin Fold. *iScience* **2020**, *23* (8), 101423.

Kepiro, I. E.; Marzuoli, I.; Hammond, K.; Ba, X.; Lewis, H.; Shaw, M.; Gunnoo, S. B.; Santis, E. D.; Łapińska, U.; Pagliara, S.; Holmes, M. A.; Lorenz, C. D.; Hoogenboom, B. W.; Fraternali, F.; Ryadnov, M. G. Engineering Chirally Blind Protein Pseudocapsids into Antibacterial Persisters. *ACS Nano* **2020**, *14* (2), 1609–1622.

Hammond, K.; Lewis, H.; Faruqui, N.; Russel, C.; Hoogenboom, B. W.; Ryadnov, M. G. Helminth Defense Molecules as Design Templates for Membrane Active Antibiotics. *ACS Infect. Dis*. **2019**, *5* (8), 1471–1479.

Pfeil, M-P.; Pyne, A. L. B.; Losasso, V.; Ravi, J.; Lamarre, B.; Faruqui, N.; Alkassem, H.; Hammond, K.; Judge, P. J.; Winn, M.; Martyna, G. J.; Crain, J.; Watts, A.; Hoogenboom, B. W.; Ryadnov, M. G. Tuneable poration: host defense peptides as sequence probes for antimicrobial mechanisms. *Sci. Rep.* **2018**, *8* (1), 14926

The following manuscripts are submitted or in preparation:

Hammond, K.; Hoogenboom, B. W; Ryadnov, M. G. Membrane disrupting peptides: mechanistic elucidation of antimicrobial activity. In *Amino Acids, Peptides and Proteins;* Ryadnov, M. G., Hudekz, F., Eds.; The Royal Society of Chemistry, **2021**; Vol. 44, pp 115–139

Hammond, K.; Cipcigan, F.; Nahas, K. A.; Losasso, V.; Lewis, H.; Cama, J.; Martelli, F.; Simcock, P.; Stansfeld, P. J.; Pagliara, S.; Hoogenboom, B. W.; Keyser, U. F.; Sansom, M. S. P.; Crain, J; Ryadnov, M. G. A single side-chain switch between poration and floral ruptures in phospholipid bilayers. *Ready for submission.*

Acknowledgements

Firstly, I thank my supervisors Prof. Bart Hoogenboom (UCL) and Dr. Maxim Ryadnov (NPL) for their continued guidance, inspiration and support over the course of this research. I also thank Dr. Richard Thorogate (LCN) for AFM training and maintenance of equipment, as well as my second supervisor, Dr Isabel Llorente Garcia for her input throughout the project, and the National Physical Laboratory, for supporting this research. Special thanks go to Dr. Alice Pyne, for training me in AFM, for pioneering the lipid-peptide experiments conducted in this thesis, and for being a constant source of friendship, support and advice.

I am grateful to the many collaborators whose work has informed and improved my own, especially Kareem Al Nahas (Cambridge University) and Dr. Flaviu Cipcigan (IBM Research Centre UK). I acknowledge the Nano Life Science Institute (NanoLSI), Kanazawa University, for funding a four-week collaborative research project into charge-mapping of peptide-treated membranes, with particular thanks to Prof Takeshi Fukuma, for his informative discussion and to Kaito Hirata, for all of his help with experiments. As well, I am grateful to both Dr. Jonathon Moffat (Oxford Instruments) and Dr. Chris Mulcahy (Oxford Instruments) for their interest in collaborating, for providing instrument access and for giving their time to help with experiments.

I thank the Hoogenboom group – past and present – for providing such an enjoyable working environment and for the discussions and input that have helped to shape this project. My particular thanks go to Dr. Adrian Hodel and Dr. Ed Parsons for their lipid knowledge and to Georgina Benn and Dr. Bernice Akpinar for being great friends as well as always having useful input into my work. As well, I thank the Biometrology group at NPL for their input, support and friendship over the past three years, and for training me in peptide design, synthesis and biophysics. In particular I am grateful to Dr. James Noble for his continued support with making sure I had time for this thesis and Dr. Helen Lewis, who provided *in vitro* biological data presented here.

Finally, I thank my family and friends. To my parents, Clare, Becca and James for your continued and unwavering support - in so many aspects - over the past three years. To all of my friends, but particularly to Nell, Clare, Lewis, Jake, Chloe, Katie, Saoirse, Alex, Purnank, Smita and Jack for always being so enthusiastic about my work and for keeping me sane, and to Luci and Starkey for the perspective you provide.

Table of contents

List of figures

List of tables

List of abbreviations

ACN	acetonitrile
AFM	atomic force microscopy
ALPS	amphipathic lipid packing sensor
AM-AFM	amplitude mode atomic force microscopy
AMP	antimicrobial peptide
Boc	tert-butyloxycarbonyl protecting group
CD	circular dichroism
CL	cardiolipin
cryoEM	cryogenic electron microscopy
D_f	fractal dimension
DIPEA	N, N-diisopropylethylamine
DLPC	1,2-dilauroyl-sn-glycero-3-phosphocholine
DLPG	1,2-dilauroyl-sn-glycero-3-phosphoglycerol
DLS	dynamic light scattering
DMT	derjaguin-muller-toporov model
ELS	electrophoretic light scattering
Fmoc	fluorenylmethoxycarbonyl protecting group
GUV	giant unilamellar vesicle
HBTU	2-(1*H*-Benzotriazol-1-yl)-1,1,3,3-tetramethyluronium-hexafluorophosphate
HDM	helminth defence molecule
KPFM	kelvin probe force microscopy
LB	langmuir blodgett
L_d	liquid disordered phase
LPS	lipopolysaccharide
L_o	liquid ordered phase
MALDI	matrix assisted laser desorption ionization
MD	molecular dynamics
MIC	minimum inhibitory concentration
MOPs	4-morpholinepropanesulfonic acid
MRE	mean residue ellipticity
MRSA	methicillin-resistant *Staphylococcus aureus*
MS	mass spectrometry
Mtt	4-methyltrityl

NMR	nuclear magnetic resonance
OCD	oriented circular dichroism
OD_{600}	optical density at 600 nm
OLEMP	open loop electric potential microscopy
Pbf	2,2,4,6,7-pentamethyIdlhydrobenzofuran-5-sulfonyl protecting group
PC	phosphatidylcholine
PE	phosphatidylethanolamine
PFT	PeakForce Tapping
PG	phosphatidylglycerol
POPC	1-palmitoyl-2-oleoyl-sn-glycero-3-phosphocholine
POPG	1-palmitoyl-2-oleoyl-sn-glycero-3-phosphoglycerol
PS	phosphatidylserine
RP-HPLC	reversed-phase high-performance liquid chromatography
SAM	self-assembled monolayer
SLB	supported lipid bilayer
S_o	gel phase
SPPS	solid phase peptide synthesis
SUV	small unilamellar vesicle
t-Bu	*tert*-butyl protecting group
TFA	trifluoroacetic acid
TFE	2,2,2-trifluoroethanol
TIS	triisopropylsilane
T_m	melting temperature
ToF	time of flight
Trt	trityl protecting group
UV	ultraviolet
VRE	vancomycin-resistant *enterococci*

In addition to the above, a list of the amino acid abbreviations (three and single letter variations) is provided in Table A.1

1 Introduction

Much of this introduction has been published in: Hammond, K.; Ryadnov, M. G.; Hoogenboom, B. W. Atomic Force Microscopy to Elucidate How Peptides Disrupt Membranes. *Biochim. Biophys. Acta - Biomembr*. **2021**, *1863* (1), 183447

1.1 Antimicrobial peptides: structure and function

Antimicrobial peptides (AMPs) are a vast family of peptides secreted by nearly all organisms as defence against invading pathogens.[1] Humans alone secrete more than 100 different types,[2] with surface epithelial cells expressing an arsenal of AMPs that continuously prevent infection [3] and neutrophil granules storing high concentrations that are released during phagocytosis.[4] Whilst conventional antibiotics target intracellular processes, many AMPs act by permeabilising the pathogen membrane.[5] This alternative mode of action attacks a conserved structural component of the pathogen, reducing its ability to develop resistance.[6] Indeed, despite coevolution with bacteria over millions of years, high-level resistance to these peptides has not emerged.[7] Bacterial defences to AMPs include proteolytic degradation, cell membrane modifications to reduce peptide activity, secretion of proteins to sequester the peptides and the presence of a capsule to restrict access to the membrane surface.[7],[8] Most of these mechanisms are non-specific, have wider implications for the cell physiology and confer only moderate resistance.[7] This leads to slow decreases in cell susceptibility rather than the highly effective resistance observed for conventional antibiotics, which can quickly spread through horizontal gene transfer of dedicated resistant genes.[9] Daptomycin, an AMP in therapeutic use since 2003, provides clinical evidence for this with bacterial resistance observed at both low frequency and low potency.[10]

AMPs are multifunctional agents. They are active against a wide range of organisms beyond bacterial cells, including fungal cells,[11]–[13] cancerous cells,[14]–[16] parasites,[17]–[19] biofilms,[12],[20] and viruses.[21]–[26] In addition to direct attack of the pathogen membrane, these peptides can have intracellular targets.[27] Furthermore in higher organisms, they can act indirectly by modulating the host immune response to infection, inducing chemotaxis, stimulating cytokine release and reducing inflammation.[28] This thesis focuses on their disruption to the cellular membrane. The cellular membrane is a complex system consisting of hundreds of species of lipids and proteins, which can be further modified with a wide range of sugars. Driven by hydrophobic interactions between lipids, this system self-organises into a fluid lipid bilayer packed with transmembrane and integral proteins. The membrane is highly dynamic; its local organisation results from factors such as transient protein-protein, protein-lipid and lipid-lipid interactions as well as from associations with the underlying cytoskeleton.[29] Many AMPs target the lipid assembly, exerting their activity by inducing

pores and defects in the lipid packing that can ultimately lead to permeabilisation and cell death.[30] Every cell type has a distinct mixture of lipids and proteins,[31] and the ability of a particular AMP to target a particular membrane depends on this distinct composition.[32]

Over 3000 antimicrobial peptides have been discovered to date. Sequences are typically between 10 and 100 amino acids long and are of varying composition, secondary structure, charge and hydrophobicity (Fig 1.1).[2] Non-ribosomally produced peptides can further diversify through the inclusion of non-proteinogenic amino acids, cyclisations and additional functionalisations.

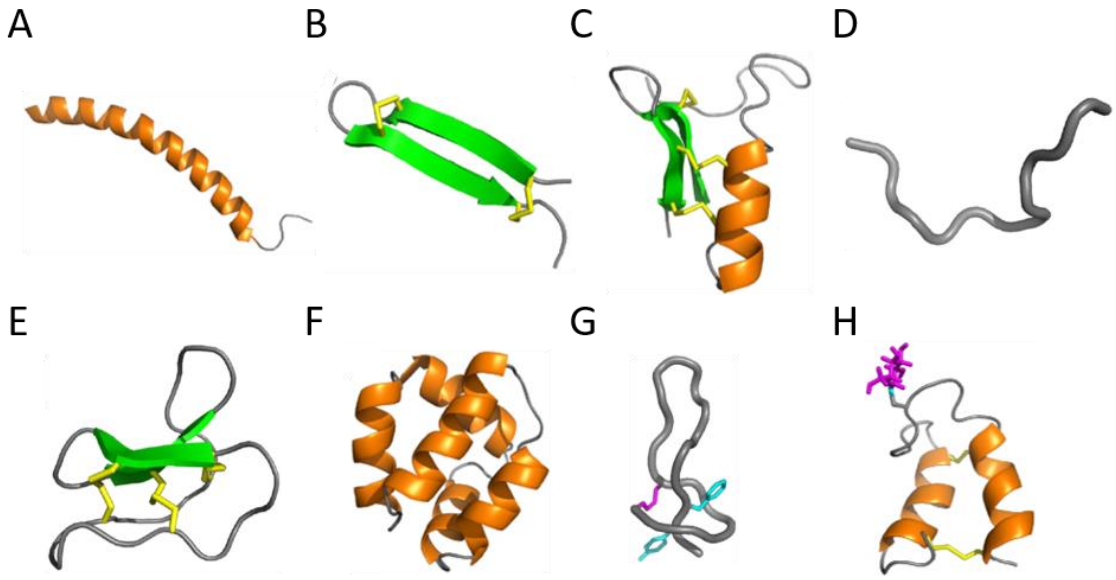

Figure 1.1. The structural diversity of AMPs. The four main structural classes of AMPs are (A-D); α-helical, β-sheet, mixed α/β and extended. Examples of more complex topologies such as (E, F) backbone cyclised peptides; (G) head to side chain cyclised peptides; and (H) functionalised peptides containing e.g. glucose (shown in magenta). Figure is adapted from ref. [33]*, with permission from Elsevier. PDB IDs of NMR structures are 2K6O, 1KFP, 1ICA, 1G89, 1NB1, 1E68, 1Q71, 2MIJ, for A-H respectively. α-helices are shown in orange, β-sheets in green and disulphide bonds in yellow.*

Despite this variety, conserved properties can be found that pre-dispose the peptides to interact with their target membranes. These include the ability to fold into an amphipathic structures, as well as the possession of a net cationic charge.[5] Amphipathicity drives membrane binding and insertion by enabling simultaneous interaction with the hydrophilic lipid bilayer surface and its hydrophobic core.[34],[35] Cationic charge can increase the selectivity of AMPs, as this facilitates binding to bacterial membranes, since these are rich in anionic phospholipids such as cardiolipin (CL) and phosphatidylglycerol (PG).[36] In contrast, mammalian membranes sequester anionic phospholipids to the inner leaflet, leaving the outer leaflets less attractive for AMP binding.[37] Indeed, malignant transformations can lead to increased exposure of anionic phospholipids in the outer leaflet, and, along with other changes in lipid composition, this increase in surface charge results in increased cell susceptibility to AMP attack.[16],[38] For

example, the anti-cancer activity of the AMP temporin-1CEa correlates directly with the overexpression of phosphatidylserine (PS).[39] The exact relationships between peptide sequences and their membrane activity are complex and creating more effective sequences (existing or *de novo*), i.e. with a better therapeutic index, remains challenging. Antimicrobial potency can depend on a variety of biophysical parameters such as charge, hydrophobicity, kinetics of peptide self-assembly, and structural amphipathicity.[40] Increases in hydrophobicity, however, often come at the expense of increased toxicity; for improved therapeutic function, fine-tuning the biophysical parameters of native peptide sequences is commonly achieved through mass screening studies rather than through rational design.[6]

1.2 Resolving membrane disruption mechanisms

1.2.1 The use of model membranes

To study the mechanisms of lipid disruption induced by AMPs, and the fundamental peptide-lipid interactions taking place, simplified phospholipid systems such as bilayers, monolayers and vesicles are often used. Phospholipids are the main component of biological membranes.[37] They are composed of a phosphate group attached to a glycerol with two esterified fatty acyl chains (glycerophospholipids, Fig 1.2A) or to a sphingosine with a single amidated acyl chain (phosphosphingolipids, Fig 1.2D), and spontaneously assemble into bilayers and vesicles in aqueous environments by packing their acyl chains into a hydrophobic core. Chains are typically 14 to 24 carbons long and can be saturated, mono-unsaturated or poly-unsaturated (see, e.g. Fig 1.2B). The phosphate head group is further esterified to a hydrophilic group such as ethanolamine, choline, serine or glycerol, giving rise to phospholipids with differing charge and curvature (see, e.g. Fig 1.2C). The specific lipid composition dictates the thickness, surface charge and packing of the resulting bilayer and, in model systems, can be chosen to better mimic the properties of the target membrane.

1.2.2 Current findings

Using such model systems, the mechanisms of AMP-disruption have been studied extensively over the past few decades by a wide variety of experimental techniques. Fluorescent dye leakage assays have been used to confirm permeabilisation and quantify the size and kinetics of defects,[41]–[43] NMR has been used to resolve the 3D structure and organisation of peptide in lipid membranes,[44]–[47] circular dichroism (CD) spectroscopy and oriented circular dichroism (OCD) spectroscopy have been used to measure peptide conformation and alignment to the membrane surface,[48],[49] and neutron diffraction has been used to detect changes to the lipid thickness and order, as well as detecting the size and abundance of pores.[50]–[53] In parallel, molecular dynamic (MD) simulations are increasingly used to provide atomic-level structural descriptions.[54]–[58]

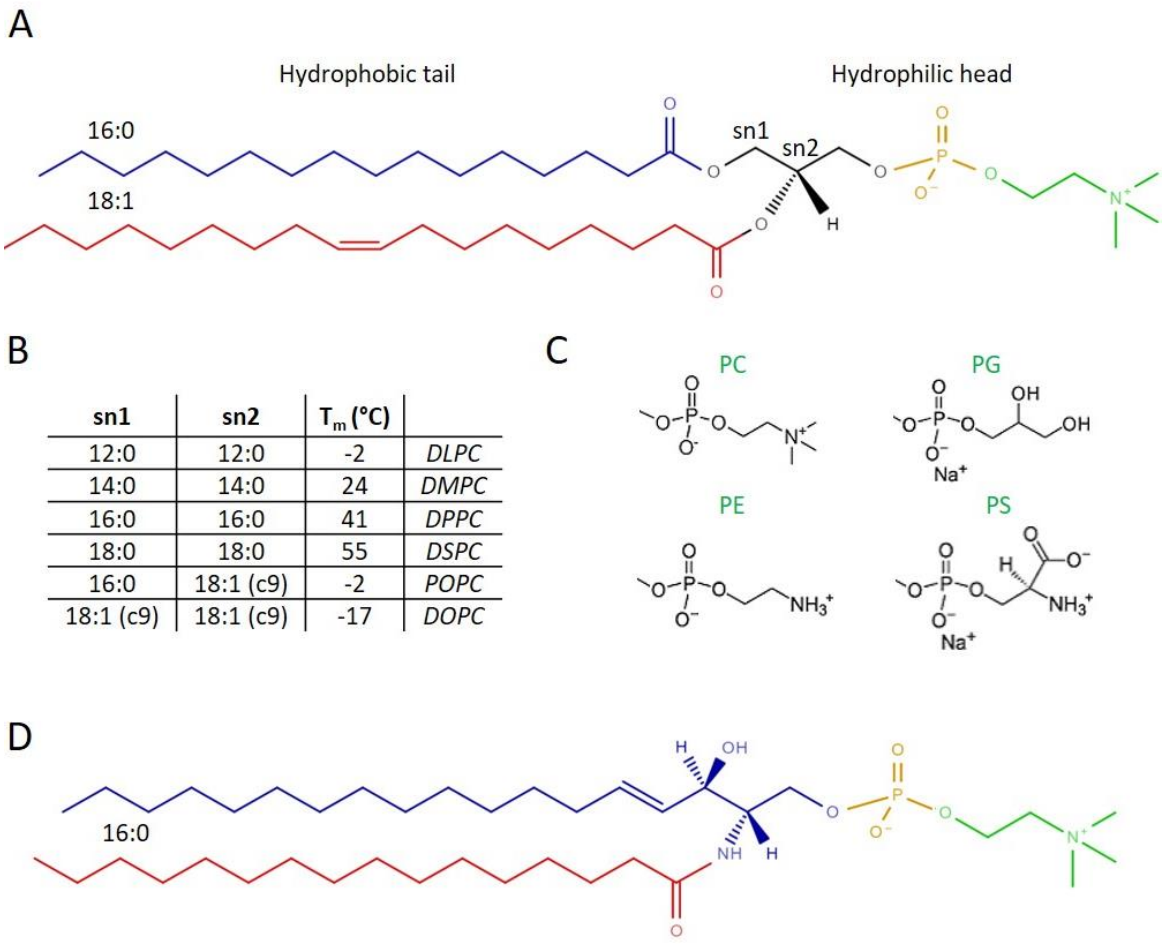

sn1	sn2	T_m (°C)	
12:0	12:0	-2	*DLPC*
14:0	14:0	24	*DMPC*
16:0	16:0	41	*DPPC*
18:0	18:0	55	*DSPC*
16:0	18:1 (c9)	-2	*POPC*
18:1 (c9)	18:1 (c9)	-17	*DOPC*

Figure 1.2. Phospholipids are the main lipid component of biological membranes. (A) General structure of a glycerophospholipid. A phosphate group (green) is attached to a glycerol group (black) with fatty acyl chains esterified at its sn1 and sn2 hydroxyl groups (here 16:0 orange and 18:1 red), and to a hydrophilic head group (here choline); (B) Examples of common acyl chain combinations with corresponding abbreviations. In this thesis DL and PO lipids are used; (C) Examples of common hydrophilic head groups, with corresponding abbreviations. In this thesis PC and PG phospholipids are used; (D) General structure of a phosphosphingolipid. A phosphate group (green) is attached to a sphingosine (blue) with a single amide acyl chain (here 16:0, red) and to a hydrophilic headgroup (here choline).

This variety of techniques has shown that different peptide sequences can re-arrange lipid assemblies in different ways [30] and has led to a number of disruption models (Fig 1.3). The barrel-stave poration model features peptides that insert into the membrane, interacting with lipid head and tail groups, and form pores that do not require rotational rearrangement of the membrane lipids (Fig 1.3A).[59] The toroidal poration models feature peptides that remain bound to the lipid head groups and form pores by pulling the lipid head groups inward. Such pores are larger and are lined with both peptides and lipids (Fig 1.3B).[60],[61] Non-porating models include the carpet model, in which the peptide material remains surface bound, roughening and disrupting the lipid packing (Fig 1.3C).[62] At threshold concentrations, the lateral pressure can result in membrane collapse. Other models proposed are charge-based phospholipid clustering (Fig 1.3D), the induction of non-lamellar phases (Fig 1.3E) and

localised thinning and thickening effects (Fig 1.3F-H). Although not all models lead directly to permeabilisation, the creation of boundary edges compromises membrane integrity and introduces discontinuities in the membrane where solutes may more easily pass through.[63] Furthermore, segregation of lipids into discrete domains restricts their lateral mobility, reducing the ability of the bilayer to repair.[64]

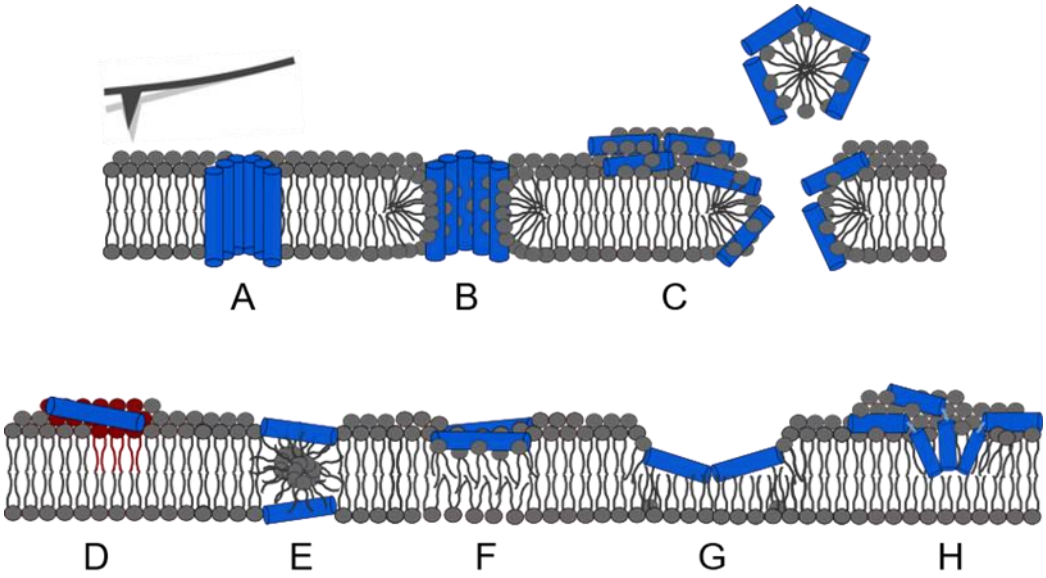

Figure 1.3. Different sequences exert different modes of membrane disruption. This includes (A) barrel-stave poration; (B) toroidal pores; (C) carpet disruption leading to micellization; (D) phospholipid clustering; (E) induction of non-lamellar phase; (F) bilayer thinning; (G) monolayer removal; and (H) nanoscale pits. Each mode of disruption can be resolved by AFM.

Unlike the case for pore-forming proteins that form well-defined structures in lipid bilayers that are amenable to cryoEM and AFM imaging,[65]–[70] much of the details of peptide-membrane interactions remains unclear.[6] Peptides are smaller and more disordered, and their membrane interactions appear to be less static and less well defined than their supramolecular protein counterparts. Current studies indicate that peptide-induced membrane permeabilisation is a dynamic process, with defects consistent with different models able to grow, re-seal and inter-convert.[30] Furthermore, defect formation can be hard to resolve as it is occurs on a nanoscale and can be heterogenous across the surface. Consequently, different biophysical techniques can give conflicting results. This issue is exemplified through the case of the archetypal membrane permeabilising peptide melittin: despite five decades of investigation, the mechanism of the peptide is still disputed with conflicting reports over pore diameter, peptide orientation and the reversibility of permeabilisation of target membranes.[71]

One technique well-suited for dynamic mechanistic analysis of peptide sequences is in-liquid atomic force microscopy (AFM). The basic principle of AFM (discussed in detail in section 2.4.) is that a nanometre sharp tip mounted on a flexible cantilever is scanned across a surface; the distance-dependent interaction forces between the tip and the sample are used to detect the

proximity of the surface and to build an image as the tip follows the surface contours. Since its invention in 1986 and subsequent adaptation for imaging in liquid, AFM has made significant contributions to our understanding of biological systems.[72] Samples can be visualised under near-native conditions, at (sub)nanometre resolution over timescales of seconds to hours. Over the past decade, in-liquid AFM has successfully been used to directly observe different peptide-induced disruption mechanisms, discussed in section 1.3.

1.3 In-liquid AFM to study peptide-disruption

1.3.1 Supported lipid bilayers (SLBs)

As with other biophysical techniques, AFM studies of peptide-lipid interactions have predominantly used model membrane systems. To be amenable to AFM analysis, lipid assemblies are prepared on an underlying solid support. This is typically done using Langmuir Blodgett (LB) [73] or vesicle fusion methods.[74],[75]. The LB method uses sequential deposition of lipid monolayers. The vesicle fusion method relies on the spontaneous adsorption and rupture of liposomes onto a hydrophilic surface to produce supported lipid bilayers (SLBs), as shown in Figure 1.4. The process depends on the electrostatic interactions between the lipids and the substrate. Optimal bilayer formation can be controlled by adjusting the pH and ionic strength of the solution.[76] For AFM studies, the underlying substrate is typically mica as it can be cleaved to produce an atomically flat surface. SLBs prepared on mica are flat to within a few Ångströms, enabling high-resolution imaging.[77]

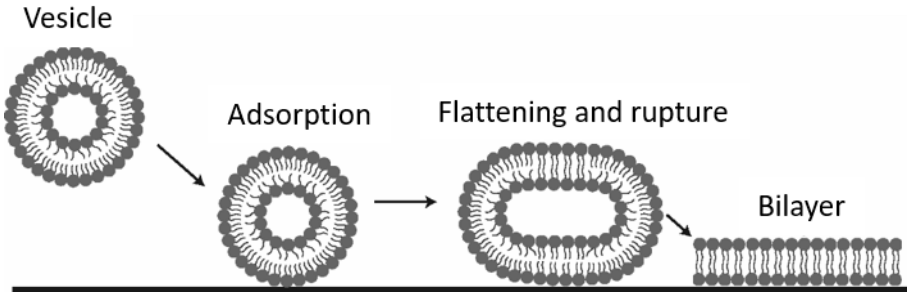

Figure 1.4. Schematic showing the vesicle fusion method. Vesicles are adsorbed onto a hydrophilic surface where they flatten and rupture to form a continuous bilayer.

Another consideration when preparing an SLB is the desired fluidity. Lipid bilayers can form as fluid liquid disordered phases (L_d) or more solid gel state phases (S_o) depending on the temperature and the composition of the lipids, with every lipid having a unique melting temperature (T_m) below which they constitute membranes in a solid gel state and above which they preferentially adopt liquid phases. Biological membranes control their compositions to exist as liquid phases and, with the exception of very specific examples (see, e.g. [78]), the gel-state phase is not physiologically observed. These liquid membrane phases have traditionally been considered as 2D fluids, with lipids and proteins freely diffusing.[79] Evidence for lateral heterogeneity and the formation of discrete domains is updating this to a more complex picture

of the membrane as a compartmentalised system.[29] In eukaryotic cells particularly, fluidity across the membrane is not homogenous. Sterols such as cholesterol can interact preferentially with lipids such as sphingomyelin, condensing into so-called liquid ordered phase (L_o) domains, which show increased packing density and lateral order of acyl chains whilst retaining fluidity.[80] The mammalian plasma membrane is rich in cholesterol and recent analysis of the plasma membrane of live HeLa cells measured 76% L_o regions to 24% L_d regions.[81]

Unlike mammalian cells, bacterial membranes lack high quantities of L_o-promoting lipids and hydrophobic molecules, and are typically modelled by single phase, anionic L_d SLBs. Some evidence now indicates they may also contain domains [36],[82] with regions of higher fluidity driven by clustering of lipid II molecules,[83] and regions of lower fluidity induced by the presence of hopanoids, proposed to act as a functional equivalent to cholesterol and detected in some bacterial strains.[84] Factors such as lipid curvature preference, protein interactions and the underlying cytoskeleton can also lead to heterogenous lipid segregation in live cells.[29],[82],[85] As our understanding of the bacterial membrane organisation increases, adjustments to single fluid phase bilayers as bacterial membrane models may be required.

The spatial resolution limit of AFM imaging of SLBs is largely defined by experimental conditions rather than by instrumentation. When lipid assemblies are prepared below the fluid-to-gel transition temperature, the lateral diffusion of lipids within the assembly is slow (with diffusion coefficient D ~10^{-3} μm^2 s^{-1}).[37] AFM imaging of such assemblies has resolved individual lipid head groups with sub-nanometre lateral resolution.[86] However in more physiologically relevant fluid bilayers the diffusion of each lipid is orders of magnitude faster than even the highest-speed AFM can currently acquire an image (D ~2 μm^2 s^{-1}) [37] meaning a temporal average of the bilayer is visualised and individual lipids are not resolved.

1.3.2 More physiological models

As used in AFM experiments, SLBs obviously differ from physiological membranes by being in close proximity to the solid support. The hydration layer between the lower leaflet lipids and the underlying support (around 1 nm thick) [87] conserves lipid fluidity and dynamics, but – depending on lipid composition – the diffusion coefficient in SLBs can be around two times smaller than in free standing bilayers such as GUVs.[88] This is thought to be due to atomic scale corrugation on the substrate surface.[89] Model membranes such as tethered and polymer-cushioned bilayers have been used to introduce a spacer between the solid support and the lipids, reducing the influence of the substrate.[90],[91] Recent advances in the preparation of floating bilayers, with tuneable aqueous layers of 10-30 nm represent more accurate biomimetic models [92] and their use for AFM membrane disruption studies may increase if they lead to significantly different results than that obtained on SLBs. However, the compatibility of these systems with AFM imaging is yet to be confirmed. Another approach is pore-spanning bilayers, which retain the free-standing nature but introduce solid support at the pore edges. Such systems

can be imaged by AFM and have been prepared with diameters of up to 600 nm, yet it remains to be established what resolution can be obtained in imaging AMP-induced membrane disruption.[93]

Secondly, SLBs are composed of simple phospholipid mixtures that clearly do not reproduce the complexity of the cell membrane, and advances in AFM studies of more physiological models are also being developed. Native membranes such as rod outer segment disc membranes and purple membranes have been extracted, ruptured and adsorbed onto mica substrates for AFM imaging [94],[95] providing both native lipid mixtures and incorporation of membrane proteins. Recently, high resolution imaging of a vesicular bacterial chromatophore, i.e., a curved native membrane, was also reported, despite it being supported only by the fluid in the vesicle and the mechanical properties of the membrane itself.[96]

Studies have also been conducted on whole pathogen cells. Many have been conducted in air (see, e.g., refs [97]–[105]) although dynamic information gained from in-air studies remains limited, and the risk of introducing drying artefacts cannot be ignored. A number of in-liquid AFM studies with live cells have also been attempted.[106]–[113] These studies focused on general changes across the membrane surface, as the spatial resolution was not as high as for model membranes. For example, Fantner et al imaged surface roughening of *E. coli* cells after peptide treatment, correlating the kinetics of roughening with cell death.[113] Thanks to improvements in immobilisation protocols and AFM technology, it is now possible to image the surface of live bacteria at a spatial resolution that is comparable to that obtained on SLBs [114],[115] and it may now be possible to visualise local peptide-membrane interactions in live cells.

Whilst more physiological approaches have advantages, model membranes are currently better suited to study the fundamental basics of peptide-lipid interactions. AFM is a surface technique that provides no chemical identification, and, in more complex, native environments, drawing meaningful information from AFM studies can be challenging. Interpretation of live cell studies is complicated further by obstacles such as deconvoluting direct peptide activity from cell-stress induced membrane changes. As well, SLBs provide access to larger length and timescales than would be possible in live cells, and the highly controlled experimental conditions enable the contribution of different variables (e.g. lipid charge, fluidity, thickness) to be directly assessed. Therefore, the focus of this thesis is on AFM imaging of peptide-induced lipid disruption within a model membrane system. In section 1.3.3, we review the findings of previous model membrane studies.

1.3.3 In-liquid AFM studies of peptide-induced membrane disruption

Over the past decade, direct observation has been made of membrane topographies consistent with barrel stave poration models,[116],[117] carpet disruption,[118] toroidal pores,[119]

bilayer thinning,[120],[121] transitions to non-lamellar phase,[120]–[122] and formation of localised domains.[118],[123]–[126] Through parallel experiments, domain formation has been attributed to peptide-induced lipid clustering,[123] localised membrane thinning or thickening [118],[124],[125] and localised changes to lipid fluidity.[126]

What is perhaps surprising is that different peptide sequences interact with lipids in very different ways to elicit disruption and permeabilisation. Even amongst sequences containing the same secondary structure and similar biophysical properties, divergent modes of disruption are induced.[30] To emphasise the diversity of mechanism observed, Figure 1.5 shows examples of disruption modes observed for peptides with shared biophysical properties. All peptides are linear amphipathic α-helices, contain only proteinogenic amino acids, and possess a net cationic charge.

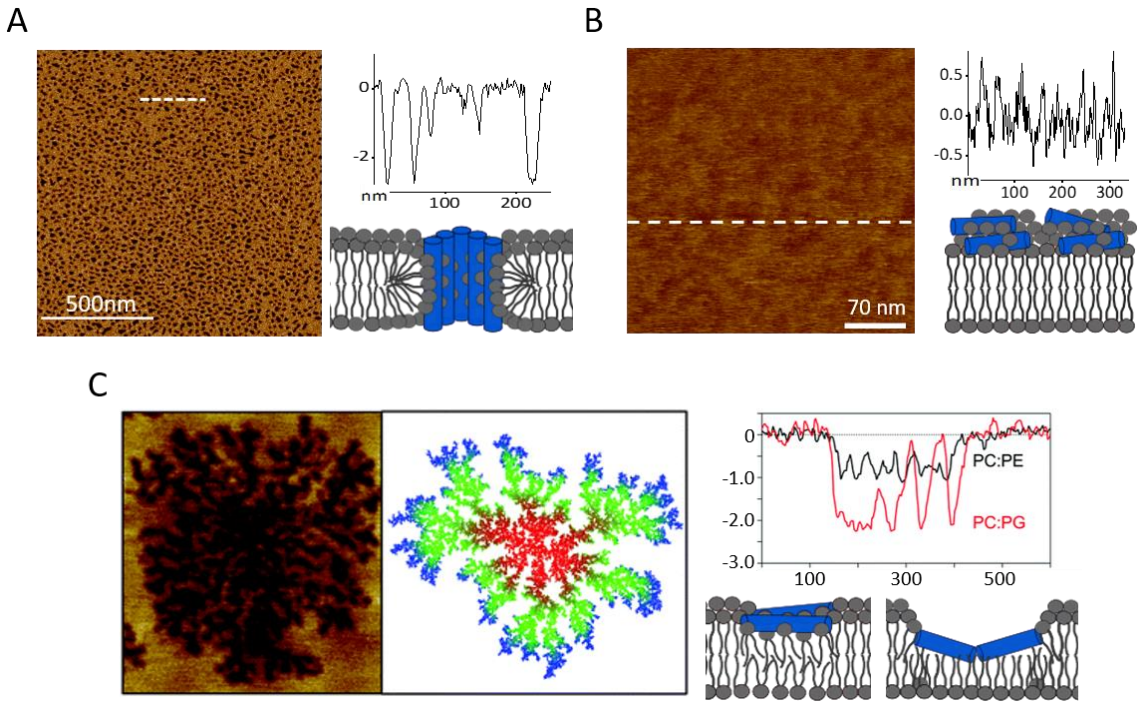

Figure 1.5. Variable modes of membrane disruption can be induced by linear amphipathic α-helices with a cationic net charge. AFM topography images of peptide treated SLBs show that (A) magainin 2 induces SLB poration, with pores of 3 nm deep and around 20 nm wide, consistent with a toroidal pore model; (B) cecropin B induces surface roughening, with variation in topography of +/- 0.5 nm, consistent with the carpet disruption model; and (C) Smp-43 induces fractal-like defects in the upper bilayer leaflet, with defect depths dependent on the lipid composition, consistent with bilayer thinning in PC:PE (1 nm deep) and monolayer removal in PC:PG (2 nm deep). Adapted from (A) ref. [119] *with permission, © 2019 American Chemical Society; (B) ref.* [118] *licensed under CC BY 4.0, and (C) ref.* [127] *licensed under CC BY-NC 3.0, Published by The Royal Society of Chemistry.*

Magainin 2 is a 23 amino acid sequence secreted by the African clawed frog *Xenopus laevis* and folds into an amphipathic α-helix with a net charge of +4. It is observed to form pores in SLBs consistent with the toroidal pore model (between 10 and 20 nm in diameter, Fig 1.5A).[119] Cecropin B is a 35 amino acid sequence secreted by the giant silk moth, *Hyalophora cecropia*

and folds into an amphipathic α-helix with a net charge of +7. It is observed to act via a non-porating mechanism, roughening the surface of SLBs, consistent with a carpet-like model (Fig 1.5B).[118] Smp-43 is a 43 amino acid sequence secreted in the venom of the Egyptian scorpion *Scorpio maurus palmatus*, and folds into an amphipathic α-helix with a net charge of +4. It is observed to form defects in SLBs that are confined to the upper leaflet lipids and expand in a distinctive fractal-like morphology (Fig 1.5C).[127] Depending on the lipid composition of the SLB, the depth of these defects is consistent with domains of peptide induced bilayer thinning (PC:PE) and domains of peptide-induced monolayer removal (PC:PG).

Whilst sequences with similar biophysical properties can exert very different effects, sequences with very different biophysical properties can induce similar effects. (P)GKY20, a peptide modelled on the Gly271 to Ile290 sequence of the human thrombin, folds into a linear amphipathic α-helix, and is observed to induce charge-based phospholipid clustering in multi-compositional SLBs.[126] Colistin is an AMP secreted by the bacteria *Bacillus polymyxa*, with entirely different properties (Fig 1.6A). It consists of only 10 amino acids, 7 of which form a peptide ring structure (Fig 1.6A, blue) and 3 of which form an exocyclic chain. A fatty acid tail is functionalised to the end of the chain (Fig 1.6A, green), and the peptide contains non-proteinogenic amino acids. Despite the difference in sequence and structure, it too is observed to act via lipid clustering.[123] Addition of colistin to multi-compositional POPC/LPS SLBs induced membrane separation into LPS-colistin rich domains and LPS-colistin poor domains (Fig 1.6B). Collectively these results demonstrate two things. Firstly, that membrane permeabilisation can occur through a number of well-defined modes. Secondly, that subtle, currently poor-defined properties of the peptide sequence control the mode of disruption that is induced.

1.3.3.1 The role of amphipathicity

A noteworthy finding from AFM studies is that imperfect amphipathicity can impart a common mode of action to otherwise disparate sequences. Henderson et al examined the effect of 13 different AMPs of differing charge, composition and secondary structure.[120] 12 of the peptides fold into imperfect amphipathic arrangements (either through poor segregation of amino acids, or through breaks in the symmetry of secondary structural elements), while one peptide, alamethicin, shows perfect amphipathicity. AFM demonstrated that alamethicin was the only sequence that was not able to lower the line tension of a lipid bilayer. When lipid bilayers are prepared as patches rather than continuous assemblies, the patches spontaneously form compact, round areas, due to the line tension that arises from the energy cost of re-arranging lipids at the boundary edges. All 12 imperfect amphipathic sequences caused significant elongation of the patch boundary. In contrast, alamethicin showed no line active behaviour.

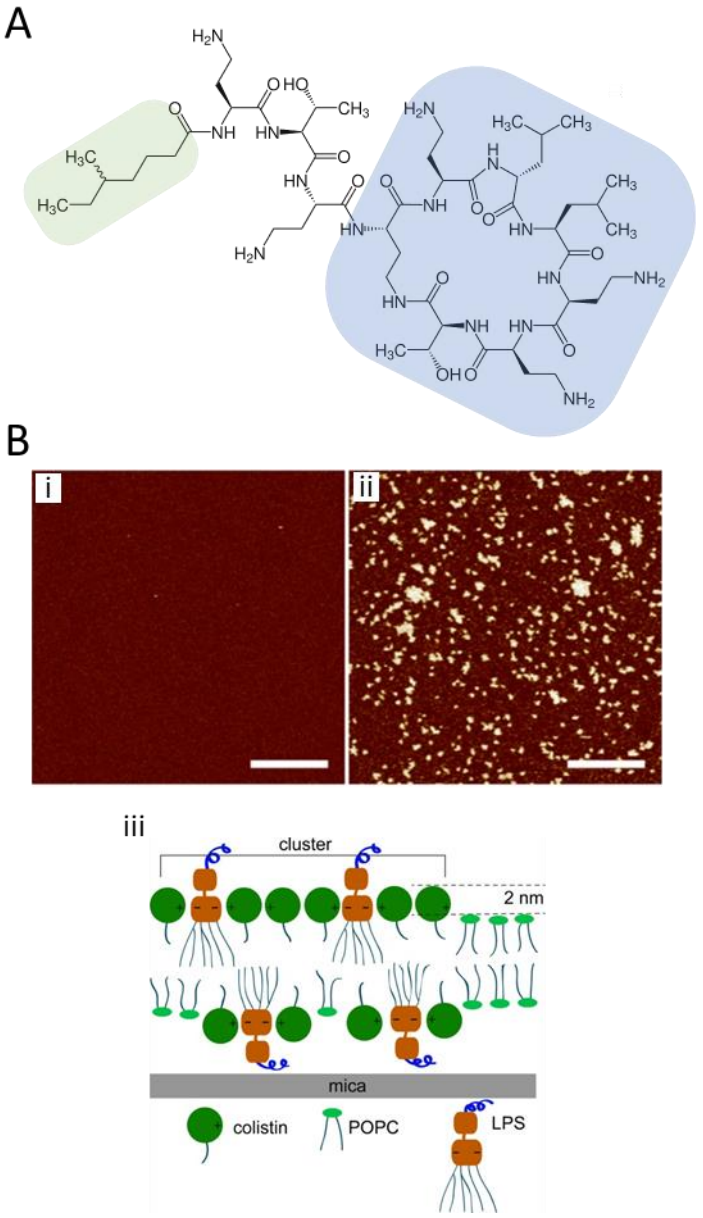

Figure 1.6. Colistin induces phospholipid clustering in mixed SLBs. Chemical structure of colistin consists of a 7- amino acid cyclic ring (blue), a 3 amino acid exocyclic chain, and a fatty acid tail (green); (B) AFM topography image of an SLB before (i) and after (ii) treatment with colistin. Clusters 2 nm high appear across the membrane surface. A model schematic is shown in (iii). Reproduced from ref. [123] *licensed under ACS AuthorChoice, © 2018 American Chemical Society. Scale bars 1 µm.*

The authors propose that imperfect amphipathicity is a prerequisite for peptides to adopt to the curvature of membrane edges if they are to stabilise and propagate boundaries. This idea has been proposed previously [128] and is consistent with other AFM studies of imperfect amphipathic sequences with SLB patches [121],[129] and with AFM studies on phase separated L_o/L_d bilayers (see, e.g. Fig 1.7).[130],[131] In L_o/L_d SLBs, there is a hydrophobic mismatch between the two phases and L_o domains form in compact round patches to minimise the boundary length (Fig 1.7A). Line-active AMPs such as melittin can, besides inducing poration, cause domain edges to become extended and heterogenous in shape (Fig 1.7B).

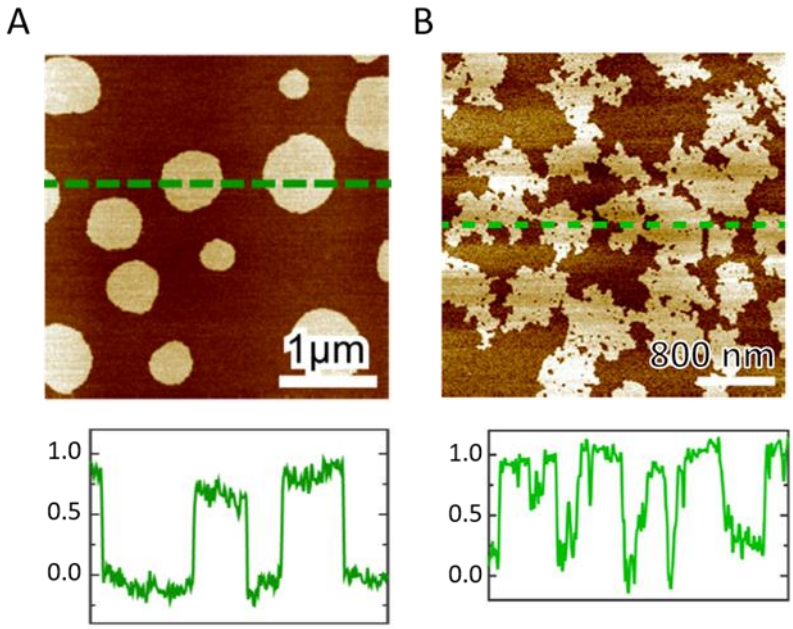

Figure 1.7. Melittin-induced remodelling of lipid boundary edge. (A) AFM topography image of a phase separated L_o/L_d SLB, where domains are formed in compact round patches to minimise their boundary length. Depth profile shown across the dotted line shows 1 nm height difference between L_o (brighter) and L_d (darker) domains; (B) Topography image after addition of melittin. Besides causing poration, the peptide induces heterogenous L_o domains with extended boundary edges. Adapted from ref. [130] *with permission, © 2016 American Chemical Society.*

1.3.3.2 Resolving disruption dynamics

While time-resolved studies remain limited, those that have been conducted indicate that peptide disruption mechanisms are highly dynamic. Rakowska et al were the first to show that peptide induced defects can grow over time.[132] A *de-novo* peptide sequence termed amhelin, designed to fold into amphipathic cationic α-helices long enough to span a lipid bilayer, induced pores that expanded and merged. Consistent with subsequent studies, defect growth progressed in a heterogenous way.[130],[132],[133] The authors proposed that once formed, pores may act as a site of recruitment, driving the migration of peptide from a surface bound state to the pore edge.

Defect growth can also progress in an organised manner. The scorpion-derived α-helical AMP Smp-43, demonstrates fractal-like expansion (Fig 1.5C).[127] The morphology of the defects is consistent with a two-dimensional diffusion-limited aggregation model. In this model diffusing particles that come into contact with aggregates are immediately trapped at the aggregate edge, preventing the particle from diffusing to the aggregate centre and resulting in fractal expansion. Similarly, peptide monomers diffusing across the membrane surface may have a higher probability of sticking to a defect edge and removing lipid than diffusing to the defect centre, leading to fractal-like growth.

As well as expanding, defects can get smaller and even disappear. By disabling the slow axis, AFM can be used to scan laterally back and forth in the same y position with a high temporal resolution. Kim et al used this to show that a synthetic AMP pHD108 can form both stable and metastable pores, the latter fluctuating on sub-second timescales.[134] With a temporal resolution of 0.3 s, some pore like features remain unchanged, whereas others are highly dynamic and appear, disappear and re-appear. These observations support previous proposals of membrane recovery and pore sealing.[135]

1.3.3.3 Beyond the peptide sequence

Modes of disruption are not only controlled by the sequence of the peptide but on the lipid composition of the membrane and on environmental conditions. The controlled nature of SLB experiments enables in-depth analysis of factors that enhance or reduce peptide activity. Detailed comparative studies have been conducted on the effect of lipid fluidity, thickness and charge [119],[127],[129],[130],[136]–[141], the pH and ionic strength of solution,[134] and peptide concentration.[119],[120],[123],[137],[139],[142]

Membrane fluidity has a significant effect on peptide action, with peptide insertion nearly always observed to be more effective in more fluid lipid bilayers (see, e.g. [130],[136]). Lower fluidity bilayers, such as those containing cholesterol (liquid ordered L_o) or those prepared below the gel-fluid transition temperature (gel-state S_o) have higher lateral order and increased hydrophobic interactions between fatty acyl chains, resulting in an increased energy barrier for peptide insertion.

Incorporation of anionic phospholipids generally increases the activity of cationic peptides.[127],[139],[141] This is expected as there will be increased electrostatic attraction and peptide binding. In some cases, the peptide is only active if negatively charged phospholipids are present, and no activity is observed for zwitterionic bilayers.[119] This is consistent with many other studies that show that AMPs are charge selective.[34] It is only for hydrophobic AMPs, of which the mode of action is driven by their interactions with lipid tails rather than with lipid head groups, that charge does not influence their disruption ability.[130],[140] Peptide concentration also has a significant effect on activity, and, as may be expected, increasing peptide concentration generally increases the extent of defect formation.[123],[137],[139]

Whilst different factors increase or reduce peptide activity at the membrane surface, a more interesting observation is that different modes of disruption can also be elicited. For example, magainin 2 has been observed to form stable pores in SLBs containing anionic phospholipids, but to solubilise zwitterionic SLBs in a detergent like way.[121] Similarly, differences in lipid fluidity can alter the mechanism. A synthetic sequence based on Aβ peptides induced very different effects in the gel-state and fluid-state SLBs.[138] Most surprisingly the concentration

of the peptide itself can alter its mechanism of action. As shown in Figure 1.8, protegrin-1 (PG-1), an 18 amino acid β-hairpin peptide causes boundary remodelling at low concentration (Fig 1.8B), bulk poration at a higher concentration (Fig 1.8C) and induction of a non-lamellar worm-like phase at higher concentrations still (Fig 1.8D).[143] Collectively, these results demonstrate that AMPs are highly flexible agents that can adapt their modes of membrane disruption under different conditions.

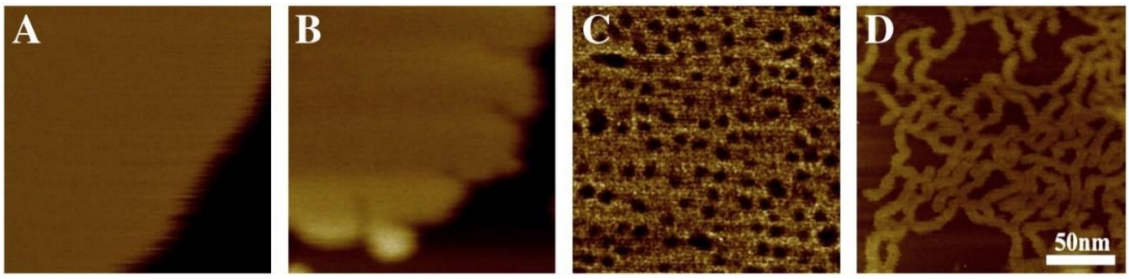

Figure 1.8. The AMP protegrin-1 induces different modes of membrane disruption at different concentrations. (A) With no peptide, the SLB is defect free and line-tension maintains a smooth boundary edge; (B) with low concentration of PG-1, the peptide acts at the SLB edges, elongating the boundary; (C) with increased concentration of PG-1 poration is observed and (D) at high concentrations of PG-1 the bilayer is transformed into a structure with much-reduced thickness, consistent with worm-like micelles. Reproduced from ref. [143] *with permission from Elsevier.*

1.3.3.4 Tuning disruption modes

It is clear that the precise mode of action that a peptide sequence exerts depends on multiple driving forces. It is difficult to predict the subtle contributions of all factors to produce a favoured mode of disruption. To tune the disruption mode, native AMP sequences can be used as templates to produce combinatorial libraries of sequences and conduct high-throughput screening to identify analogue sequences with more desirable lipid interactions (e.g. vesicle lysis at lower peptide concentration).[144] The change in mode of action can then be validated by AFM. This apprach was used for the peptide melittin, a 26 amino acid peptide toxin produced in honeybee venom.[145] The first-generation analogue, MelP5, elicited defects with depths in two main populations, 0.3 nm deep and 1 nm deep. (Fig 1.9B,C). In contrast, the second-generation sequence, macrolittin70, elicited defects at a range of depths from 0.3 to 4 nm (Fig 1.9A,C). Intriguingly, both improved analogues show variable defect depth, with increase in potency correlating with increase in variability. These results may indicate that AMPs with more versatile modes of action are more favourable.

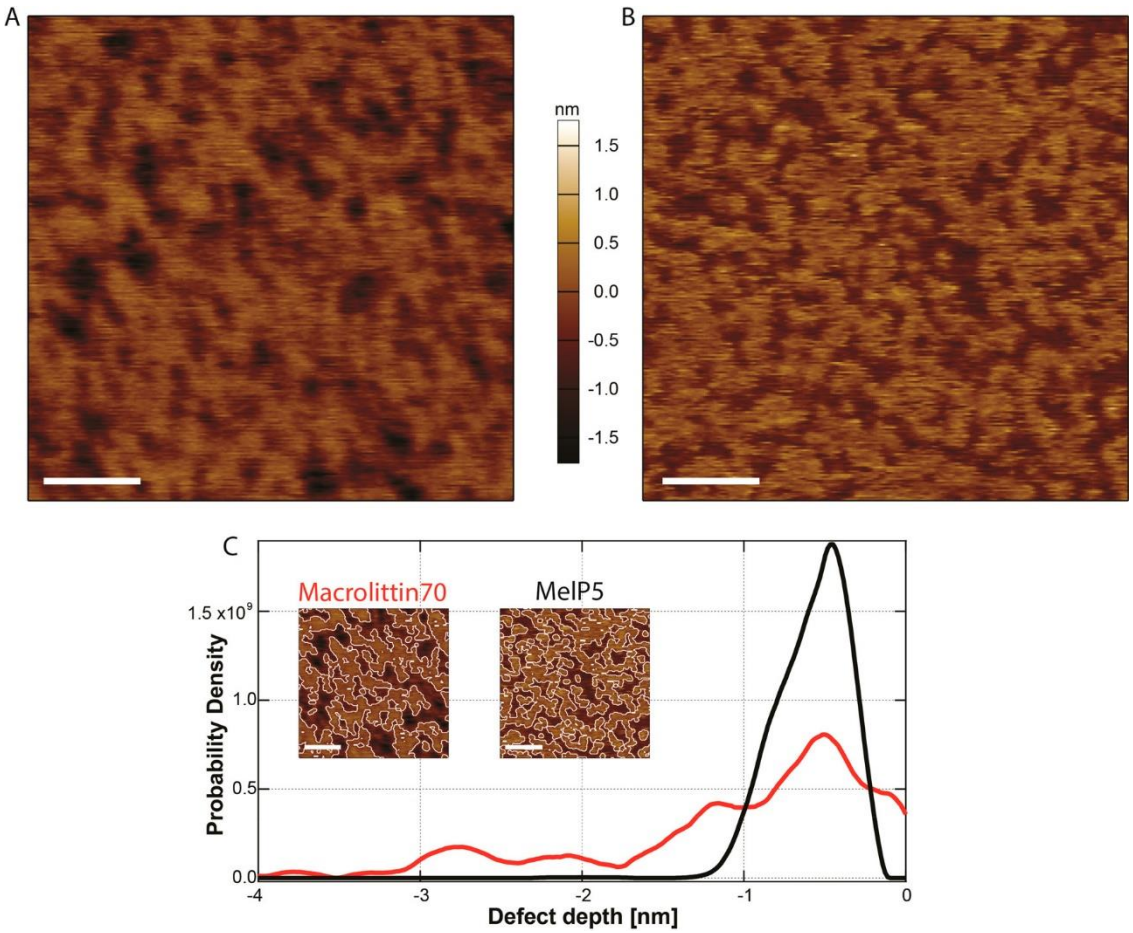

Figure 1.9. Comparison between two sequences resulting from high-throughput screening of melittin-like peptides. AFM topography images of SLBs treated with (A) the second-generation analogue, macrolittin 70 and (B) the first-generation analogue, MelP5. Scale bars 50 nm; (C) The defect depth distribution for each sequence. Both sequences disrupt the bilayer, with macrolittin70 showing greater variability in defect depth. Reproduced from ref. [145] *with permission, © 2018 American Chemical Society.*

An alternative approach in tuning the mode of disruption is to attempt to promote certain modes by making sequence modifications that are known to enhance or reduce specific lipid-peptide or peptide-peptide interactions. Whether the intended effect has taken place can then be validated using AFM. Some work has been conducted in this area, on the α-helical AMP cecropin B. The peptide sequence (NH_2-KWKVFKKIEKMGRNIRNGIVKAGPAIAVLGEAKAL-$CONH_2$) contains an AGPA motif (Ala-Gly-Pro-Ala), known to introduce kinks in alpha helices.[146] The C terminal region of CecB which is separated by the AGPA motif has a net neutral charge, a single cationic residue, minimal hydrophobicity with an abundance of alanines and as such, a low ability to interact with and rearrange membranes. In contrast, the N-terminal region is highly cationic and hydrophobic and pre-disposed to membrane insertion and poration. The full peptide is observed to remain surface bound and cause membrane roughening (as shown in Fig 1.5B).[118] Removing the C terminal region removes the barrier to membrane insertion and results in a sequence that inserts into the bilayer in a transmembrane orientation (validated by simulations), and can form transmembrane channels in SLBs (validated by AFM).[118]

In the same study, Pfeil et al demonstrate the effect of promoting helix-helix interactions.[118] Glycine zipper motifs, $G(X)_nG$ where X is any residue and n = 3 to 6, act to weaken α-helicity, and this motif is used in AMP sequences to tune membrane-responsive folding and to reduce helix oligomerisation.[147],[148] Cecropin B contains 3 glycine zipper motifs and CD indicates it exists as monomeric helices. By removing the first and the third glycine zipper, and further promoting helix-helix interactions by converting i, i+7 spacings of similar residues to i, i +3 and i, i +4,[149] CD indicates the sequence now exists as coiled-coils. This promotion of peptide-peptide interactions also alters the mode of disruption. The surface roughening observed for the native peptide is converted to monolayer poration. The AGPA motif and C terminal domain continue to prevent full insertion, but the now favourable helix-helix interactions promote peptide oligomerisation into organised pores rather than independent lipid-peptide interactions.

1.4 Concluding remarks

AMPs are a highly diverse family of peptides, linked by their common ability to disrupt lipid bilayers. It is now well accepted that different sequences disrupt and rearrange lipid bilayers in different ways, and that even for single sequence, peptide- lipid interactions can be highly dynamic, heterogenous and responsive to different environments. This versatility explains - at least in part - why AMPs are so challenging to study: different experimental technqiues, with different experimental conditions and different temperal and spatial resolutions, may well result in contradictary findings.

Whilst in-liquid AFM imaging of model membranes has its disadvantages (lack of chemical information, proximity of the solid support), its ability to directly resolve lipid-peptide assemblies the nanoscale without losing information to ensemble averaging makes this technique a powerful tool for better understanding the physical basis of membrane disruption mechanisms. Over the past decade, in-liquid AFM studies have visualised a wide variety of defect morphologies, with different sequences shown to exhibit distinct but well-defined modes of permeabilisation. Disruption kinetics have also been resolved, with defects observed to expand, to remain static and to reseal.

Despite this success, in-liquid AFM remains an underutilised technique compared to more traditional methods of characterising peptide activity. Furthermore, studies to date have predominantly focused on resolving the mechanisms of native sequences, and do not attempt to resolve more generalised relationships between peptide sequence and disruption modes. The research described here addresses this challenge. The thesis focuses on how different antimicrobial motifs affect lipid-peptide interactions, from the level of single amino acids in Chapter 3 to supramolecular systems in Chapter 6. In contrast to most previous studies, AFM imaging is here employed not just to the system of interest but to a range of closely related sequences. By focusing on the change in lipid disruption mechanisms induced by small, controlled changes in sequence, under otherwise identical experimental conditions, sequence to

function relationships can be elucidated. Furthermore, the findings are then compared to the biological activity of the peptides.

Using this approach, this thesis investigates both simplified model sequences, and more complex native systems. In Chapter 3 we start with an idealised α-helical antimicrobial template, as a tool to trigger distinct lipid interactions with single amino acid mutations. In Chapter 4, we expand this archetypal AMP α-helical template, and demonstrate that the expansion confers additional membrane properties to the sequence. In Chapter 5, we move from single helix peptides to a native, clinically promising, bacteriocin with a more complex, multihelical fold. We demonstrate that the multi-helix arrangement supports a hitherto uknown multimodal mechanism of membrane disruption, and that this is conserved across the bacteriocin class. In Chapter 6, we move to a supramolecular level, characterising a self-assembling antimicrobial system and revealing the differences in membrane disruption mechanisms when compared with monomeric AMPs. The results described provide novel insights into AMP sequence to function relationships, and will help to inform the future optimisation of antimicrobial sequences for application either as laboratory tools or for clinical development. However, the lack of chemical information that AFM-imaging can provide means that molecular-level insights remain speculative. To address this limitation, the final chapter of this thesis (Chapter 7) discusses our initial attempts to improve the chemical and structural specificity of AFM, towards resolving the individual peptides and lipids themselves.

2 Materials and methods

2.1 Preparation of AMPs

The peptides in this thesis were made chemically, using microwave-assisted solid phase peptide synthesis (SPPS), explained in detail in the following sections.[150],[151] I synthesised and purified all peptides, with the exception of some described in Chapter 5, which were provided by Dr Brunello Nardone at the National Physical Laboratory (D- epidermicin, α1/α2, α2/α3, α3/α4, α1/α2/α3, α2/α3/α4, and Arg- mutant).

2.1.1 General principles of solid phase peptide synthesis (SPPS)

In SPPS a peptide chain is anchored to an insoluble polymeric resin, and next grown from its C→ N terminus by sequential addition of amino acids. This approach allows reagents and side-products to be washed away after each reaction step.[150] Amino acid building blocks used in SPPS have protecting groups at all reactive sites except the α-carboxylic acid. The polymeric resin on which peptide synthesis takes place is functionalised with a chemical linker, and the first amino acid is attached to the linker via its α-carboxyl. Once the first amino acid has been attached to the resin, its N-α protecting group is selectively removed to leave a free amine. The second amino acid is then coupled to this via its α-carboxyl group to form an amide bond. To facilitate the coupling reaction, the α-carboxyl is activated to increase its electrophilicity (see below for further details).[152] The peptide is assembled by repeating this two-step process of selective deprotection of the N-α protecting group of the anchored peptide, followed by coupling to the next amino acid, until the final peptide is assembled. A schematic is shown in Figure 2.1.

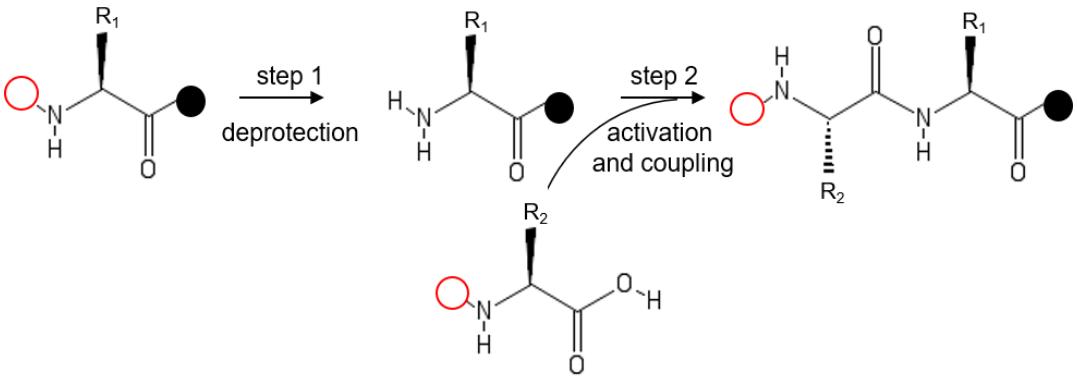

Figure 2.1. The two-step process in C→ N SPPS. The first amino acid, protected at its α-amino group (red circle), is attached via its α-carboxyl to a polymeric resin support via a chemical linker (black filled circle). In step 1 selective deprotection of the N-α protecting group leaves a free amine. In step 2 the second amino acid is coupled to the chain. This requires activation of the α-carboxyl of the second amino acid, to increase its electrophilicity.

2.1.1.1 Protecting groups

The most common protection scheme employed in SPPS is the orthogonal Fmoc/^{t}Bu protection scheme.[153],[154] A base-labile Fmoc group protects the α-amine (Fig 2.2A), whilst acid-labile groups such as Boc and ^{t}Bu protect reactive side chains (Fig 2.2B). The orthogonality allows selective deprotection of the α-amine during synthesis under relatively mild basic conditions (Fig 2.2C), with no premature cleavage of side chain protection groups.[153]

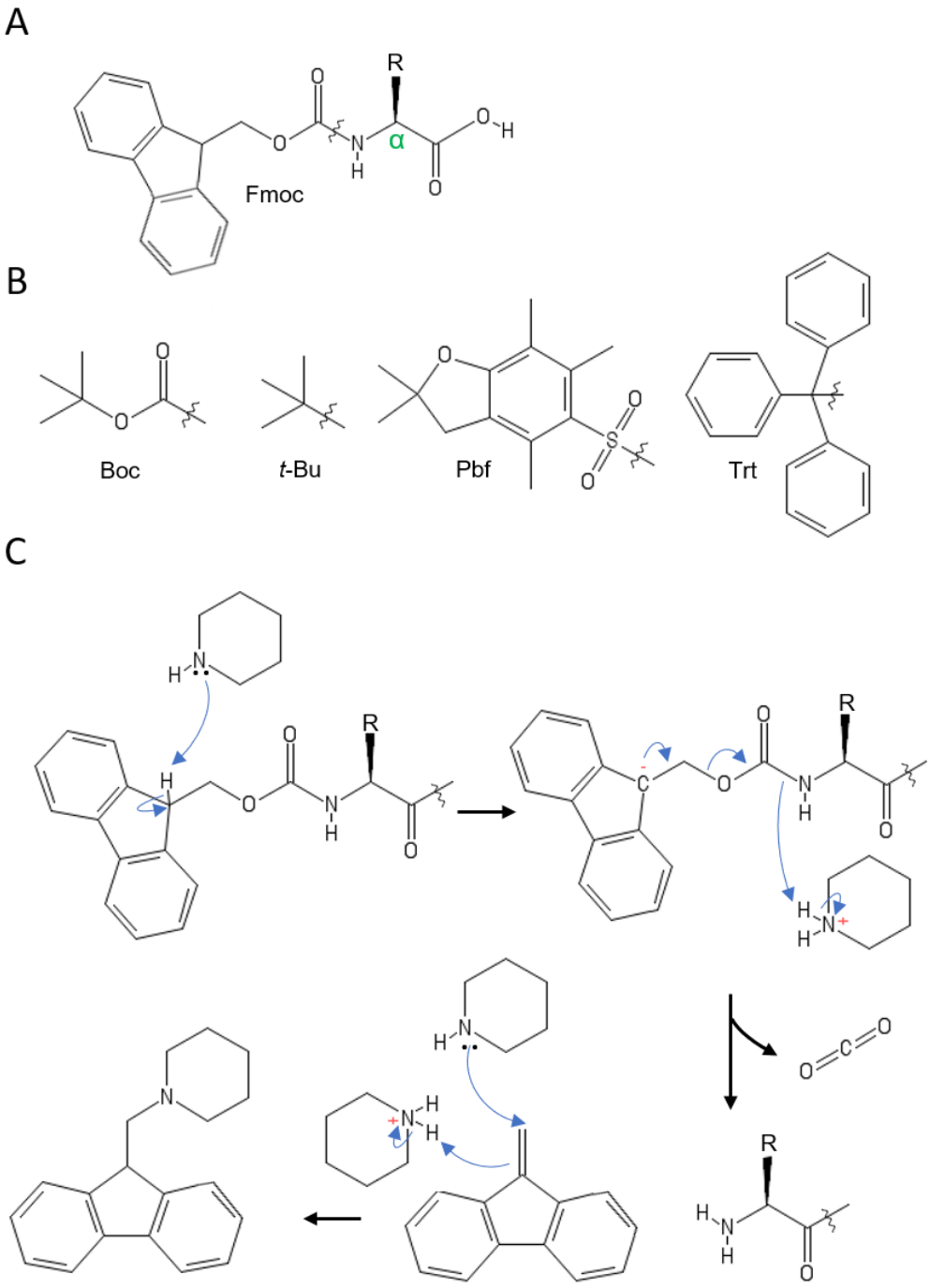

Figure 2.2. Fmoc/^{t}Bu protection scheme. (A) The base-labile Fmoc group protects the α- amine group; (B) acid-labile groups protect reactive side chains, with Boc commonly used for amines (Lys, Trp), t-Bu for carboxylic acids and alcohols (Asp, Glu, Tyr, Ser, Thr), Pbf for guanidinium (Arg) and Trt for amides, imadazoles and thiols (Asn, Gln, His, Cys); (C) Piperidine removes the Fmoc group from the amino acid resulting in a free α-amine. The dibenzofulvene by-product is scavenged by more piperidine.

2.1.1.2 Activation of the α-carboxyl

Coupling reagents are used to increase the electrophilicity of the α-carboxyl. A general schematic is shown in Figure 2.3A. The coupling reagent reacts with the α-carboxyl group via nucleophilic acyl substitution reactions to generate a more electrophilic carbonyl carbon with better leaving groups.[155] In this thesis, the aminium salt HBTU was used as a coupling reagent. HBTU is used in combination with the tertiary amine base DIPEA, as the first step of the reaction requires attack by the carboxylate anion. The full mechanism is provided in Figure 2.3B, and results in a benzotriazolyl ester. This can then be attacked by the amine of the growing peptide chain, to form an amide bond.

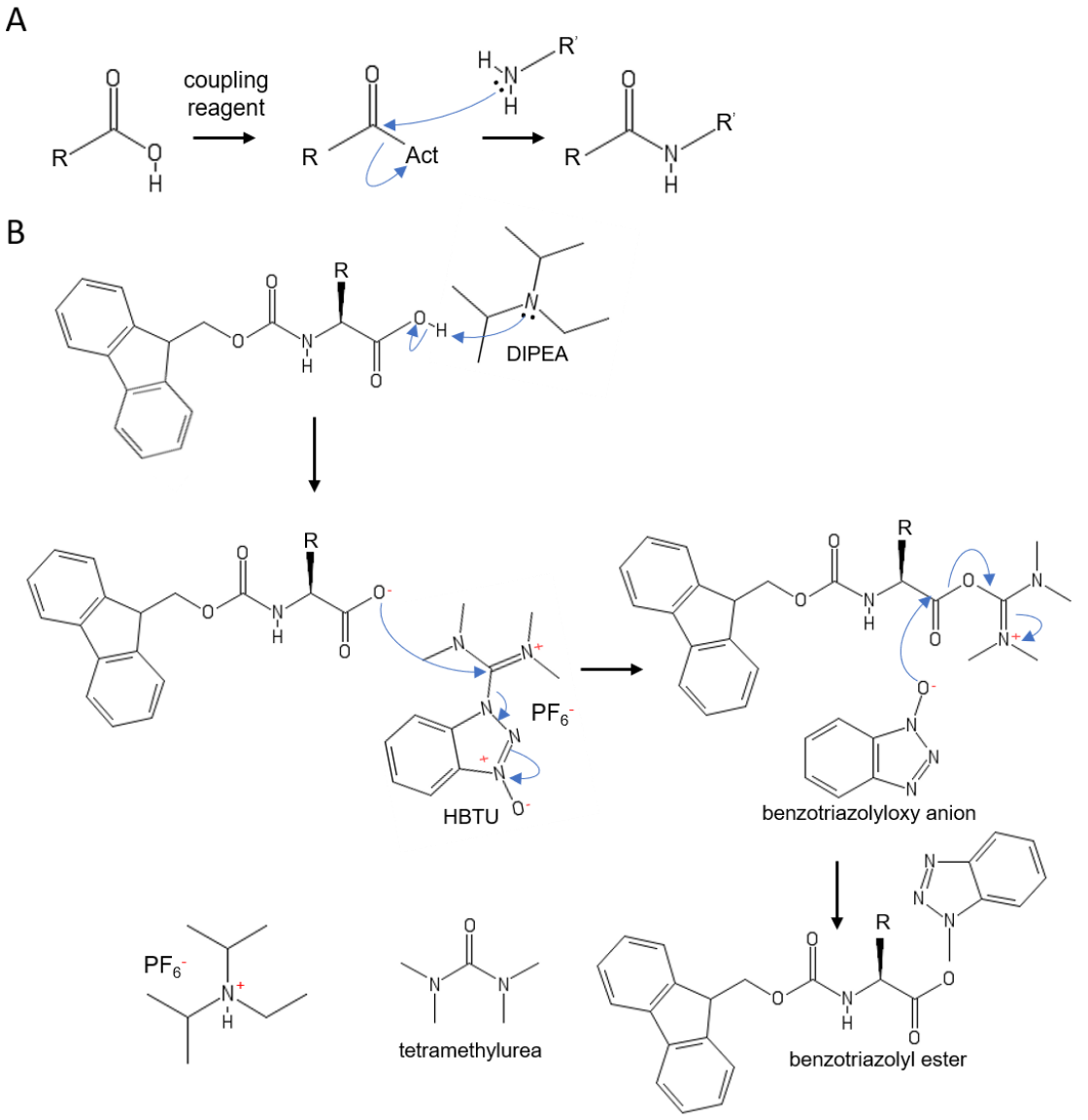

Figure 2.3. Coupling reagents in SPPS. (A) The general mechanism for activation of the α-carboxyl group is a nucleophilic acyl substitution reaction that results in a more electrophilic carbonyl, enabling amidation; (B) Mechanism for activation by HBTU. The tertiary amine base DIPEA deprotonates the α-carboxylic acid to form a carboxylate ion. This can then attack the electrophilic HBTU, with benzotriazolyloxy anion acting as a leaving group. The benzotriazolyloxy anion then reattacks the intermediate ester to form the benzotriazolyl ester.

2.1.1.3 Chemical linkers and resins

The resin itself consists of an inert, insoluble cross-linked polymer. Polystyrene crosslinked with 1-2 % divinylbenzene is widely used, as are polyethylene glycol based resins.[156],[157] The polymer is functionalised with an acid-labile linker to enable attachment of the growing peptide chain. The choice of linker determines the C-terminal functionality of the final peptide.[158] Most commercial resins contain linkers that produce C-terminal acids and amides although linkers that produce C- terminal alcohols, aldehydes and thioesters are also available.

2.1.1.4 Cleavage of the acid-labile linker and acid-labile protecting groups

Following assembly, an excess of concentrated trifluoroacetic acid (TFA) is used to cleave the peptide from the solid resin support and remove the protecting groups on amino acid side chains (see, e.g. Fig 2.4). Reactive carbocations are generated during the cleavage reactions and scavengers containing mobile protons such as triisopropylsilane (TIS) and H_2O are added to the cleavage mixture to minimise unwanted side-products.[159]

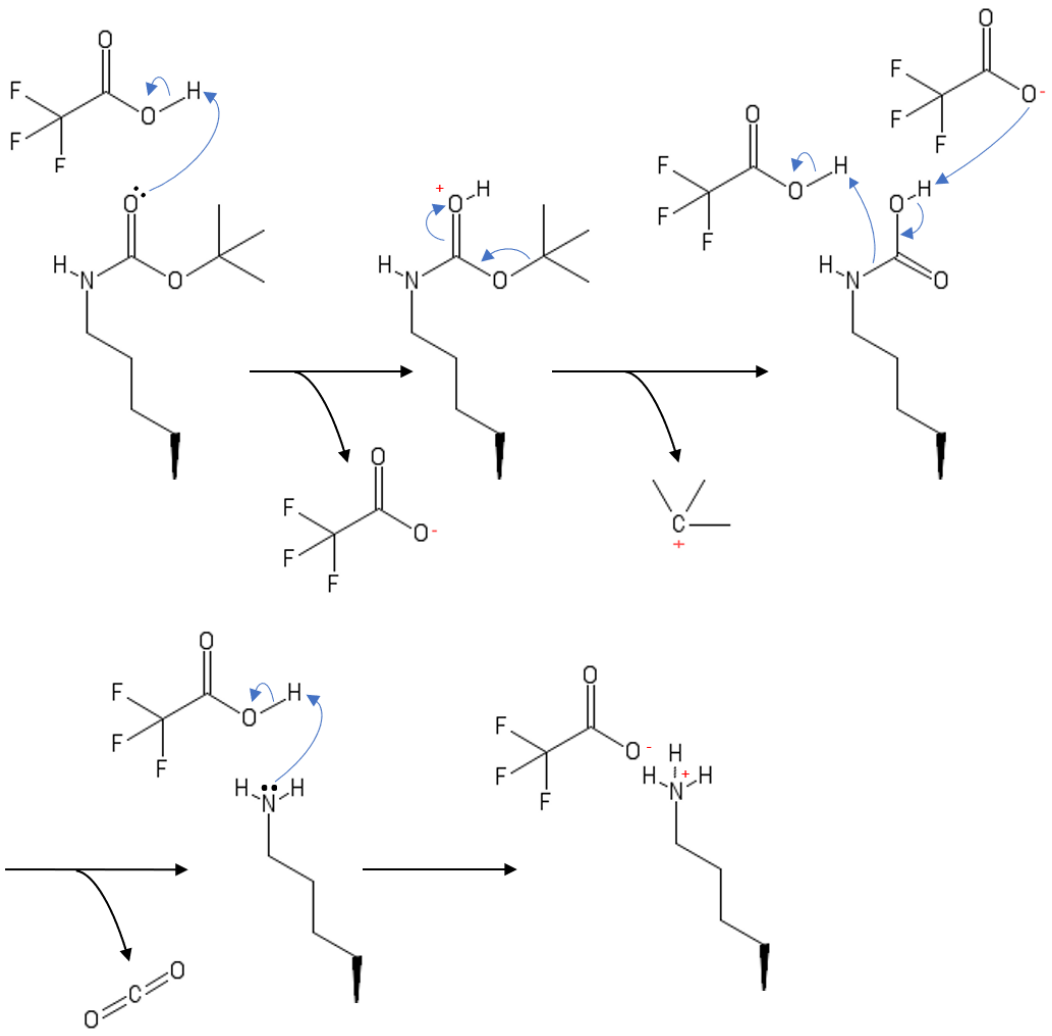

Figure 2.4. TFA cleavage of acid-labile Boc protecting group from the ε-amino group of Lys. Only the amino acid side chain is shown. The resulting product is a TFA salt.

2.1.2 Synthesis conditions used in this thesis

All peptides were assembled on a Liberty Blue microwave peptide synthesiser (CEM Corporation) using standard Fmoc/ ^{t}Bu protocols. Peptides were made at 0.1 mmol scale. Resin loading was between 0.3 mmol / g and 0.6 mmol / g. The choice of resin depended on the desired C terminus functional group. For carboxylic acids, pre-loaded Wang resins were used. For amides, 4-methylbenzhydrylamine (MBHA) rink amide resins were used. Amino acids were added in 5x excess (0.5 mmol). HBTU/DIPEA were used as coupling reagents (0.5 mmol HBTU, 1.0 mmol DIPEA). N-α Fmoc deprotection was achieved using 20 % piperidine in DMF. Exemplary conditions used for microwave deprotection and coupling are given in Table 2.1. For longer sequences, double coupling was performed. For Arginine, both deprotection and coupling was performed at a lower temperature for a longer time (deprotection 75°C, 60W, 180s; coupling 75°C, 60W, 300s). Following synthesis, the peptide was cleaved using 95 % TFA, 2.5 % TIS and 2.5 % H_2O (v/v), precipitated from the acidic solution using cold diethyl ether, re-suspended in H_2O and lyophilised using a VirTis Benchtop Pro 8ZL Freeze Dryer to give a crude peptide powder.

Table 2.1. Standard coupling cycles used for SPPS of peptides in this thesis.

	Conditions		
Step	Temperature, °C	Power, W	Time, s
	Deprotection		
1	25	0	5
2	78	100	20
3	88	60	10
4	90	20	60
	Coupling		
1	25	0	5
2	80	100	20
3	86	60	15
4	90	30	120

2.1.3 Additional protocols for more challenging sequences

Some of the peptides synthesised required additional procedures. In Chapter 5, the peptide epidermicin NI01 contains an N-terminal formyl group. Formylation was performed on the resin with p-nitrophenyl formate used as the formylation agent. 5 equivalents of p-nitrophenyl formate, 10 equivalents of DIPEA and 1 mL dimethylformamide were added to the resin, which was rotated for 16 hours. The peptide was then cleaved as normal. For the triskelion capzip discussed in Chapter 6, a two-step synthesis was used. First, a tripeptide was synthesised on a rink amide resin: [NH_2- β-Ala- Lys (Mtt)- Lys (Mtt)- MBHA rink amide resin]. Mtt is an acid-labile protecting group that can be selectively removed in 1% TFA without cleaving the peptide from the resin. This produces [NH_2- β-Ala- Lys- Lys- MBHA rink amide resin], a tri-functional hub to which three peptide arms (RRWTWE) were then attached via standard SPPS procedures.

2.1.4 Purification of peptides

The peptide product obtained from SPPS requires purification. Coupling reactions may not reach completion leading to deletions in the sequence, side reactions such as guanidinylation can cause premature termination of peptide chains that result in truncated sequences, and side-products can be produced during TFA cleavage.[160] The desired peptide can be separated from these impurities using reverse-phase high performance liquid chromatography (RP-HPLC).[161]

2.1.4.1 Basic principles of gradient RP-HPLC

The basic principle in RP-HPLC separation is that peptides adsorb to a hydrophobic stationary phase packed into a column, and only elute when the mobile phase running through the column is sufficiently non-polar to compete with the hydrophobic forces that are driving adsorption. Each peptide has a unique affinity for the stationary phase, meaning different components elute from the column at different times. In this way, the target peptide can be separated from its impurities. The stationary phase consists of silica particles functionalised with hydrophobic alkyl chains (Fig 2.5). For purification of most peptides, C18 functionalisation is used. For very hydrophobic peptides, C8 or C4 columns are better as they decrease the affinity of the peptide for the stationary phase.

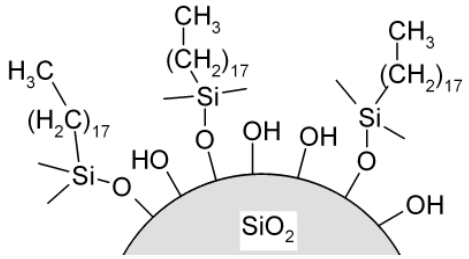

Figure 2.5. Schematic of a C18 stationary phase. The stationary phase is packed with silica particles (5 μm in diameter) that are functionalised with alkyl chains.

The mobile phase begins as a polar phase and is gradually shifted to a non-polar phase. In this thesis the mobile phase consisted of aqueous acetonitrile (ACN), starting from 10% (v/v) and increasing to 70% (v/v). To improve the separation that can be achieved, TFA is commonly added to the mobile phase to act as an ion-pairing reagent. The negatively charged trifluoroacetate (TFA-) binds to positively charged amino acids and reduces their hydrophilicity through neutralisation. This increases retention times and prevents hydrophilic peptides from flushing through the column.

2.1.4.2 Analysis of RP-HPLC fractions

Eluates are monitored by UV spectroscopy and collected from the column in fraction: the amide bond absorbs UV light at wavelengths around 214 nm and aromatic side groups at 280 nm. Each fraction containing peptide material is next analysed by mass spectrometry (MS). One of the

most widely used MS methods is matrix assisted laser desorption ionization coupled to time of flight analysers (MALDI- ToF). Advantages of this technique include soft ionization, which allows mass determination of intact peptides, high sensitivity allowing small quantities for analysis and high speed of acquisition allowing large sample sets to be analysed quickly.[162] Following MS analysis, fractions that contain only the peptide of the correct mass are combined. The purity is then confirmed by analytical RP-HPLC. The presence of a single peak indicates that no peptide contaminants are present. If additional peaks are observed, the percentage purity can be calculated by integration of the peaks.

2.1.4.3 Protocols used in this thesis

All crude peptides were dissolved in H_2O prior to purification. Semi-preparative RP-HPLC was performed on a Thermo Scientific Dionex HPLC system (Ultimate 3000) using a semi-preparative Vydac C18 5 μm column. The mobile phase was made up of two solutions: A (10 % aqueous ACN, 0.1 % TFA) and B (90 % aqueous ACN, 0.1 % TFA), (v/v). A gradient was initially run from 10- 70 % solution B over 30 min with a flow rate of 4.7 mL / min. The gradient, run-time and flow rate were then optimised for each peptide to improve separation. UV detection was at 214 and 280 nm.

MS analysis of peptide containing fractions were manually acquired using an Autoflex III mass spectrometer and the FlexControl software (version 3.0) (Bruker Daltonik, GmbH). 1 μL of each fraction was combined with 1 μL of 2,5-Dihydroxybenzoic acid, deposited onto a steel Mtp 384 Target Plate (Bruker Cooperation) and allowed to air dry (15 min) before MS characterisation. Pure fractions were combined and analytical RP-HPLC performed on a 300 μL sample using a Thermo Scientific Dionex HPLC system (Ultimate 3000) with an analytical Vydac C18 5 μm column and two solutions: A (10 % aqueous ACN, 0.1 % TFA) and B (90 % aqueous ACN, 0.1 % TFA), (v/v). A gradient was run from 10 - 70 % solution B over 30 min with a flow rate of 1 mL / min. UV detection was at 214 and 280 nm. If > 90 % purity was observed the fractions were lyophilised using a VirTis Benchtop Pro 8ZL Freeze Dryer and stored at -80 °C until use. If < 90 % purity was observed fractions were re-purified. The final MALDI-ToF mass spectrometry spectra and analytical RP-HPLC traces for all peptides synthesised in this thesis are shown in the appendix (Fig A.1- A.8). The yields, calculated from the theoretical mass of the peptide produced from 0.1 mmol synthesis scale, ranged from 5% (more complex or longer sequences such as epidermicin NI01 (Chapter 5) and Capzip (Chapter 6) to 20% (simple linear sequences, bienA and bienK (Chapter 3) and triAMP (Chapter 4).

2.1.5 Preparation of peptide stock solutions for use in experiments

For use in experiments, lyophilised peptide was brought to room temperature and 1 mg was dissolved in 1 mL H_2O. The concentration of this stock solution was determined using the

Beer-Lambert Law (Eq. 2.1, where A = absorbance, ε = molar extinction coefficient, (M^{-1} cm^{-1}), c = concentration, (M) and l = optical path length, (cm)).

$$A = \varepsilon c l \qquad (2.1)$$

The molar extinction coefficient ε of peptides at 280 nm can be theoretically estimated through Equation 2.2 below. This combines the contribution of the intrinsic protein chromophores that absorb at 280 nm; aromatic tryptophans and tyrosines, and disulphide bonds.[163]

$$\varepsilon = n_W \varepsilon_W + n_Y \varepsilon_Y + n_C \varepsilon_C \qquad (2.2)$$

$\varepsilon_W = 5500$ M cm^{-1}, $\varepsilon_Y = 1490$ M cm^{-1}, $\varepsilon_C = 125$ M cm^{-1} and $n_{W,Y,C}$= number of tryptophan, tyrosine and cysteine residues in the sequence.

If no tryptophan, tyrosine or cysteine was present in the sequence, the molar extinction coefficient of the peptide at 214 nm was estimated. Absorption at 214 nm is dominated by the amide peptide bond, but also contains contributions from amino acid side chains and the theoretical estimation of ε at 214 nm combines experimentally calculated contributions from both.[164] Following concentration determination, stock solutions were aliquoted (5 μL), flash frozen, and stored at – 80 °C. Single aliquots were removed when needed and discarded after use, avoiding freeze-thaw cycles that can lead to peptide degradation.

2.2 Biophysical characterisation of AMPs by circular dichroism (CD) spectroscopy

Throughout this thesis, circular dichroism (CD) spectroscopy is used to assess the secondary structure of peptides in different conditions.

2.2.1 Basic principles of CD

CD spectroscopy measures the differential absorption of circularly polarised light. Chiral molecules absorb left- and right-handed circularly polarised light to different extents, giving rise to positive CD signals when more left-handed light is absorbed and to negative CD signals when more right-handed light is absorbed (Eq. 2.3, where $A_{L/R}$ = absorbance of left/right-handed circularly polarised light, $\varepsilon_{L/R}$ = molar extinction coefficient of left/right-handed circularly polarised light, (M^{-1} cm^{-1}) c = concentration of chromophore (M) and l = optical path length, (cm)).[165] Achiral molecules absorb left and right-handed polarisations equally and do not give a CD signal.

$$\Delta A = A_L - A_R = \varepsilon_L c l - \varepsilon_R c l \qquad (2.3)$$

2.2.2 Resolving peptide secondary structure

The peptide amide bond has two transitions accessible for CD analysis, a ππ* transition at ~ 190 nm and a nπ* transition at ~ 222 nm. Although the peptide bond is achiral, the spatial arrangement of amide bonds in the chiral field of the protein leads to a CD signal, as coupling of electronic transitions between peptide groups results in composite transitions that are optically

active.[166],[167] The composite electronic transitions are highly sensitive to the backbone orientation of the peptide bond, such that different secondary structures give characteristic CD spectra (Fig 2.6). This is extremely powerful and has led to widespread use of CD spectroscopy for determination of the secondary structure of peptides and proteins in solution.[165] For example, α-helices give CD spectra with 3 bands, a positive band at 192 nm from a perpendicular ππ* transition, a negative band at 208 nm from a parallel ππ* transition, and a negative band at 222 nm from the nπ* transition.[167]

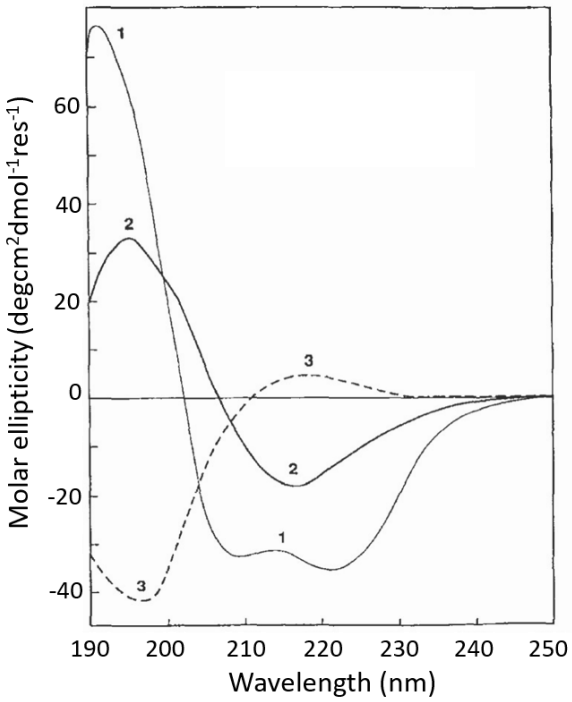

Figure 2.6. Characteristic CD spectra of different secondary structures. α-helix (1), anti-parallel β-sheet (2) and random coil (3). Reproduced from ref. [168] *with permission, © 1969, American Chemical Society.*

2.2.3 Processing and analysis

2.2.3.1 Units of measurement

Left-handed and right-handed circularly polarised light of equal magnitude superimpose to give linearly polarised light (Fig 2.7A). After interaction with a chiral sample, differential absorption of the left-handed and right-handed components means that the resulting vector is no longer linearly polarised, but traces an ellipse (Fig 2.7B). The ellipticity, θ, is the angle whose tangent is the ratio of the minor to major axis of the ellipse. This is the standard unit of measurement used in CD instruments.[169] θ is numerically related to the differential absorption ΔA by a factor of 32.98 (Eq. 2.4).

$$\theta = 32.98 \times \Delta A \qquad (2.4)$$

2.2.3.2 Normalisation

The CD signal is the sum of all peptide chromophores in the sample. In order to compare spectra recorded for peptides of different lengths and at different concentrations, θ (deg) is converted to mean residue ellipticity (MRE, [θ], (degcm^{2}dmol^{-1} res^{-1})) by Equation 2.5 (where MRW is the mean residue molecular weight, c (moldm^{-3}) is the peptide concentration and l is the path length (cm)). This normalises for the concentration of the sample and for the number of amide bonds.

$$[\theta] = \frac{\theta \times MRW \times 100}{c \times l} \qquad (2.5)$$

The use of [θ] also allows the fraction helicity of any peptide to be estimated (Eq. 2.6). This estimation is derived from experimental calculations of $[\theta]_{222}$ for proteins with 0% (3000 degcm^{2}dmol^{-1}) and 100% (33,0000 degcm^{2}dmol^{-1}) helical content.[170],[171]

$$fraction\ helicity = \frac{-([\theta]_{222}+3000)}{33000} \qquad (2.6)$$

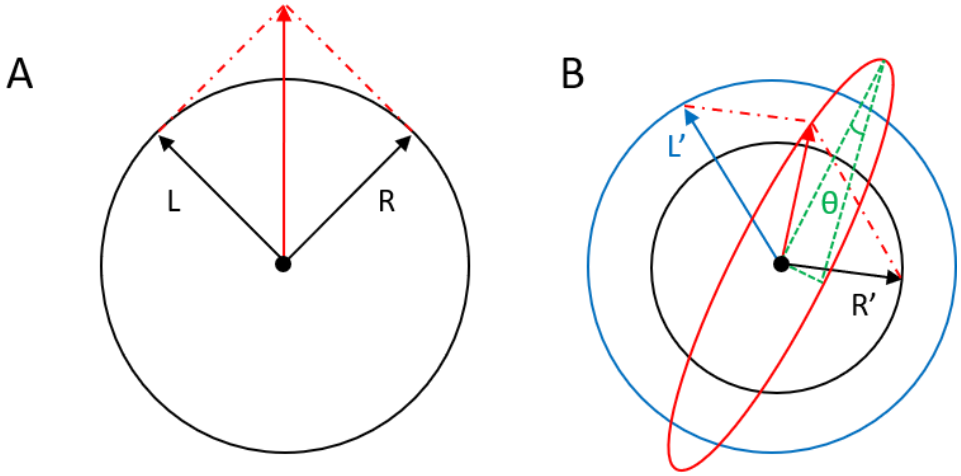

Figure 2.7. Schematic of circular dichroism. (A) The left (L) and right (R) components of circularly polarised light combine to give linearly polarised light (red); (B) After interacting with a chiral substance, the left (L') and right (R') components are no longer equal in magnitude, and their vector sum produces elliptically polarized light (red). θ, the ellipticity, is the angle whose tangent is the ratio of the minor to major axis of the ellipse.

2.2.4 Conditions used in this thesis

All CD spectra presented in this thesis were recorded on a JASCO J-810 spectropolarimeter fitted with a Peltier temperature controller. The spectra presented are the average of 4 scans. The measurements were taken in ellipticities θ (mdeg) and, after baseline correction, were converted to mean residue ellipticities [θ] (degcm^{2}dmol^{-1} res^{-1}). The data was collected from 300 to 190 nm, with a 1 nm step and 1 s collection time per step. Only data with a HT voltage below 600 V was used, as above this limit the signal to noise ratio is too low. Therefore, for some samples, spectra are truncated below 200 nm. Peptides were analysed in 10 mM phosphate buffer, pH 7.4, at 20 °C, with and without lipid vesicles (preparation described in 2.2.5) In Chapter 5 peptides were also analysed with increasing % of the solvent 2,2,2-Trifluoroethanol

(TFE). TFE promotes the formation of intramolecular hydrogen bonds and is used to assess the maximum helical propensity of a peptide.[172]

2.2.5 Preparation of small unilamellar vesicles (SUVs) for CD analysis

Four different phospholipids were used throughout this thesis to make SUVs: POPC (1-palmitoyl-2-oleoyl-sn-glycero-3-phosphocholine), POPG (1-hexadecanoyl-2-(9Z-octadecenoyl)-sn-glycero-3-phospho-(1'-rac-glycerol)), DLPC (2-dilauroyl-sn-glycero-3-phosphocholine) and DLPG (1,2-dilauroyl-sn-glycero-3-phospho-(1'-rac-glycerol)). All lipids were purchased from Avanti Polar Lipids (Alabaster, AL) in powder form and stored at – 20 °C.

For the preparation of zwitterionic SUVs, PC phospholipids were used (POPC in Chapter 5 and 7, and DLPC in Chapters 3, 4 and 6). For the preparation of anionic SUVs a 3:1 molar ratio of PC:PG phospholipids were used (POPC:POPG (3:1 molar ratio) in Chapters 5 and 7, and DLPC:DLPG (3:1 molar ratio) in Chapters 3, 4 and 6). PO phospholipids reflect the thickness and saturation commonly found in plasma membranes. DL phospholipids produce slightly thinner bilayers. Their use in Chapter 3, 4 and 6 was to enable direct comparison with computational studies performed by our collaborators.

SUVs were prepared using the vesicle extrusion method.[173] 10 mg of lipid was weighed out in a clean glass vial and dissolved in 100 μL chloroform to a concentration of 100 mg / mL. For single lipid suspensions (DLPC, POPC) this lipid-in-chloroform solution was dried under a stream of nitrogen to give 10 mg of lipid as a thin film. For mixed lipid suspensions (DLPC:DLPG (3:1 molar ratio), POPC:POPG (3:1 molar ratio)) 75 μL PC solution (100 mg / mL) and 25 μL PG solution (100 mg / mL) were combined in a new glass vial and dried under nitrogen to give a 10 mg lipid film with a 3:1 PC:PG molar ratio. The films were rehydrated in 1 mL 10 mM phosphate buffer, pH 7.4 and vortexed (3 mins) on a Vortex-Genie 2 (Scientific Industries) to give a cloudy vesicle suspension (indicative of large multilamellar vesicles with a diameter greater than the wavelength of visible light) with a final lipid concentration of 10 mg / mL. The suspension was then bath sonicated at 37 kHz for 30 min in a Fisherbrand FB11201 bath sonicator (Fisher Scientific) and forced through a mini extruder (Avanti Polar Lipids, Inc.) a minimum of 21 times. The extruder was equipped with a 50 nm polycarbonate membrane (GE Healthcare Lifesciences) and the final extruded suspension was taken from the opposite side to the initial insertion to ensure that all vesicles in the final solution have passed through the membrane. This gives a clear solution of SUVs with diameters ~ 50 – 100 nm. For CD analysis, peptide: lipid ratios of 1:100 were used. The required volume of 10 mg / mL SUV solution was combined with the required volume of peptide stock solution, before being diluted with 10 mM phosphate buffer, pH 7.4 to give a sample volume of 300 μL and the final peptide concentration stated.

2.2.6 Thermal melts

CD spectroscopy is also commonly used to assess protein secondary structure as a function of temperature.[174] Depending on stability, proteins lose some or all of their secondary structures at higher temperatures. For α-helices, the change in mean residue ellipticity at 222 nm with increasing temperature provides information about the unfolding process. A single sigmoidal curve reveals that unfolding occurs as a single transition, whereas overlapping sigmoidal curves show unfolding occurs via one or more stable intermediates (see e.g. Fig 2.8A and B respectively).[175] A sharp sigmoidal transition from folded to unfolded states indicates that unfolding is cooperative, whereas a gradual unfolding curve indicates either a less well defined starting structure or a heterogenous population.[165],[174] The midpoint of each transition T_m, is defined as the melting temperature, and can be used to compare protein stability. The reversibility of unfolding is determined by cooling the sample down and comparing the full protein spectra taken before and after heating. For many proteins, unfolding is irreversible as aggregation and or precipitation can occur at higher temperatures.[176]

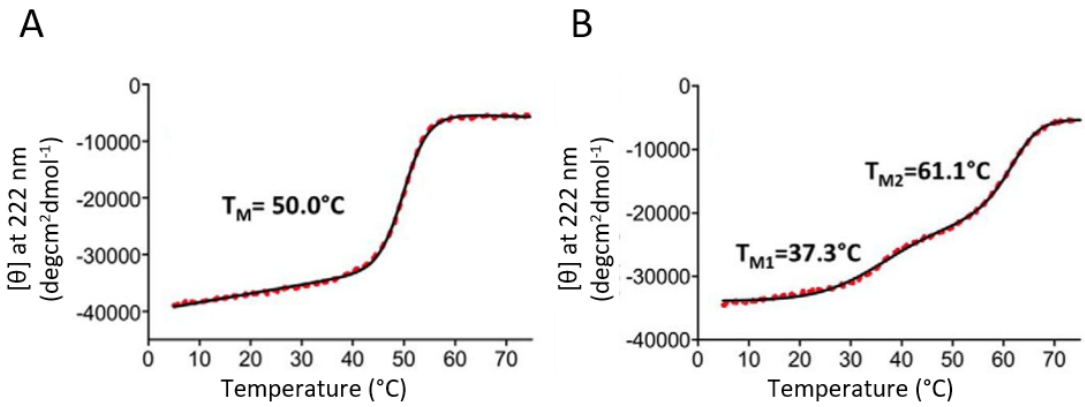

Figure 2.8. Example unfolding curves at 222 nm for two α-helical proteins. (A) a single sigmoidal curve is observed showing a single transition from a folded to an unfolded form takes place; (B) two sigmoidal curves are observed, showing two distinct transitions take place via a stable intermediate. The T_M for each transition is shown. Proteins are (A) wild type tropomyosin rat protein (1-131) and (B) a A109L mutant. Adapted from ref. [177], *licensed under CC-BY.*

In Chapter 5, thermal melts were conducted for epidermicin NI01 and aureocin A53. Spectra (300 nm to 190 nm) were taken at 2 °C intervals, with 180 s equilibration time for each, from 20 °C to 90 °C, with 2 °C / min ramp rate. Unfolding curves at 222 nm were simultaneously recorded. Peptides were analysed in 10 mM phosphate buffer, pH 7.4, at 20 µM concentration.

2.3 Biophysical characterisation of AMPs by dynamic light scattering (DLS) and electrophoretic light scattering (ELS)

In Chapter 5, the size distribution of epidermicin NI01 in solution is assessed by dynamic light scattering (DLS). In DLS, a laser light (λ = 633 nm) is shone through the sample and the scattered light is detected. Due to Brownian motion, the distance between particles in solution changes with time and the scattered light undergoes continuous constructive and destructive

interferences, giving rise to fluctuations in intensity. In DLS measurements, autocorrelation in intensity is measured. At short time delays, the intensity is similar as particles have not moved for from their original position. At longer time delays, the intensity begins to show decreased correlation which decays exponentially until there is no correlation between the scattered intensity. The autocorrelation relates to the diffusion constant of the particle, with faster moving particles decaying more quickly. As such, numerical models can be fitted to the autocorrelation function to determine the diffusion constant and, through the Stokes-Einstein equation, the hydrodynamic radius of the particles can be determined (Eq. 2.7, where D is translational diffusion constant, k_B is Boltzmann's constant, T is temperature, η is dynamic viscosity and r is the hydrodynamic radius).

$$D = \frac{k_B T}{6\pi\eta r} \qquad (2.7)$$

In addition, the approximate surface charge of epidermicin NI01 is assessed by electrophoretic light scattering (ELS). Here, an electric field is applied to the sample. Charged particles move towards the opposite electrode and, due to their mobility, the scattered light from the sample is doppler shifted compared to the incident light. The change in frequency is measured, and relates to the particle velocity by Equation 2.8 (where υ is particle velocity, θ is the scattering angle and λ is the incident wavelength). From the particle velocity, the electrophoretic mobility μ_E can be determined (Eq. 2.9, where E is the applied electric field). The zeta-potential ζ (the potential at the particle-fluid interface), can then be estimated using Henry's equation (Eq. 2.10, where ε is the solvent dielectric constant, ζ is the zeta-potential, $F(\kappa a)$ is Henry's function and η is the viscosity)[178].

$$\Delta f = \frac{2\upsilon \sin\left(\frac{\theta}{2}\right)}{\lambda} \qquad (2.8)$$

$$\mu_E = \frac{\upsilon}{E} \qquad (2.9)$$

$$\mu_E = \frac{2\varepsilon\zeta F(\kappa a)}{3\eta} \qquad (2.10)$$

For both zeta-potential and hydrodynamic radius measurements, a Zetasizer Nano (ZEN3600, Malvern Instruments, UK) was used. Epidermicin NI01 was resuspended in 10 mM phosphate buffer, pH 7.4, at a final concentration of 900 µM. DLS and ELS measurements were carried out at 25 °C (in low volume disposable cuvettes and folded capillary cells, respectively). From DLS and ELS measurements, hydrodynamic radii and zeta-potential values were obtained through the fitting of autocorrelation data using the manufacturer's software, Zetasizer Software (version 7.03), as outlined above. Zeta-potential is a mean of three independent measurements, with each measurement consisting of 10 recordings. Hydrodynamic radius is also a mean of three independent measurements, with each measurement consisting of 20 recordings.

2.4 In-liquid AFM

Following the synthesis and biophysical characterisation of AMPs, high-resolution imaging of their membrane disruption mechanisms was conducted using in-liquid AFM.

2.4.1 AFM principles

A schematic of a standard in-liquid AFM setup is shown in Figure 2.9A. A nanometre sharp tip is mounted on the free end of a flexible cantilever. The cantilever acts as a linear spring. As the tip is raster-scanned across the surface, the cantilever deflection (x) changes due to distance-dependent interaction forces between the tip and the sample (F), according to Hooke's Law (Eq. 2.11, where k is the cantilever spring constant).

$$F = -kx \qquad (2.11)$$

These cantilever deflections are continuously monitored during scanning by reflecting a laser beam off the back of the cantilever onto a quadrant photodiode.[179] The photodiode converts the intensity of the laser spot at any given time into a voltage signal. The difference in voltage between top and bottom quadrants corresponds to the vertical motion of the cantilever whilst the difference between left and right quadrants corresponds to the torsional movement.

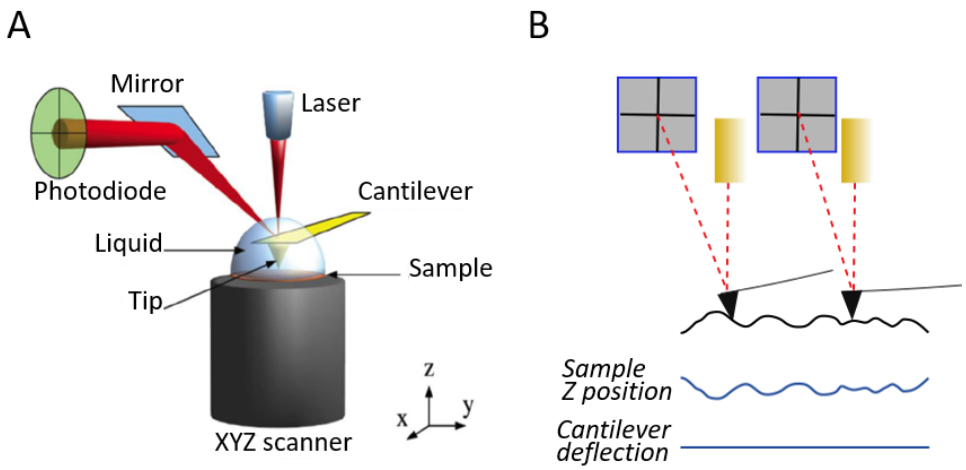

Figure 2.9. Basic principles of in-liquid AFM.A schematic of an AFM setup. The sample to be imaged is mounted on a piezoelectric scanner that can move in XYZ. A nanometre sharp tip extending from the free end of a cantilever is raster scanned across the surface. A detection laser is aligned on to the back of the cantilever and reflected onto a position sensitive quadrant photodiode using a series of mirrors, allowing the cantilever deflection to be monitored. Reproduced from ref. [180]*, with permission from Springer Nature, © 2012; (B) A schematic showing contact mode operation. The tip stays in contact with the sample during imaging. Cantilever deflection is continuously measured and a feedback system adjusts the Z position of the sample to maintain a constant, pre-defined deflection value.*

In the simplest mode of AFM operation, the tip remains in contact with the sample as it is raster scanned across the surface. The cantilever deflection is kept constant during scanning by a feedback system that continuously adjusts the Z position of the sample with a piezoelectric

positioner (Fig 2.9B).[1] Protrusions in the sample topography increase tip-sample interaction forces (and therefore cantilever deflection), and the feedback system lowers the Z position of the sample in response. Conversely, depressions in the sample decrease tip-sample interactions (and therefore cantilever deflection), and the feedback system raises the Z position of the sample in response. These precise tip-sample adjustments reflect the sample topography and are used to reconstruct a topography image.

2.4.2 Modes of operation used in this thesis

There are many AFM modes available, but most operate on the principle of adjusting the tip-sample distance to maintain an applied force. The two imaging modes employed in this thesis, amplitude modulation AFM (AM-AFM) and PeakForce Tapping (PFT), both operate on this principle.

2.4.2.1 Amplitude modulation AFM (AM-AFM)

In AM-AFM the cantilever is oscillated near to its resonance frequency at a pre-defined amplitude, which changes when the AFM tip comes in proximity of the sample surface. The imaging force depends on a set value of the amplitude, with lower amplitude setpoints corresponding to higher forces. As the cantilever is scanned across the surface, protruding sample features will dampen the amplitude of oscillation, and the feedback system will increase the tip-sample distance in response. Similarly, lower features lead to an increase in the amplitude of oscillation and cause the feedback system to decrease the tip-sample distance. A main advantage of AM-AFM is that the tip only encounters the sample at the bottom of each oscillation, removing the high lateral forces present in contact mode.[72] AM-AFM is also the fastest mode of imaging and, with suitable cantilevers, controllers, piezoelectric scanners and detection systems, this mode can be operated at up to ~10 frames per second.[181]

Cantilever oscillation in AM-AFM is generally achieved via a piezoelectric actuator attached to the cantilever holder. This method is simple, but subjects the entire fluid cell to mechanical excitation leading to a 'forest of peaks' that can couple to and distort the resonance peak of the cantilever during operation (Fig 2.10A).[182] To avoid this, direct methods of cantilever excitation have been developed including photothermal,[183] magnetic [184] and electrostatic [185] approaches. In photothermal actuation a second laser is focused near the base of the cantilever. The power of laser irradiation is modulated, causing time-dependent thermal stress in the cantilever, which induces oscillation. The modulation is adjusted to match the cantilever resonance frequency and a single, sharp peak can be obtained (Fig 2.10A). This enables stable imaging over long periods of time. However, the actuation laser can affect sensitive samples. We found that when using a drive laser with 1 mW DC power, 405 nm wavelength, spot

[1] In some AFM setups, it is the Z-position of the cantilever that is continuously adjusted.

diameter ~ 5µm and AC10 cantilevers, significant artefacts were observed in the sample topography (Fig 2.10B). Upon zooming out from areas that were subject to continuous scanning, the original scanned area appeared significantly different from its surroundings. At 0.3 mW DC power, 405 nm wavelength and spot diameter ~ 5µm no such artefact was observed (Fig 2.10C).

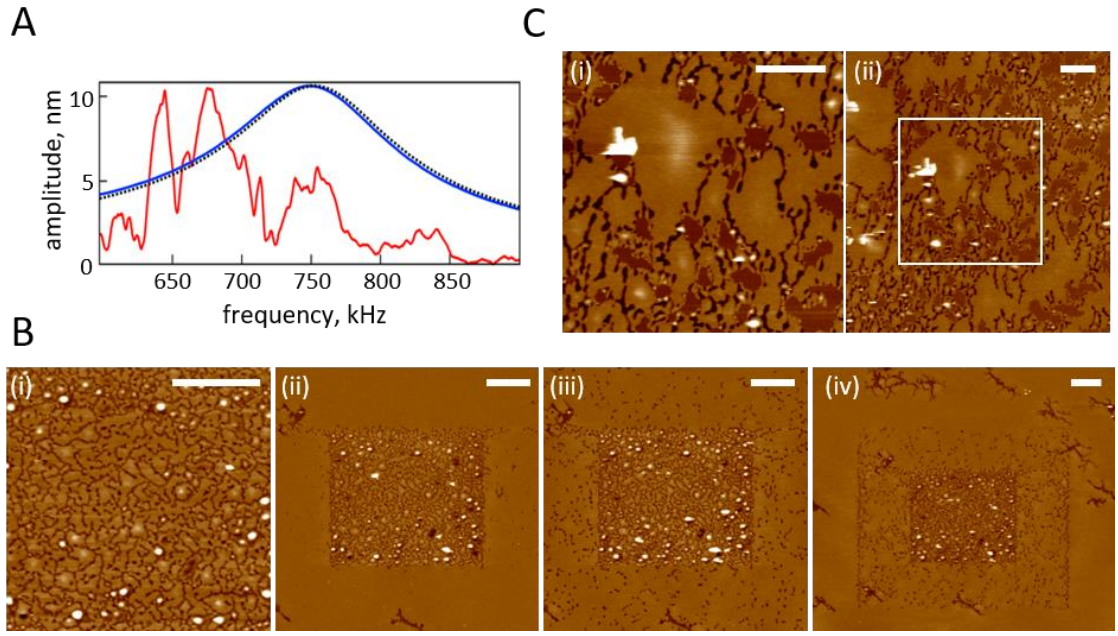

Figure 2.10. Photothermal excitation. (A) Comparison of cantilever response (amplitude vs frequency) for piezoelectric cantilever excitation (red) and photothermal excitation (blue). Piezoelectric excitation subjects the entire fluid cell to mechanical excitation resulting in multiple peaks. Photothermal methods directly excite the cantilever, resulting in a single peak. Spectra taken in water, reproduced from ref. [186]*, with permission © Microscopy Society of America 2018; (B) Scanning artefacts introduced by high input power. A 4 µm^2 topography image taken after multiple scans (i) can clearly be identified in a wider 6 µm^2 scan taken later in the same area. Persistent scanning of the 6 µm^2 area (iii) leads more scanning artefacts, and in a later, larger scan of the same area (iv) both the 4 µm^2 and the 6 µm^2 scan areas can clearly be identified; (C) Scanning artefacts are not introduced at a lower input power. A 4 µm^2 scan area subject to continuous scanning (i) is indistinguishable from surrounding sample topography subsequently recorded at a larger scale (ii). Scale bars 1 µm in (B) and (C). 1 mW DC power used in (B) and 0.3 mW in (C), both with wavelength 405 nm and spot diameter~ 5µm. All images taken on a Cypher ES system with an AC10 probe.*

2.4.2.2 PeakForce Tapping (PFT)

Another mode of AFM operation is force-distance curve based imaging.[187] PeakForce Tapping (PFT) (Bruker) is one such example and is the main imaging mode used throughout this thesis. In PFT, a sinusoidal modulation is applied to the *Z* axis at a significantly lower frequency than the cantilever resonance (typically between 1-8 kHz). A schematic of the cantilever deflection during each oscillation cycle is shown in Figure 2.11A, with the corresponding attractive and repulsive forces on the tip shown in Figure 2.11B. The cantilever response is continuously monitored throughout the oscillation cycle and proprietary algorithms

convert the deflections into force curves (Fig 2.11C). Depending on the scan speed and pixel density, around 4 force curves are produced for each pixel. The maximum deflection of each oscillation is maintained at a pre-defined value by continuous adjustments to the tip-sample distance ("Peak Force", Fig 2.11C (e)). As with other imaging modes the adjustments of the tip or sample position are used to reconstruct the sample topography.

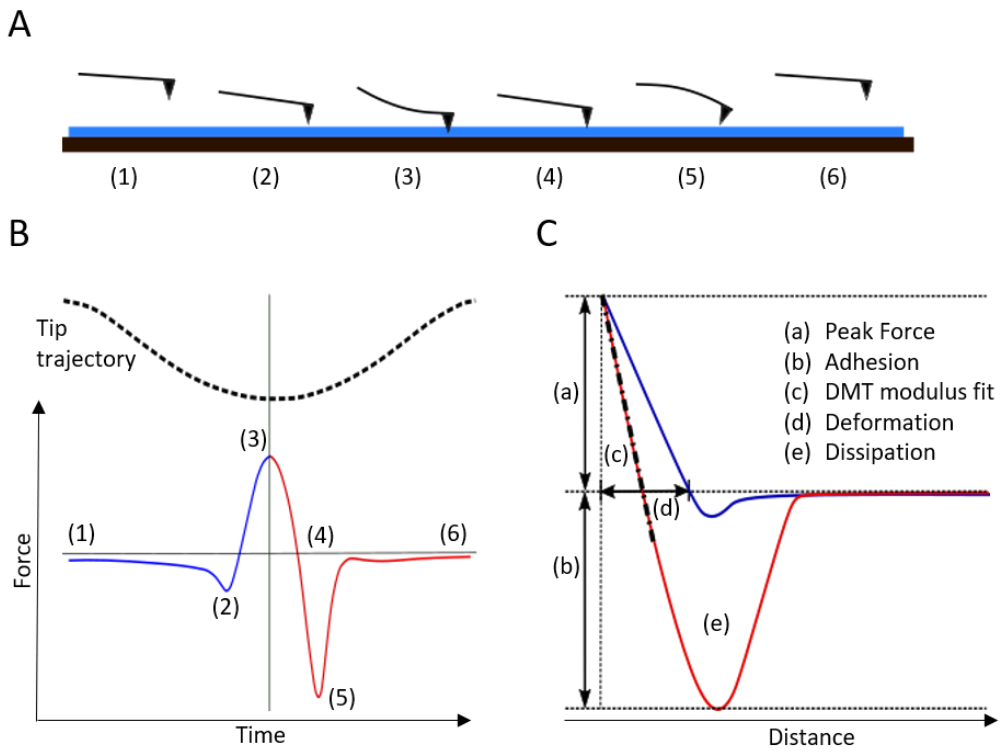

Figure 2.11. Schematic showing PeakForce Tapping operation. (A) Cantilever deflections and (B) tip-sample forces during one oscillation. The tip begins far from the sample (1) and experiences no interaction forces. As the cantilever approaches the sample it experiences attractive forces until it reaches the sample surface (2). Continued approach pushes the tip into the sample until the deflection setpoint (peak force) is reached (3). The cantilever is then retracted from the sample (4) and experiences adhesive forces (5) until contact is broken and no interaction forces are present (6); (C) Force-distance curves can be derived from the force-time curves in (B). The different mechanical properties that can be extracted are labelled (a-e) respectively. Note that dissipation (e) is found from the area inside the curve.

A main advantage of PFT is that the imaging force is highly controlled. The reference point for zero-force (Fig 2.11B, label (1), (6)) is updated with each oscillation. This allows for proper referencing of the free deflection signal (as measured when the AFM tip is not in contact with the sample), which can otherwise be affected by drift, leading to poorly defined imaging forces in AM-AFM and in contact mode AFM. Hence in force-distance based imaging, the applied force at the deflection setpoint is a more reliable measure of the tip-sample force. This enables low imaging forces (< 100 pN) to be maintained over long imaging periods.[188] The production of force curves also allows various mechanical properties of the sample to be extracted in real-time (Fig 2.11C, (b-e)). We have used PFT for its access to stable low-force imaging rather than for its ability to investigate mechanical sample properties. Only in Chapter

6, as part of the characterisation of self-assembled peptide capsules, was the modulus map used. The modulus is calculated using the Derjaguin-Muller-Toporov (DMT) model [189] from the fit of the linear gradient shown by the dot-dashed line in Figure 2.11C, label (c).

2.4.3 Cantilevers and microscopes

The majority of the data in this thesis was obtained using a MultiMode 8 AFM (Bruker) in PFT mode with MSNL-E (Bruker) silicon nitride cantilevers, with silicon tips sharpened by oxidation.

2.4.3.1 Imaging parameters

A list of the typical parameters used is provided in Table 2.2 although the exact values were regularly adjusted during scanning to optimise the imaging quality. Imaging force was kept as low as possible without deterioration of the tracking of the surface. Forces between 10 – 25 mV were used. For MSNL-E cantilever, with a spring constant of 0.1 N / m and a deflection sensitivity of ~ 40 nm / V, this corresponds to an imaging force of 40 – 100 pN. Feedback gains were adjusted throughout the experiments to yield optimal imaging conditions (sharpness and contrast of the images, low noise and no noticeable degradation of tip or sample). If the feedback is too low, the tip does not track the surface well, distorting the observed topography and making tip contamination more likely. If feedback is too high, the feedback loop artefactually enhances noise in the images. For the PeakForce amplitude, values of 10 – 20 nm were used. A low amplitude maximises the fraction of the force cycle in which the tip is in contact with the sample and topography information can be obtained. For the Lift Height, values between 7 – 15 nm were used. Lift Height is the height used to determine and remove background signals that may be affecting the data. A correct value will produce stable imaging. Most images were recorded with a scan size of 4 µm x 4 µm and a pixel density of 512 x 512, giving a pixel size of 7.8 nm. The PeakForce frequency was kept at 2 kHz and the scan rate at 1 Hz (1 line per second). This gives 2000 oscillations per line, which, when combined with a pixel density of 512 x 512, results in 4 force-distance curves per pixel.

Table 2.2. Typical imaging parameters used in PFT mode on a MultiMode 8 AFM (Bruker) with MSNL-E (Bruker) cantilevers.

Parameter	
Scan size	1000 – 5000 nm
Resolution	512 x 512
Scan rate	1 Hz
Feedback gain	20 - 50
PeakForce Setpoint	10 - 25 mV
PeakForce Amplitude	10 – 20 nm
PeakForce Frequency	2 kHz
Lift Height	7– 15 nm

2.4.3.2 Accuracy of the measurements

MSNL-E cantilevers have a nominal spring constant of 0.1 N / m, a nominal tip radius of 2 nm and a nominal tip side angle of 22.5 °. Whilst the nominal tip radius of 2 nm provides a limit to the lateral resolution of the images presented, the side angle geometry means that protruding surface features with steep edges can still be subject to broadening, and depressions in the surface can appear smaller than their true size if the geometry of the depression does not allow full entry of the AFM tip. The defects in the membrane analysed throughout the thesis are much larger than the tip (10 – 100s of nanometres) meaning that both the morphology and depth can be measured by MSNL-E cantilevers without significant risk of such tip-artefacts.

AFMs use piezoelectric materials, which expand or contract in response to an applied voltage, to control XYZ movement. The accuracy of the resulting images relies on a well-defined relationship between the applied voltage and the distance moved. All piezoelectric scanners show non-linearities in X, Y and Z, which is corrected for by calibration of the scanner. Depths reported in this thesis are therefore given with a ± 10 % confidence intervals to allow for differences in scanner calibrations.

Piezoelectric ceramics also show inherent hysteresis and creep effects that are not corrected for in calibration.[190] Hysteresis effects are such that the same drive signal does not correspond to the same position in different scan directions, resulting in a lateral shift between forward and backwards scans. To reduce artefacts from hysteresis, sequential images in time-course experiments are all taken from the same scan direction. Creep occurs when an abrupt change in voltage is applied to the scanner and the scanner continues to deform despite the voltage no longer changing. This is most apparent in AFM imaging when the scan size or location is altered. To avoid imaging artefacts, the scanner is always given time to re-stabilise before capturing more data. Creep can also lead to overshoot in the Z axis when tracing steep protrusions or depressions. This effect is unavoidable but can be reduced by using higher feedback gains. Furthermore, the MultiMode 8 uses a piezoelectric tube scanner for controlling XYZ movement. The setup of a tube scanner results in spurious coupling between the XY and Z direction that can lead to errors in the measurement of vertical angles. As the angle of membrane defect edges is not investigated here, this scanning artefact does not affect the interpretation of data.

2.4.3.3 Cypher ES

For the images in Figures 5.5F, 5.6A, 5.6C, 5.7, 5.16 and Video A.1, A.2, a Cypher ES AFM was used. These experiments were conducted with Dr. Jonathon Moffat (Oxford Instruments). The Cypher ES incorporates an additional position sensor that measures position independently of the applied voltage and applies a corrective voltage to counter the effects of hysteresis and

creep. It also uses piezoelectric stacks which decouple XY and Z electrodes, giving more accurate measurement of vertical angles than a tube scanner. The Cypher ES was operated in AM-AFM mode, using photothermal excitation, with an Olympus AC10 probe (nominal resonance frequency in air = 1500 kHz; nominal spring constant = 0.1 N / m, tip radius < 10 nm, tip side angle = 10 °). As with PFT imaging, the imaging parameters were continuously optimised to obtain the lowest imaging force without sacrificing resolution.

2.4.3.4 Post image processing

All image processing was done using Gwyddion (http://gwyddion.net/). During scanning the sample and the probe are never completely perpendicular. This introduces a tilt across the image which is removed by plane-fitting and first-order line fitting. Furthermore, piezoelectric tube scanners follow an arc not a plane meaning that all raw images taken on the MultiMode 8 show bow. This can be removed from images by subtracting higher order polynomial fits. Following plane fitting and polynomial levelling, the height at the membrane surface was centred at 0 nm to allow comparison between all images. All depth profiles were plotted using Origin (OriginLab Corporation).

2.4.4 Sample preparation for AFM analysis

2.4.4.1 AFM imaging buffer

AFM imaging buffer was prepared with 120 mM NaCl and 20 mM MOPs dissolved in Milli-Q water. The pH of the buffer was adjusted to pH 7.4 using 1 M solutions of NaOH and HCl.

2.4.4.2 Preparation of SUVs

SUVs were prepared in the same way as described in 2.2.5., but at lower lipid concentrations and in different buffer solution. 1 mg lipid was weighed out and dissolved in 100 µL chloroform to a concentration of 10 mg / mL. Single lipid suspensions (DLPC, POPC) were dried to form 1 mg lipid films and for mixed lipid suspensions (DLPC:DLPG (3:1 molar ratio), POPC:POPG (3:1 molar ratio)), 75 µL PC solution (10 mg / mL) and 25 µL PG solution (10 mg / mL) were combined in a new glass vial and then dried under nitrogen, to give a 1 mg lipid film with a 3:1 PC:PG molar ratio. The lipid films were rehydrated in 1 mL of AFM imaging buffer to give lipid suspensions of 1 mg / mL. These were vortexed, sonicated and extruded as described in 2.2.5., to give a final SUV suspension of 1 mg / mL. Again, PO phospholipids are used in Chapter 5 and 7 while DL phospholipids are used in Chapter 3, 4 and 6.

2.4.4.3 Preparation of AFM substrates

All imaging was done on mica substrates. These were prepared on steel discs (⌀ 15 mm, Agar scientific) (Fig 2.12A) to be compatible with magnetic AFM sample holders. The top surface of the steel disc was made hydrophobic with a self-adhesive fluorinated ethylene propylene (FEP)

coated Bytac laminate (Sanit-Gobain Performance Plastics Corp) (Fig 2.12B). A smaller mica disc (⌀ 9.9 mm, Agar scientific) was then glued to the FEP surface with Araldite® 2-part epoxy resin (Huntsman Advanced Materials) (Fig 2.12C). This gives a hydrophilic (mica) surface, surrounded by a hydrophobic (FEP) layer, which reduces leakage of the aqueous solution during imaging.

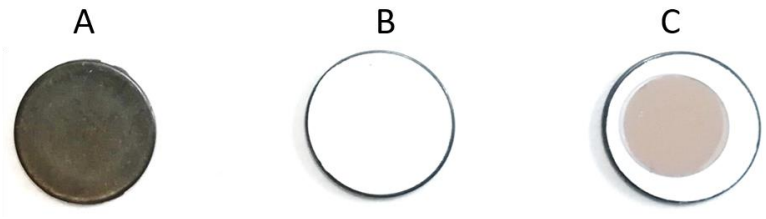

Figure 2.12. Assembly of mica substrates for AFM. (A) Magnetic steel sample disc; (B) PTFE adhered to magnetic steel sample disc; (C) Mica disc glued to PTFE surface using Araldite® 2-part epoxy resin.

2.4.4.4 Formation of SLBs

Supported Lipid Bilayers (SLBs) were formed using the vesicle fusion method.[74],[75] The success of vesicle adsorption and rupture into a continuous lipid bilayer depends a number of factors including favourable lipid-substrate interactions, vesicle curvature costs and the availability of neighbouring vesicles or pre-formed bilayer patches to induce vesicle rupture.[76] Bilayer formation can be optimised by increasing the ionic strength of solution, such as to screen charges between lipid head groups and to enable increased packing and van der Waals interactions between acyl chains; by adjusting the pH to enhance lipid-substrate interactions; and by increasing the density of vesicles to promote neighbour induced vesicle rupture. Furthermore, the addition of divalent cations (Mg^{2+}, Ca^{2+}) can have a significant effect on bilayer formation as besides screening electrostatic charges, these cations can form a bridge between the mica substrate and the phosphate head groups.[191],[192] Vesicle size also affects the quality of the bilayer produced. Discontinuities arise if a stable vesicle adsorbs close enough to a membrane patch to prevent further vesicles adsorbing in the gap. This effect is significantly reduced for smaller vesicles [76] and we found that trapped vesicles were not observed with SUVs < 100 nm.

The following protocol was developed to reliably produce defect free SLBs. Mica discs are cleaved using scotch tape to obtain an atomically flat, clean surface. This is immediately hydrated with 70 µL AFM imaging buffer and 1.5 µL 1 M $MgCl_2$ (giving a final concentration of 20 mM Mg^{2+}). Freshly prepared SUVs (5 µL 1 mg / mL) are added and the solution is mixed thoroughly. The sample is left for 45 minutes to allow vesicles to adsorb and rupture into a fluid and continuous bilayer. Following incubation, the bilayer is washed 10 times by buffer exchange with fresh AFM imaging buffer to remove excess vesicles from solution. The SLB is then ready for subsequent AFM imaging.

It should be noted that when lipid mixtures are used, the vesicle fusion method does not always produce homogenous bilayers. Phospholipids with smaller headgroups (e.g. PE) are known to preferentially assemble in the inner leaflet of vesicles and asymmetry in the adsorbing vesicles will likely propagate to asymmetry in the resulting bilayer.[193] Phospholipids with negative charge have stronger interactions with the mica substrate via bridging divalent cations and preferentially accumulate on the proximal leaflet of the SLB, resulting in a reduced amount of anionic lipid in the distal leaflet.[194] For the PC:PG (3:1 molar ratio) phospholipid bilayers used in this thesis, the accessible amount of PG lipid in the distal leaflet may therefore be lower than 25 %.

2.4.4.5 Addition of peptide to the SLB

All peptide solutions were prepared in AFM imaging buffer, so no change in the ionic strength or pH of solution was introduced. It was found that a larger volume of more dilute peptide resulted in a more uniform response across the bilayer surface. The fluid cell used in this thesis has a volume of about 100 µL and generally, peptide solution was prepared at twice the desired final concentration with 50 µL added. Injection was performed parallel to the bilayer surface to prevent mechanical damage to the SLB, and the AFM tip was withdrawn from the surface during injection. In some experiments, imaging the disruption to the bilayer surface was more challenging and it was found that cleaner imaging was obtained if the bilayer surface was washed after peptide addition (Fig 5.8, 5.9, 5.12, 5.13, 5.14). In these cases, peptide solution was added to the SLB and incubated for 15 min, before washing the SLB 6 x by buffer exchange. This removed excess peptide and lipid from solution that was otherwise interfering with imaging. Finally, in-situ injection of peptide was performed for the images shown in Figures 5.5F, 5.6A, 5.6C, 5.7, 5.16 and Video A.1, A.2. Peptide solution was injected directly into the fluid cell via a syringe / tubing system. The imaging solution in the fluid cell is entirely replaced with the injected solution and as such, the concentration of the peptide solution was prepared at the final desired concentration.

2.5 *In vitro* biological assays

Throughout this thesis the interaction of peptides with phospholipid bilayers is compared with their activity on live cells. The assays presented were performed by Dr. Helen Lewis at the National Physical Laboratory. I assisted with the assays in Chapter 3 and 4, and Dr. Florie Desriac at Plymouth University performed some of the assays presented in Chapter 5. A brief overview of the techniques is provided below.

2.5.1 Minimum inhibitory concentrations (MICs)

A common method to measure the *in vitro* activity of an antibiotic against a bacterial isolate is to use broth microdilution assays. Sequential two-fold dilutions of an antibiotic solution are added to consecutive wells of a microwell plate. A broth suspension of the bacterial strain is

then added to each well and the plate is incubated at 37 °C for 24 hours to allow bacterial growth. The minimum inhibitory concentration (MIC) is defined as the lowest concentration of antibiotic that prevents any visible growth of bacteria. This is determined by measuring the optical density of the sample at 600 nm (OD_{600}). Positive and negative controls (bacterial suspension with no antibiotic solution, broth only) are used to give reference points for growth and no growth. At concentrations above the MIC, the solution will appear clear, with an OD_{600} typically < 0.04. At concentrations below the MIC, the solution will appear turbid, with an OD_{600} typically > 0.1.

In this thesis, 100 µL of bacterial suspension in Mueller Hinton media broth was added to 100 µL of peptide solution in a 96-well plate, and incubated for 24 hours at 37 °C on a 3D orbital shaker. Peptides were generally tested at a final concentration of 100 µM, 50 µM, 25 µM, 12.5 µM, 6.25 µM, 3.125 µM, 1.5625 µM and 0.78125 µM. All tests were done in triplicate. In broth microdilution assays, the bacterial suspension added to each well should be approximately 5 x 10^5 colony forming units per mL (CFU / mL). The CFU / mL of a bacterial suspension can be calculated by incubating dilutions of the suspension on an agar plate and counting the number of colonies formed. It can also be estimated by the OD_{600} of the suspension. In our lab, for the bacterial strains tested, a CFU / mL of 5 x 10^5 is found to correspond to an (OD_{600}) of ~ 0.002 OD. As such, bacterial suspensions were prepared at an OD_{600} of 0.004 for addition to the microwell plate.

2.5.2 Haemolysis assays

To assess the biological selectivity of the peptides, their haemolytic activity was also determined. Haemolysis is assessed by incubating peptide solution with human erythrocytes for 1 hr in phosphate buffered saline, centrifuging the sample, and analysing the absorbance of the supernatant at 550 nm.[195] This gives a measure of the concentration of haemoglobin released from the cells. Reference values of 100 % and 0 % haemolysis are given by incubation with deionized water and phosphate buffered saline respectively.

3 Switching modes of membrane disruption via a single amino acid mutation

The results in this chapter are part of a manuscript ready for submission to a peer-reviewed scientific journal: Hammond, K.; Cipcigan, F.; Nahas, K. A.; Losasso, V.; Lewis, H.; Cama, J.; Martelli, F.; Simcock, P.; Stansfeld, P. J.; Pagliara, S.; Hoogenboom, B. W.; Keyser, U. F.; Sansom, M. S. P.; Crain, J; Ryadnov, M. G. A single side-chain switch between poration and floral ruptures in phospholipid bilayers. *Ready for submission.*

3.1 Introduction

Native AMPs are often long sequences, containing a wide variety of amino acids, and - as they can have multiple functions - they may not be optimised for membrane disruption. This adds to the complexity of linking peptide sequence and structure to resulting lipid interactions, as emphasised by the ability of apparently disparate peptide sequences to induce similar modes of membrane disruption, and apparently similar sequences to induce disparate modes (shown in Fig 1.5 and Fig 1.6). To begin to address more fundamental sequence-to-mechanism relationships, it can be useful to reduce antimicrobial sequences to their very basics. The major biophysical properties that drive membrane interactions in α-helical AMPs are widely accepted to be amphipathicity and a cationic charge. This gives rise to a number of questions. What are the limits of sequence redundancy in native peptides? If amphipathicity and cationic charge are maintained, can a highly simplified sequence still induce membrane disruption, and if so, is antimicrobial activity also maintained? Within such a simplified system, at what level of complexity is the mechanism of lipid disruption controlled? Can different disruption pathways be determined at the level of an individual amino acid? If so, does this translate to disparate biological activities? To answer these questions, the first results chapter of this thesis presents a simplified peptide template, designed to trigger two distinct modes of membrane disruption via a single amino acid mutation. The template maintains the biophysical properties of amphipathicity and cationic charge but is ultrashort (7- 11 residues) and contains only two amino acid types. As well as providing a highly simplified model to study sequence to function relationships, shorter sequences with narrow amino acid compositions have lower production costs and are more attractive for translational development.

3.1.1 A simplified antimicrobial template to trigger two disruption pathways

The simplified template is an amphipathic α-helix consisting of arginine and leucine. Both possess high helical propensity, ensuring a well-defined secondary structure.[196] Furthermore, both exhibit strong interactions with lipids. Leucine is the most abundant hydrophobic residue found in AMP sequences,[2] whilst arginine forms a network of electrostatic interactions with

phospholipid headgroups.[197] As such, the designed sequence is expected to be membrane-active.

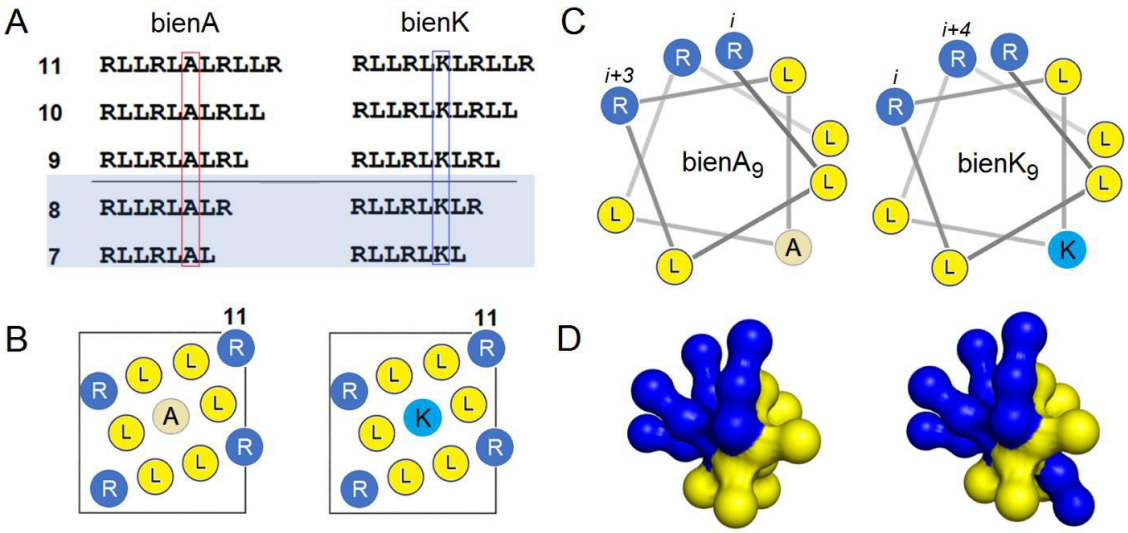

Figure 3.1. The design of two peptide series linked by a single mutation. (A) Primary sequence of the series. Peptides are designed to fold into amphipathic α-helices with leucine and arginine faces. A single mutation to alanine or lysine (bienA and bienK respectively) is placed in the middle of the hydrophobic face. To illustrate this (B) helical nets, (C) helical wheels and (D) spatial coarse-grained models are shown, with arginine in blue and leucine in yellow. This figure is part of a manuscript currently being submitted for publication in a peer-reviewed scientific journal. [2]

To activate two distinct disruption pathways of membrane disruption from this construct, a residue in the centre of the hydrophobic face was mutated. The residue was changed to either alanine (bienA series; *bi*nary *en*coded with alanine;) or to lysine (bienK series; *bi*nary *en*coded with lysine)(Fig 3.1). Alanine was chosen for the first series as a control residue. Alanine removes all sidechain atoms past the β-carbon whilst maintaining the peptide backbone structure, and alanine mutagenesis is commonly used to directly resolve the influence of specific sidechains.[198] In this case, the mutant should maintain perfect amphipathicity without introducing additional hydrophobicity (Fig 3.1A-D). This allows any changes observed for the second series to be directly attributed to the lysine side chain.

Lysine was chosen for the second series as, when protonated, the sidechain is cationic. This will cause significant disruption to the hydrophobic face of the peptide and compete with the cationic face of the peptide for lipid head group interactions (Fig 3.1A-D). Indeed, simulations run by Dr. Flaviu Cipcigan at IBM research UK predict that a cationic mutation at this location in amphiphilic α-helical peptides will induce the highest degree of orientational frustration (calculated using "data-driven helical wheels," described in ref. [199]). Therefore, bienK is expected to adopt a different conformation in the membrane to bienA peptides, which may in turn trigger a different mode of disruption. Whilst arginine could equally have been chosen, the

[2] Spatial coarse-grained models were provided by Patrick Simcock (Oxford University).

lysine sidechain can exist in its deprotonated form in a membrane environment and we hypothesised that lysine would provide a better balance between instigating distinct lipid interactions whilst maintaining membrane induced folding and activity.[197]

For both series peptides are investigated with lengths from 7 to 11 amino acids, with the mutation at residue six (Fig 3.1A). The use of ultrashort peptides, all of which are less than 3 helical turns, will further ensure that the single mutation has significant impact on peptide folding and activity.

3.1.2 Computational predictions

Simulations run by Dr. Flaviu Cipcigan at IBM research centre confirmed that the two designed series behave differently in a membrane environment. For membrane-bound bienK α-helices, the lysine side chain was observed to re-orient toward the phospholipid head groups, breaking amphipathicity and inducing significant orientational frustration to the helical structure (Fig 3.2, right) while membrane-bound bienA α-helices were observed to maintain perfect amphipathicity (Fig 3.2, left).

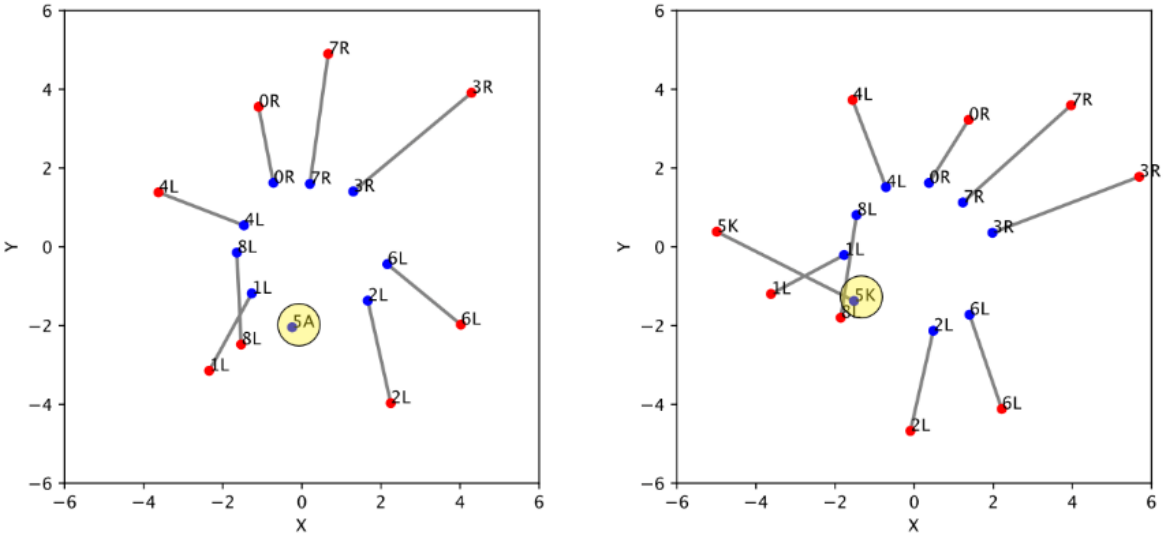

Figure 3.2. Data-driven helical wheels for bienA$_9$ (left) and bienK$_9$ (right). MD simulations are run in which the peptide sequence is initialised as an α-helix and placed in the upper leaflet of an equilibrated DLPC:DLPG (3:1 molar ratio) lipid bilayer. Blue and red circles represent the average centre of mass of amino-acid backbone and side-chain atoms respectively. Positive Y-coordinates represent proximity to the lipid head groups whilst negative values represent proximity to lipid tail groups. A mutation to lysine results in significant orientational frustration as lysine reorients its side chain toward lipid head groups. The simulations used Martini forcefields. These forcefields represent alanine as a single A bead, and consequently there is no sidechain representation for this residue. [3]

Furthermore, a substantially higher energy was required to pull bienK peptides to the centre of the lipid bilayer than to pull bienA peptides, as estimated from potentials of mean force for deliberately positioning the peptides in the bilayer in the simulations (Fig 3.3). This indicates

[3] Data was provided by Dr. Flaviu Cipcigan at IBM research UK.

that deeper membrane insertion will be less favourable for bienK. Consistent with this, 1 µs MD simulations showed bienK molecules were more likely to orient perpendicular to the membrane normal and remain in the upper leaflet whereas bienA molecules showed an increased propensity for transmembrane orientations, deeper penetration, and a higher probability of water molecules penetrating the bilayer.

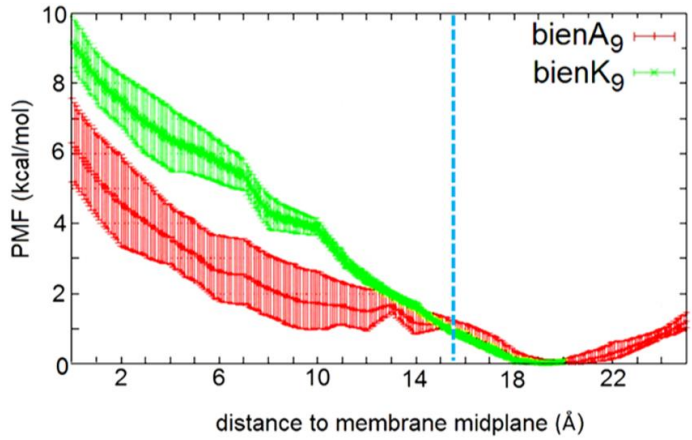

Figure 3.3. Potential mean force (PMF) calculations show that bienK$_9$ is less prone to membrane insertion. To force the peptides from the bilayer surface (dotted blue line) to the middle of the bilayer requires more energy for bienK$_9$ (green) than for bienA$_9$ (red). A DLPC:DLPG (3:1 molar ratio) lipid bilayer was used. [4]

Collectively, computational analysis indicates that the two series will induce disparate lipid-bilayer disruption modes, with bienK predicted to fold into a destabilised α-helix that results in shallower bilayer insertion and decreased permeabilisation. In this chapter, we provide experimental evidence that confirms these predictions. We resolve the two distinct modes of disruption using high-resolution AFM imaging and relate the different mechanisms to the secondary structure and biological activity of the peptides, as well as to theoretical models of membrane poration.

3.2 Results and discussion

It should be noted that throughout this chapter, the used anionic membranes consist of DLPC:DLPG (3:1 molar ratio) - consistent with the computational analysis- whilst zwitterionic membranes consist of DLPC only.

3.2.1 Secondary structure in membrane environments

BienA peptides folded into expected α-helical structures in anionic vesicles (Fig 3.4A). The degree of helicity increases with peptide length. This can result from a number of factors such as increased backbone interactions between i, i+4 residues, increased hydrophobic interactions with lipid tails and increased cationic interactions with lipid head groups. The most significant increase we observe is between bienA$_9$ and bienA$_{10}$, correlating with an increase in the size of

[4] Data was provided by Dr. Flaviu Cipcigan at IBM research UK.

the hydrophobic face (from 6 to 7 amino acids). In contrast, BienK peptides showed only partial helicity in anionic vesicles, confirming that the mutation destabilises α-helix formation (Fig 3.4B). Furthermore, no length dependent folding is observed.

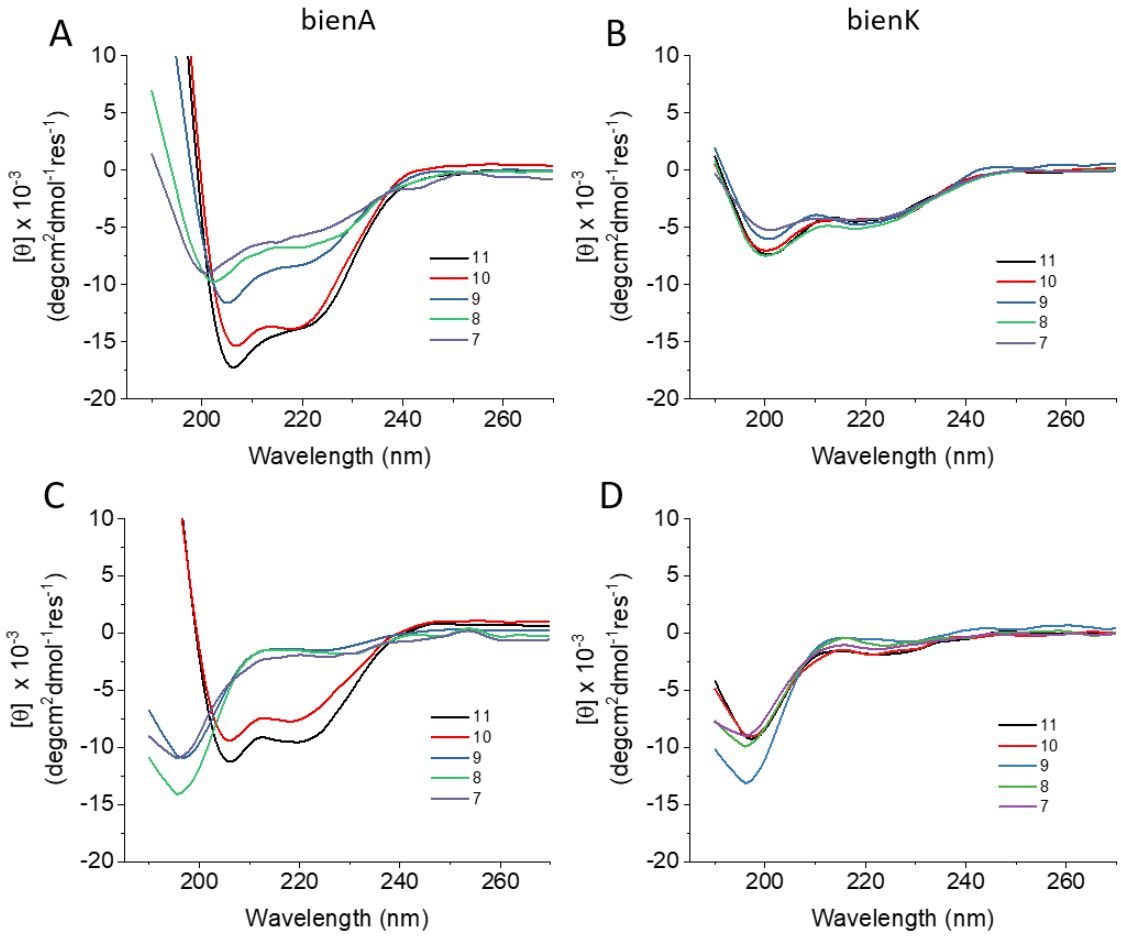

Figure 3.4. Secondary structures of bienK and bienA in SUVs. CD spectra taken in anionic SUVs (A, B) and zwitterionic SUVs (C, D) for 7-11-mers. Peptide concentration 40 μM.

When bienA peptides were incubated with zwitterionic vesicles, only bienA$_{10}$ and bienA$_{11}$ folded into α-helices (Fig 3.4C). Folding in zwitterionic vesicles relies more heavily on hydrophobic interactions with the lipid tails, as electrostatic interactions between cationic residues and negatively charged phospholipid headgroups are no longer present. The cut off in folding indicates that a hydrophobic face of 7 amino acids is the minimum length to instigate folding. This is also consistent with the large increase in helicity observed for bienA$_{10,11}$ in anionic SLBs.

BienK peptides showed no folding in zwitterionic SUVs (Fig 3.4D). This agrees with a previous study by Hawrani et al, which shows that inserting a positively charged residue to the hydrophobic face of an AMP can abolish its ability to fold in neutral bilayers.[200] The authors of the study propose that impairing the peptide ability to interact with neutral lipids is therapeutically advantageous as it will lead to reduced haemolysis (as mammalian plasma membranes contain a high proportion of neutral lipids), without reducing antimicrobial activity.

The biological activity we observe for bienK and bienA series (discussed later on in section 3.2.3.), corroborates this hypothesis.

3.2.2 Mechanisms of membrane disruption

3.2.2.1 A single mutation causes a switch in disruption mode

Having confirmed that the two series form different secondary structures in anionic lipid bilayers, we next assess their membrane interactions using AFM. Topography images of anionic SLBs following incubation with both series are shown in Figure 3.5. With the colour scale used to indicate variations in height, membranes treated with bienA peptides display darker defects, 3-4 nm in depth, consistent with transmembrane poration. In contrast, membranes treated with bienK peptides display lighter defects, 1-2 nm in depth. This provides experimental confirmation that highly simplified sequences maintain the ability to rearrange lipid bilayers, and that a single mutation can activate different modes of membrane disruption. Such distinct pathways are observed down to 9 amino acids, with shorter sequences bienA$_7$, bienK$_7$ and bienA$_8$ showing little to no disruption effects. Furthermore, not only do the peptides induce different depths, the morphology of the defects is distinct. Whilst bienA induces defects that appear more circular, bienK induces defects with fractal-like morphology.

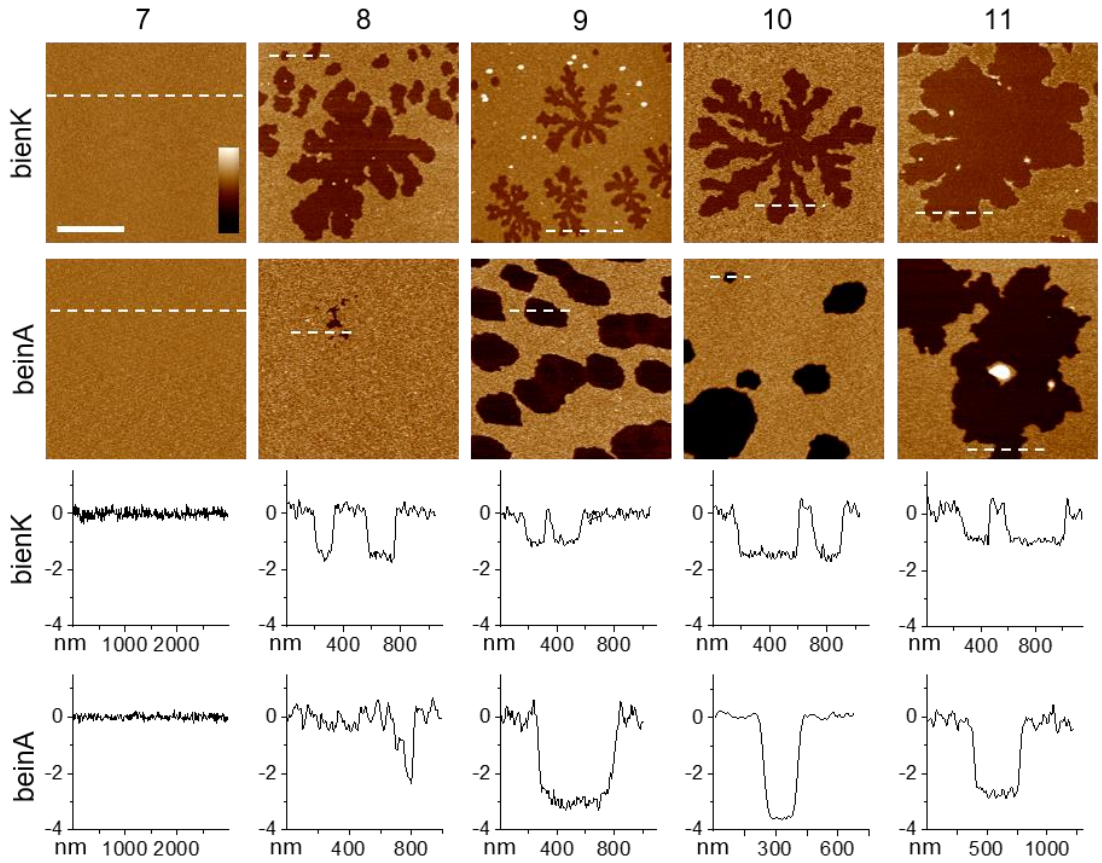

Figure 3.5. BienA and bienK activate distinct disruption modes in SLBs. AFM topography images showing anionic SLBs treated with bienK$_{7\text{-}11}$ and bienA$_{7\text{-}11}$. Corresponding line profiles are also shown. BienA is consistently observed to form deeper defects than bienK. Furthermore,

the two series induce defects with distinct morphologies. Colour scale 7 nm, length scale 1 µm. Peptide concentration 0.3 µM.

3.2.2.2 Fractal-like defects

A fractal can be defined as a self-similar object with a non-integer dimension. When a self-similar object is divided into parts each part represents a smaller copy of the full object. Objects showing self-similarity follow the scaling law (Eq. 3.1), where N is the number of segments created when dividing the object, L is the length of each segment and D is the dimension of the object. Simple geometries such as line segments ($D = 1$), squares ($D = 2$) and cubes ($D = 3$) are self-similar and have integer dimensions. Fractals are self-similar but have non-integer dimensions.

$$N = L^{-D} \qquad (3.1)$$

The box-counting method is a common approach to calculate the dimension of a fractal (D_f). In this method, the fractal is covered with a mesh of square boxes of length (L) and the number of boxes that contain a part of the fractal (N) are counted (see, e.g. Fig 3.6A).

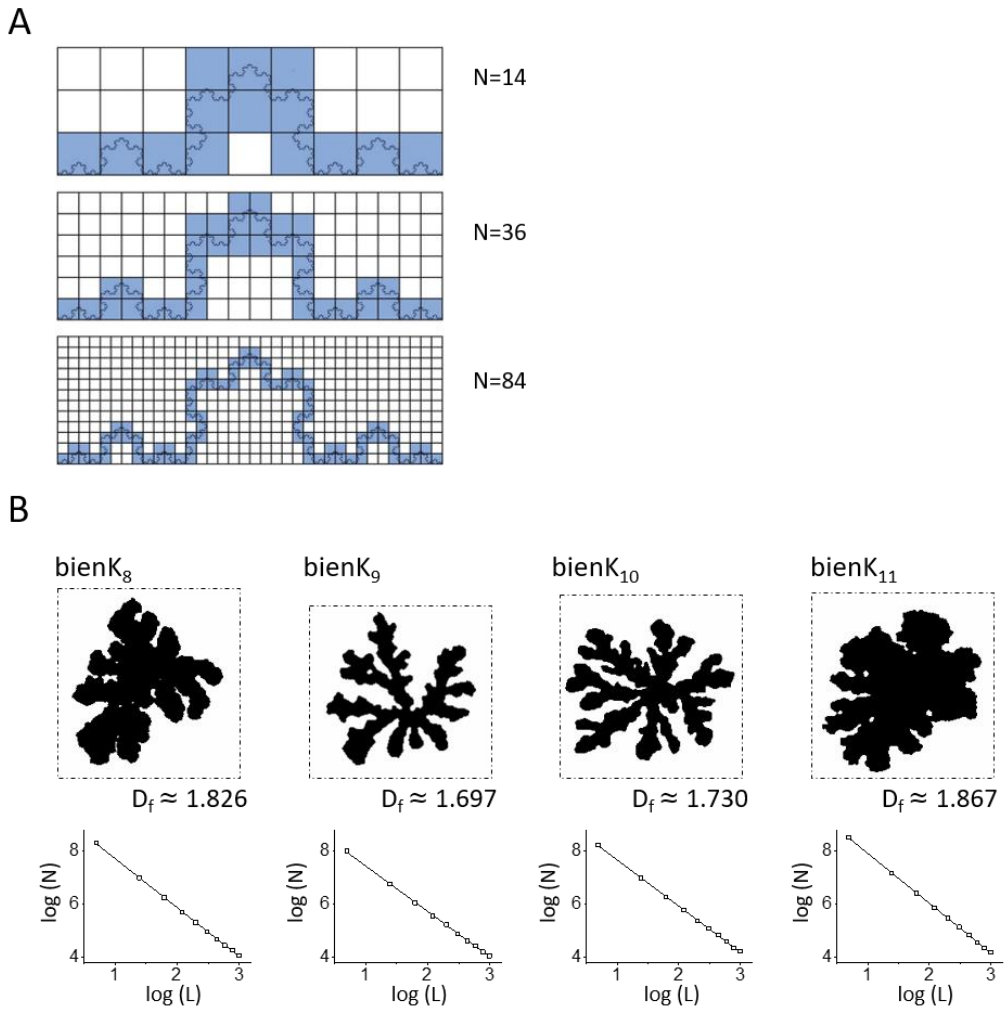

Figure 3.6. Box counting method to determine fractal dimension D_f. (A) Example of the box-counting method applied to the archetypal fractal, the Koch curve. A mesh of squares is

superimposed on the fractal, and the number of squares (N) that contain the pattern are counted. This is repeated using squares of different sizes (L). A plot of $log\ L$ vs $log\ N$ allows calculation of D_f. (B) Analysis of bienK induced defects. The defects analysed (top row) are taken from the AFM images shown in Figure 3.5. Calculated D_f values as well as corresponding log-log plots are shown. All defects show a linear relationship between $log\ L$ vs $log\ N$ and a non-integer value of D_f, consistent with fractals. Fractal analysis was performed using ImageJ, on the area shown with a dotted line. Pixel width is 200, and box sizes of 2,4,6,8,10,12,14,16,18 and 20 pixels were used.

Using the scaling law (Eq. 3.1) a plot of $\log L$ vs $\log N$ for a fractal-like defect will produce a linear relationship with a gradient $-D_f$. For all bienK peptides, plots of $\log L$ vs $\log N$ show the expected linear relationship that indicates self-similarity, and calculation of D_f give the expected non-integer dimensions characteristic of fractals (Fig 3.6). For approximately circular defects, D_f will be close to 2. Therefore, comparison of D_f values induced by different bienK peptides can provide an indication of how much the fractal morphology deviates from circular morphology. We find that D_f becomes lower with decreasing peptide length: bienK$_{11}$ (1.867), bienK$_{10}$ (1.730) and bienK$_9$ (1.697). For shorter sequences, a single lysine mutation will have a greater impact, and this may explain the increased divergence observed in defect morphology.

However bienK$_8$ does not fit the trend, showing a more similar D_f to bienK$_{11}$ (1.826). Visual inspection of the defects induced by bienK$_{11}$ and bienK$_8$ confirms a similar morphology. Furthermore, both peptides exhibit similar dynamics, forming defects that can rapidly expand and merge to the point of complete membrane disruption (Fig 3.7). This is in contrast to bienK$_9$ and bienK$_{10}$ which induce thinner fractals that show slower growth that does not proceed to complete membrane disruption over the timescale analysed (Fig 3.7).

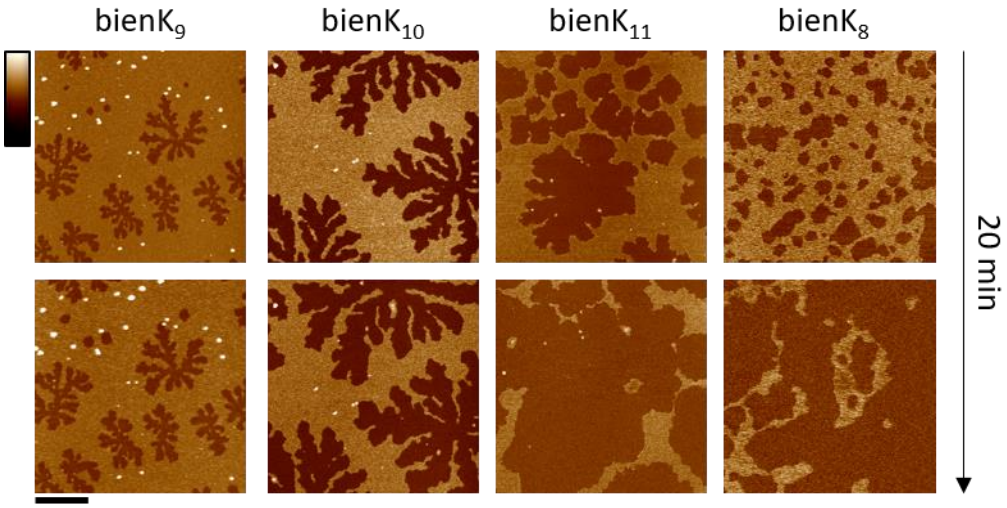

Figure 3.7. Dynamic behaviour of bienK– induced membrane disruption. AFM topography images showing the change in anionic SLBs treated with bienK over 20 min. bienK$_9$ and bienK$_{10}$ induced fractals grow slowly on this time scale. In contrast, bienK$_{11}$ and bienK$_8$ induced defects rapidly expand and merge over 20 min leading to complete membrane disruption. Colour scale 10 nm, length scale 1 µm. Peptide concentration 0.3 µM.

Examination of the sequences shows that bienK$_{11}$ and bienK$_8$ feature a C-terminal arginine, whereas bienK$_{10}$ and bienK$_9$ have C-terminal leucine. Arginine exhibits strong interactions with lipid head groups, and its location in the sequence may well influence the precise mode of membrane disruption.[197] As such, the similarity in mechanism between the two sequences with faster expansion and growth may result from the consistent location of arginine at the C-terminus.

3.2.2.3 Comparison to theoretical models of peptide-induced membrane disruption

In the classical model for membrane poration, membranes are treated as thin films under externally applied lateral tension with poration driven by the external lateral tension (σ), and opposed by the line tension of the pore (γ).[201],[202] In the case of peptide-driven poration, peptide accumulation on the membrane surface can create a stress equivalent to lateral tension σ, driving poration, whilst peptide binding to the pore edge will lower the line tension γ, further facilitating poration.[203] The energy of a pore of radius r is defined by Equation 3.2, and has a maximum at the critical radius r^* (Eq. 3.3), below which pores are unstable and may reseal and above which pores can expand.

$$E\,(r) = 2\pi r\gamma - \pi r^2\sigma \qquad (3.2)$$

$$r^* = \frac{\gamma}{\sigma} \qquad (3.3)$$

The pores formed by bienA, which have circular morphology and are observed to grow and merge over time, are consistent with this model (Fig 3.8). However, the classical model for poration cannot be used to describe the defects induced by bienK. The assumption that pores have a cylindrical, transmembrane nature does not fit either the fractal-like morphology observed, or the restriction of defects to the bilayer upper-leaflet.

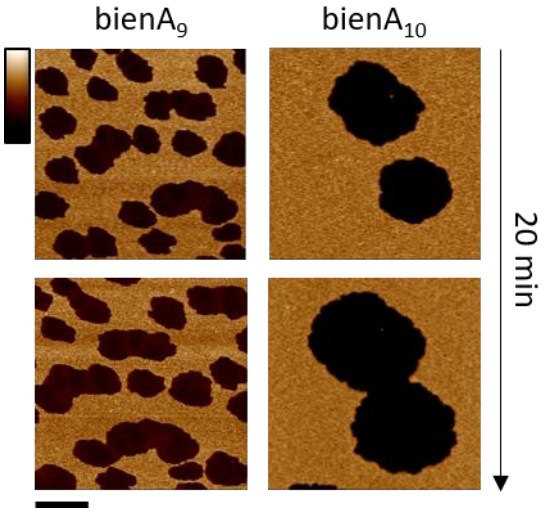

Figure 3.8. Dynamic behaviour of bienA– induced membrane disruption. AFM topography images showing the change in anionic SLBs treated with bienA over 20 min. Both bienA$_9$ and

bienA$_{10}$ induce defects that expand and merge on this time scale. Colour scale 7 nm, length scale 1 µm. Peptide concentration 0.3 µM.

Fractal-like rupture in supported membranes has previously been observed by Gözen et al, for multilamellar vesicles spreading onto a surface.[204] To describe the observations, the authors treated the membrane not as a thin film under external tension, but as a viscous fluid. Some ruptures they observed were consistent with Saffman-Taylor fingering instabilities which arise when a less viscous fluid displaces a more viscous fluid.[205] The authors proposed that in the case of supported membranes, the propagating defect can be treated as a less viscous fluid and the untreated bilayer as the more viscous fluid. Other ruptures they observed were more consistent with invasion percolation displacement, in which one fluid displaces another in a porous media.[206] Unlike Saffman-Taylor dynamics, invasion percolation occurs in bursts with the invading fluid taking the path of least resistance. The propagating defect can be thought of as the displacing fluid, with membrane heterogeneity resulting in islands of intact membrane and a fractal-like morphology. Gözen et al proposed that the spontaneous rupture they observed for multilamellar bilayers spreading on a solid support was driven by membrane-membrane adhesion. They argued that as adhesion is common in biology (such as plasma membrane adhesion to the underlying cytoskeleton) these rupture mechanisms may well occur in cell membranes.

In the case of our experiments, rupture formation and propagation are peptide induced. Despite this difference, both the morphology and the calculated fractal dimensions of the peptide-induced defects described here are consistent with the previous study, indicating that modelling the membrane as a viscous fluid is equally applicable here. For fractal-like morphology to occur in our systems, the velocity of rupture propagation must be faster than the relaxation time required for rearrangement into more favourable circular interfaces. Whether this is the case will depend on specific peptide-lipid interactions, which in turn will dictate factors such as line tension of defects and membrane viscosity. Further work is required to resolve and quantify the peptide-lipid interactions that support fractal like morphologies. Here we simply highlight that for such disruption modes, defects can be better modelled as displacement of a viscous fluid than as applied lateral tension on a thin film.

3.2.3 Biological implications for the switch in mechanism

Next, we discuss our findings in relation to the biological activity of each peptide series. The minimum length required for antimicrobial activity was found to be 9 amino acids, consistent with the cut-off length for initiating two distinct pathways of membrane disruption in SLBs (Fig 3.5). Both series are found to be active against Gram-negative and Gram-positive strains, with similar potency (Table 3.1). As such, whilst the mutation promotes a different mode of bilayer disruption, it does not appear to affect the overall antimicrobial activity.

The two series show different activity against human erythrocytes. At the same peptide concentration, bienA peptides show 25 % haemolysis whilst no haemolytic effects are observed for bienK. Collectively, and in agreement with previous studies, these results reveal that incorporation of a cationic amino acid to the hydrophobic face of a helical AMP reduces its haemolysis whilst retaining antimicrobial activity, and that this change in activity correlates with a reduced interaction with neutral lipids.[200],[207]

Table 3.1. Biological activities of bienA and bienK peptides. MIC assays show the antimicrobial activity of each series against a range of Gram-negative and Gram-positive bacterial strains. Haemolytic activity against human erythrocytes is also shown. [5]

	bienA			bienK		
	11	10	9	11	10	9
Cell	*Minimum Inhibitory Concentration, μM* [a]					
E. coli (ATCC 15597)	3	3	6	3	3	3
S. aureus (ATCC 6538)	3	3	25	12	25	12
P. aeruginosa (ATCC 27853)	3	25	50	12	25	6
S. typhimurium (DA6192)	12	6	50	50	50	50
K. pneumoniae (NCTC 5055)	6	3	50	>50	>50	>50
B. subtilis (ATCC 6633)	6	1.5	6	3	6	3
M. luteus (ATCC 49732)	1.5	1.5	1.5	1.5	1.5	1.5
	% haemolysis at 250 μM					
Human erythrocytes	25	25	25	0	0	0

[a] shorter sequences show no activity, > 100 μM

Whilst MIC assays give a good indication of antimicrobial activity, more insight into mechanism can be obtained through single cell experiments. Such experiments were carried out by our collaborators at Exeter University using a multi-channel microfluidics device, as described previously.[208] Each channel traps one cell, and is connected to a main microchamber to allow control over the incubation solution. The device is mounted on an inverted microscope, to enable bright-field images to be acquired of the channels throughout peptide treatment. Figure 3.9 shows the effects of bienA and bienK peptides on single *E. coli* cells. The cells were exposed to peptide solution for 3 hours, washed in media and incubated overnight to test for regrowth, and then stained with propidium iodide to identify cells with compromised membranes. Both bienA and bienK were found to cause cell death by compromising the cell membrane (Fig 3.9). However, with addition of bienA, susceptible cells show no growth before cell death, whereas with addition of bienK, susceptible cells are observed to elongate before cell death (Fig 3.9, top and bottom respectively). The two series showed disparate behaviour whilst still resulting in cell death. This corroborates the AFM experiments that show the two series activate different modes of disruption in lipid bilayers, and the MIC assays which indicate that despite this difference, both series remain active.

[5]Assays were performed by Dr. Helen Lewis (National Physical Laboratory) with assistance from myself.

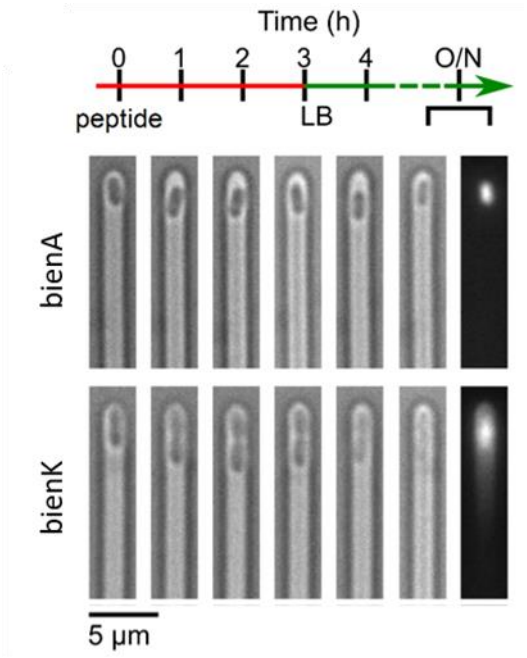

Figure 3.9. Example optical micrographs for single E. coli cells treated with bienA (top) and bienK (bottom). Peptide is added to the channels at t = 0 and bright-field micrographs taken at hourly intervals. After 3 hours of incubation with peptide the cells are flushed with fresh lysogeny broth (LB) and incubated to determine cell re-growth. Micrographs are taken at t = 4 hrs and after overnight incubation, t = O/N. The cells are then stained with propidium iodide, revealing that both peptides kill bacteria by compromising the membranes. Peptide concentration is 10 µM. [6]

3.3 Conclusions

In this chapter we have demonstrated that if amphipathicity and cationic charge are maintained, a highly simplified sequence can still induce membrane disruption, as well as antimicrobial activity. Simple, ultrashort peptides that maintain these two biophysical properties were observed to induce similar mechanisms of membrane disruption and to possess similar antimicrobial potency as native sequences, supporting the development of reduced peptide systems. A minimum length requirement of 9 amino acids was found.

Within such a simplified system, we then demonstrated that the mechanism of lipid disruption can be controlled at the level of an individual amino acid. A single mutation in the hydrophobic face, from alanine to lysine, destabilised the α-helix formed in an anionic membrane environment and switched the disruption mechanism from classical transmembrane poration with a circular boundary length, to fractal-like morphology confined to the upper leaflet. The observations agree with MD simulations that predicted helix destabilisation and shallower peptide insertion for bienK series. The defects induced by bienK cannot be explained by classical models of poration, and using parallels to a previous study on rupture mechanics of supported membranes, we propose that such modes of peptide-induced membrane disruption can be better modelled as a viscous fluid being displaced by a second invading fluid. The

[6] Experiments were performed by collaborators at Exeter University.

introduced mutation not only triggers a distinct mode of lipid disruption, but also translates to disparate biological activity, showing that this too can be controlled at the level of individual amino acids. Single-cell experiments indicate that, despite having the same antimicrobial end point, each peptide series attacks the cell in a different way. Furthermore, biological assays performed on the two series show that the mutation, despite maintaining antimicrobial activity, removes haemolytic effects. This is consistent with previous studies and correlates with the loss in ability of the peptide to interact with neutral lipids.

Having demonstrated that a simplified peptide model that maintains the core biophysical properties of native helical AMPs (cationic, amphipathic) can maintain similar lipid disruption and biological activity, the next chapter addresses whether these core biophysical properties of antimicrobial peptides can be expanded on, by incorporating motifs from other membrane-active sequences.

4 Helminth defence molecules as design templates for novel AMPs

The results presented in this chapter have been published in: Hammond, K.; Lewis, H.; Faruqui, N.; Russel, C.; Hoogenboom, B. W.; Ryadnov, M. G. Helminth Defence Molecules as Design Templates for Membrane Active Antibiotics. *ACS Infect. Dis*. **2019**, *5* (8), 1471–1479.

4.1 Introduction

To assess whether the biophysical properties of α-helical cationic AMPs can be expanded on and whether there is any advantage in this, we designed and characterised a model peptide template which, instead of folding into a two-faced hydrophobic: cationic helix, folds into a three-faced hydrophobic: cationic: T/S rich helix. This conserves not just the properties of native AMPs but also incorporates properties of α-helical peptides secreted by helminth parasites. The latter are membrane-active but non-lytic sequences, and we hypothesise that incorporating elements of these sequences may confer additional membrane properties to the template when compared to conventional AMPs.

Helminth parasites secrete many molecules whilst infecting their host. These molecules facilitate the absorption of nutrients, enable migration of the parasite through the host organism, and interact with the host immune system.[209],[210] The helminth defence molecules (HDMs) are a family of immunomodulatory peptides secreted by human trematode parasites.[211] FhHDM-1, an archetypal HDM secreted by *Fasciola Hepatica*, acts to supress the inflammatory response of its host by neutralising bacterial endotoxins,[211] preventing the activation of inflammasomes,[212] and inhibiting vacuolar ATPases in macrophages.[213]

A conserved C-terminal α-helix is found across the HDM family (Fig 4.1A,B).[211] Intriguingly, this helix shares many biophysical properties with α-helical AMPs.[211] It is amphipathic, contains cationic residues, and has polar to hydrophobic ratios of approximately 3:2.[214] Despite structural similarities to AMPs, however, the HDM α-helix does not lyse cellular membranes.[215]

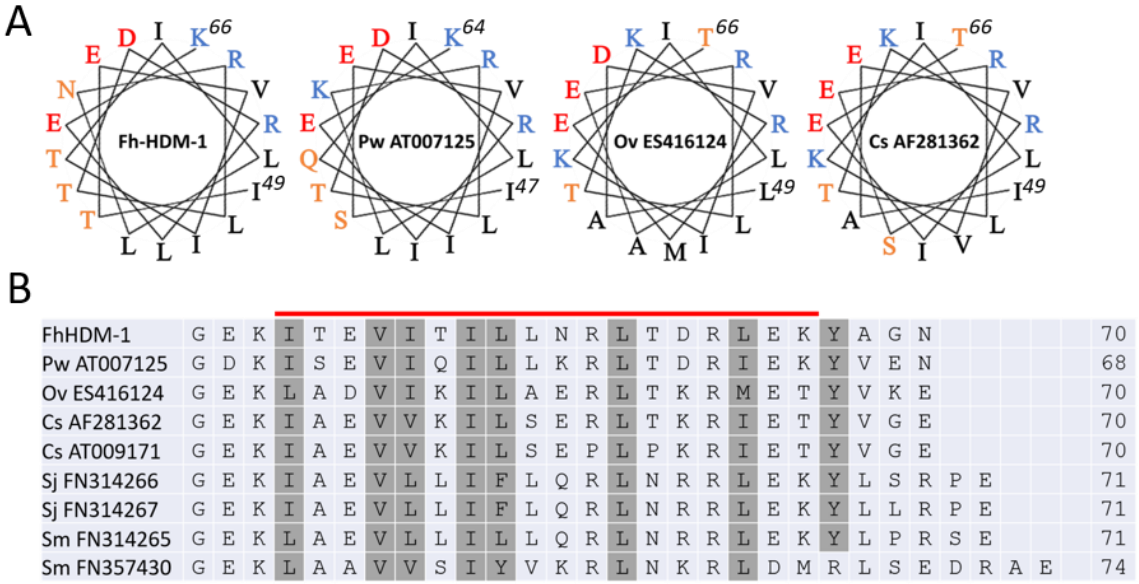

Figure 4.1. Helminth defence peptides. (A) Helical wheel diagrams of four HDM peptides. The conserved C terminal α-helix shown is highlighted by the red line in (B); (B) HDM primary sequence alignment as performed by Robinson et al.[211] *Alignment was performed against FhHDM-1. Conserved residues contributing to the hydrophobic face of the amphipathic helix are shaded in grey.*

This difference in lytic activity may be related to specific differences between HDM and AMP sequences. In AMPs, glutamic acid and aspartic acid are depleted when compared to their natural abundance in proteins (Table 4.1), whilst in HDMs, anionic amino acids appear more prominent. This lowers the net charge of the α-helix and prevents the formation of a substantial cationic face (Fig 4.1A).

Table 4.1. Comparative abundance of amino acids in α-helical AMPs

Amino acid	UniProt, %[a]	α-helical AMPs, %[b]	Relative abundance in α-helical AMPs, %
Ala	8.2	9.6	+17
Arg	5.5	5.8	+5.5
Asn	4	2.6	-35
Asp	5.4	2.0	-62.9
Cys	1.3	1.35	+3.8
Gln	3.9	2.7	-30.7
Glu	6.7	2.6	-61.2
Gly	7	9.9	+41.4
His	2.2	2.5	+13.6
Ile	5.9	7.6	+28.8
Leu	9.6	11.0	+14.5
Lys	5.8	14.3	+146.5
Met	2.4	1.2	-50
Phe	3.8	5.2	+36.8
Pro	4.7	2.8	-40.4
Ser	6.6	5.5	-16.7
Thr	5.3	2.9	-45.2
Trp	1	2.1	+110
Tyr	2.9	1.3	-55.2
Val	6.8	6.9	+1.5

[a] in all proteins calculated for the total of 559,228 entries in UniProt, *accessed Feb 13th, 2019*

[b] across 273 native α-helical antimicrobial peptide sequences collated by Eliseev et al[216] and originally sourced from the APD2 database.[217]

[c] Calculated as $\left(\frac{\alpha-\text{helical AMP \%}}{\text{UniProt \%}}\ x\ 100\right) - 100$

Furthermore, whilst threonine and serine residues are depleted in AMPs (Table 4.1), they consistently appear within the conserved HDM α-helix (Fig 4.1A). Threonine has one of the highest helical penalties among amino acids capable of forming secondary structures and the recurrent incorporation into the HDM α-helix indicates a functional role.[196] Indeed in some HDM α-helices, particularly FhHDM-1, T and S cluster together. This is reminiscent of Amphipathic Lipid Packing Sensor (ALPS) motifs, a structure used by proteins to sense and bind specific membranes.[218],[219] ALPS motifs are amphipathic α-helices with a polar face rich in T and S but lacking in charged residues (see, e.g. Fig 4.2). The absence of charged residues is thought to make the motif sensitive to both membrane curvature and to packing defects as, without electrostatic interactions to push lipid molecules apart and insert their hydrophobic residues, ALPS motifs must instead rely on pre-existing defects for insertion into a bilayer.[219]

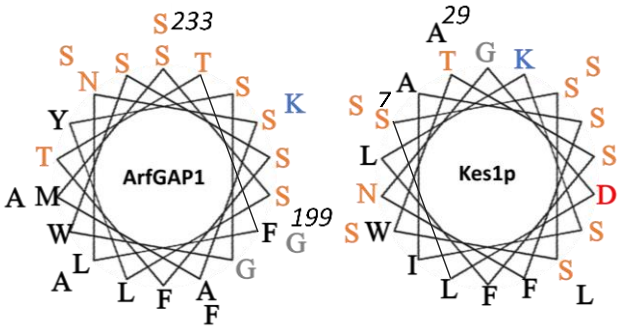

Figure 4.2. Helical wheel diagrams of two archetypal ALPS motifs. The α-helix is amphipathic, with an uncharged polar face rich in threonine and serine. Left, ArfGAP1 (res 199-223) and right, Kes1p (res 7-29).

The FhHDM-$1_{49\text{-}66}$ α-helix is unique in supporting three distinct faces; charged: hydrophobic: T/S rich (Fig 4.3A). Whilst the sequence does not lyse membranes, it is predisposed to interact with lipids and has been observed to bind to the macrophage plasma membrane.[220] We propose that this three-faced arrangement can be used as a novel antimicrobial template. In this chapter we test this hypothesis by characterising a novel antimicrobial sequence based on the FhHDM-$1_{49\text{-}66}$ template, termed triAMP (Fig 4.3A, B). In triAMP, the run of threonines from FhHDM-$1_{49\text{-}66}$ is conserved, and the T/S rich face is extended by replacing E (res 65) with S. However, the acidic residues D (res 62) and E (res 51), and the hydrophobic residue I (res 55) were replaced with the basic residue K to provide a continuous cationic face and a cationic net charge, typical of AMPs. Finally, the basic residue R (res 63) was replaced with the hydrophobic residue I, to give a continuous hydrophobic face. As such, triAMP represents an

idealised three-faced α-helix, incorporating both the T/S rich face of ALPS motifs and the cationic face of AMPs. Due to the inclusion of a more substantial cationic face and a net cationic charge, we hypothesise that the sequence will become membrane lytic. Furthermore, we propose that the additional T/S rich face may provide additional membrane active properties when compared with conventional two-faced hydrophobic: cationic AMPs.

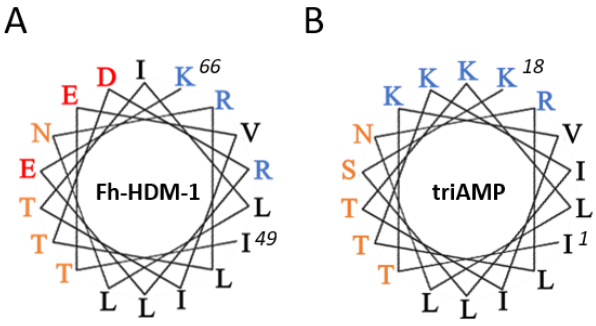

Figure 4.3. Helical wheel diagrams of (A) the native FhHDM-1$_{49-66}$ sequence and (B) the newly designed triAMP. The design is an idealised, three-faced α-helix, maintaining and extending the T/S rich face of FhHDM-1$_{49-66}$, replacing acidic residues with basic residues to form a cationic face and net cationic charge often found in AMPs, and replacing interrupting residues to ensure continuous hydrophobic : cationic : T/S rich faces. The design is expected to function as an archetypal AMP, but may possess additional properties due to the inclusion of the T/S rich face, reminiscent of ALPS motifs.

4.2 Results

It should be noted that throughout this chapter, DLPC and DLPC:DLPG (3:1 molar ratio) are used for zwitterionic and anionic vesicles (CD spectra) and SLBs (AFM data). Peptide concentrations are 40 μM for CD spectra.

4.2.1 Membrane interactions of the native FhHDM-1$_{49-66}$ α-helix

The native template, FhHDM-1$_{49-66}$, is unfolded in aqueous solution but folds into an α-helix in the presence of zwitterionic and anionic lipid vesicles (Fig 4.4A). It shows minimal distinction between the two lipid environments, consistent with ALPS motifs which fold in membranes independent of their charge.[218],[219] Despite folding in lipid bilayers, FhHDM-1$_{49-66}$ does not cause disruption to the lipid arrangements on a scale resolvable by AFM (Fig 4.4B). After 30 min incubation of both anionic and zwitterionic SLBs with a high concentration of FhHDM-1$_{49-66}$, both membranes remain flat and featureless. This confirms the lack of membrane lytic behaviour previously reported for the peptide.[215]

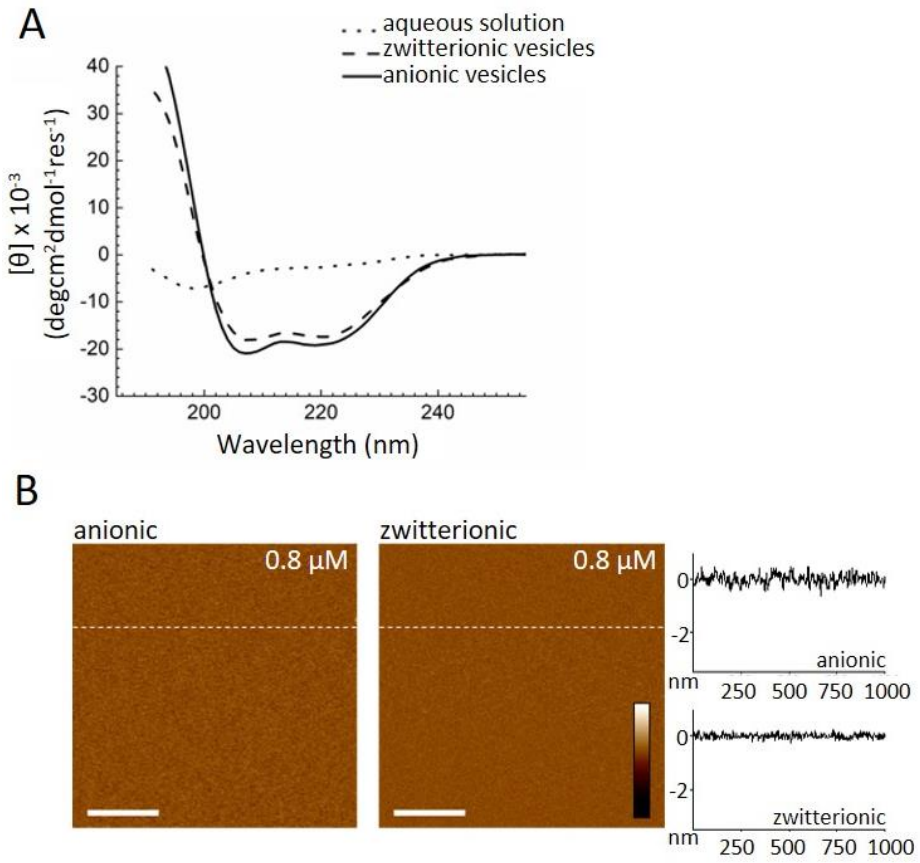

Figure 4.4. Membrane activity of FhHDM-1$_{49-66}$. (A) CD spectra showing the secondary structure of FhHDM-1$_{49-66}$ in aqueous solution and with SUVs; (B) AFM topography images of SLBs treated with 0.8 µM peptide, with corresponding depth profiles. No disruption is observed. Images are taken 30 min after peptide addition, scale bar 250 nm, colour bar 6 nm.

4.2.2 Membrane interactions of triAMP

TriAMP is unfolded in aqueous solution, but folds into an α-helix in the presence of both zwitterionic and anionic lipid vesicles (Fig 4.5A). As such, it maintains the folding behaviour of FhHDM-1$_{49-66}$. However, unlike FhHDM-1$_{49-66}$, triAMP porates anionic SLBs (Fig 4.5B (i)). Circular pores, 4 nm deep and around 25 nm wide appear across the membrane surface. This confirms that the new design is membrane lytic. TriAMP also disrupts zwitterionic SLBs, but, in the absence of electrostatic attraction, its lipid interactions differ. A higher peptide concentration is required for lipid rearrangement and, instead of poration, thinned regions appear across the surface with depths of 0.8 nm and diameters of 50-100 nm (Fig 4.5B (ii,iii)).

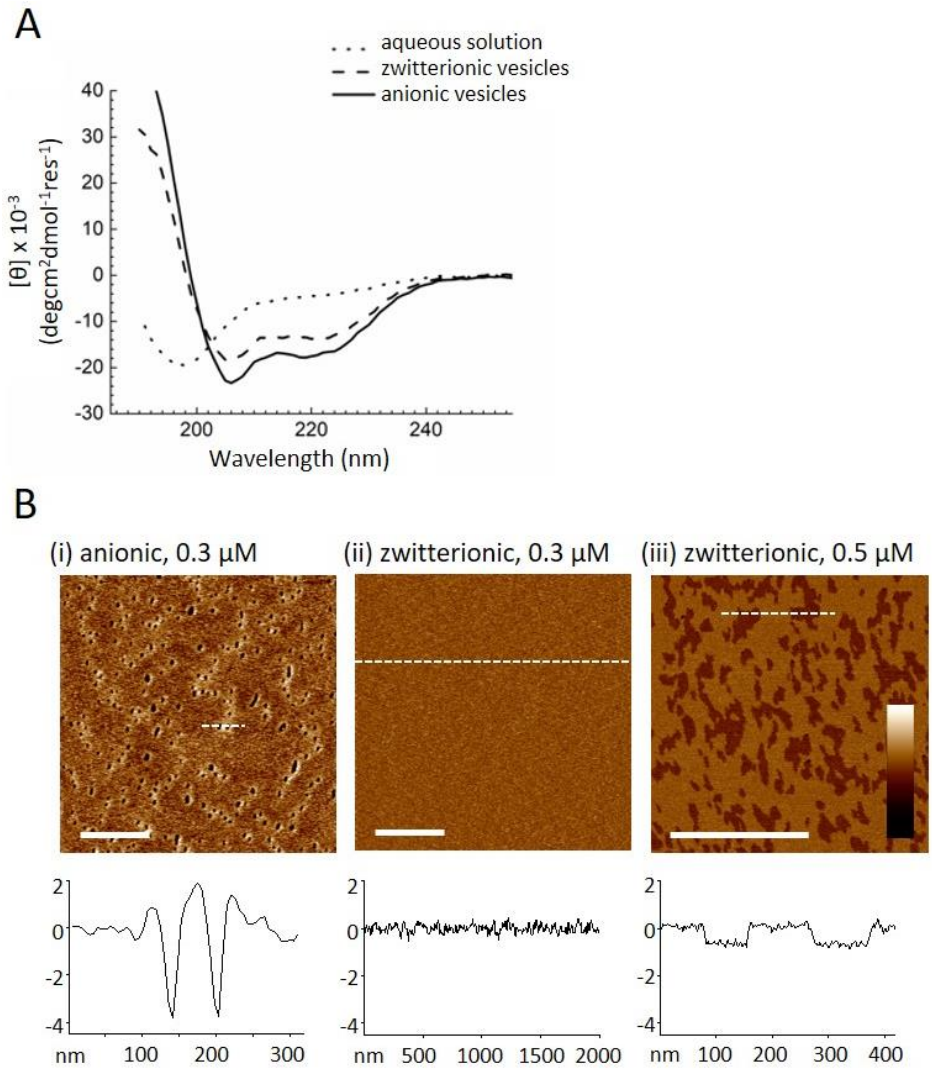

Figure 4.5. Membrane activity of triAMP. (A) CD spectra showing the secondary structure of triAMP in aqueous solution and with SUVs; (B) AFM topography images and corresponding line profiles of triAMP-treated SLBs: (i) anionic SLB after addition of 0.3 µM peptide, (ii) zwitterionic SLB after addition of 0.3 µM peptide and (iii) zwitterionic SLB after addition of 0.5 µM peptide. Images taken approx 30 mins after peptide addition, scale bar 500 nm, colour bar 6 nm.

Collectively, the membrane behaviour of triAMP is notable. Whilst responsive folding and poration of anionic SLBs is typical of cationic α-helical AMPs, responsive folding in zwitterionic vesicles and a distinct effect on zwitterionic SLBs is more unusual. For comparison, Figure 4.6 shows the membrane activity of an archetypal α-helical AMP, magainin 2. Unlike triAMP, the peptide folds only in anionic membranes, remaining unfolded in zwitterionic vesicles (Fig 4.6A). And unlike triAMP, whilst the peptide porates anionic lipid bilayers (Fig 4.6B (i)) it causes no disruption to zwitterionic SLBs, even at a 2.5-fold increase in peptide concentration (Fig 4.6B (ii)).

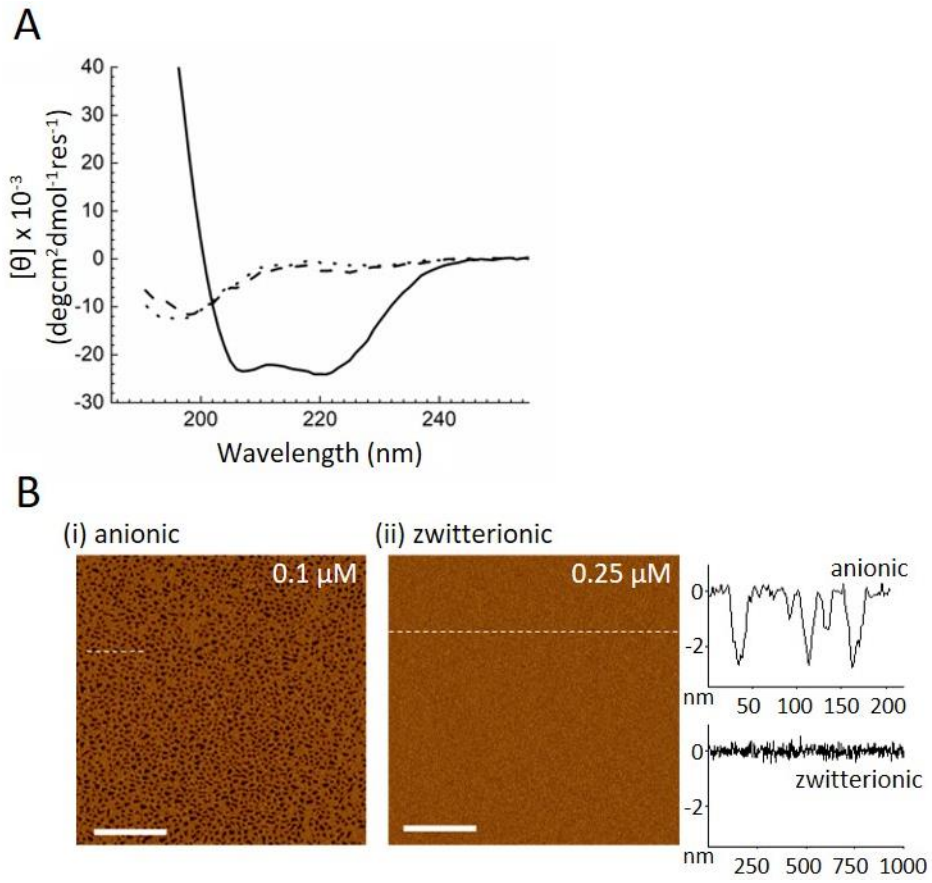

Figure 4.6. Membrane activity of an archetypal α-helical AMP magainin 2. (A) CD spectra showing the secondary structure of magainin 2 in aqueous solution and with SUVs; (B) AFM topography images and corresponding line profiles of (i) anionic and (ii) zwitterionic SLBs treated with magainin 2. No disruption of zwitterionic SLBs is observed, even at 2.5 fold increases in concentration. Images taken approx 30 mins after peptide addition, scale bar 250 nm, colour bar 6 nm.

4.2.3 Biological activity of triAMP

The biological activity of triAMP was assessed by MIC and haemolysis assays (Table 4.2). The peptide was found to be active against both Gram-negative and Gram-positive bacterial strains, with a potency comparable to archetypal AMPs and peptide toxins (magainin 2, cecropin B and melittin respectively). It was also found to be selective, with no lysis of human erythrocytes observed at 100 µM peptide. For comparison, the FhHDM-$1_{49\text{-}66}$ template was also assessed. Consistent with previous studies, no activity against bacterial cells or human erythrocytes was observed.

Taken together, results from CD, AFM and biological assays confirm that the three-faced FhHDM-$1_{49\text{-}66}$ template can be used to design a membrane lytic, antimicrobial sequence with biological selectivity. The native peptide is converted from a membrane responsive sequence, that binds and folds in lipid bilayers but has no biological activity and no ability to disrupt lipid packing, to a membrane disruptive sequence, which shows both biological activity and membrane poration. This demonstrates that the design space of *de novo* antimicrobial sequences can be extended to three distinct faces. More intriguingly, triAMP maintains the folding

behaviour of FhHDM-1_{49-66}. For many α-helical AMPs, there is a correlation between their ability to interact with zwitterionic lipid bilayers and their haemolytic activity.[221],[222] TriAMP does not follow this trend. It can fold in zwitterionic vesicles and interact with zwitterionic SLBs, whilst still functioning as a biologically selective antimicrobial peptide. To investigate this behaviour further, we design and characterise a series of triAMP mutants.

Table 4.2. Minimum inhibitory concentrations (MICs) and lysis assays of triAMP compared to archetypal α-helical AMPs (magainin 2 and cecropin B), peptide toxins (melittin) and the FhHDM-1_{49-66} template. All tests were done in triplicate. The values that are given without standard deviations are those for which no variations were found within triplicates.[7]

Cell	Peptide				
	triAMP	magainin 2	cecropin B	melittin	FhHDM-1_{49-66}
	Minimum Inhibitory Concentration, μM				
E. coli (ATCC 15597)	3.1	25	<1	2.3±1.1	>100
S. aureus (ATCC 6538)	15±2.5	>50	50	<1	>100
P. aeruginosa (ATCC 27853)	25	>50	1.5	9.4±4.4	>100
S. typhimurium (6192)	40±5	>50	1.5	3.1	>100
K. pneumoniae (NCTC 5055)	50	12	1.5	3.1	>100
B. subtilis (ATCC 6633)	15±2.5	3.1	>50	3.1	>100
M. luteus (ATCC 49732)	1.5	<1	<1	<1	>100
	% Haemolysis at 100 μM peptide				
Human erythrocytes	0	0	0	100	0

4.2.4 Investigating the role of triAMP faces

4.2.4.1 Design rationale of triAMP mutants

The five mutants are shown in Figure 4.7. In mutant 1, all T/S residues are replaced with glutamine. This maintains a three-faced template of cationic: hydrophobic: uncharged-polar, but changes the properties of the uncharged-polar face, allowing the specific contribution of T/S residues to be determined. Mutant 2 removes the T/S face completely, replacing T/S residues with isoleucine and leucine to give a cationic: hydrophobic: hydrophobic peptide. This wide hydrophobic face is typical of peptide toxins, and it is expected to act as a control sequence that interacts with zwitterionic lipids whilst also causing haemolysis. In mutant 3, the hydrophobic face is disrupted by Q to give a cationic: disrupted-hydrophobic: T/S rich peptide. This mutant was designed to confirm the necessity of the hydrophobic face for the properties of triAMP. Mutant 4 and 5 contain single amino acid mutations in the T/S rich face. In mutant 4, T13 is replaced with S, to determine whether T and S are interchangeable. In mutant 5, T6 is replaced with A to assess the whether the T/S rich face can accommodate an interrupting residue whilst maintaining its function. For both mutants, the continuous run of three threonines found in FhHDM-1_{49-66} and maintained in triAMP is disrupted.

[7] Assays were performed by both Dr. Helen Lewis (National Physical Laboratory) and myself.

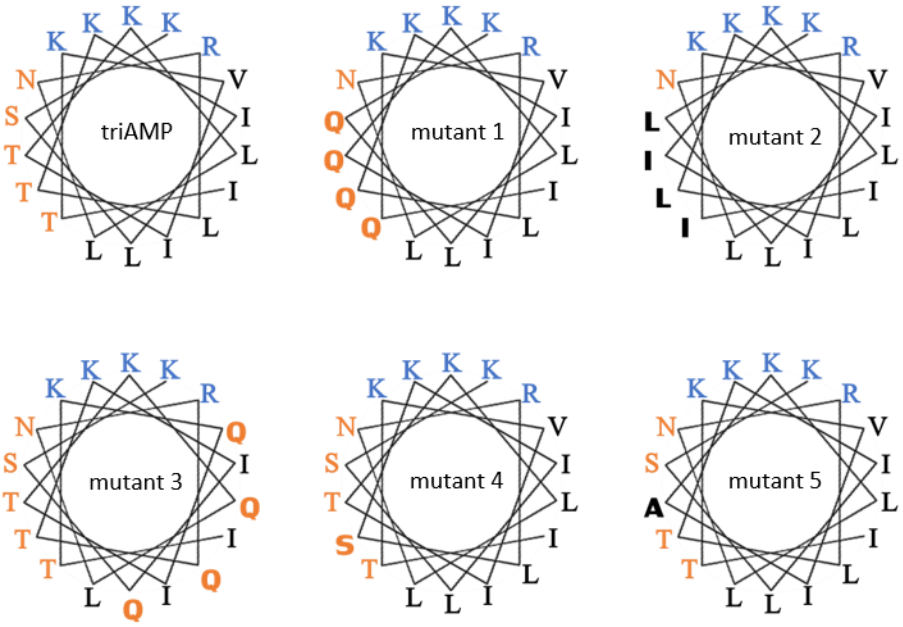

Name	Sequence	Alteration made
triAMP	ITKVITKLLNRLTKILSK	[cationic: hydrophobic: T/S rich]
mutant 1	IQKVIQKLLNRLQKILQK	[cationic: hydrophobic: Q rich]
mutant 2	IIKVIIKLLNRLLKILLK	[cationic: hydrophobic: hydrophobic]
mutant 3	ITKQITKQLNRQTKIQSK	[cationic: disrupted- hydrophobic: T/S rich]
mutant 4	ITKVITKLLNRLSKILSK	[cationic: hydrophobic: T/S rich, but without run of three Ts]
mutant 5	ITKVIAKLLNRLTKILSK	[cationic: hydrophobic: T/S rich, but with interrupting residue]

Figure 4.7. Design of triAMP mutants. Helical wheels (top) and corresponding sequences (bottom) of the triAMP mutants. Mutated residues are shown in bold and a description of the alteration to the three faced arrangement is provided.

4.2.4.2 Secondary structure of triAMP mutants

Mutant 1 only folds into an α-helix in the presence of anionic lipid vesicles (Fig 4.8A). Replacing the T/S rich face with Q leads to the loss of folding in zwitterionic vesicles, providing evidence that it is threonine and serine residues that trigger ALPS like folding. Mutant 2 has significant β-structure in all environments (Fig 4.8B). Extension of the hydrophobic face induces a switch in the preferred secondary structure of the peptide. Mutant 3 remains unstructured in all environments (Fig 4.8C). Disrupting the hydrophobic face removes the ability of the peptide to fold in lipids, showing that a continuous run of hydrophobic residues is required for the peptide to function.

Mutant 4 and mutant 5 both fold into an α-helix in the presence of zwitterionic and anionic lipid vesicles (Fig 4.8D and E respectively). This demonstrates that conserving the three faced, cationic: hydrophobic: T/S rich arrangement, conserves the ALPS like folding in which the peptide can fold in lipids despite an absence of electrostatic attraction. However, the single

mutations to the T/S rich face of triAMP do have an observable effect on peptide-lipid interactions.

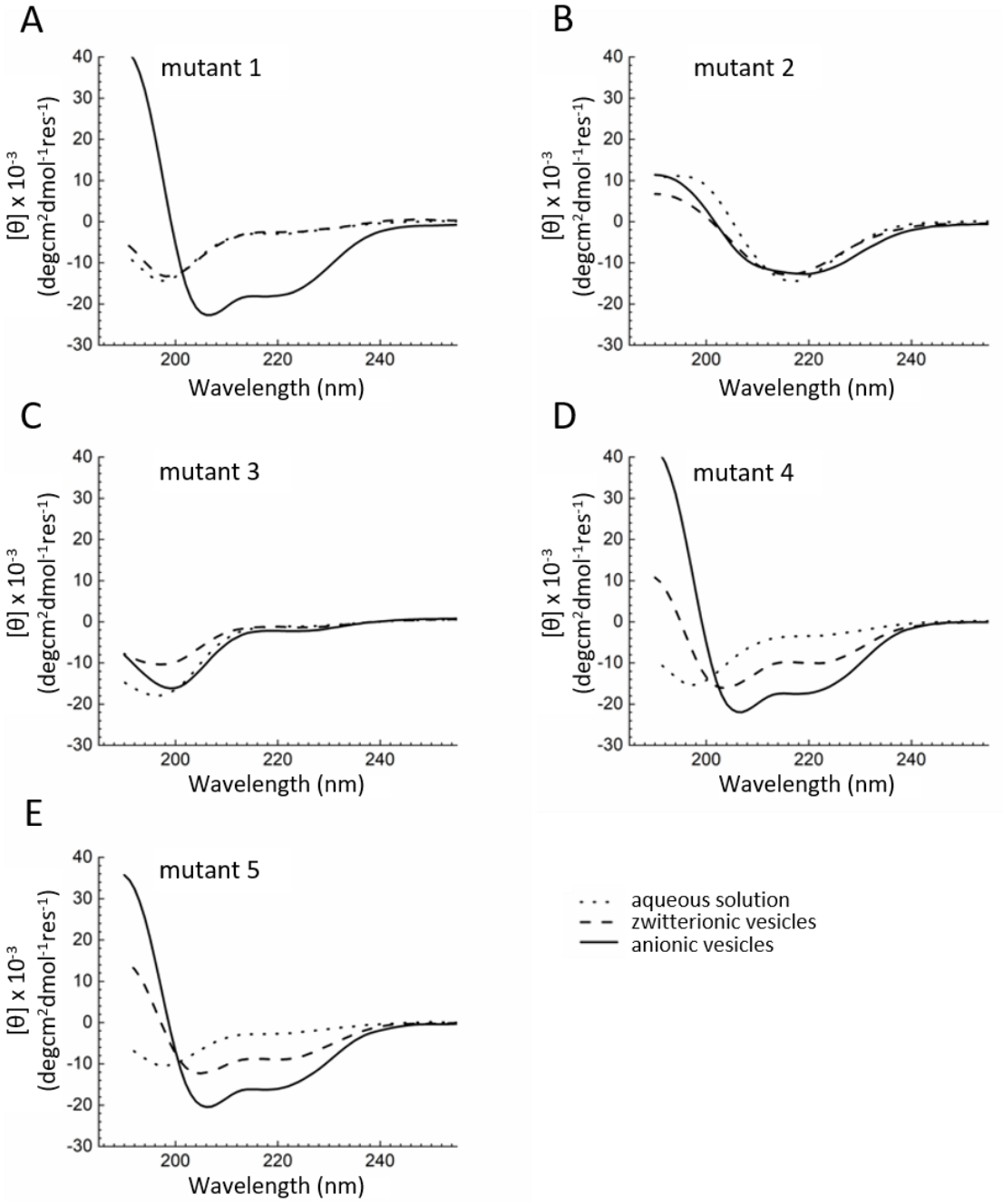

Figure 4.8. Secondary structure of triAMP mutants. (A-E) show mutants 1-5 respectively.

Whilst the helical content in anionic lipids remains similar across all three peptides, the helical content in zwitterionic lipids does not (Table 4.3). TriAMP maintains 77.5% folding in zwitterionic vesicles, whereas mutant 4 and 5 show reduced folding in zwitterionic lipids (27.6 % and 44.9 % respectively). As such, mutation to the T/S rich face of triAMP impacts the folding of the peptide with zwitterionic lipids but not with anionic lipids. This indicates that the T/S rich face in triAMP is driving lipid interactions in the absence of electrostatic attraction, but has a less significant role when electrostatic interactions are present.

Table 4.3. Comparison of percent helicity for triAMP, mutant 4 and mutant 5 in different lipid environments. Calculated using the following equation[170],[171]*:* $fraction\ helicity = \frac{(-[\theta]_{222})+3000}{33000}$

Peptide	helicity in unilamellar vesicles		$\frac{\text{zwitterionic folding}}{\text{anionic folding}}$
	zwitterionic	anionic	
triAMP	32.3 %	41.7 %	77.5 %
mutant 4	11.8 %	42.7 %	27.6 %
mutant 5	18.0 %	40.1 %	44.9 %

4.1.1.1. Effect of triAMP mutants on SLBs

Mutant 1 induces transmembrane pores in anionic SLBs, but causes no visible disruption to zwitterionic SLBs, even at higher concentrations (Fig 4.9A). This is consistent with its lack of folding in zwitterionic lipids. Overall, mutant 1 is behaving like an archetypal AMP. Mutant 2 induces transmembrane pores in anionic SLBs and disrupts zwitterionic SLBs at the same concentration (Fig 4.9B). This is consistent with its ability to form secondary structures in all lipid environments and its enhanced hydrophobic face, which will drive hydrophobic interactions with lipid tails and decrease the reliance of the peptide on electrostatic interactions. Mutant 4 and mutant 5 show strikingly similar behaviour to triAMP. Both mutants porate anionic SLBs and, at increased concentration, form thinning defects across zwitterionic SLBs (Fig 4.9C, D). For mutant 5, some patches of thinned bilayer could also be observed in zwitterionic SLBs at a lower peptide concentration (Fig 4.9D (ii)).

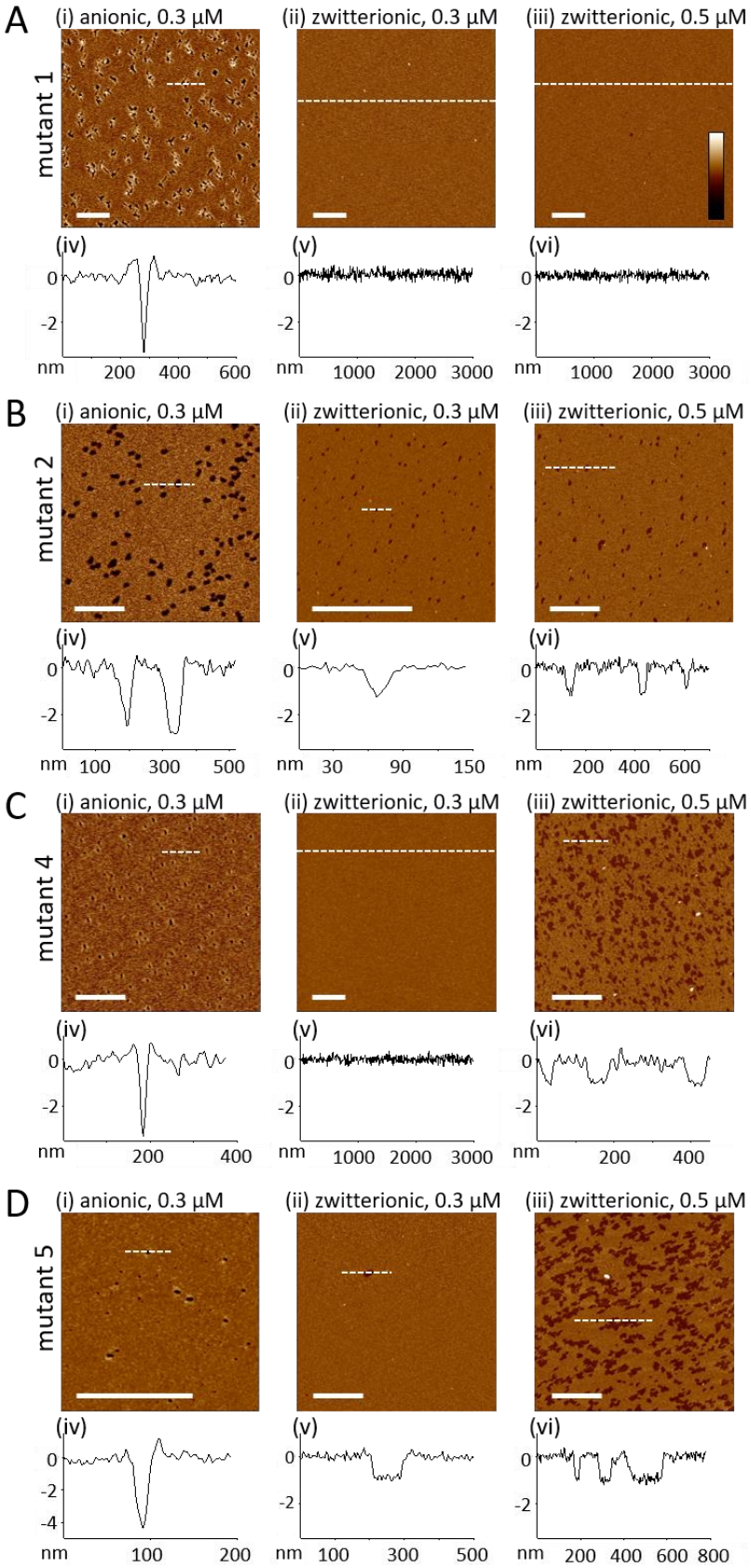

Figure 4.9. AFM topography images of SLBs treated with mutants 1, 2, 4 and 5 (A-D respectively)(i) Anionic SLB treated with 0.3 µM peptide; (ii) zwitterionic SLB treated with 0.3 µM peptide; and (iii) zwitterionic SLB treated with 0.5 µM peptide. Corresponding depth profiles are shown in (iv-vi) respectively. Scale bar in all images: 500 nm. Colour bar: 6 nm. Images taken 30 mins after peptide addition.

To further assess whether there are observable differences between triAMP and mutant 4 and 5, time-resolved AFM imaging was performed (Fig 4.10). The disruption dynamics induced by all three peptides are the same. The pores formed in anionic SLBs are stable, and do not grow over the imaging time. In contrast, the thinned regions formed by the three peptides in zwitterionic SLBs can expand and merge. Despite single mutations to the T/S rich face resulting in observable differences in the folding of the peptide with zwitterionic SLBs, no notable difference was detected in the disruption of SLBs by AFM.

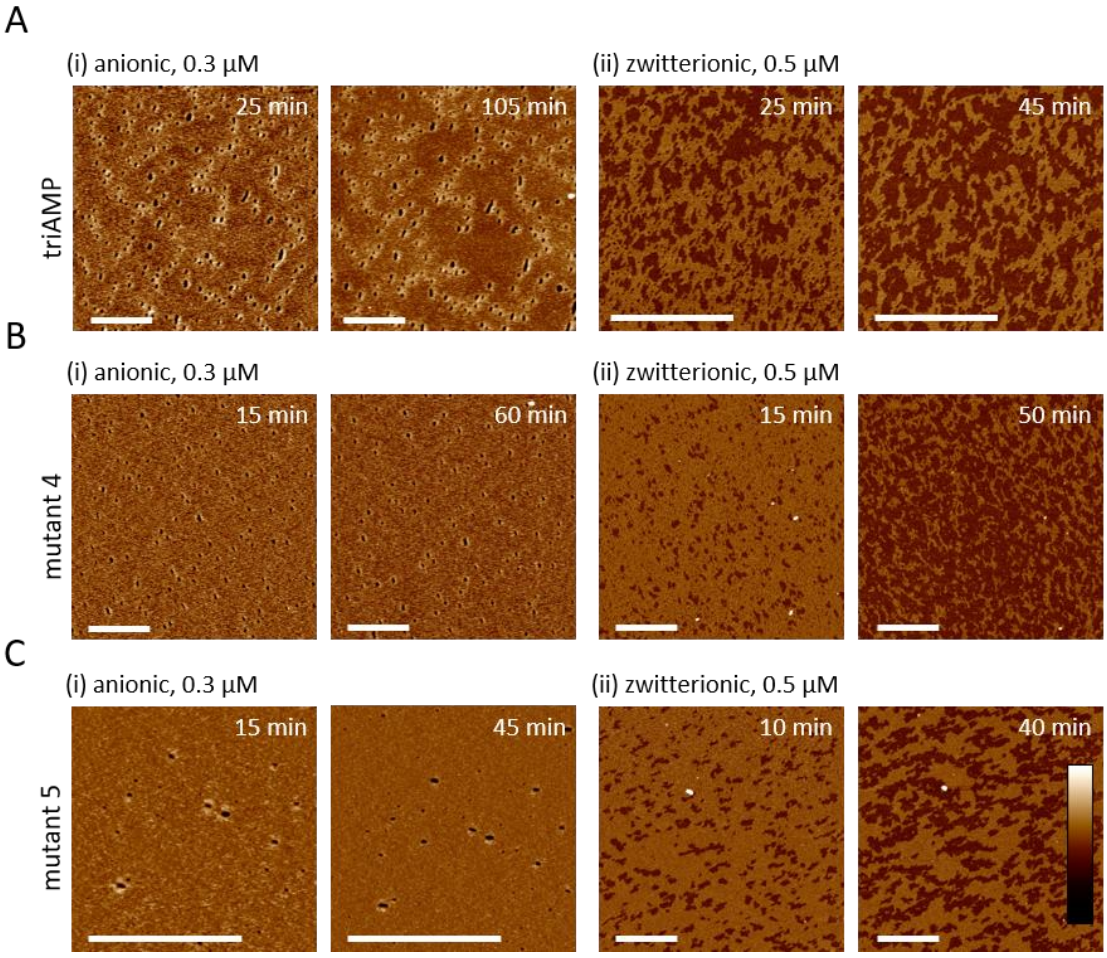

Figure 4.10. Dynamic behaviour of triAMP and mutant 4, 5. AFM topography images showing anionic SLBs (i) and zwitterionic SLBs (ii) treated with triAMP, mutant 4 and mutant 5 (A-C respectively). Time-stamps are stated in the images. Scale bar 500 nm, colour bar: 6 nm. Note that Fig 4.10A (i) 25 min is the same image as used in Fig 4.5B (i).

4.2.4.3 Biological activity of triAMP mutants

Finally, the biological activity of the mutants was determined (Table 4.4). Mutant 1 showed activity against both Gram-negative and Gram-positive bacterial strains, and no lysis of human erythrocytes. As with its membrane interactions, the sequence is behaving as an archetypal AMP. Mutant 2 showed minimal antibacterial activity but 100 % lysis of human erythrocytes. AFM reveals that the peptide self-assembles into amyloid like fibres (Fig 4.11). This is consistent with the β-sheet like secondary structure observed by CD and provides an

explanation for the toxicity but lack of antimicrobial activity. Mutant 3 showed no biological activity. This is consistent with its inability to fold in any lipid environment. Mutant 4 and mutant 5 showed activity against both Gram-negative and Gram-positive bacterial strains, as well as partial lysis of human erythrocytes at 100 μM peptide. Whilst the single mutations made to the T/S rich face of triAMP do not appear to impact the antimicrobial activity of the peptide, they do have a significant impact on its biological selectivity.

Table 4.4. Minimum inhibitory concentrations (MICs) and lysis assays of mutants 1-5 All tests were done in triplicate. The values that are given without standard deviations are those for which no variations were found within triplicates.[8]

Cell	Peptide				
	Mutant 1	Mutant 2	Mutant 3	Mutant 4	Mutant 5
	Minimum Inhibitory Concentration, μM				
E. coli (ATCC 15597)	3.1	>50	>100	2.08±0.9	3.1
S. aureus (ATCC 6538)	>50	50	>100	>50	5.2±1.8
P. aeruginosa (ATCC 27853)	3.1	>50	>100	2.08±0.9	3.1
S. typhimurium (6192)	20.8±7.2	>50	>100	16.7 ±7.2	16.7 ±7.2
K. pneumoniae (NCTC 5055)	12.5	>50	>100	25	12.5
B. subtilis (ATCC 6633)	4.2 ±1.8	37.5 ±17.68	>100	4.2 ±1.8	4.7 ±2.7
M. luteus (ATCC 49732)	1.05±0.44	25	>100	1.05±0.44	1.05±0.44
	% Hemolysis at 100 μM peptide				
Human erythrocytes	0	100	0	21.2 ± 6.8	34.01 ± 10.6

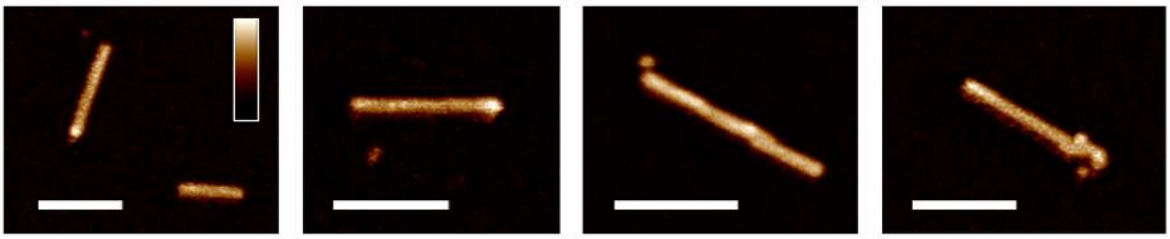

Figure 4.11. AFM topography images of mutant 2 self-assembled into fibres. Peptide was pre-incubated (2 hours, 20 mM HEPEs, 50 μM), added to freshly cleaved mica pre-hydrated with imaging buffer (120 mM NaCl, 20 mM MOPs) and visualised by AFM. Scale bars 100 nm, colour bar 6 nm.

4.3 Discussion

Firstly, we have shown that triAMP has potent activity against Gram-negative and Gram-positive bacteria and exhibits biological selectivity, showing no lysis against human erythrocytes. As such, it fulfils the basic requirements for a *de novo* AMP design. This demonstrates that the design space for antimicrobial peptides can be extended beyond the typical [cationic: hydrophobic] α-helix to an α-helix that contains an additional T/S rich face.

[8] Assays were performed by both Dr. Helen Lewis (National Physical Laboratory) and myself.

Secondly, we have shown that unlike many AMPs, triAMP does not show correlation between ability to interact with zwitterionic lipid bilayers and haemolytic activity.[221],[222] It folds in zwitterionic vesicles and can rearrange the lipid packing of zwitterionic SLBs. Yet, this behaviour does not impact on its biological selectivity. Our data indicates that to achieve both selective antimicrobial activity and auxiliary zwitterionic membrane interactions reminiscent of ALPS motifs, requires all three faces of the design. The necessity of a cationic face is demonstrated by FhHDM-$1_{49\text{-}66.}$ Without a continuous cationic face, the presence of a T/S rich face and a hydrophobic face can initiate membrane response, but not membrane disruption or antimicrobial activity. The necessity of a hydrophobic face is demonstrated by mutant 3. When the hydrophobic face is disrupted, the peptide is unable to drive membrane interactions and exhibits no biological activity. The necessity of the T/S rich face is demonstrated by mutant 1. When T and S are replaced with Q, the peptide behaves like an archetypal AMP and no longer binds, folds or disrupts zwitterionic SLBs. This provides direct evidence that it is the T/S rich face that drives the interaction of triAMP with zwitterionic lipids.

We also show that whilst the T/S rich face of triAMP drives interaction with zwitterionic lipids, it does not appear to play a major role in the interaction of the peptide with anionic lipids. When a single mutation is made to the T/S rich face (mutant 4, mutant 5), the folding of the peptide in anionic lipids remains the same. The hydropathy index of both serine and threonine is close to zero.[223] Being on the edge of hydrophobic and hydrophilic residues may enable the T/S rich face to be overruled by stronger electrostatic interactions between the cationic residues and anionic lipids by accommodating sub-optimal environments and allowing the three-faced peptide to adopt archetypal AMP poration mechanisms.

In contrast, we find that a single mutation to the T/S rich face of triAMP has a notable impact both on the folding of the peptide in zwitterionic lipids and on the biological selectivity of the peptide. In mutant 4, a T13S mutation results in reduced folding demonstrating that, despite the similar properties of the two residues, T and S are not interchangeable at this location. In mutant 5, a T6A mutation again results in reduced folding despite A being more hydrophobic than T and therefore expected to promote folding in zwitterionic lipids. Furthermore, mutant 4 and 5 both exhibit increased haemolysis. For both mutants, the continuous run of three threonines found in the FhHDM-$1_{49\text{-}66}$ template and conserved in triAMP is disrupted. This may indicate that the threonine cluster has a synergistic role which can promote folding and interaction with zwitterionic lipids without inducing lysis. To test this hypothesis, further mutants, and techniques such as NMR to resolve specific peptide- lipid interactions would be required. In any case, triAMP represents the only arrangement tested here that maintains biological selectivity whilst providing auxiliary lipid interactions in the absence of electrostatic attraction. This combines properties of AMPs and ALPS motifs, and as such, represents a novel membrane-active antimicrobial design.

The two results chapters presented so far describe the modes of lipid disruption of simplified peptide designs based on a single α-helix. However, native AMP sequences can have more complex folds than a single α-helix or β-strand. The current models to describe lipid disruption (poration, thinning, roughening) assume a single mode per peptide sequence. This raises the question: are more complex structures simply a matter of structural redundancy that deliver the same mechanism of disruption, or do more complex folds induce more complex mechanisms? To address this, the following results chapter investigates the membrane interactions of a native antimicrobial sequence with a multi-helix structure.

5 Resolving multimodal mechanisms of multi-helix bacteriocins

Many of the results presented in this chapter have been published in: Hammond, K.; Lewis, H.; Halliwell, S.; Desriac, F.; Nardone, B.; Ravi, J.; Hoogenboom, B. W.; Upton, M.; Derrick, J. P.; Ryadnov, M. G. Flowering Poration—A Synergistic Multi-Mode Antibacterial Mechanism by a Bacteriocin Fold. *iScience* **2020**, *23* (8), 101423.

5.1 Introduction

More complex folds are often found among bacteriocins, a family of antimicrobial peptides secreted by bacteria. These peptides are further divided into subclasses according to factors such as their structural organisation, producer strains, microbial targets and size.[224] The most recently reported subclass, class IId, are single-chain, cysteine free and do not contain a leader sequence.[225] They possess a highly conserved structure consisting of four to five α-helices arranged in a compact helical bundle, driven by hydrophobic residues packing together to form a hydrophobic core. The helical arrangement contains a saposin-like fold with two α-helices forming a v-shape segment and a third α-helix lying perpendicular (Fig 5.1A).[226] Other conserved features include solvent-exposed tryptophan residues (Fig 5.1B) and a high cationic surface charge (Fig 5.1C).[227]

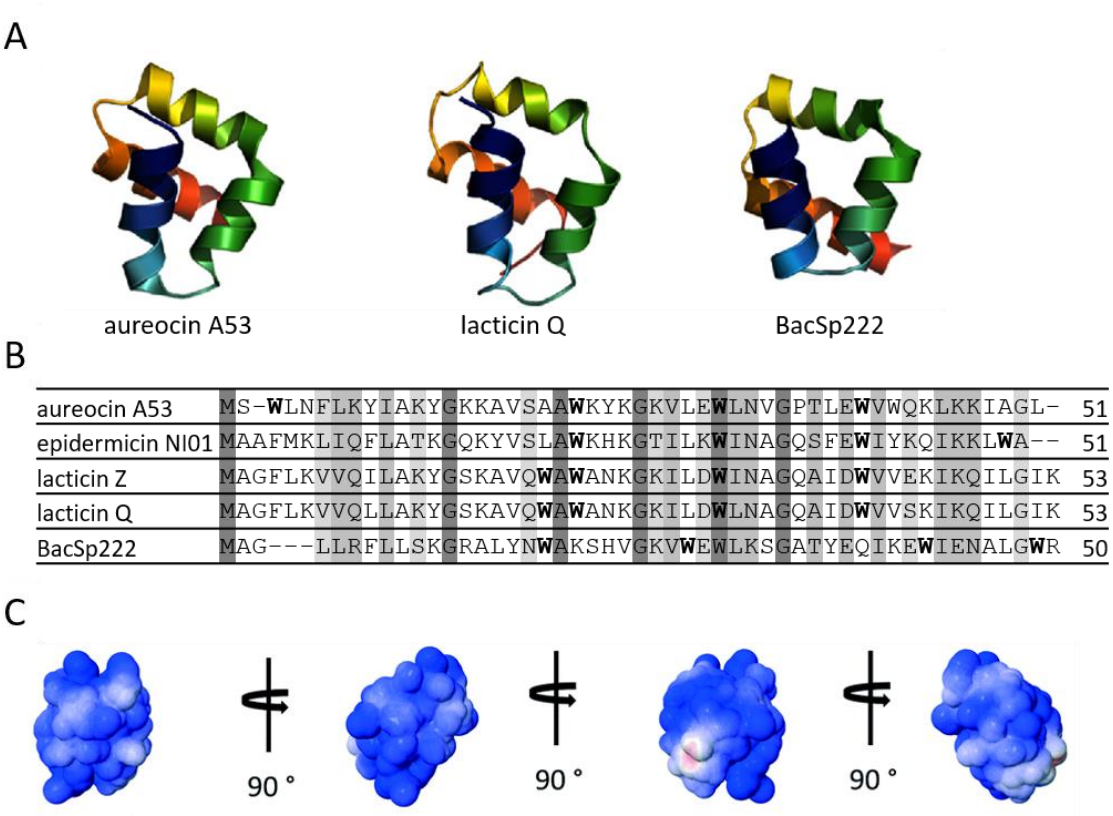

Figure 5.1. The structural organisation of class IId bacteriocins. (A) NMR solution structures of members of the subgroup, with N-terminus (blue) to C-terminus (red). The characteristic

saposin-like fold can be observed (two α-helices in a v-shape and a third α-helix oriented perpendicular); (B) Clustal Omega primary sequence alignment for members of the family, with solvent exposed tryptophan residues in bold; (C) Electrostatic potential map of lacticin Q, with cationic regions (blue) and anionic regions (red) showing a cationic surface charge, reproduced from ref. [226]*, licensed under CC BY 3.0, published by The Royal Society of Chemistry.*

Current findings indicate that these peptides are membrane active and do not require a receptor.[228]–[230] The proposed mechanism of action is that the high cationic surface charge drives initial membrane binding via electrostatic interactions, and that subsequent membrane insertion is promoted by both the amphiphilic nature of the exposed tryptophan residues, and a transition in the arrangement of α-helices from a closed to an open conformation.[226] This transition increases hydrophobic interactions between the core of the peptide and the lipid bilayer, as observed for other proteins containing the saposin-like fold.[231] In agreement with this proposed mechanism, a recent conformational study demonstrates that Bacsp222 does not remain surface bound, but inserts its α-helices into the lipid bilayer.[232]

Thus far, there have been no direct experimental observation of bacteriocin-induced poration from this class, and the modes of disruption are unknown. Given that their structures are multi-helix folds, these peptides may support more complex multimodal mechanisms of membrane disruption than single-helix AMPs derived from animals. In this chapter, we address this hypothesis by characterising the membrane activity of epidermicin NI01, an archetypal member of the class. Our findings agree with and significantly expand on the current mechanistic understanding of this bacteriocin family. Furthermore, NI01 is of interest as a promising candidate for therapeutic development.[233] *In vitro* studies show potent activity against methicillin-resistant *Staphylococcus aureus* (MRSA) and vancomycin-resistant *enterococci* (VRE).[233] *In vivo* studies show that injection of NI01 into *Galleria mellonella* larvae confers protection against MRSA with no adverse toxicity[234] and topical applications can treat nasal infections of MRSA in cotton rats.[235] A single application clears the nasal infection, a marked improvement over the current drug of choice.[235] The novel modes of membrane disruption revealed in this chapter will help to progress the therapeutic development of the peptide.

5.2 Results and Discussion

Throughout this chapter, POPC and POPC:POPG (3:1 molar ratio) are used for zwitterionic and anionic vesicles (CD spectra) and SLBs (AFM data). Unless otherwise stated, peptide concentrations are 20 μM for CD spectra and 0.25 μM for AFM imaging. Whilst I synthesised and purified epidermicin NI01 and aureocin A53, the remainder of the peptides described in this chapter (D- epidermicin, α1/α2, α2/α3, α3/α4, α1/α2/α3, α2/α3/α4, and Arg- mutant) were provided by Dr. Brunello Nardone at the National Physical Laboratory. The two videos (Video A.1 and Video A.2) were taken with the help of Dr. Jonathon Moffat (Oxford Instruments).

5.2.1 The crystal structure of epidermicin NI01

The crystal structure of NI01 was recently solved by Samantha Halliwell and Prof Jeremy Derrick at Manchester University.[236] Like other members of its class, the peptide forms a four-helix bundle (Fig 5.2B). The characteristic v-shape of the saposin-like fold is formed by α1 and α2, as well as by α3 and α4, which both show similar up-down helical hairpin topographies.

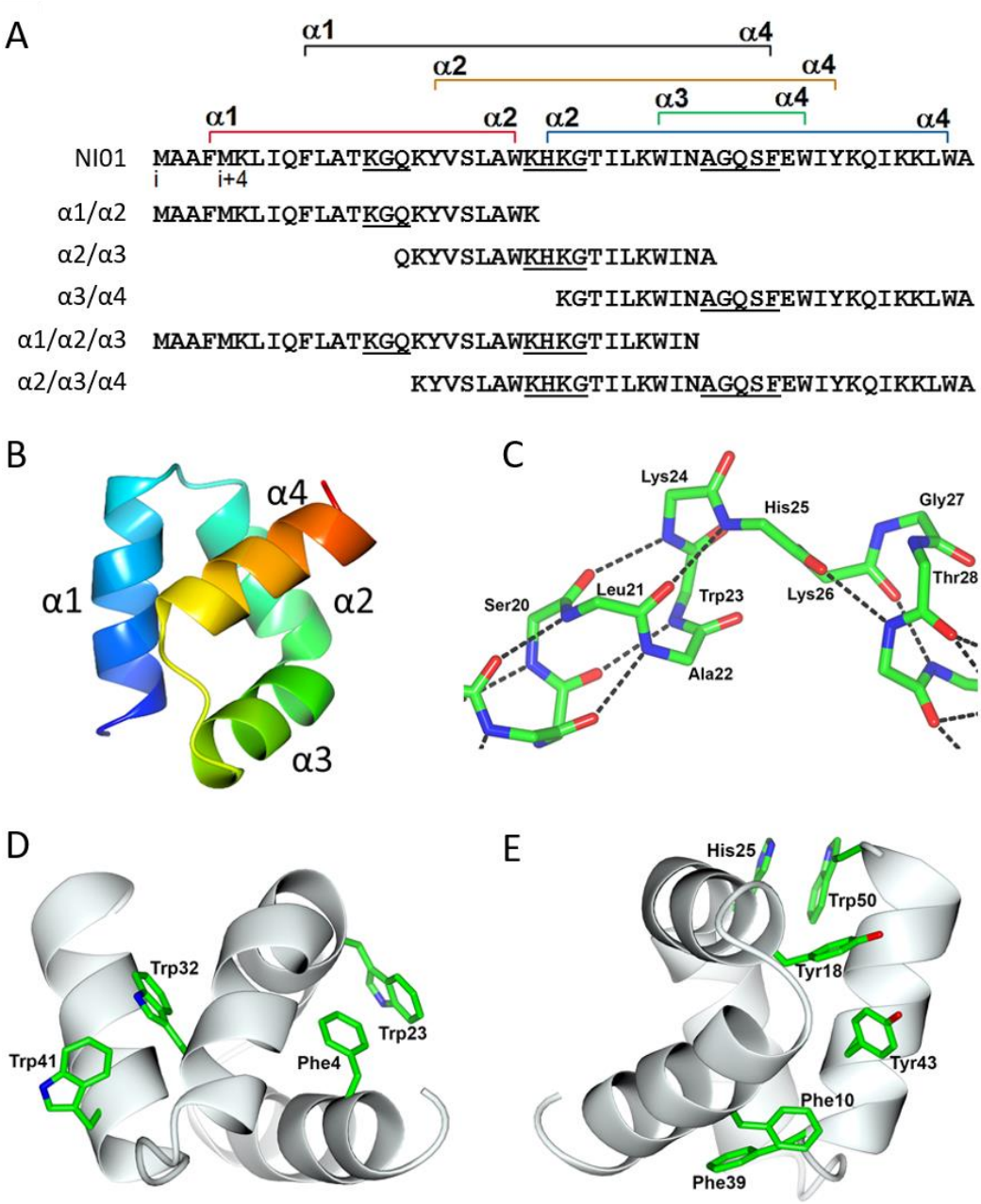

Figure 5.2. The structure of epidermicin NI01.Primary structure of NI01 and its constituent α-helices, labelled α1 to α4. Coloured staples indicate π-π interactions between different α-helices. The helical methionine stretch is highlighted by i, i+4. Turns are underlined in the sequences; (B) Crystal structure of NI01, with N-terminus (blue) to C-terminus (red); (C) Stick representation of the central kink linking α2 to α3 at H25; (D) Two aromatic pairs, F4-W23 and W32-W41 between sequential helices (α1 to α2, and α3 to α4, respectively); (E) Remaining three aromatic pairs, all involving α4: H25-W50, Y18-Y43 and F10-F39. Reproduced from ref. [236]*, licensed under CC-BY-NC-ND.*

α2 and α3 lie perpendicular to one another, mediated by H25 which forms a kink at an obtuse angle (Fig 5.2C). The hydrophobic residues are buried in the core of the bundle, but the aromatic residues are not. Instead, the side chains of aromatic residues are locked in paired π-π interactions, which act as staples between spatially adjacent helices, stabilising the global helical arrangement of the peptide. There are 5 pairs of π-π interactions in total. Two of these link sequential helices: α1 to α2 and α3 to α4 (Fig 5.2D). The remaining three π-π interactions link α4 to α2 and α1 (Fig 5.2E). α2 and α3 share no staples which is to be expected as they lie at an obtuse angle.

5.2.2 Biophysical properties of epidermicin NI01 in solution

Consistent with its crystal structure, epidermicin NI01 is α-helical in aqueous solution (Fig 5.3A). Folding is independent of peptide concentration, and $[\theta]_{222/208}$ values are characteristic of helical bundles and coiled-coils,[237]–[239] revealing that significant helix-helix interactions are present. NI01 is found to be fully folded in buffer solution, with addition of the helical promoting solvent TFE causing no increase in % helicity (Fig 5.3B).[172] Instead, TFE causes a decrease in $[\theta]_{222/208}$ to a value more typical of isolated α-helices, consistent with its ability to displace interhelical hydrophobic interactions.[237] In the presence of anionic and zwitterionic lipid vesicles, NI01 remains fully folded but again shows a decrease in $[\theta]_{222/208}$ (Fig 5.3C) demonstrating that lipid-binding induces global α-helical rearrangement, with helix-helix interactions replaced by helix-lipid interactions. A similar effect has been observed for lacticin Q, and is consistent with the hypothesis that proteins with a saposin-like fold transition from a closed to an open conformation upon membrane binding.[226],[229],[231]

Thermal melts (Fig 5.3D) show the secondary structure of NI01 is highly stable; even at 90 °C, the peptide remains appreciably α-helical, and $[\theta]_{222/208}$ remains > 1. Unfolding is fully reversible with nearly identical spectra collected before and after the melt (Fig 5.3E). This is consistent with NI01 retaining antimicrobial activity after being subject to elevated temperatures (80 ºC),[233] and illustrates that no precipitation or aggregation occurs at higher temperatures. The sigmoidal unfolding curve at $[\theta]_{222}$ (Fig 5.3F) shows cooperative unfolding with a single melting temperature (T_M) observed at 60 ºC. Collectively these results reveal NI01 to be a stable, fully folded peptide, with strong interhelical interactions in solution that are replaced by lipid-helix interactions in vesicles.

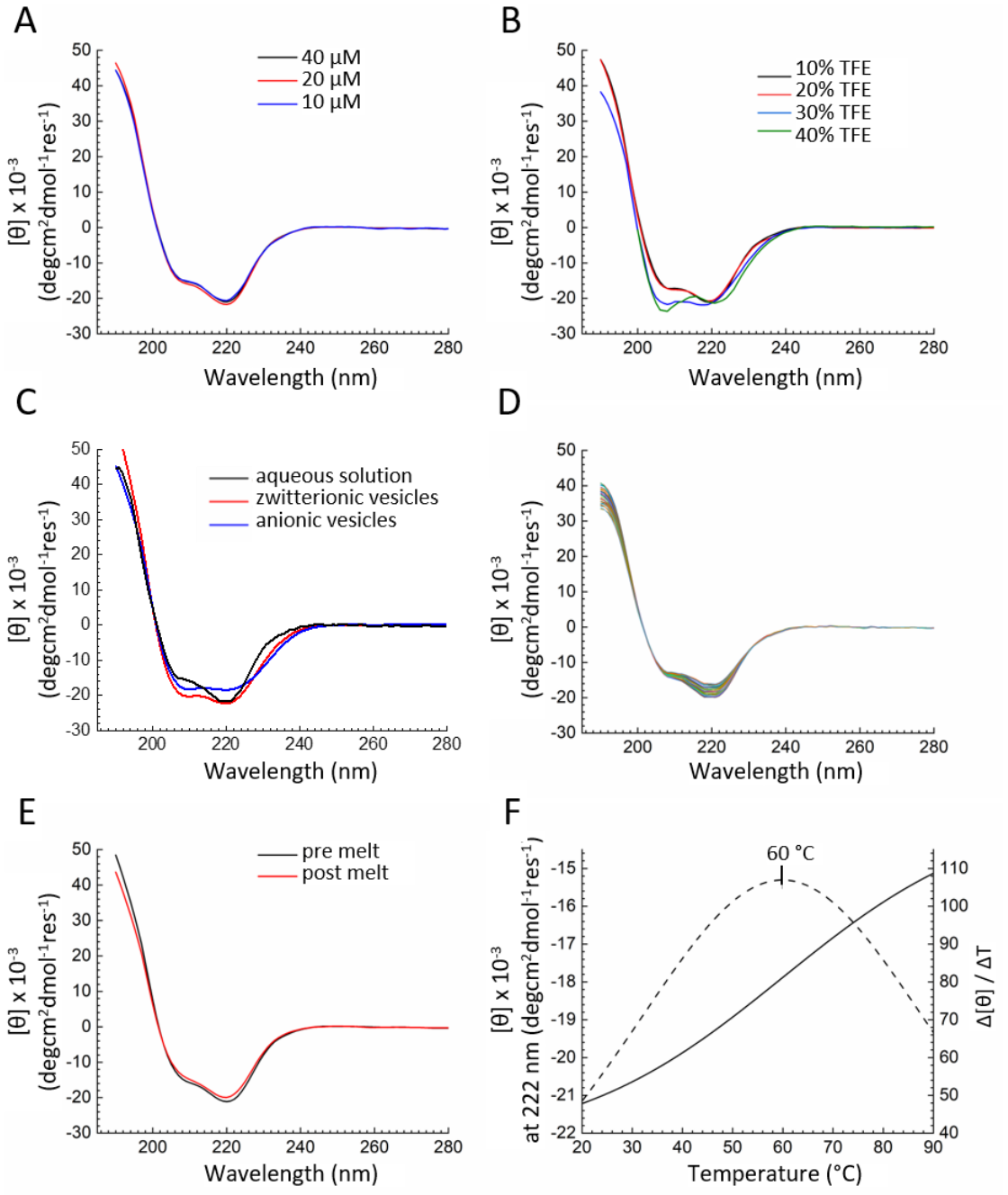

Figure 5.3. CD spectra for epidermicin NI01 under different conditions. (A) At varied peptide concentration in aqueous solution; (B) With increasing % 2,2,2,-Trifluoroethanol; (C) With zwitterionic and anionic vesicles; (D) At 2 ºC intervals during the thermal unfolding from 20 ºC to 90 ºC; (E) Before and after thermal denaturation; (F) The thermal unfolding curve at 222 nm and its first derivative. A single transition point (T_M) is found.

Further biophysical measurements show that NI01 exists as a monomer in solution. DLS (Fig 5.4A) show a monomeric dispersion with a diameter of 2 nm and no higher order oligomers or aggregates observed. The peptide is cationic with a net charge of +8 at neutral pH, and, like other members of its class, the crystal structure of NI01 confirms that polar side chains are found on the exterior of the peptide. A cationic surface charge is confirmed by zeta potential measurements (Fig 5.4B, ζ-potential of 20.8 ± 3.8 mV). This will act to stabilise the monomeric

dispersion by preventing aggregation. By extrapolation, we can assume that NI01 binds to lipid membranes as a monomer.

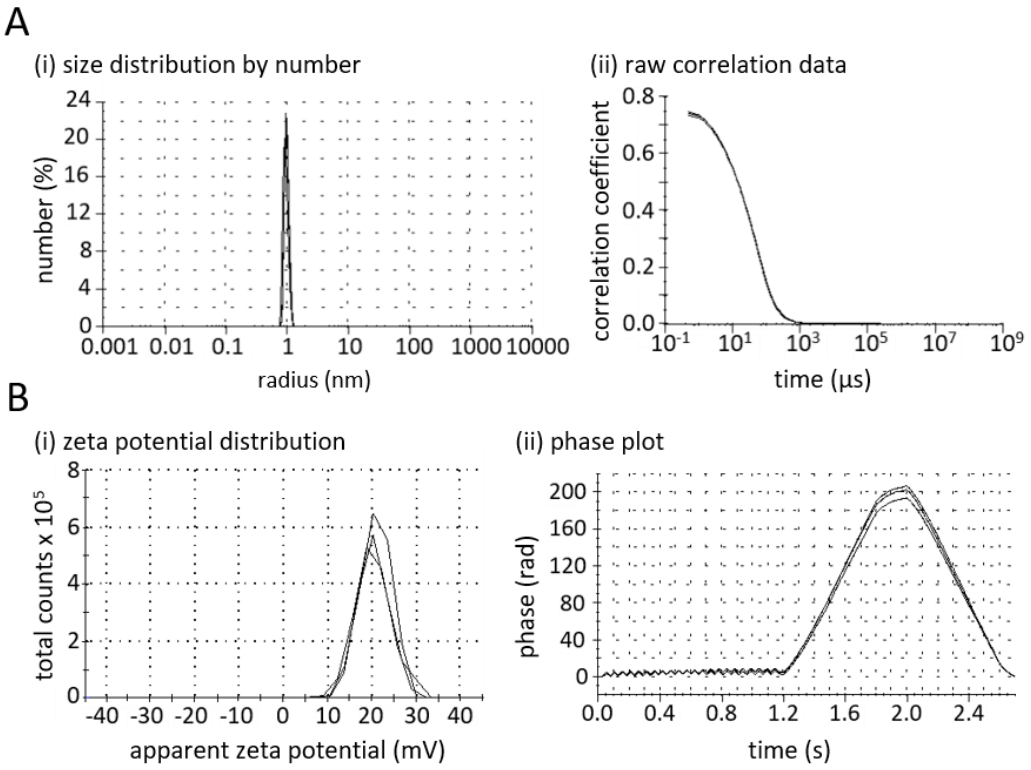

Figure 5.4. Monodispersity of epidermicin NI01 in aqueous solution. (A) (i) Size distribution by dynamic light scattering of epidermicin NI01 with (ii) correlograms showing rapid correlation decreases from high intercepts, characteristic of monodisperse, small particles; (B) (i) ζ-potential distribution frequency showing a net positive surface charge with (ii) phase plot showing the phase shift due to electrophoresis. High signal to noise ratio is observed. Conditions: 0.9 mM peptide in 10 mM phosphate buffer, pH 7.4 at 25 °C.

5.2.3 Direct visualisation of the effect of NI01 on lipid bilayers

Like many AMPs, we find that NI01 is charge selective. Zwitterionic SLBs remain featureless when incubated with NI01 (Fig 5.5A, B), with no disruption to the lipid packing observed. In contrast, incubation with anionic SLBs induces significant disruption even at lower concentrations (Fig 5.5C-F). Furthermore, disruption is multimodal. Channels with a depth corresponding to the full width of the bilayer (Fig 5.5C-E, blue) and patches with a depth of 2 nm (Fig 5.5C-E, black) can be observed across the membrane surface. Each separate mode of disruption is consistent with commonly reported mechanisms for AMPs, namely transmembrane channel formation and localised patches of membrane thinning.[118],[130] The two modes are mutually exclusive with no transmembrane channels occurring within patches of membrane thinning. In addition, the two disruption modes rarely occur in isolation, with channels seeming to originate from patches of thinned membrane (Fig 5.5D). This relationship is confirmed by imaging the initial formation of a defect (Fig 5.5F, showing selected snapshots from Video A.1). The formation and growth of a patch of membrane thinning is followed by the sequential appearance of four transmembrane channels originating from this patch.

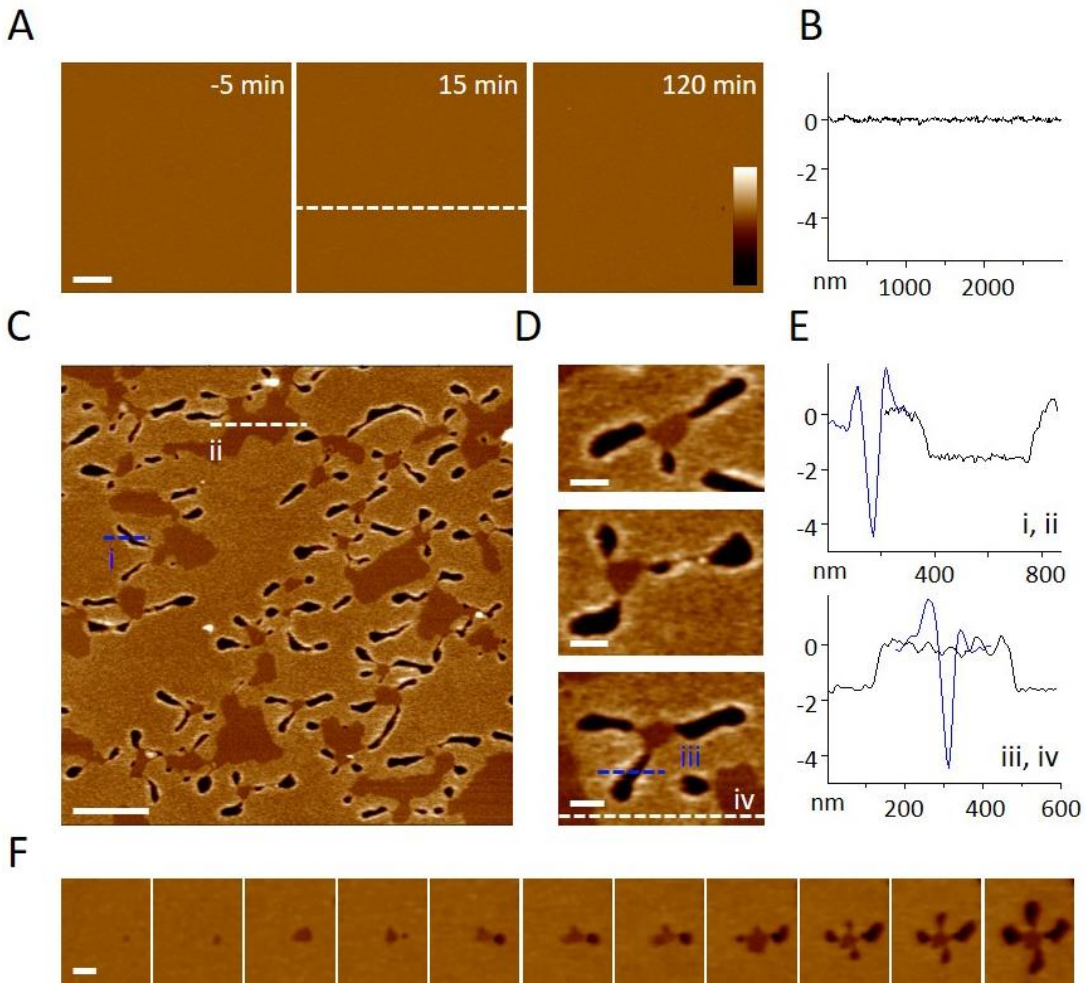

Figure 5.5. AFM imaging of SLBs treated with NI01. (A) Topography of zwitterionic SLBs treated with 0.6 μM NI01, with height profile along the dotted line shown in (B). NI01 causes no observable disurption to zwitterionic (POPC) SLBs, with the membrane surface remaining flat and featureless; (C) Topography of anionic (POPC: POPG (3:1 molar ratio)) SLB treated with 0.25 μM NI01, with higher magnification images (D) and height profiles along the dotted lines shown in (E). Both transmembrane channels and patches of membrane thinning appear across the surface in a highly organised, networking pattern; (F) Topography images of anionic SLB treated with 0.375 μM NI01, showing the formation of transmembrane channels from a patch of membrane thinning. Images are selected snapshots from Video A.1, over a period of 20 min. Colour scale bar in all images is 15 nm in all images, length scale bars are 500 nm for (A) and (C), 100 nm for (D) and (F).

These results provide the first direct observation of a highly organised, multimodal mechanism of membrane disruption by an AMP. We next conduct a detailed analysis of the dynamics of this mechanism. Figure 5.6A shows formation and expansion of defects over a wider, 4 μm scan (selected frames from Video A.1). After an initial lag time (~ 1 min), defects form and grow until a plateau is reached (~ 10 min) and minimal further changes occur (Fig 5.6B). The same behaviour is observed at higher peptide concentrations (Fig 5.6C, selected frames from Video A.2) but the rate of defect formation and expansion is faster, resulting in a larger coverage of defects across the surface, and a plateau is reached more quickly (Fig 5.6D). This reveals that, like for other AMPs, the kinetics of NI01-induced disruption are concentration limited.[123],[137],[139] The mechanism itself is not concentration dependent, however, with

NI01 able to execute the same modes of disruption at high and low peptide concentrations. Indeed, even at very low peptide concentrations where final defect coverage is small (Fig 5.6E), both transmembrane channels and patches of thinned membrane can be observed.

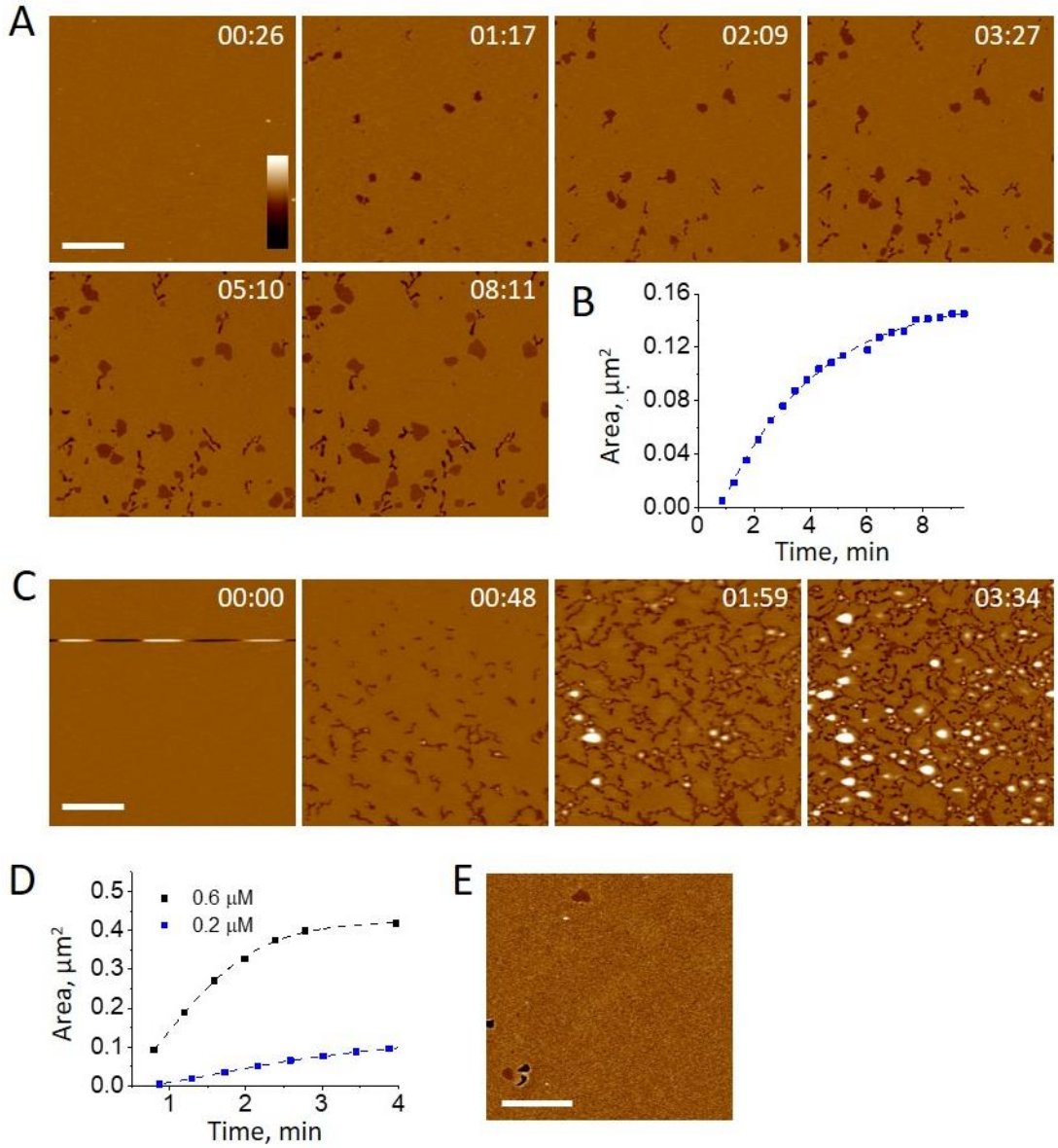

Figure 5.6. Time-resolved studies of NI01-induced disruption. (A) Topography images of anionic SLBs during the first 10 min of treatment with 0.375 µM NI01. After an initial lag time, both membrane thinning and transmembrane channels form and grow, before reaching a plateau where minimal further change is observed. Images are selected frames from Video A.1; (B) A plot of total defect coverage (including both channels and thinned areas) vs time for anionic SLBs treated with 0.375 µM NI01. The behaviour of (i) lag time, (ii) growth and (iii) plateau can clearly be observed; (C) Topography images of anionic SLB treated with 0.75 µM NI01. The mechanism appears independent of concentration, but the kinetics of disruption are faster. Images are selected frames from Video A.2; (D) Comparison of defect coverage vs time for anionic SLBs treated with 0.375 µM and 0.75 µM NI01. At the higher concentration, growth of defects is faster and a plateau is reached more quickly; (E) Topography of anionic SLBs treated with 0.008 µM NI01 after 2 hours of incubation. Even at a very low concentration of peptide, both membrane thinning and transmembrane channels can be induced. Colour scale bar is 15 nm in all images, length scale bars are 500 nm.

The plateauing of defect growth is noteworthy, as some AMP sequences induce defects that continue to expand and grow to the point of complete membrane disruption.[127],[130],[132],[133] An obvious explanation for the plateau is a lack of available peptide to continue expanding the defects. To test this hypothesis, Figure 5.7A shows the response of the membrane to further injection of NI01 after a plateau was reached (selected frames from Video A.1). Renewed defect formation and expansion is observed before a second plateau, and this behaviour is repeated for three consecutive injections. We therefore confirm that plateauing occurs when there is no longer enough free peptide to drive further growth.

While the net effect of additional peptide is a larger coverage of defects, a conversion effect is observed immediately after peptide injection. The total defect area across the membrane surface temporarily decreases (Fig 5.7A). Closer inspection of the topography reveals that, in response to peptide injection, patches of thinned membrane decrease in size, show significant remodelling of their boundary, and form new transmembrane pores at their edges (exemplified in Fig 5.7B and 5.7C, and shown over a larger area in 5.7D). This effect is instantaneous, occurs across all patches of membrane thinning, and is reproduced for every additional injection of peptide (Video A.1). Significant remodelling of the boundary area signifies NI01 binding [120] and collectively, this behaviour is reminiscent of pore forming proteins such as lysenin and equinatoxin which are known to preferentially bind and induce pores at phase boundaries.[240],[241] The intrinsic disorder of lipids at the boundary edge may offer less resistance to poration. Furthermore, increased local concentration of protein at the boundary means that the threshold concentration required for poration will be reached more quickly.[35],[241] Following this initial response, both defect types continue to grow (Fig 5.7B-D). This is the first time that a pump-like mechanism, with lipid domains recruiting peptide and directly converting into transmembrane channels, has been resolved by AFM.

Based on the results described thus far and the parallels to pore forming proteins, we propose the following working model for NI01's multimodal disruption. NI01 binds to the membrane as a monomer. Peptide accumulation on the surface can result in either membrane thinning or transmembrane poration, with both defects requiring a threshold concentration. The threshold concentration for thinning the membrane is lower than for forming channels, and thinned patches are therefore observed first. The lag-time reflects the time taken for fluctuations in local concentrations of surface bound peptide to result in a sufficient concentration for defect formation. Once formed, thinned patches create boundary edges which then actively recruit more NI01. Increased local concentration enables the threshold concentration for channel formation to be reached, consistent with transmembrane channels preferentially forming at thinned boundary edges (isolated channels can also occur when fluctuations in local concentrations of surface bound peptide result in a high enough concentration). Once formed, channel edges can also act as recruitment sites and both defect types can grow. As such, a

multimodal mechanism can enhance disruption by recruiting peptide through membrane thinning and eliciting poration even at low bulk concentration. The proposed mechanism resembles four- and five- helix peptide toxins which assemble in the upper leaflet before rearranging into pores.[242],[243]

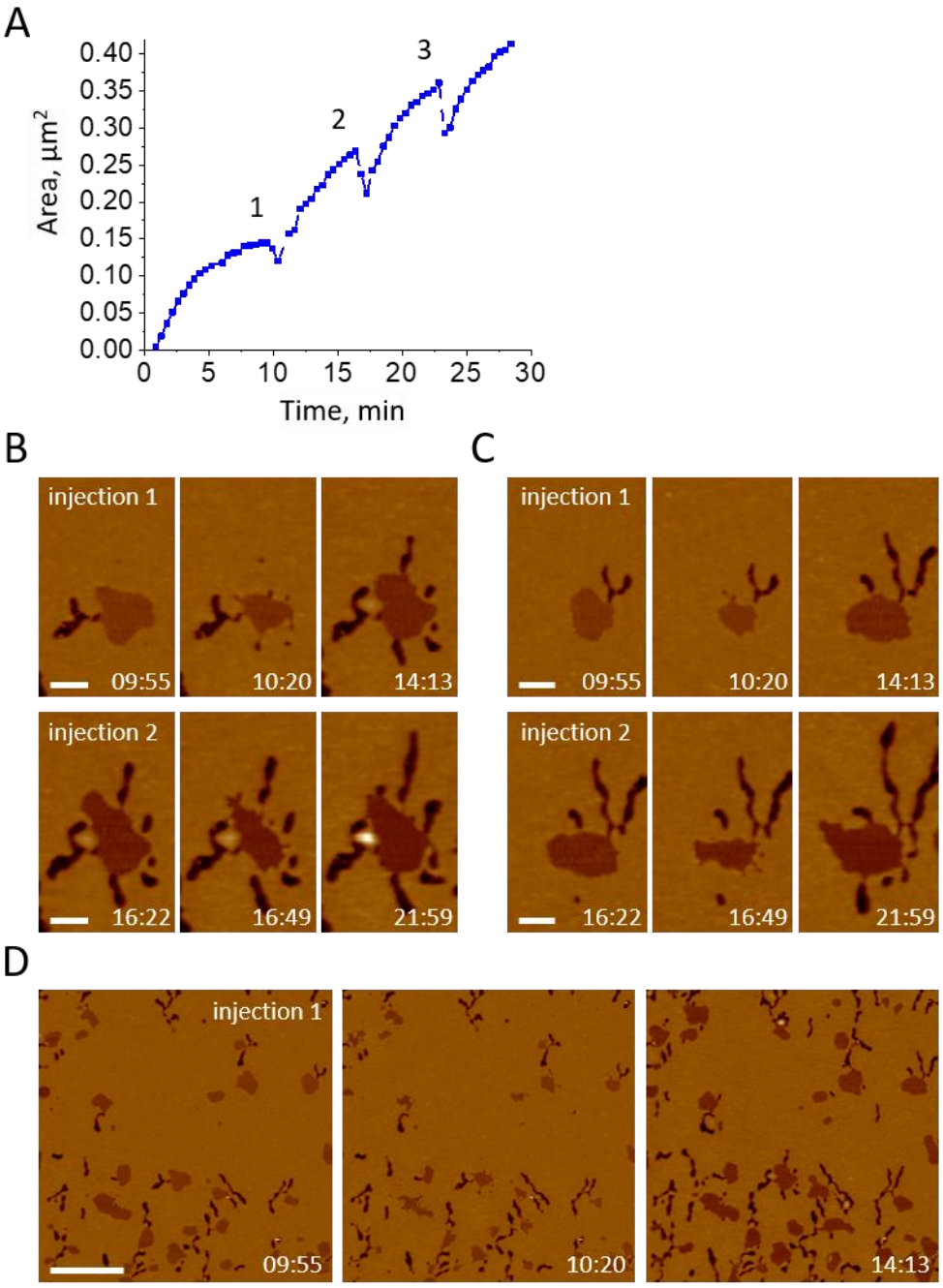

Figure 5.7. Response of NI01-treated SLBs to further peptide injection. (A) Defect coverage by area vs time, for all frames in Video A.1. Over 30 min of imaging there are 3 additional injections of peptide and each peptide injection restarts defect growth; (B - D) selected frames before, immediately after, and ~5 min after additional injection of peptide. Two individual defects are shown in (B) and (C) respectively, with a wider scan area shown in (D). Thinned membrane patches shrink in response to peptide injection, remodelling their boundary edges and converting into transmembrane pores. After this initial response, both defect types continue to grow. Colour scale bar is 15 nm in all images, length scale bars are 200 nm (B, C) and 1000 nm (D).

5.2.4 Subcomponents of NI01 activate distinct modes of membrane disruption

We have demonstrated that a multi-helix peptide can support a multimodal disruption mechanism. This prompts a hypothesis that subcomponents of the sequence can induce independent modes of disruption, that are then combined in the full sequence. To test this hypothesis, we characterize two- and three- helix segments of NI01. In validation of our hypothesis, we find that two helix segments, α1/α2 and α2/α3, can independently elicit each of the modes observed for NI01, with α1/α2 inducing transmembrane channels (Fig 5.8A) and α2/α3 inducing patches of membrane thinning (Fig 5.8B). α3/α4 can cause multimodal disruption with both membrane thinning and transmembrane defects (Fig 5.8C) but unlike NI01, the two effects no longer network, and the transmembrane defects are no longer channels but wider areas of lipid removal.

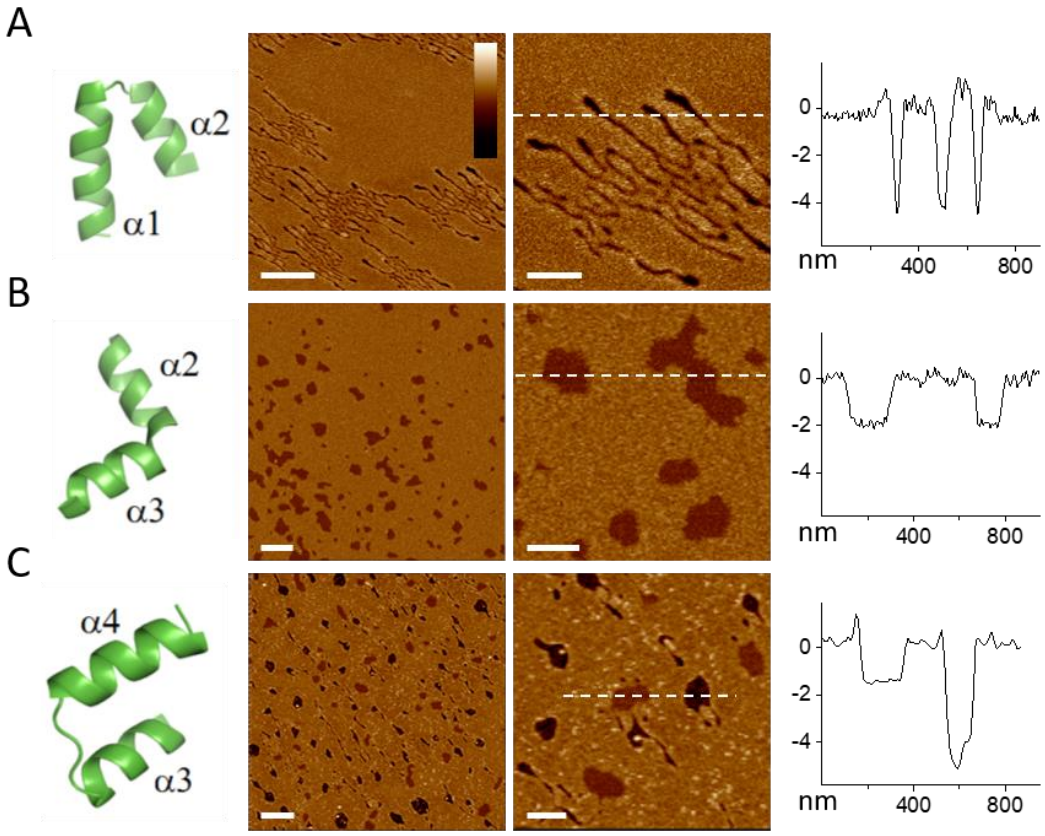

Figure 5.8. Disruption modes of two-helix segments of NI01. Topography images of anionic SLBs treatred with α1/α2, α2/α3 and α3/α4 (A-C respecitvely), with depth profiles measured along the dotted line. α1/α2 induces transmembrane channels, α2/α3 induces patches of membrane thinning and α3/α4 induces isolated patches of membrane thinning and large transmembrane defects. Scale bar 500 nm (left image) and 200 nm (right image). Colour scale 15 nm.

Three helix segments are found to be modular combinations of two-helix segments (Fig 5.9). α1/α2/α3 combinates the effects of α1/α2 and α2/α3 with both membrane thinning and channel formation observed, but no networking between them (Fig 5.9A). Similarly α2/α3/α4 combines the effects of α2/α3 and α3/α4 (Fig 5.9B). Membrane thinning patches dominate the mechanism,

with some transmembrane defects present but no channel formation observed. Again, no networking between defect types is observed. These results confirm that subcomponents of NI01 can individually induce distinct modes of its disruption mechanism, while emphasising that all helical components are required to reproduce the mechanism of the full peptide. Furthermore, the data provides a number of insights into molecular contributions to NI01's mechanism, discussed below.

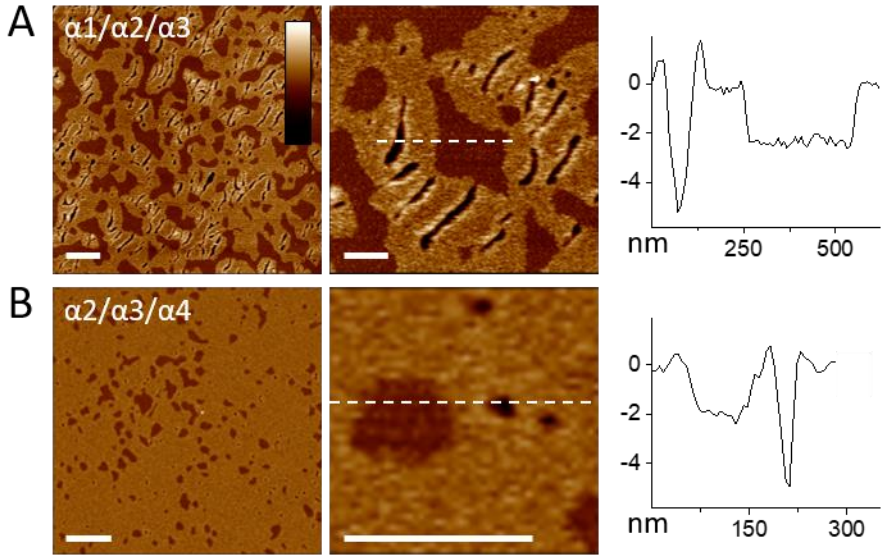

Figure 5.9. Disruption modes of three-helix segments of NI01. Topography images of anionic SLBs treatred with (A) α1/α2/α3 and (B) α2/α3/α4, with depth profiles measured along the dotted lines. α1/α2/α3 induces isolated transmembrane channels and patches of membrane thinning while α2/α3/α4 induces predominantly membrane thinning, with some transmembrane pores observed. Scale bar 500 nm (left image) and 200 nm (right image). Colour scale 15 nm.

Firstly, a terminal α-helix is needed for transmembrane poration. This is perhaps not surprising as α1 and α4 are more than twice the length of α2 and α3, and are better able to support transmembrane insertion. Consistent with this observation, both α1 and α4 contain motifs known to initiate membrane insertion. α1 features terminal methionines at i, i + 4 spacing. The i, i + 4 spacing of amphipathic residues is a motif found in fusion proteins of envelope viruses to drive membrane insertion.[244] Amphipathic amino acids can exist in both polar and hydrophobic environments and therefore promote membrane insertion of aqueous protein by supporting hydrophobic interactions with membrane lipids. In α4, an amphipathic tryptophan residue in the penultimate position of the helix can exert the same effect, as observed for other AMPs.[245]

Secondly, the central part of the molecule drives the formation of membrane thinning patches, with the effect only observed when α3 is present. α2/α3, which indepently induces thinning effects, exist as a boomerang-like shape in the crystal strcuture of the full sequence. In this configuration, it presents four lysine residues on its exposed solvent face which, through simultaneous electrostatic attraction to anionic membranes, will drive binding to the bilayer

surface, corroborating its role for membrane thinning. Furthermore, the crystal structure reveals that the positioning of lysine residues in α2/α3 appear to be predisposed to facilitate a transition from upperleaflet binding to membrane insertion. The motifs in α1 and α4 known to initiate bilayer insertion can align with K26 and K30 in α3 and K17 and K24 in α2 respectively (Fig 5.10), enabling electrostatic interaction with the surface to be maintained during insertion.

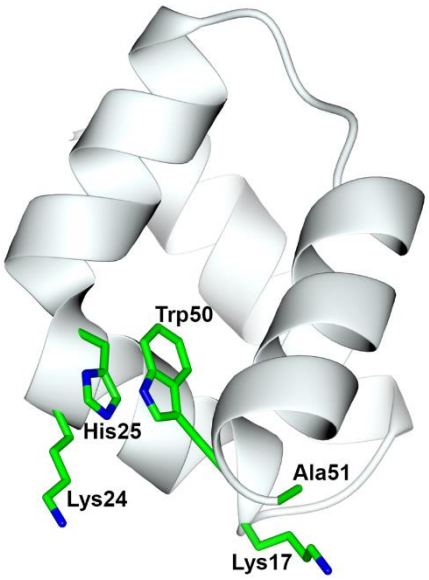

Figure 5.10. Cooperative structural arrangements in NI01. Solvent exposed K24 and K17 form a planar face with W50, facilitated by π-π interactions between W50 and H25. Reproduced from ref. [236]*, licensed under CC-BY-NC-ND.*

Thirdly, of the two terminal helices, α1 emerges as the main driving force for channel formation, with the morphology of NI01 channels only reproduced when α1 is present (Fig 5.8A, Fig 5.9A). When α1 is missing and transmembrane defects are driven by α4, a wider variety of transmembrane morphologies are observed (Fig 5.8C, Fig 5.9B). α4 contains four of the five π-π staples that stabilise the global helical arrangement of NI01 and its main role may instead be controlling overall structue of the peptide.

5.2.5 The importance of NI01's fully folded structure

Despite some helical segments being able to induce multimodal poration, they are unable to produce a networking effect. This prompts a hypothesis that the overall tertiary arrangement of helices plays an important role in ensuring a synergystic mechanism. To probe this, the folding behaviour of NI01's helical segements is shown in Figure 5.11.

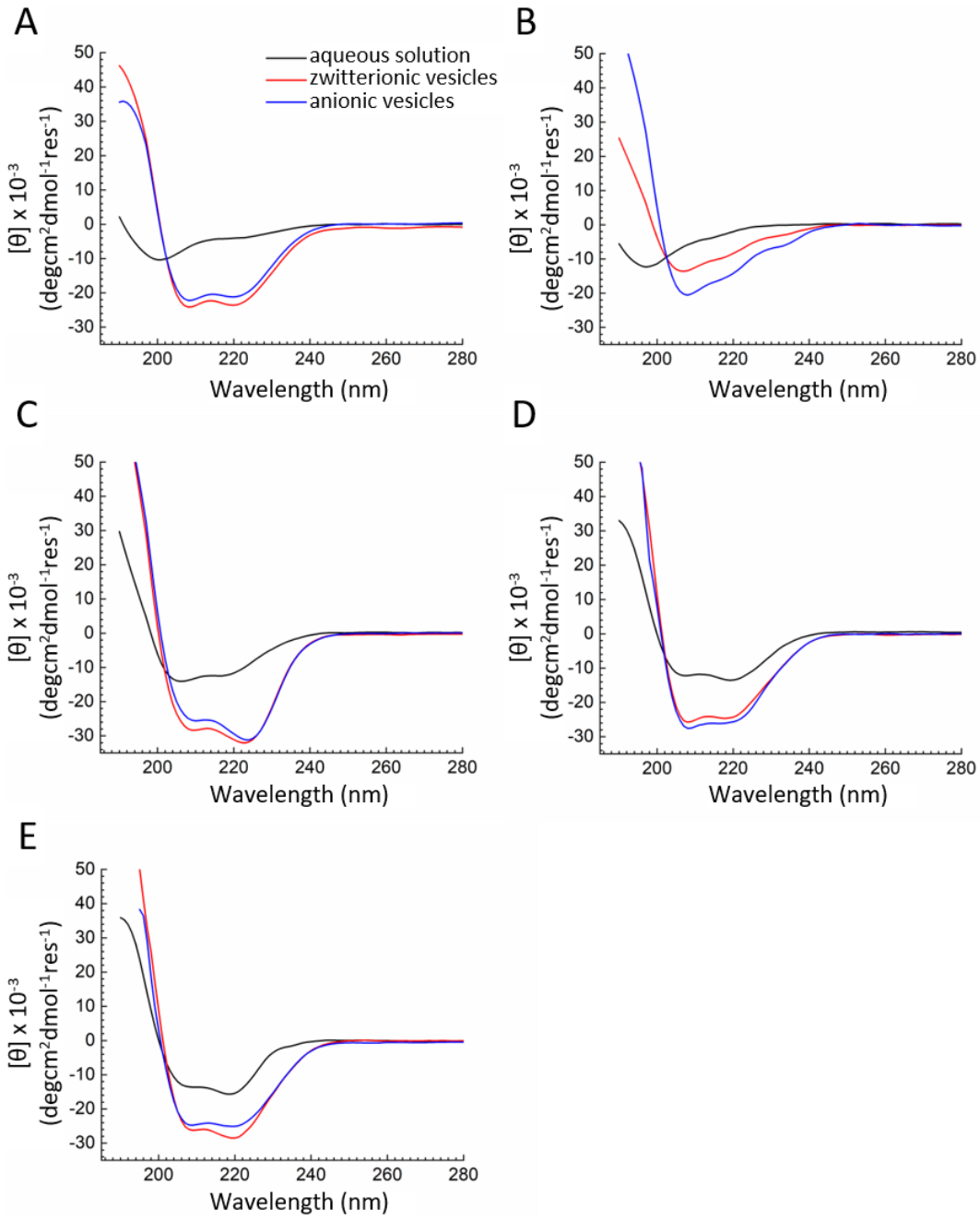

Figure 5.11. CD spectra for NI01 helical segments in aqueous solution and with lipid vesicles. (A) α1/α2; (B) α2/α3; (C) α3/α4; (D) α1/α2/α3; (E) α2/α3/α4.

Helical segments capable of inducing the two modes of membrane disruption, α3/α4, α1/α2/α3, and α2/α3/α4 are folded in aqueous solution (Fig 5.11C-D). Unlike NI01 however, their helicity significantly increases upon membrane binding, demonstrating that interhelical interactions that drive and stabilise a fully folded structure are compromised in these segments. Loss of cooperativity between helices provides a possible explanation for the loss of cooperativity in the resulting mechanism of membrane disruption, and is supported by data shown in Figure 5.12. Simultaneous addition of α1/α2 and α3/α4 to anionic SLBs does not reproduce the networking mechanism of the full peptide, despite all helical components of NI01 being present, with channels and thinned patches occuring in isolation.

α1/α2 and α2/α3 show no secondary structure in solution (Fig 5.11A, B) However, whilst α1/α2 can fold into strong helical structures in response to membrane binding, the structure of α2/α3 remains poorly defined, even in a membrane environment. As the only segment to exhibit weak folding in membranes, and the only segment to induce solely membrane thinning effects, this indicates more flexible structural requirements for this mode of action. This is supported by our findings in Chapter 3, in which bienK peptides also showed partial folding and induced membrane thinning effects.

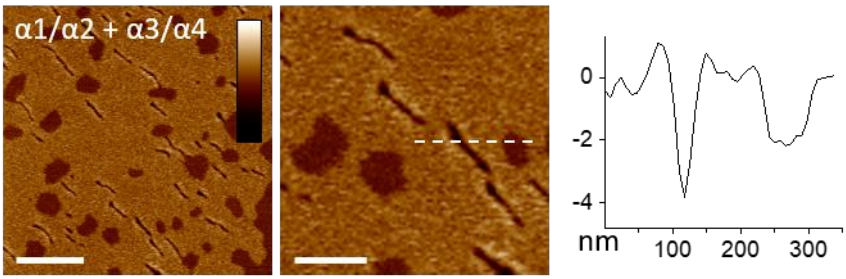

Figure 5.12. Simultaneous addition of α1/α2 and α3/α4. AFM topography images, with depth profile measured along the dotted line for anionic SLBs treated with both α1/α2 and α3/α4. Isoltated transmembrane channels and patches of thinned membranes appear across the surface. Scale bar 500 nm (left image) and 200 nm (right image). Colour scale 15 nm. Peptide concentrations 0.25 μM.

5.2.6 Promoting a single mode of disruption can abolish the multimodal mechanism

To test the resiliance of NI01's mechanism, we next compare the activity of NI01 to a mutant, in which all lysines are replaced by arginine (Fig 5.13). This retains the distribution of positive charge and the nature of electrostatic interactions, but increases the ability of the peptide to bind to the membrane surface. Arginine residues exhibit stronger electrostatic interactions with phospholipid head groups, providing five hydrogen-bond donors and resulting in tighter binding to upper leaflet phospholipids.[197],[246] Consistent with this, the peptide preferentially induces membrane thinning, with no transmembrane defects observed. This implies that to achieve multimodal poration, a strong preference for a single poration mode should be avoided.

In the mutant, the central H25 was also replaced with arginine, again maintaining the position of positive charge but abolishing the π-π staple between α2 and α4. Loss of this staple results in only partial folding in solution, demonstrating that every interhelical interaction is important in controlling the conserved tertiary structure of NI01 (Fig 5.13C). Together, the Arg mutant reveals that both the multimodal poration and fold regulation of NI01 result from a delicate balance of electrostatic and aromatic interactions.

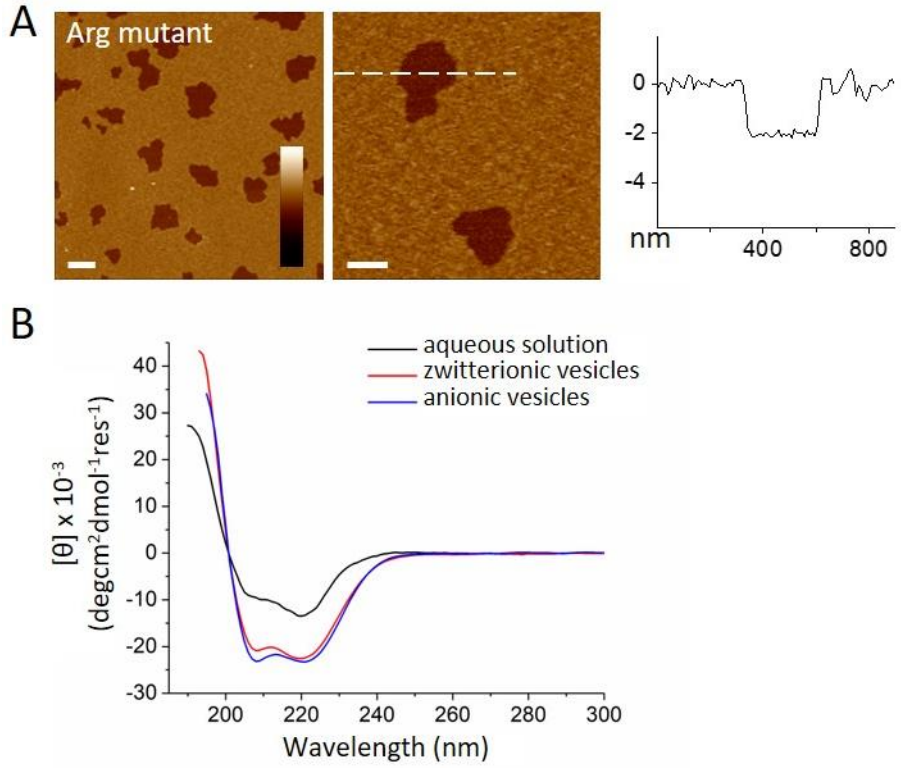

Figure 5.13. Disruption and folding of an Arg-mutant. (A) Topography images of an anionic SLB treated with an Arg mutant of NI01, with depth profiles measured along the highlighted lines. The mutant induces patches of membrane thinning. Scale bar 500 nm (left image) and 200 nm (right image). Colour scale 15 nm; (B) CD spectra for the Arg mutant of NI01 in aqueous solution and with lipid vesicles.

5.2.7 NI01 combines the biological activity of its α-helical segments

We have shown that helical segments of NI01 induce distinct modes of membrane disruption in SLBs. Consistent with this, minimum inhibitory concentration (MIC) assays conducted against a range of Gram-positive and Gram-negative bacteria show that all helical segments of the peptide are independently antimicrobial (Table 5.1). Like many bacteriocins from Gram-positive organisms, NI01 shows strong preference for killing Gram-positive bacteria. Gram-negative strains are protected by an additional outer membrane, rich in lipopolysaccharides (LPS), which can form barrier to bacteriocins, shielding the cytoplasmic membrane.[247],[248] Although preferential activity against Gram-positive strains is still observed for the helical segments, a significant increase in activity against Gram-negative strains is found.

To further probe the effect of LPS, the activity of NI01 and its helical segments against *E. coli* (ATCC 15597) was compared with *E. coli (SBS363)* and *E. coli (ML35).* SBS363 is a short-chain LPS or rough strain, whereas ML35 is a smooth strain, comprising full-length, mature O-chains.[249] All peptides show increased activity for short-chain LPS strain and decreased for the full-length mature O-chains, confirming an inherent susceptibility of NI01 and its derivatives to the LPS virulence factor.

Table 5.1. Biological activities of NI01 and its constituent parts. Antimicrobial activity against Gram-positive and Gram-negative bacterial strains assessed by minimum inhibitory concentration (MIC) assays, and haemolytic activity by lysis of human erythrocytes.[9]

	Peptide						
	L- NI01	D- NI01	α1/α2	α2/α3	α3/α4	α1/α2/α3	α2/α3/α4
Cell	*Minimum Inhibitory Concentration, μg / mL, Gram-positive*						
S. aureus (ATCC 6538)	5	5	8	>120	5	6	6
EMRSA (12817)	4	4	4	>128	4	32	16
EMRSA (12845)	4	4	2	>128	4	32	16
EMRSA (12873)	4	8	4	>128	4	32	16
B. subtilis (ATCC 6633)	3	3	16	14	3	6	6
M. luteus (ATCC 49732)	2	2	3	2	9	6	3
	Minimum Inhibitory Concentration, μg / mL, Gram-negative						
E. coli (ATCC 15597)	18	18	8	14	19	6	6
E. coli (SBS363)	8	8	1	8	4	4	4
E. coli (ML35)	64	64	8	32	32	64	32
S. typhimurium (DA6192)	>300	>300	32	>50	40	20	12
K. pneumoniae (NCTC 5055)	>300	>75	16	28	40	20	12
P. aeruginosa (ATCC 27853)	>300	>300	>140	14	>80	12	6
	HD_{50},[a] *μg / mL*						
Human erythrocytes	500	600	150	UD[b]	150	200	200

[a]median haemolytic doses to achieve 50% lysis; [b]undetectable

No single segment shows stronger activity across the range of pathogens tested, with each showing subtle preferences for different strains. Differences in the make-up of the cell wall and plasma membrane of each strain will have unique effects on the activity of each component. Noteworthy contrast is observed for the activity profile of α2/α3, the only component to show no activity against *S. aureus* or its related methicillin-resistant strains. The distinct behaviour of α2/α3 is mirrored in our biophysical studies, being the only segment unable to induce transmembrane poration in SLBs (Fig 5.8B) and the only segment without a well-defined secondary structure in solution or in membranes (Fig 5.11B). The inability of α2/α3 to kill *S. aureus* strains impacts on α1/α2/α3 and α2/α3/α4, which feature α2/α3 as a significant component and show reduced activity against methicillin resistant *S. aureus* strains compared to the full sequence and to components that do not contain α2/α3.

As NI01 has potential for therapeutic development, its selectivity is of interest. The producer organism of NI01, *S. Epidermidis* (strain 224), is a common bacterial coloniser of mammalian skin.[233] In order to maintain a commensal relationship, NI01 is therefore expected to be able to distinguish between host and bacterial cells. Indeed, it shows no haemolytic activity for concentrations that are > 100 x MIC as measured on target Gram-positive strains (Table 5.1). In marked contrast, all helical segments of NI01 show significant increase in haemolytic activity (Table 5.1). Whilst subdomains can independently produce strong antimicrobial effect, they do

[9] Assays were performed by Dr. Helen Lewis (National Physical Laboratory) and Dr. Florie Desriac (Plymouth University).

not exhibit specificity. The exception again is seen for α2/α3 which, as well as showing reduced antimicrobial activity, shows no haemolysis even at high concentrations. From this, we can conclude that the full sequence synergistically combines the independent activities of subdomains into a potent but differential mechanism.

5.2.8 The major target for NI01 is achiral

As discussed, AMPs can have a range of targets beyond the pathogen membrane. To confirm that membrane disruption is the main mode of NI01's activity, we conducted analysis of the enantiomeric D-form. The enantiomeric form adopts the same helical structure in solution, (Fig 5.14A) acts interchangeably with achiral phospholipids (Fig 5.14B) and, crucially, shows identical activity to L-NI01 in minimum inhibitory concentration (MIC) assays conducted against a range of Gram-negative and Gram-positive pathogens (Table 5.1). MIC data corroborates the assumption throughout this chapter that NI01 attack does not rely on additional chiral targets such as receptors, as this would be expected to result in a significant decrease in activity.

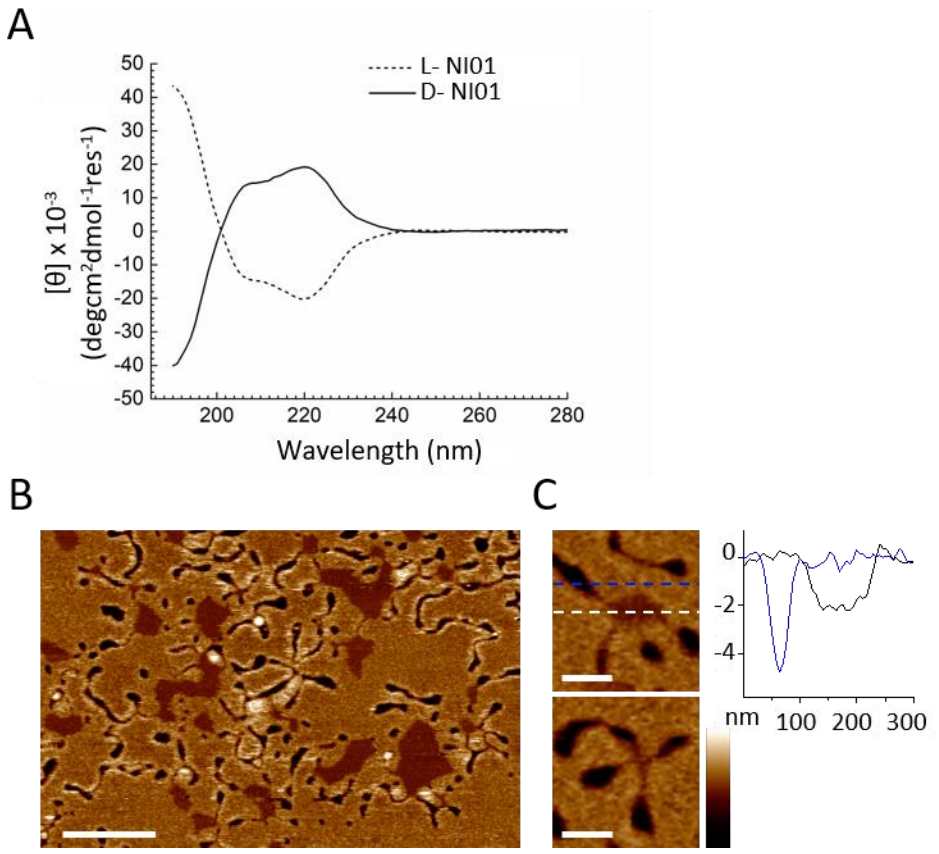

Figure 5.14. Characterisation of D- NI01. (A) CD spectra of D- NI01 in aqueous solution is the mirror image of L- NI01; (B, C) Topography images of anionic SLBs treated with D- NI01, with depth profile along the highlighted lines. The enantiomeric form reproduces the same mechanism of disruption. Scale bar 500 nm (B) and 100 nm (C). Colour scale 15 nm.

5.2.9 Extension across the bacteriocin class: aureocin A53

In this chapter, we have demonstrated that the bacteriocin NI01 exerts a novel antibacterial mechanism by inducing multimodal poration in model bacterial membranes. Cooperative interactions between helices produce a highly stable, fully folded peptide that can combine the activity of individual helical segments into a synergystic mechanism. The tertiary arrangement of the four helix bundle is conserved across the bacteriocin class, raising the final question: does a multimodal mechanism extend across this class?

To answer this, we investigate a second member of the class, aureocin A53. The NMR structure of A53 was recently solved and shows a conserved helical arrangement to NI01 (Fig 5.1A).[250] Consistent with this, we find A53 exhibits strinkingly similar folding in solution (Fig 5.15). The peptide folds independently of concentration, with a nearly identical helical content to NI01 and a ratio of $[\theta]_{222/208}$ characteristic of helical bundles (Fig 5.15A, B). TFE does not increase % helicity (Fig 5.15C) showing that A53 is also fully folded in buffer solution,[172] but again decreases $[\theta]_{222/208}$ reflecting a loss of interhelical hydrophobic interactions.[237] A53 is equally stable, with a T_M of ~ 54°C, retaining appreciable helicity even at 90°C, and exhibiting reversible folding (Fig 5.15D-F).

Consistent with its highly conserved structure, A53 induced a similar, multimodal mechanism of membrane disruption (Fig 5.16). Simultaneous patches of thinned membrane and transmembrane channels form across the surface, with transmembrane channels orginating nearly exclusively from patches of thinned membrane. The depth profiles of each mode, and the cooperativity between modes is identical to that observed for NI01. Unlike NI01, thinned membrane is the dominant mode of disruption and these patches exhibit branch like structure. Whilst the overal mechanism is conserved, difference in the primary sequence of each peptide likely control the specific morphology and growth of each defect type.

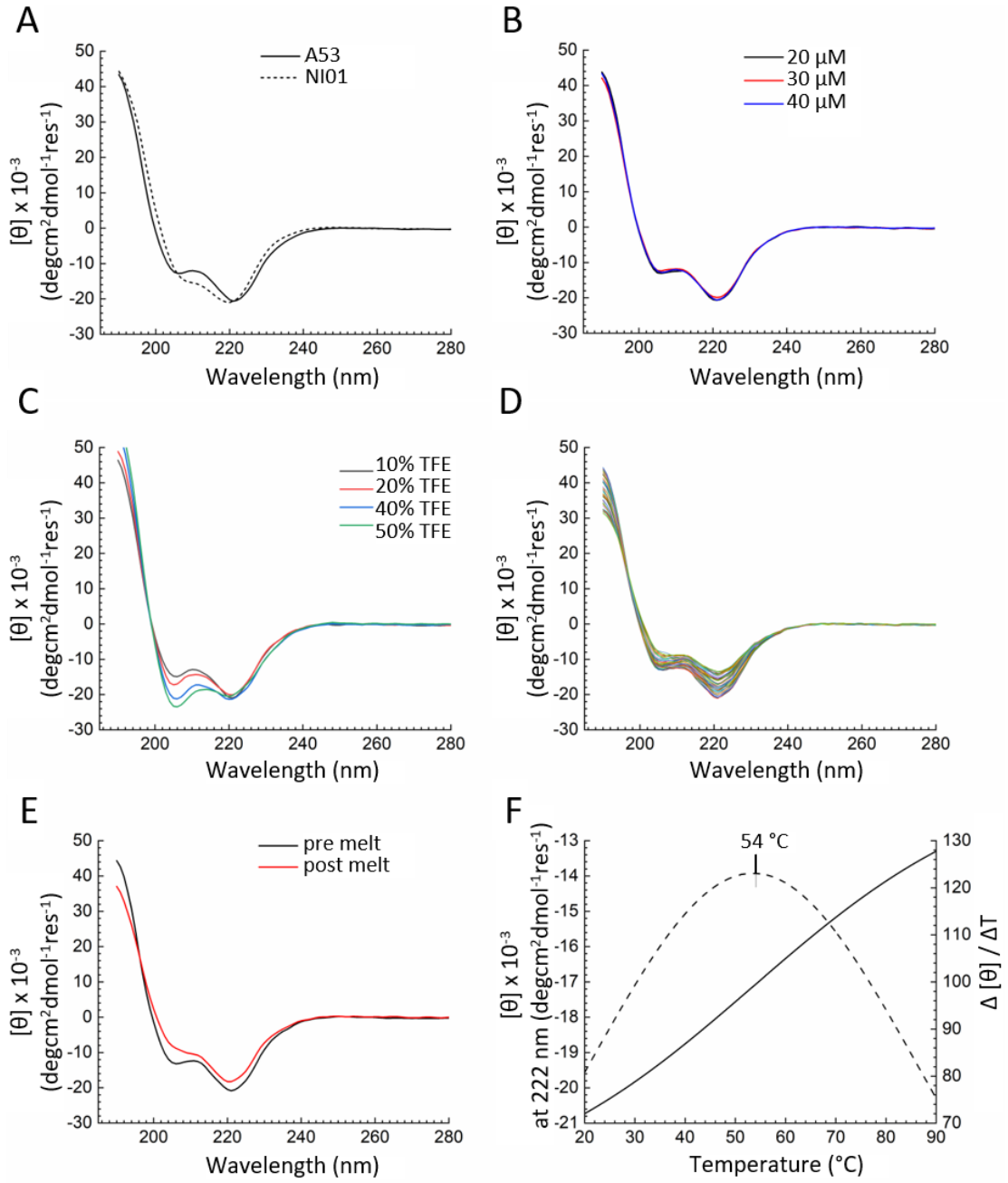

Figure 5.15. CD spectra for aureocin A53 under different conditions. (A) Comparison to epidermicin NI01 in aqueous solution; (B) At varied peptide concentration in aqueous solution; (C) With increasing % 2,2,2,-Trifluoroethanol; (D) At 2 ºC intervals during the thermal unfolding from 20 ºC to 90 ºC; (E) Before and after thermal denaturation; (F) The thermal unfolding curve at 222 nm and its first derivative. A single transition point (T_M) is found.

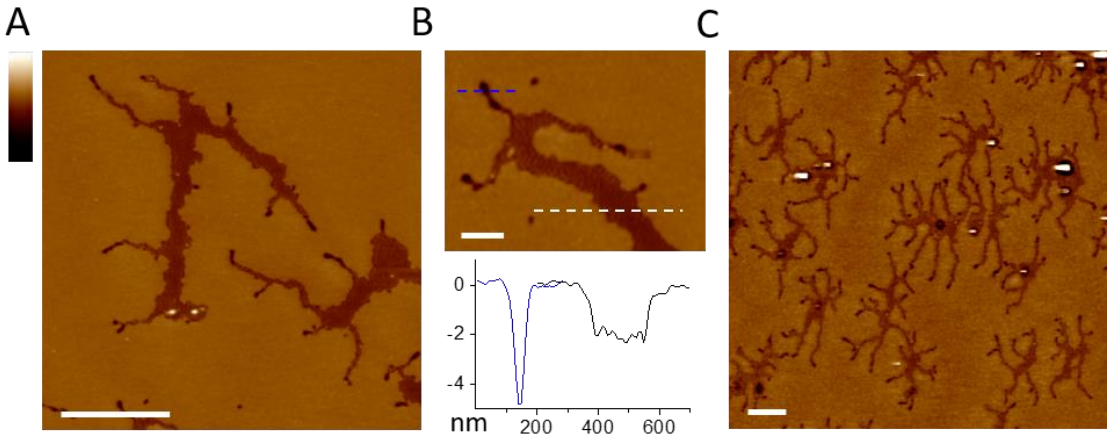

Figure 5.16. Disruption modes of A53. (A- C) Topography images of anionic SLBs treated with A53, with depth profiles measured along the highlighted lines in (B). Scale bar 1000 nm (A, C) and 200 nm (B). Colour scale 15 nm.

5.3 Conclusions

In this chapter we have presented detailed analysis of the membrane disruption induced by NI01. AFM data provides the first observation of a networking, multimodal mechanism, confirming the initial hypothesis that more complex folds support more complex mechanisms of membrane disruption. Time-resolved studies reveal dynamics that are reminiscent of pore-forming proteins such as lysenin and equinatoxin. Our proposed model, whereby NI01 self-concentrates at thinned boundaries to enable poration thresholds to be reached more quickly, may enable disruption to occur at lower concentrations. Indeed, we demonstrate that while the kinetics of defect growth are concentration limited, the mechanism itself is not. Furthermore, analysis of helical segments of the peptide reveals that subcomponents can elicit specific modes of NI01's disruption, as well as being independently antibacterial. The full peptide combines the activities of subcomponents into a synergistic and selective mechanism. Comparison to its enantiomeric D-form confirms membrane disruption as its main mechanism of attack. Finally, we demonstrate that this novel mode of disruption extends to another bacteriocin of the same class, further supporting the hypothesis that multi-helix peptides can support more complex, multimodal mechanisms than single helix animal derived AMPs.

Thus far, this thesis has investigated the effect of peptide motifs on membrane interactions at increasing levels of complexity, a single amino acid mutation to the face of a single α-helix, the addition of a T/S rich face to a single α-helix, and, here, the effect of multiple α-helices. This leads to the next question, addressed in Chapter 6: can membrane disruption mechanisms also be controlled at the supramolecular level?

6 A self-assembling antimicrobial peptide capsule

Many of the results presented in this chapter have been published in: Kepiro, I. E.; Marzuoli, I.; Hammond, K.; Ba, X.; Lewis, H.; Shaw, M.; Gunnoo, S. B.; Santis, E. D.; Łapińska, U.; Pagliara, S.; Holmes, M. A.; Lorenz, C. D.; Hoogenboom, B. W.; Fraternali, F.; Ryadnov, M. G. Engineering Chirally Blind Protein Pseudocapsids into Antibacterial Persisters. *ACS Nano* **2020**, *14* (2), 1609–1622.

6.1 Introduction

6.1.1 Higher-order peptide systems

Peptide sequences can be designed to self-assemble into supramolecular structures such as matrices, hydrogels, nanofibers and nanoparticles.[251] Such higher order systems are increasingly being used to modify and improve the biological activity of AMPs.[252] A variety of design approaches have been adopted. Micellar nanoparticles can be assembled by conjugating antimicrobial peptides to lipid moieties. Such assemblies have potent activity against drug-resistant bacteria, yeast and fungi,[253] as well as *in vivo* activity against *C. neoformans* induced meningitis in rabbits.[254] Hydrogels can be assembled using single amino acid or dipeptides functionalised with an N-terminal aromatic groups such as Fmoc to drive self-assembly through π- π interactions. Addition of a C-terminal pyridinium group increases potency, and results in gels with strong bactericidal effects.[255] Nanofibers can be formed by conjugating antimicrobial peptides to β-sheet forming peptides, restricting the AMP conformation and resulting in improved therapeutic index .[256] Spherical peptide cages can be assembled using trigonal peptide conjugates with directed intermolecular interactions.[257] This mimics viral capsid proteins and vesicle coat proteins which, through three-fold rotational symmetry, spontaneously assemble into polyhedral lattices that close into spherical constructs (see, e.g. Fig 6.1).[258]

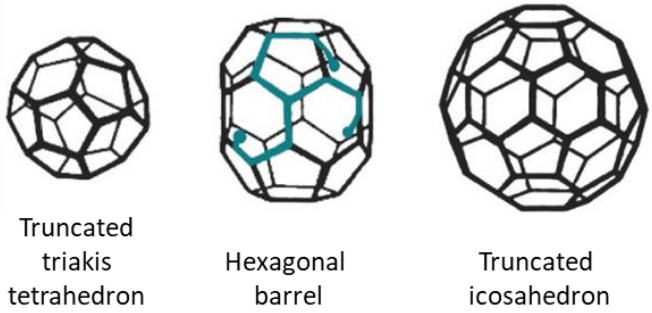

Figure 6.1. Schematic showing example structures that can form when proteins with three-fold rotational symmetry and directed intermolecular interactions self-assemble into polyhedral lattice cages. A single clathrin triskelion within the hexagonal barrel is shown in blue. Figure is reproduced from ref. [258]*, with permission from Springer Nature,* © 2004.

Our group has used this approach to design a self-assembling peptide cage termed “capzip”. The construct is based on a native antimicrobial sequence and the resulting assemblies show potent activity against Gram-negative and Gram-positive bacteria.[259]

6.1.2 Introduction to capzip

Capzip consists of three copies of a self-complementary sequence, conjugated to a trimeric hub βAla-Lys-Lys-NH_2 (Fig 6.2A). Each peptide monomer shows three-fold rotational symmetry (Fig 6.2B), and every arm is designed to spontaneously pair with the arm of another monomer (Fig 6.2C). The sequence itself is based on the active component of bovine lactoferricin, an antimicrobial hexapeptide RRWQWR.[260] This has a high propensity for β-sheet formation, with an alternating PHPHP motif. Furthermore, the WQW motif in the core of the sequence is analogous to tryptophan zipper motifs, WTW, which promote antiparallel β-sheet assembly by packing together tryptophan rings on opposing peptide strands.[261] To capitalise on this interaction, glutamine was replaced by threonine. Finally, the C-terminal arginine was replaced with glutamic acid to produce electrostatic interactions between opposing terminals.

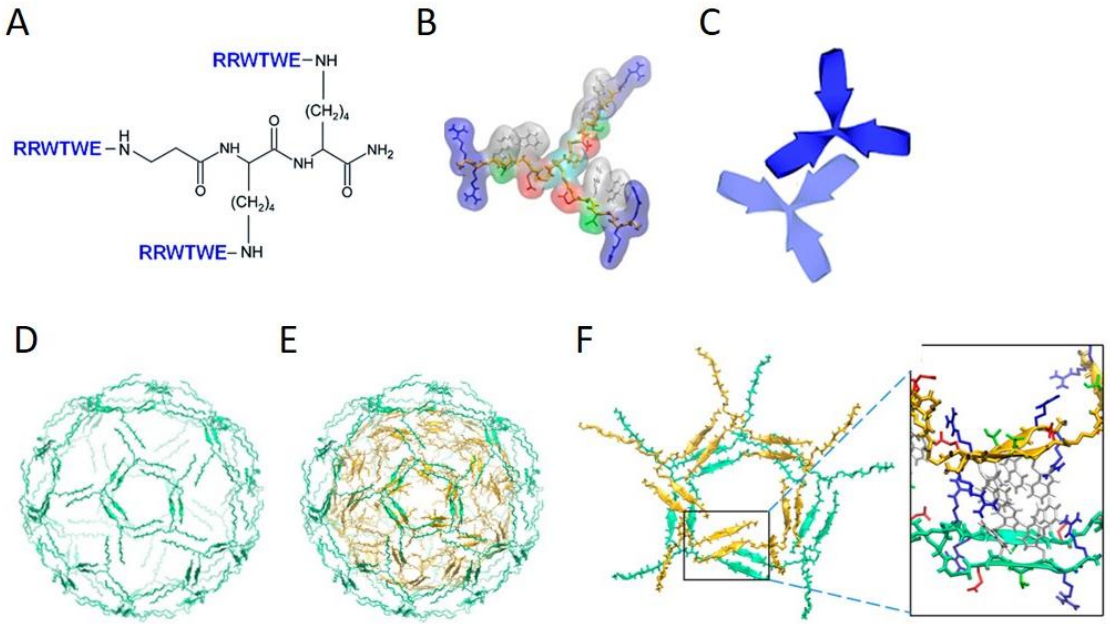

Figure 6.2. Capzip design. (A) Chemical structure of the trigonal conjugate, with a βA-K-K-NH_2 hub and three self-complementary RRWTWE arms. (B) Molecular model of the peptide monomer. (C) Schematic showing anti-parallel β-sheet association between arms of different monomers. (D) Single-walled icosahedron assembly of the peptide monomer and (E) double-walled assembly. (F) Snapshot of molecular dynamic simulations showing a double walled pentagonal assembly unit, with a higher resolution image (inset) showing the two β-sheet walls (green and yellow) form an internal interface of tryptophan side chains.(A) and (C) are reproduced from ref. [259]*, licensed under CC BY-NC 3.0, published by The Royal Society of Chemistry; (B) and (D-F) reproduced from* [262]*, licensed under ACS AuthorChoice, © 2019 American Chemical Society.*[10]

[10] Molecular dynamics simulations were performed by Irene Marzuoli (King’s College London).

The resulting construct is predicted to spontaneously assemble into pentagonal and hexagonal containing β-sheet lattices, with increasing curvature of the lattice as well as "sticky edges" of individual peptide strands promoting closure into a 3D sphere. Molecular dynamics (MD) simulations confirmed that the peptide monomer can support such structures (Fig 6.2D, E).[262] Peptide cages were found to be more stable as double walled structures. Monolayer β-sheet capsules (Fig 6.2D) collapsed within 600 ns of simulation, whereas bilayer β-sheet capsules (Fig 6.2E) were stable over 1 μs simulations. Unlike the single walled structure, the bilayer structure packs hydrophobic tryptophan side chains into a hydrophobic core (Fig 6.2F), preventing unfavourable exposure to an aqueous environment.

Assembly of capzip was confirmed experimentally by the biometrology group at the National Physical Laboratory, using a combination of in-air AFM, transmission electron microscopy and scanning electron cryomicroscopy. Particles of heterogeneous sizes were observed, with diameters predominantly between 20 – 200 nm.[259] Such a polymorphic assembly indicates that capzip monomers adjust their local conformation in response to different packing requirements. This behaviour is consistent with many viral capsids which, through conformational flexibility, adopt polygonal assemblies of different sizes.[263],[264] In addition, the trimeric hub of capzip is asymmetric. The asymmetry will propagate into assemblies that contain distinct pairing combinations, and this may result in a range of preferences for local curvature. The antimicrobial activity of the assembly was confirmed by both MIC assays and by live-dead imaging. Furthermore, the capsules were shown to be membrane-active, with in-liquid AFM imaging performed by Dr. Hasan Alkassem resolving individual capsules embedded into SLBs and converting directly into pores. Collectively, the results show capzip to be a promising higher-order peptide system with biological activity.

However, many open questions remain. Self-assembly has been postulated to offer protection against proteolysis, a major hurdle for peptide antibiotics.[252] However, it is unknown whether capzip assemblies are stable to proteolysis and also whether self-assembly can provide the same level of protection as synthesis via D- amino acids. Secondly, high resolution characterisation of capzip assemblies in aqueous solution has not yet been optimised. Most self-assembled capsule systems are currently characterised using electron microscopy techniques (transmission electron microscopy, scanning electron microscopy, cryogenic electron microscopy).[257] We hypothesise that using in-liquid AFM with an imaging mode that continuously records force-vs-distance curves at the surface may provide unique access to high resolution topographical and mechanical mapping of assemblies under near-native conditions. Finally, and most importantly, it has not yet been shown whether self-assembly offers a mechanistic advantage over monomeric peptides with respect to its modes of membrane disruption.

6.2 Results

It should be noted that throughout this chapter, capzip is pre-assembled by overnight incubation in 10 mM MOPS (pH 7.4) at a peptide concentration of 100 μM. The composition of SLBs for AFM imaging is DLPC:DLPG (3:1 molar ratio).

6.2.1 Stability assays

Peptides made from all D- amino acids are more therapeutically promising than their L-counterparts, being less likely to trigger immunogenic responses, and less susceptible to proteolytic degradation.[265],[266] However, self-assembly may also provide protection against proteolysis.[252] To determine whether D-capzip shows increased stability when compared to L-capzip, we test the susceptibility of both assembled constructs to the archetypal protease trypsin, an enzyme found in the small intestine of many vertebrates. Trypsin cleaves proteins at the carboxylic side of underivatized arginine and lysine residues.[267] It is an endoprotease and cannot release terminal amino acids. Capzip contains a trypsin-susceptible site at the second arginine of each RRWTWE arm, with each cleavage expected to release a dipeptide RR with a mass of 312 m/z.

15 min incubation of L-capzip with trypsin produces species at 3092.9 m/z, 2779.9 m/z (-313), and 2468.9 m/z (-624) (Fig 6.3A, left). These masses are consistent with intact L-capzip, L-capzip with RR cleaved from one arm, and L-capzip with RR cleaved from two arms. After 24 hr incubation, these higher masses are no longer present (Fig 6.3A, right). A peak occurs at 2157.2 m/z (-935.7), the expected mass for capzip with RR cleaved from all 3 arms. No intact capzip can be observed. Collectively these results show that trypsinisation of capzip begins rapidly and proceeds to completion. This is supported by analytical RP-HPLC analysis (Fig 6.3B). After 24 hr incubation, no peak is observed at the original retention time, verifying that no L-capzip remains intact. Furthermore, the longer retention time observed is consistent with the trypsinised product; loss of arginine will increase hydrophobicity and result in slower elution.

In contrast, D-capzip shows no susceptibility to trypsinisation. After 24 hr incubation, a single peak at the expected mass of capzip is observed (Fig 6.3C). Similarly, analytical RP-HPLC traces of D-capzip before and after 24 hr incubation are identical, verifying that no degradation takes place (Fig 6.3D).

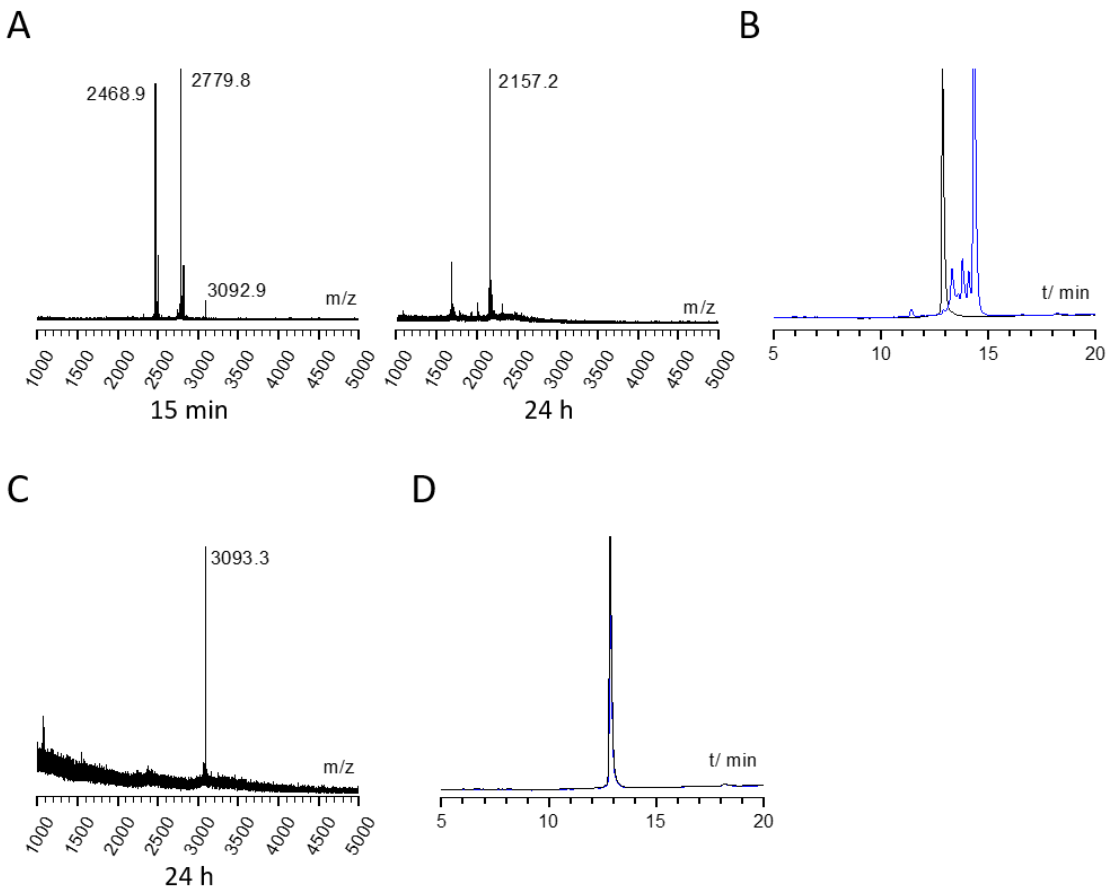

Figure 6.3. Comparative stability of L- and D- capzip assemblies to proteolytic degradation.. (A) Mass spectra of L-capzip following 15 min and 24 hr incubation with trypsin. After 15 min, species are observed at 2779.8 m/z and 2468.9 m/z, consistent with capzip with an RR dipeptide cleaved from one and two arms respectively. Some intact capzip still remains (3092.9 m/z). After 24 hr, a species at 2157.2 m/z is observed, consistent with capzip with RR dipeptides cleaved from all three arms. No intact capzip is seen. (B) Analytical RP-HPLC of L-capzip before (black) and after (blue) 24 hr incubation with trypsin. After incubation, no peak at the original retention time is observed, confirming that no intact peptide remains. A main product with a longer retention time indicating a more hydrophobic peptide is seen. (C) Mass spectra of D-capzip following 24 hr incubation with trypsin. A single species at the expected molecular weight of capzip is observed. (D) Analytical RP-HPLC of D-capzip before (black) and after (blue) 24 hr incubation with trypsin. The traces are identical, confirming that no degradation has taken place. All incubation was performed at 37 °C.

6.2.2 Characterisation of self-assembly

6.2.2.1 Confirmation of capzip secondary structure

Having demonstrated the increased stability of D-capzip to proteolytic degradation, we next confirm its structure and assembly. Figure 6.4 shows a comparison between the secondary structure of the two assembled systems. Identical folding is observed for D-capzip (Fig 6.4, solid line) and L-capzip (Fig 6.4, dashed line), demonstrating that the two enantiomers adopt the same secondary structures in capsules. The L-capzip spectra show a maxima at ~ 190 nm, double minima at 200 and 214 nm and a maxima at 225 nm (Fig 6.4, dashed line), and the D-capzip spectra show the exact opposite. Such a signal is consistent with a combination of β-turn,

β-sheet and aromatic tryptophan interactions [261],[268],[269] and is therefore compatible with the molecular dynamics prediction for capzip assembly, with β-turn like folding within the trigonal conjugate and β-sheet and tryptophan zipper interactions between the arms of different conjugates.

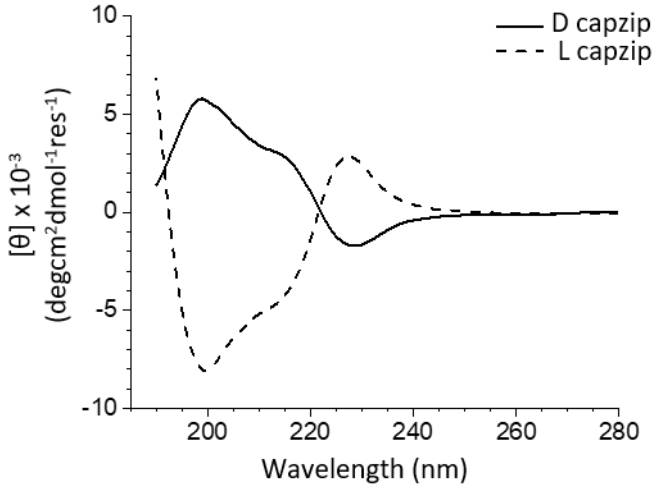

Figure 6.4. CD spectra for assembled L- and D- capzip. The enantiomers fold into the same secondary structures. Spectra taken at 100 μM peptide, pH 7.4, 10 mM MOPS, 20˚C.

6.2.2.2 Optimising in-liquid AFM characterisation of capsules

Experimental observation of capsule formation was previously conducted using transmission electron microscopy, scanning electron cryomicroscopy and in-air AFM.[259] In-liquid AFM was also used, but was performed on gold substrates, which do not provide atomically flat backgrounds and no high-resolution images were obtained (see ref. [259], Fig S3). Furthermore, for all characterisation techniques, a relatively small population of capsules were resolved (see ref. [259] Fig 2, Fig S2, S3). We set out to optimise in-liquid AFM imaging conditions to enable the characterisation of a large population of capsules in a more native environment.

To give an atomically flat background, freshly cleaved mica is used as a substrate. However, very few capsules are observed with the imaging conditions developed previously (milliQ water, 5 μL assembled capzip). Reasons for this may include that capsules do not bind to the mica surface, or that the capsule binding is so weak that the scanning AFM probe moves the capsules and thus prevents them from being imaged. We obtain significantly improved binding when substrates are hydrated by a solution of a higher ionic strength (120 mM NaCl, 20 mM MOPs, pH 7.4). In addition, we obtain greater particle coverage by increasing the volume of pre-assembled capsules added to 50 μL. Under these conditions, large populations of assembled D-capzip are resolvable by in-liquid AFM (see e.g. Figure 6.5A, B, D).

The size distribution of over 400 capsules is shown in Figure 6.5C. Particle diameter is determined by capsule height, which is less subject to tip-broadening effects than the capsule

width.[270] Assemblies range from 15 to 45 nm, in good agreement with recent characterisation of D-capzip assemblies by transmission electron microscopy.[262] The range is consistent with findings from the previous study (20-200 nm). However, with many more particles analysed, and no labelling or drying effects present, the distribution provided here gives a more reliable assessment of size. In support of this, MD simulations show that capzip monomers readily accommodate assemblies in this range (Fig 6.5E). Furthermore, having determined particle size experimentally, the number of peptide monomers per capsule can be calculated (Fig 6.5E).

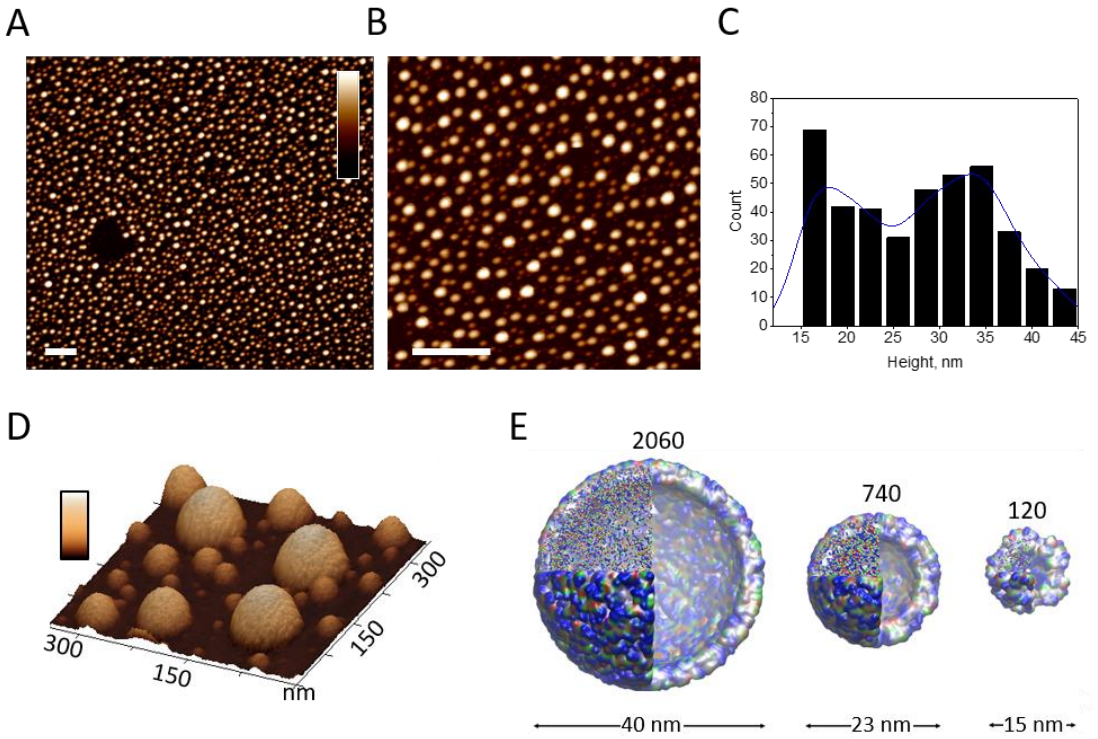

Figure 6.5. In-liquid AFM imaging of D-capzip assemblies. (A,B) Topography images of pre-assembled D-capzip capsules bound to a mica substrate at (A) lower and (B) higher magnification. Scale bar 500 nm and colour bar 50 nm in both. (C) Size distribution of D-capzip assemblies, measured by particle height using the topography image in (B). Diameters range from 15 – 45 nm, with over 400 particles measured. (D) 3D representation of AFM topography image of D-capzip capsules bound to mica. Colour bar 60 nm; (E) Coarse grained MD simulations showing optimal number of trigonal peptide monomers for a double walled β-sheet assembly at each size distribution.[11]

6.2.2.3 High-resolution confirmation of a hollow nature under native conditions

Whilst topography imaging allows for the characterisation of particle size, it cannot verify the cage-like nature. Confocal microscopy was previously used to confirm that capzip assemblies are hollow: by incorporating a 1:100 mix of fluorescein-labelled capzip into the assembly, an outer peptide ring and inner cavity could be resolved (Fig 2c and S2c in ref. [259]). However, the resolution limit of confocal microscopy means that this technique can only be performed on larger capsules which represent outliers to the main size range. In addition, the introduction of a

[11] Coarse grained MD simulations performed by Irene Marzuoli (King's College London).

label may alter the assembly process. Here, we validate a cage-like assembly for particles of 15 – 40 nm, in solution and without labelling. The approach we use is force-curve-based AFM imaging. Elastic modulus maps of the assemblies can distinguish hollow and solid particles, as hollow particles may be expected to show greater compliance in their centres when compared to their surrounding edge whereas solid particles will not. This is on the assumption of the particles remaining static (i.e., not moving sideways) under AFM indentation. Having optimised the imaging conditions, we are now able to characterise the mechanical properties of a large number of capsules in high resolution in their native environment.

The corresponding topography and elastic modulus maps of capzip assemblies are shown in Figure 6.6A and 6.6B respectively. The elastic modulus is derived from the force-distance curves using the Derjaguin-Muller-Toporov (DMT) model.[189] Calculation of quantitative values requires non-trivial determination of the tip shape and radius. Here, we show the qualitative changes in the elastic modulus across the surface, described in arbitrary units (a.u.). Cross-correlation averages for the topography and elastic modulus of small, medium and large capsules are shown in Fig 6.6C, with corresponding line profiles in Fig 6.6D.

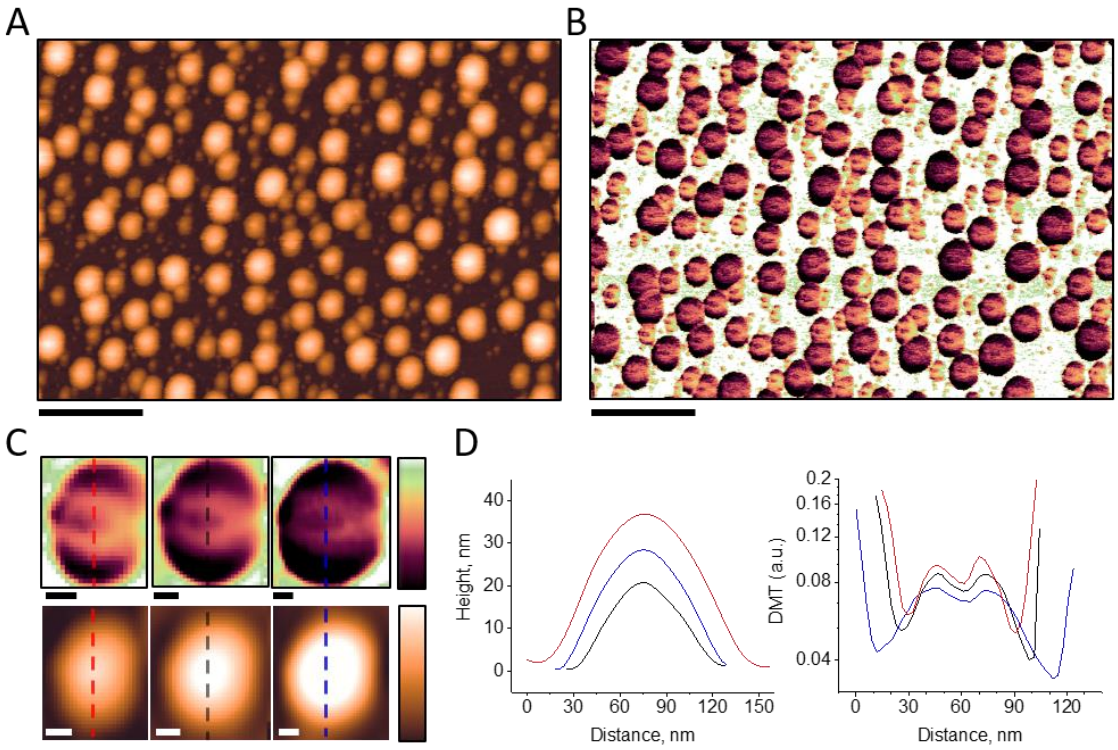

Figure 6.6. Mechanical characterisation of D-capzip assemblies. (A,B) Topography and elastic modulus maps of D-capzip assemblies, obtained simultaneously by Peak Force QNM imaging. Elastic modulus is derived from force-distance curves by using the Derjaguin–Muller–Toporov (DMT) model. Scale bars 300 nm. (C) Cross correlation average of elastic modulus (top) and topography (bottom) for small, medium and large capsules respectively. Calculated using Gwyddion (htttp://gwyddion.net). Scale bar 20 nm. (D) Topography and elastic modulus cross sections shown in (C) for small, medium and large capsules. Height scale 50 nm (topography) and qualitative increase (elastic modulus, purple to green).

Firstly, particles appear softer at their edges (Fig 6.6B-D). This is expected for any particle loosely absorbed to a surface irrespective of whether the particle is hollow or solid. During scanning, the particle will experience a sideways force from the indenting tip, causing slight movement and leading to an apparent softness at its edge. Confirmation of the artefactual nature of this edge effect is found in Fig 6.6C; particles appear more compliant at the left-hand edge than the right-hand edge, which reflects the left-to-right scan direction. Away from the edges and closer to the centre positions of the particles, the AFM tip approaches the capsules in a more vertical manner and sideways forces become negligible. Indeed, capsules appear stiffer. What is significant however, is that the very centre of the capsule appears softer again. This is indicative of hollow spheres, as for solid particles the centre would be expected to be the stiffest location. The effect is consistent across all capsules imaged, at all size ranges (Fig 6.6B-D). Together with fortuitous transmission electron microscopy observations of collapsed capzip capsules showing a double walled outer structure and hollow interior,[262] these results provide the first experimental evidence that capzip assemblies in the size range of 15 – 45 nm are forming as spherical peptide shells.

6.2.3 Interaction of D-capzip with SLBs

The proposed model for the antimicrobial activity of capzip is that each capsule binds to the bacterial membrane surface, before embedding into the lipid bilayer, disintegrating, and forming a pore at its landing point. This model is based on in-liquid AFM imaging performed by Hasan Alkassem which showed embedded capsules in an SLB (with a height of ~ 2 nm) converting into pores (over a timescale of 3-15 min).[259] We repeat these experiments with D-capzip assemblies. Our results agree with and expand upon previous findings.

6.2.3.1 Capsules disintegrate into the SLB via intermediates

Figure 6.7 (left) shows the SLB surface 5 min after addition of pre-assembled D-capzip. A range of capsule sizes are observed. Some have heights of around 15 nm above the membrane surface, consistent with freshly bound, intact capsules. Others have heights of around 5 nm above the surface, indicating disassembly of the capsule has begun. By 9 min (Fig 6.7, middle) many capsules have disintegrated into the bilayer. Remaining capsules have started the disassembly process, with heights above the membrane surface of less than 5 nm. By 13 min (Fig 6.7, right) most capsules have completed their disassembly.

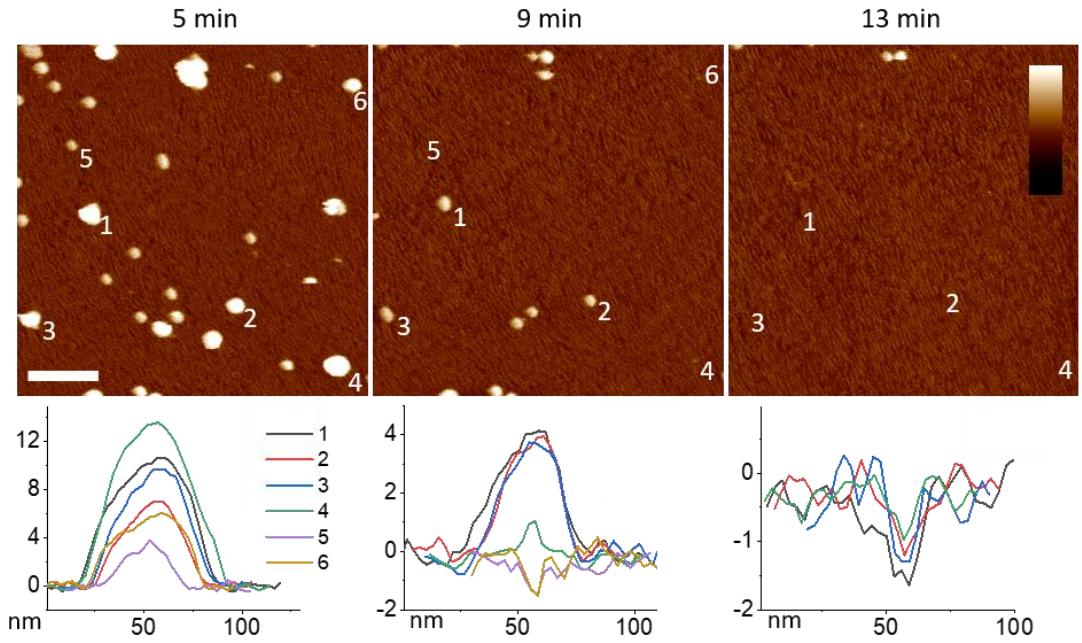

Figure 6.7. D-capzip assemblies with SLBs. Sequential topography images of an anionic SLB treated with pre-assembled D-capzip. Capsules can be observed landing, embedding and then disintegrating into the SLB, forming pores and lesions at their landing sites. Corresponding line profiles for labelled capsules (1-6) are shown at each time point. Scale bar 200 nm, colour bar 10 nm.

Line profiles taken across 6 particles over the first 15 min (Fig 6.7) show that capsules shrink in both height and in diameter before completely disassembling to leave a pore or lesion. This effect is exemplified by Figure 6.8, which overlays three of the capsule profiles as a function of time.

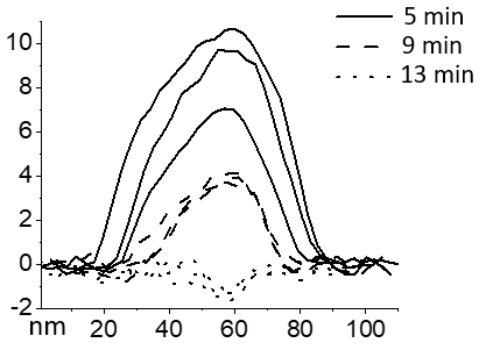

Figure 6.8. Disassembly of D-capzip capsules over time. Line profiles across three capsules (Fig 6.7, 1-3) at 5, 9 and 13 min after introduction to the SLB. All capsules shrink in height and diameter before complete disintegration takes place.

One explanation is that the capsule rearranges into smaller polygonal assemblies as peptide monomers are released to interact with the lipid bilayer. This is supported by the polymorphic nature of capzip assemblies in solution. The triskelion demonstrates conformational flexibility and could feasibly support structural rearrangement into smaller, metastable intermediates. Indeed, a similar range of intermediates has been observed by AFM for the minute virus of mice, a simple icosahedral viral capsid.[271] An alternative explanation is that the polygonal

starting structure collapses when it comes into contact with the bilayer, with the range of transitional sizes reflecting different sized aggregates of peptide monomer. In any case, the data confirms that binding to the membrane surface initiates disassembly, and reveals that disassembly proceeds via intermediate structures.

6.2.3.2 Membrane disruption occurs in under 1 min

A closer look at the first image taken after addition of D-capzip (Fig 6.7, 5 min) shows that significant disruption to the membrane has already taken place. The scan rate used is 4 min / scan, and the scan was taken from top to bottom. As such, the top of the scan represents 1 min after peptide addition. To better visualise the disruption that has occurred, a digital zoom of the scan is shown in Figure 6.9 (the top RH 500 nm^2 of the 1000 nm^2 image, representing 1 min to 3 min after peptide addition). A smaller colour scale is used to provide enhanced contrast, and the untreated membrane surface is shown for comparison. Considerable roughening of the SLB with pores and lesions is observed across the surface, indicating that many capsules have already landed and disintegrated into the SLB. As such, capsules can exert their effects in under 1 min of addition.

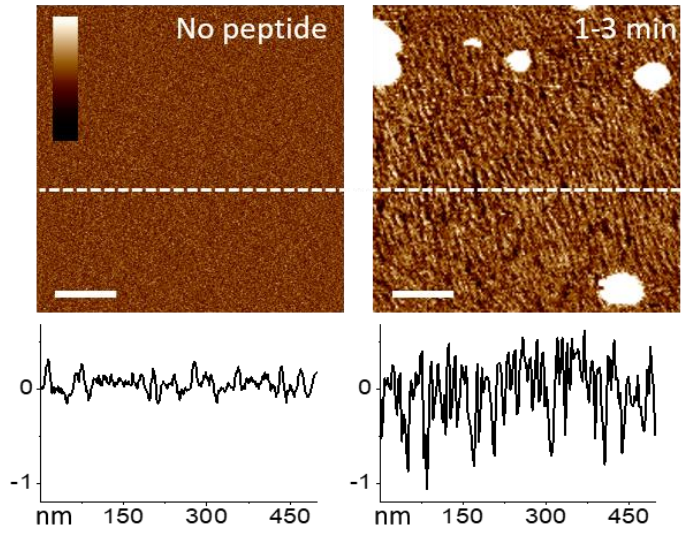

Figure 6.9. Loss of membrane integrity occurs less than 1 min after peptide addition. AFM topography images before (left) and after (right, 1-3 min from top to bottom of scan) addition of assembled D-capzip. Before peptide addition, the membrane surface is featureless and flat to within 0.2 nm. After peptide addition, significant loss of integrity is observed. Pores and lesions across the surface can be seen, up to 1 nm deep. Colour scale 2.5 nm, scale bar 100 nm. RH image is a digital zoom of Figure 6.7, 5 min, and is the top right hand 500 nm^2 of the 1000 nm^2 image.

AMPs typically exist as unfolded monomers in solution, and upon membrane binding, must transition into folded forms and oligomerise until threshold concentrations are reached.[272] This introduces a lag-time for antimicrobial activity. Indeed, in Chapter 5, the bacteriocin NI01 repeatedly showed a lag time of ~ 1 min before any disruption events were observed (see

section 5.2.3.). The peptide is pre-folded but monomeric in solution and the delay can be attributed to peptide oligomerisation on the membrane surface. A self-assembled system removes this requirement; the AMPs are pre-concentrated, landing on the membrane above their threshold concentrations, and can therefore exert instantaneous lytic effects upon binding. Indeed, time-kill assays for *S. aureus* and *E. coli* cells treated with capzip show a rapid transition from peptide binding to membrane rupture (5 – 10 min).[262]

Besides rapid antimicrobial activity, pre-concentrating the AMP may also increase its spectrum of activity. Monomeric AMPs rely on the membrane itself to promote oligomerisation. In contrast, a pre-concentrated (self-assembled) system may be less dependent on membrane-driven oligomerisation and therewith on membrane composition, with variations in factors such as membrane fluidity, charge and thickness having a smaller impact on antimicrobial activity. This hypothesis is supported by the wide range of activity observed for capzip. It can target Gram-negative and Gram-positive bacteria, including persister and multi-resistant strains.[262] That said, a rigorous validation of this hypothesis would require further investigation.

6.2.3.3 Prolonged membrane effects

Finally, whilst many capsules are observed to completely disintegrate within 10 mins of landing on the membrane surface, some particles are found to be stable in a partly disintegrated form. Figure 6.10 shows such an intermediate structure - 4 nm high – that is stable 35 min after initial addition to the membrane surface. Then, over a 15 min period, it completes its disassembly.

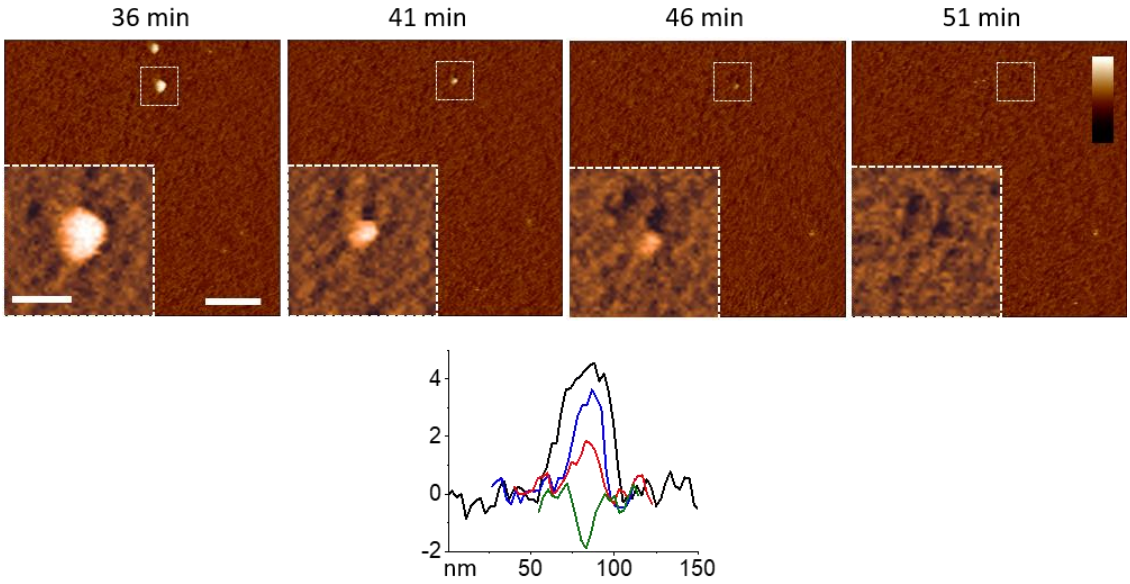

Figure 6.10. D-capzip assemblies provide a reservoir of antimicrobial peptide. AFM topography images showing some capsules have stable intermediates during disassembly. Here, a part disintegrated capsule (4 nm above the membrane surface) is stable 35 min after initial addition. Then, over a 15 min period, the capsule completes its disintegration. Digital zoom of the dotted white box is shown as an inset. Scale bars 50 nm (inset), 200 nm (main image). Colour bar 10 nm for all. Corresponding line profile across the enlarged capsule is also shown.

The particle acts a reservoir of antimicrobial peptide that is bound to the membrane surface but has not yet released its effect. Such a reservoir enables D-capzip to exert an antimicrobial effect over a more prolonged time period than conventional AMPs. Indeed, in Chapter 5, the disruption effects of NI01 plateaued after 10 min of peptide addition, and we demonstrated that this plateau was due to a lack of available peptide (see section 5.2.3.). When combined with the protection against proteolytic degradation, we hypothesise that capzip will show more sustained antimicrobial effects than conventional AMPs. In agreement with this, a single injection of capzip into *G. mellonella* larvae pre-infected with a methicillin-resistant *S. aureus* (MRSA) bacterial strain shows continued antimicrobial activity over a period of 5 days.[262]

6.3 Conclusions

In this chapter we have optimised in-liquid characterisation of capzip to enable high-resolution measurement of the size of assemblies formed, as well as validation that assemblies are hollow. The ability to effectively characterise the sizes of capsules formed is a useful tool for the future development of capzip, as the effect of adjusting the peptide sequence on its assembly can be directly observed, and can then be related to the kinetics of membrane disruption and antimicrobial activity in both *in vitro* and *in vivo* assays. Furthermore, simultaneous mechanical and topographic mapping of nanoscale systems in solution can be applied to other self-assembling systems. We have also demonstrated that the enantiomeric form of the peptide assembles and folds in the same manner as the L-amino acid form, whilst showing increased stability against proteolytic degradation. This indicates D-capzip is a more promising therapeutic target.

Finally, we have resolved the disintegration of capsules into SLBs. Our data suggests that a self-assembled system enables more rapid disruption of the surface by removing the lag-phase for membrane oligomerisation. Simultaneously, the presence of stable intermediates allows prolonged membrane disruption effects by providing a reservoir of peptides bound to the surface. Taken together these results indicate that self-assembly into peptide capsules enables AMPs to exert their antimicrobial effects over a wider timescale than monomeric peptides, confirming the therapeutic potential of self-assembled systems.

Collectively, the chapters in this thesis have provided direct visualisation of different modes of membrane disruption induced by peptide motifs at different levels of complexity. However, individual peptides could not be resolved, and the modes of action have been inferred from changes in the overall membrane topography. This illustrates two very generic limitations of AFM: its lack of chemical resolution and its difficulty in resolving small, highly dynamic and or flexible molecules. This leads to our final question, addressed in Chapter 7. Are there improvements to AFM methodology that can be made to enable more specific interactions to be resolved? If so, can an AFM based approach with improved specificity provide new insights

into peptide-lipid interactions? Could it advance the existing models of membrane disruption (membrane thinning, toroidal pore) which currently lack both detail and physical accuracy?

7 Improving the structural and chemical resolution of AFM on membranes

In this final chapter, I describe our developments of AFM methods to more specifically resolve AMPs and their interactions with lipids, using charge mapping (part one) and chemical labelling (part two). We anticipate that such developments will provide more insight into peptide-lipid interactions, and will allow us to build upon the existing models for modes of disruption (toroidal pore, carpet, membrane thinning, etc) by introducing more detail and more physical accuracy. The data presented is preliminary.

7.1 Part one: Resolving peptide-lipid interactions by charge mapping

7.1.1 Introduction to AFM- charge mapping

Local, nanoscale chemical resolution may be obtained by combining AFM with spectroscopic methods. For example, in-liquid AFM-IR is gradually progressing towards simultaneous chemical and topographical imaging at nanoscale resolution.[273],[274] For AMPs on a bacterial membrane, another way of obtaining chemical resolution is by making use of their net positive charge, which contrasts with the negative surface charge of the membrane. Hence, we may relate topographical features to AMPs or to lipids depending on their surface charge.

For mapping surface charges with nanoscale resolution, a common approach is so-called Kelvin probe force microscopy (KPFM).[275],[276] In this technique, two bias voltages are applied to the cantilever: a DC bias (V_{DC}) and an AC bias ($V_{AC}\cos\omega_m t$), where ω_m is the modulation frequency (radians / s). The resulting electrostatic force experienced by the tip, F_{es}, depends on the externally applied voltages, the surface potential of the sample, V_s and the tip-sample capacitance as a function of height, C_z'. The force can be separated into its static and dynamic components, with the latter occurring at the first and second harmonics of the modulation frequency of the applied AC voltage, F_{ω_m} and $F_{\omega_{2m}}$, described by Equation 7.1 and 7.2 respectively. In KPFM, a lock-in amplifier monitors the cantilever response induced by F_{ω_m}. A feedback loop is then used to constantly adjust V_{DC} such that it nullifies the response. Equation 7.1 shows that this occurs when V_{DC} matches V_s, and as such, the approach enables the surface potential of the sample to be determined.

$$F_{\omega_m} = -C_z'(V_{DC} - V_s)V_{AC}\cos\omega_m t \qquad (7.1)$$

$$F_{2\omega_m} = C_z'\frac{1}{4}V_{AC}^2\cos 2\omega_m t \qquad (7.2)$$

Whilst KPFM has been used extensively in vacuum, in air and in non-conductive media, it is not compatible with ionic solutions such as physiological buffer solutions. The applied voltages drive ionic currents and electrochemical reactions at the probe and/or sample surface, greatly

compromising experimental stability. This has motivated the development of alternatives, such as Open Loop Electric Potential Microscopy (OLEPM), a technique reported by Fukuma's group at Kanazawa University to enable simultaneous topographical and potential measurements in aqueous solutions.[277]–[279] In OLEPM, surface potential is calculated not by applying a matching V_{DC} bias, but by monitoring the cantilever response to both F_{ω_m} and $F_{2\omega_m}$ components. The amplitudes of induced cantilever oscillation at the first and second harmonic modulation frequencies of the AC voltage, A_1 and A_2, can be described by Equation 7.3 and 7.4, where k is the cantilever spring constant, and $G(\omega)$ is the transfer function that describes the cantilever response to a force as a function of frequency (Eq. 7.5, where Q is cantilever quality factor). From measurement of A_1 and A_2, the surface potential V_s can be calculated (Eq. 7.6, including also the phase of the cantilever φ_1 at ω_m to determine the polarity of $|V_s|$).

$$A_1 = G(\omega_m)\frac{|F_{\omega_m}|}{k} = G(\omega_m)|C_z' V_s|\frac{V_{ac}}{k} \quad (7.3)$$

$$A_2 = G(2\omega_m)\frac{|F_{2\omega_m}|}{k} = G(2\omega_m)|C_z'|\frac{V_{ac}^2}{4k} \quad (7.4)$$

$$G\ (\omega) = \frac{1}{\sqrt{\left[1-\left(\frac{\omega}{\omega_0}\right)^2\right]^2+\left[\frac{\omega}{Q\omega_0}\right]^2}} \quad (7.5)$$

$$V_s\ = cos\varphi_1 \frac{V_{AC}}{4}\frac{G(2\omega_m)}{G(\omega_m)} \times \frac{A_1}{A_2} \quad (7.6)$$

The major advantage of OLEPM is that surface potential can be calculated without the need to apply a V_{DC} bias. This reduces the induction of electrochemical reactions and unstable imaging conditions that prevent KPFM from being operated in ionic solution. Whilst the application of a V_{AC} bias could induce similar effects, modulating the voltage at a high enough frequency ω_m ensures that redistribution of ions is slow in comparison to the applied voltage and that effects on imaging are negligible.[277] In October 2019, I spent 4 weeks in Fukuma's group conducting a pilot study that explores the potential of OLEPM to resolve the distribution of cationic AMPs across the model membrane surface, as well as any peptide-induced phospholipid segregation or clustering effects. The aim of the research project was to determine whether we could obtain surface potential maps of AMP-treated SLBs, and whether these maps could provide a more detailed understanding of AMP-lipid interactions that are taking place. All experiments were performed with Kaito Hirata. Here, I report on our findings.

7.1.1.1 Basic operation of OLEPM

A schematic showing the basic set up of OLEPM is shown in Figure 7.1. Topography measurements are performed using conventional AFM imaging methods. The cantilever is oscillated at its resonance frequency f_0 by photothermal actuation, operation is performed in

AM mode, and the surface topography is measured by adjusting the tip-sample distance to maintain the cantilever oscillation at a user defined amplitude A_0. For simultaneous electric potential measurement, an AC bias voltage $V_{AC}\cos(\omega_m t)$ is applied to the tip. The cantilever response at the first and second harmonic modulations of the AC bias (A_1 and A_2) are monitored using a lock in amplifier.

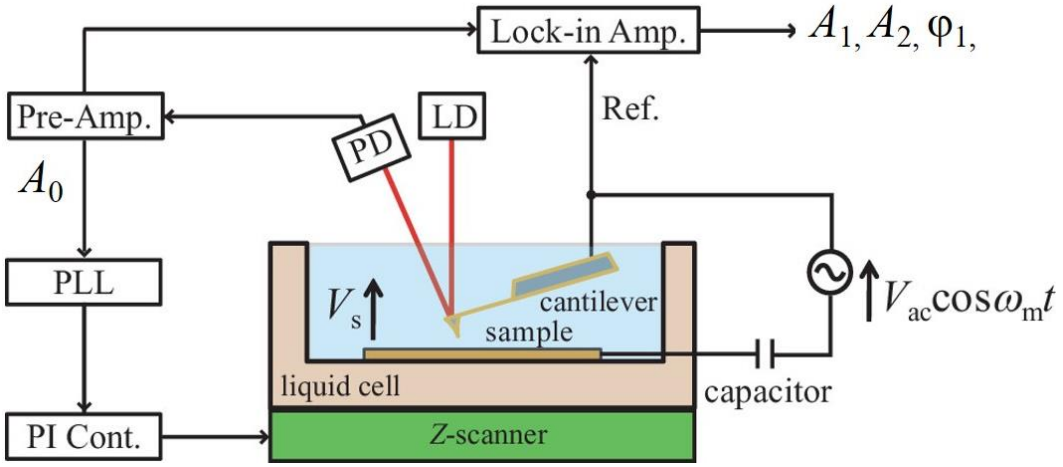

Figure 7.1. Schematic of in-liquid OLEPM set up. An AC bias voltage, $V_{AC}\cos(\omega_m t)$, is applied between the tip and the sample. The cantilever is driven by an actuation laser (omitted for clarity) and the cantilever deflection is monitored using a detection laser and a quadrant photodiode. Detection is at ω_0 for topography measurements and at ω_m and $2\omega_m$ (using lock in amplifiers) for calculation of V_s. The phase of the cantilever φ_1 at ω_m is also measured. Figure is reproduced from ref. [277]*, with permission from AIP Publishing.*

7.1.1.2 Dual frequency OLEPM

As discussed above, the modulation frequency of the AC bias voltage ω_m should be as high as possible to supress unwanted electrochemical reactions and redistribution of ions and enable OLEPM to be operated reliably in ionic solution. However, the maximum modulation frequency that can be applied is limited by the resonance frequency of the cantilever, f_0. Calculation of the surface potential requires monitoring of the cantilever response at the first and second harmonics of the modulation frequency ($f_m = \frac{\omega_m}{2\pi}$, and $2f_m = \frac{2\omega_m}{2\pi}$ respectively) and, as the cantilever response to forces rapidly deteriorates at frequencies above f_0, the modulation frequency of the applied AC bias must be low enough that $2f_m < f_0$. To reduce this limitation, dual frequency mode OLEPM has recently been developed.[278] This follows the same principles as conventional OLEPM, but applies two AC voltages with two different frequencies ($V_1\cos\omega_1 t$ and $V_2\cos\omega_2 t$), inducing frequency mixing in the cantilever response. The resulting electrostatic force on the cantilever now contains components at the first and second harmonics of the modulation frequencies (ω_1, $2\omega_1$, ω_2, $2\omega_2$) as well as components at ω_H and ω_L, where $\omega_H = \omega_1 + \omega_2$ and $\omega_L = \omega_1 - \omega_2$. It has previously been shown that the surface potential can be calculated solely by monitoring the cantilever response at ω_1 and at ω_L, via

Equation 7.7.[279] Crucially, this removes the need to measure cantilever response at the second harmonic of the modulation frequency, allowing higher modulation frequencies to be used.

$$V_S = \cos\varphi_1 \frac{A_1}{A_L}\frac{G(\omega_L)}{G(\omega_1)}\frac{V_{AC}}{2} \qquad (7)$$

All measurements in this chapter were conducted with dual frequency OLEPM. The modulation frequencies applied were $f_1 = \frac{\omega_1}{2\pi} = 700\ kHz$ and $f_2 = \frac{\omega_2}{2\pi} = 800\ kHz$. These frequencies are to be compared with the resonance frequency of the cantilever used, $f_0 = 1.3\ MHz$ in water (USC-F2-k3 (Nanoworld), nominal spring constant $k = 3\ N/m$, nominal resonance frequency in air $f_0 = 2\ MHz$ in air).

7.1.2 Protocols for OLEPM measurement of SLBs

OLEPM measurements require an electrical circuit to be formed between the cantilever and the sample, meaning that both the cantilever tip and the substrate must be conductive, which is not generally the case in AFM experiments. The following protocols were therefore developed to enable OLEPM imaging of SLBs on a conductive substrate and with a conductive tip.

7.1.2.1 Cantilever preparation

USC-f2-k3 cantilevers were used in all experiments due to their high resonance frequency (allowing high modulation frequency for the applied AC bias) but low spring constants (for soft biological imaging). The cantilevers are manufactured with gold coating on both sides, but an uncoated tip. Therefore, prior to experiments, focussed ion beam- scanning electron microscopy (FIB-SEM) was used to coat the tip with a 30 nm Au layer (Helios CX DualBeam FIB-SEM, equipped with a GIS Gas Delivery System, Thermo Fisher Scientific). FIB can be used to directly deposit thin metal films with nanoscale precision.[280] A high purity ion beam, usually from a liquid metal ion source, is finely focussed to sputter coat the surface. When combined with SEM, this allows high resolution visualisation of the sample and increased precision of deposition.

7.1.2.2 Substrate preparation

To produce a flat and conductive substrate, a mica substrate was coated with a 200 nm Au layer using thermal evaporation. This results in atomically flat islands of gold across the surface, suitable for high resolution AFM imaging. To enable SLB deposition, the gold surface must be made hydrophilic. Functionalisation of gold surfaces can be achieved through alkyl thiol self-assembled monolayers (SAMs), a technique first demonstrated by Nuzzo and Allara in 1983 and used extensively since.[281] Alkyl thiols with carboxyl, phosphate and sulphate terminal functional groups have all successfully been used for the deposition of SLBs on gold.[282],[283] In this project carboxy alkyl thiols were used. Au coated mica substrates were

submerged in a 1 μM solution of 10-carboxy-1-decanethiol in ethanol overnight to allow SAM formation. The substrate was then rinsed five times with fresh ethanol, dried under compressed air and attached to the sample holder with adhesive carbon tape. A copper wire was secured to the SAM-functionalized gold surface and placed under a protective rubber seal using stage clips (Fig 7.2).

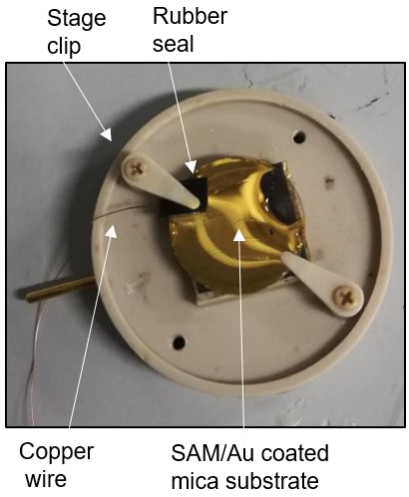

Figure 7.2. Optimised sample set-up. SAM-functionalized Au coated mica disc is attached to the sample holder with adhesive carbon tape. A copper wire is held against the SAM- functionalized gold surface using a stage clip, and a rubber seal isolates the copper wire from the imaging droplet to prevent copper ions entering the imaging solution.

7.1.2.3 SLB formation and peptide addition

Throughout the experiments, POPC:POPG (3:1 molar ratio) was used for SLBs. However, the standard physiological buffers we have used in this thesis to date (120 mM NaCl, 20 mM MOPs) are not compatible with OLEPM. The frequency of modulation that is required to supress the induction of unwanted ionic currents and unstable imaging conditions when applying the external AC bias increases with the ionic strength of solution. Kobayashi et al demonstrated that for an imaging solution with an ionic strength of 1 mM, a modulation frequency above 50 kHz is required while for a 10 mM solution a frequency above 300 kHz is required.[278] Solutions with an ionic strength above 10 mM have not yet been validated. Therefore, to ensure uncontrolled electrostatic forces were not induced, the ionic strength of solution was limited to 5 mM and the modulation frequencies were kept significantly higher than 300 kHz ($f_1 = \frac{\omega_1}{2\pi} = 700$ kHz, $f_2 = \frac{\omega_2}{2\pi} = 800$ kHz). Specifically, POPC:POPG (3:1 molar ratio) SUVs were prepared in H_2O, and, for SLB formation, vesicles (5 μL 1 mg / mL) were added to the substrate with 70 μL H_2O and 1 μL 1M $MgCl_2$ solution. After 45 min of incubation, the surface was rinsed with 4 mM NaCl, 0.67 mM MOPS pH 7.4. As such, the imaging solution has a final ionic strength solution of < 5 mM. TriAMP, described in Chapter 4, was used as the test AMP for all OLEPM experiments. Peptide solutions were prepared in H_2O

and added to the SLB during imaging through a syringe pump system, or via manual addition. The peptide concentration in the imaging droplet was approximately 0.5 -1 μM.

7.1.3 Preliminary results

7.1.3.1 OLEPM measurements of an untreated SLB

The morphology of the underlying Au-coated mica substrate is shown in Figure 7.3A, with atomically flat islands of around 500 nm in diameter observed. Figure 7.3B shows that following SAM functionalisation, SLBs can be formed on the Au surface, and that with the developed sample set up, OLEPM can produce simultaneous topography and potential maps of the surface. Good SLB coverage was achieved, with the lipid bilayer following the underlying morphology of Au islands. The potential across the SLB appeared quite uniform, with the main points of contrast occurring between individual islands.

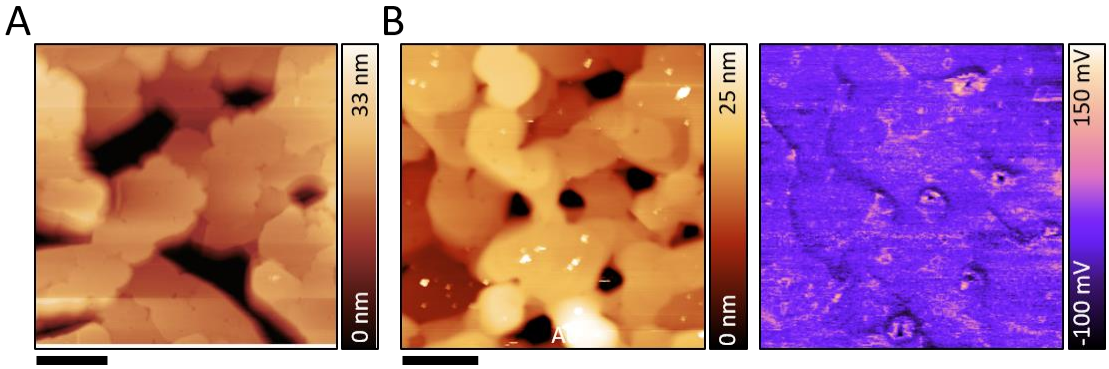

Figure 7.3. OLEPM measurements of an untreated SLB. (A) Topography measurement of the underlying Au-coated mica substrate. Au forms in atomically flat islands across the surface. (B) Topography (left) and potential (right) maps of a POPC:POPG (3:1 molar ratio) SLB formed on a SAM/Au substrate. The SLB covers the underlying SAM/Au islands, and the potential is uniform across the surface. Scale bars are (A) 250 nm and (B) 500 nm.

7.1.3.2 OLEPM measurements of an AMP-treated SLB

Figure 7.4 shows a series of images taken before, during and after the introduction of AMP to the SLB. Before peptide addition, continuous lipid bilayer forms across the underlying islands, and the potential appears uniform (Fig 7.4A). When peptide enters the system, there is a significant change in potential (Fig 7.4B). In parallel, topographical images show that the peptide is solubilising the bilayer, with the remaining lipid showing a convoluted boundary length indicative of AMP-induced lowering of the line tension (Fig 7.4B-D).

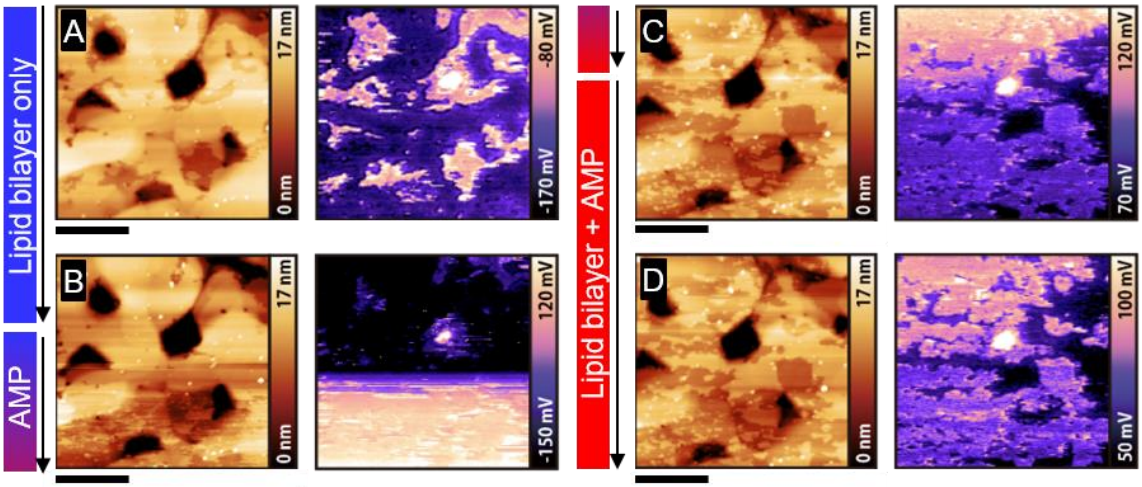

Figure 7.4. OLEPM measurements of an SLB, before during and after treatment with AMP. Simultaneous topographical images (LHS) and potential measurements (RHS) for a POPC:POPG (3:1 molar ratio) SLB prepared on a SAM/Au surface. (A) is taken before peptide addition; (B) AMP begins to flow to the surface (0.8 μM peptide, 6 mL / min, 600 μL) and (C-D) The effects of the AMP treated SLB can be observed. The system remains stable and repeated measurements can be taken. Scale bar 300 nm.

7.1.3.3 Correcting for long range surface potential before and after AMP addition.

The direct effect of the local surface potential on the tip will extend only as far as the Debye screening length, which, for a 5 mM ionic solution consisting of predominantly monovalent ions, will be < 5 nm. However, it has previously been demonstrated that OLEPM measurements can also include contribution from longer-range interactions, due to electrostatic forces acting not on the tip apex but on other parts of the cantilever.[279] As such, the images shown in Figure 7.3 and 7.4 represent qualitative but not quantitative maps of the potential distribution at the lipid bilayer surface. To obtain a more quantitative measure, the long-range contribution, which appears linearly dependent, can be empirically subtracted from the potential profile as a function of height.[279]

Figure 7.5A (blue line) shows potentials as a function of height, taken on an untreated POPC:POPG (3:1 molar ratio) SLB for distances of up to 1000 nm. Long-range contributions to the electrostatic force experienced by the tip are clearly present. Following subtraction of the long-range background, the SLB shows a surface potential of around 0 mV (Fig 7.5A, red line). This was surprising. With 25 % anionic phospholipid, the SLB was anticipated to have a negative surface potential, and the neutral value observed may imply that anionic POPG is being sequestered to the inner leaflet leaving zwitterionic POPC at the surface. Figure 7.5B (blue line) shows potentials as a function of height after adding AMP to the SLB. Following subtraction of the long-range background, the potential of the lipid surface becomes positive (Fig 7.5B, red line). This is consistent with AMP binding to, and diffusing across the lipid bilayer, indicating that even though we cannot resolve the cationic AMPs topographically, we can detect them by charge.

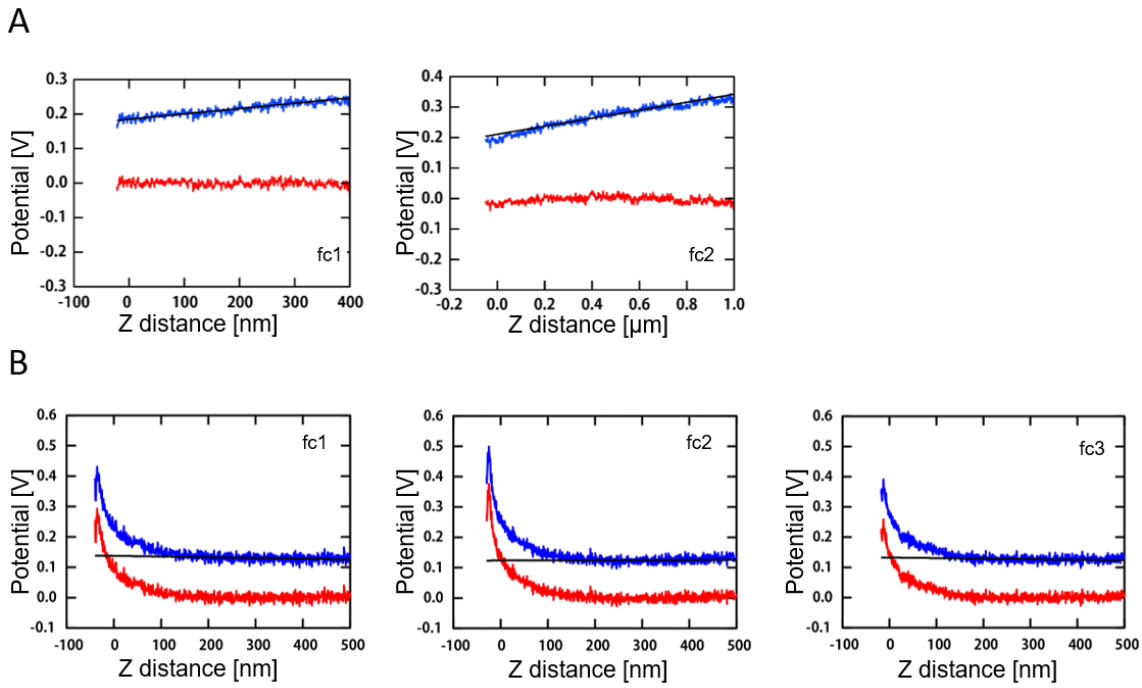

Figure 7.5. Measured potential as a function of height (distance) above the sample (blue); these enable correction for long range interactions between the tip and the sample. The long-range potential is linearly dependent and is estimated by the black line. Following subtraction of the LR contribution, a more accurate value for the surface potential is obtained (red line). (A) Measured potential versus distance taken on an untreated POPC:POPG (3:1 molar ratio) SLB. Following subtraction of the long-range potential, the untreated SLB shows a surface potential close to neutral. (B) Potential versus distance taken on a POPC:POPG (3:1 molar ratio) SLB treated with AMP. Following subtraction of the long-range contribution, the AMP-treated SLB has a positive surface potential.

7.1.3.4 An edge effect

The data described so far provides a proof-of-concept that OLEPM can be used to simultaneously map the topography and potential of AMP treated SLBs in real-time, and that changes in the surface potential can both be detected and quantified. In addition, preliminary data from higher magnification images was obtained which indicated a non-uniform charge distribution at bilayer edges for both treated and untreated SLBs. For untreated SLBs prepared as isolated patches, a more negative potential at the edge of the bilayer was observed when compared to the bilayer center (see, e.g., Fig 7.6A). This is intriguing, suggesting a higher density of anionic POPG occurs at bilayer edges. As lipid packing is different in the bulk phase and edge phase (Fig 7.6B), the two lipid species may well show different preferences for each phase, leading to lipid heterogeneity. The opposite behavior was observed for AMP-treated SLBs, with a more positive potential at the edge of lipid patches when compared to the bulk (see, e.g., Fig 7.6C). This indicates a higher concentration of AMP, consistent with many studies that have shown AMPs to preferentially bind to boundary edges (see e.g. [120]). To date, this argument has been based on their ability to reduce the line tension of the boundary edge. The preliminary data shown in Figure 7.6A indicates that there could be an additional

charge argument, in which AMPs are also driven to boundary edges by increased electrostatic attraction.

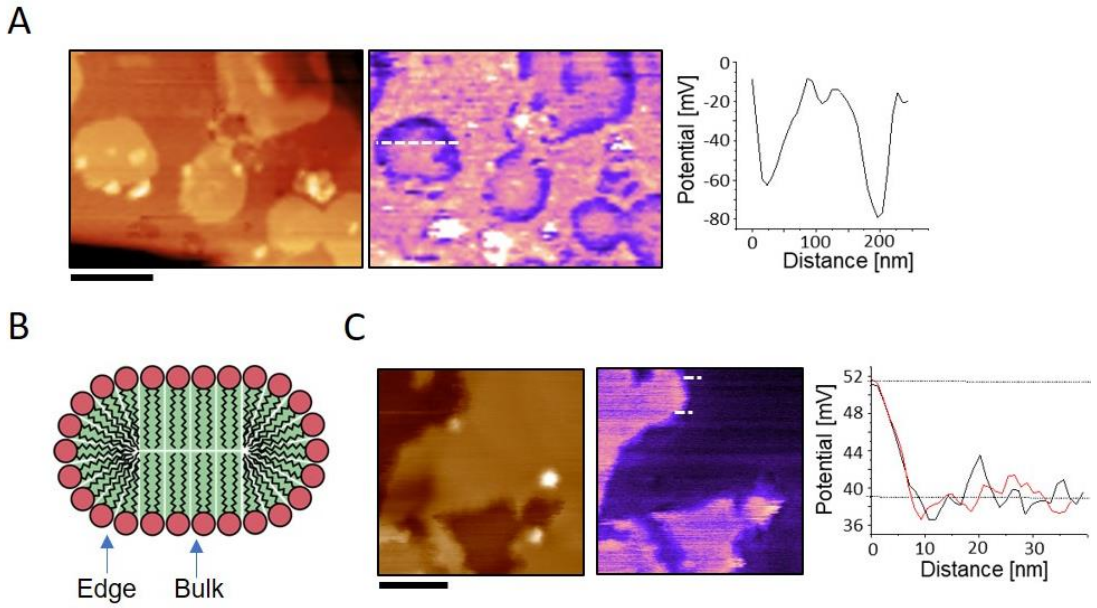

Figure 7.6. Preliminary data indicating an edge effect. (A) Topography measurements of untreated POPC:POPG (3:1 molar ratio) SLBs prepared as individual lipid patches, with corresponding potential measurements and line profile showing a more negative surface potential at the patch edge. (B) A schematic demonstrating that edge and bulk phases have different lipid arrangements. (C) Topography and potential measurements of a continuous POPC:POPG (3:1 molar ratio) SLB treated with AMP, with corresponding line profiles. The peptide has solubilised much of the bilayer, but the remaining lipid has a positive surface potential, with more positive potential at the lipid edge. Scale bars are 200 nm (A) and 100 nm (B).

7.1.4 Discussion

Overall, correlative charge mapping using OLEPM appears to be a promising avenue for future AMP-lipid experiments. We have demonstrated that OLEPM can resolve the topography and surface potential of SLBs during peptide treatment, in aqueous solution. Topographical images visualized an AMP solubilizing the lipid bilayer, with the remaining lipid exhibiting an extended boundary length characteristic of AMP-induced bilayer remodeling. Potential measurements revealed that the surface potential of the bilayer is close to neutral before peptide addition and becomes positive after peptide addition. As the peptides are cationic, this increase in surface charge indicates that AMP diffusing across the lipid surface can be detected. Finally, higher magnification images resolved a non-uniform charge distribution at the edge of lipid bilayers. In peptide treated bilayers, a more positive potential was observed, further confirming the ability of the technique to detect cationic AMP, which are known to preferentially bind at lipid edges. In untreated bilayers, a more negative potential was observed, indicating a higher proportion of POPG at lipid edges, and, consequently, an additional driving factor for the accumulation of cationic AMP at lipid edges.

Having optimized the sample setup and demonstrated that stable imaging conditions, control measurements are now required to confirm the preliminary findings and to validate the methods developed. First, confirmation is needed that the surface potential of an untreated bilayer is a reliable measure of the proportion of anionic and zwitterionic lipid present. To do this, POPC:POPG bilayers with different amounts of PG should be prepared at, e.g., 0% (i.e., POPC-only), 10%, 25% and 50%. If the surface potential does reflect the lipid composition, the measure potential value will be lower for higher POPG contents. This will validate the use of surface potential to identify clustering effects of POPC-rich or POPG-rich lipids. Secondly, confirmation is needed that POPC:POPG bilayer edges have an increased negative charge due to increased accumulation of POPG lipid. To do this, the potential distributions of POPC only patches and POPC:POPG patches should be compared. If POPG edge clustering is a real effect, we would expect to see no contrast at the edge of POPC patches, and again observe a more negative potential at the edges of the POPC:POPG patches. Finally, the peptide concentration needs to be optimized. The preliminary data presented here shows an AMP solubilizing a lipid bilayer. At lower peptide concentrations, poration and thinning effects should become visible. Furthermore, taking higher resolution images and smaller scan sizes may give more detailed contrast in the potential measurements, and enable better identification of localized lipid clustering and AMP-rich areas.

7.2 Part two: a labelling approach to distinguish lipid heads and tails in disrupted membranes

7.2.1 Improving the model for localised AMP-induced membrane thinning

In part two of this chapter, we use chemical labelling to directly address the challenge of improving on the chemical detail and physical accuracy of the current models to describe modes of membrane disruption. Specifically, we look at the case of membrane thinning (Fig 7.7).

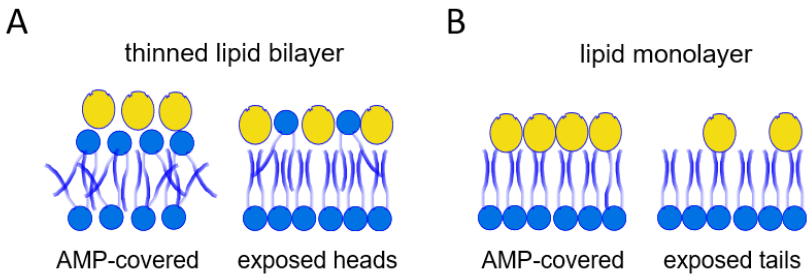

Figure 7.7. Proposed models for localised membrane thinning. (A) a thinned bilayer and (B) a lipid monolayer. For each model the domain can be entirely or partially covered by AMP.

Discrete regions of thinned membrane, 1-2 nm lower than the bilayer surface are commonly observed by AFM following AMP treatment.[118],[124],[125],[139] Indeed, in this thesis alone, localised domains of thinned membrane were repeatedly observed. However, the underlying physical nature of such domains has yet to be resolved. Current models propose either that the peptide induces a thinned bilayer by splaying the lipid tails (Fig 7.7A), or that the

peptide removes the upper leaflet lipids to result in a peptide stabilised monolayer (Fig 7.7B), with domains either entirely or partially covered in AMP. In the case of partial coverage, this would leave either exposed phospholipid head or tail groups at the surface of the domains. In this section, we use AFM combined with chemical labelling to identify such exposed phospholipid head or tail groups. In particular, we rely on biotin-streptavidin binding, noting that biotinylated phospholipids are commercially available and can be purchased with a biotin molecule attached to the phospholipid tail or head group. Streptavidin binds to biotin with extremely high affinity ($K_A \sim 10^{14}\ M^{-1}$), and, crucially, is large enough to be resolved by AFM,[284],[285] yet not so large that it completely occludes details of the membrane topography. As such, streptavidin can act as a visible marker for the biotinylated lipid and by extension, for the distribution of surface exposed lipid head or lipid tail groups.

7.2.2 Experimental methods

7.2.2.1 Concept of the assay

A schematic of the experimental design is depicted in Figure 7.8. An SLB doped with biotinylated lipid is prepared, AMP is added to induce domains of membrane thinning, streptavidin is added to bind to exposed biotins, and the surface is imaged by AFM. If streptavidin is observed in the thinned domains when biotinylated head groups are used, this will indicate exposed phospholipid head groups are present i.e. the domain is a thinned bilayer.

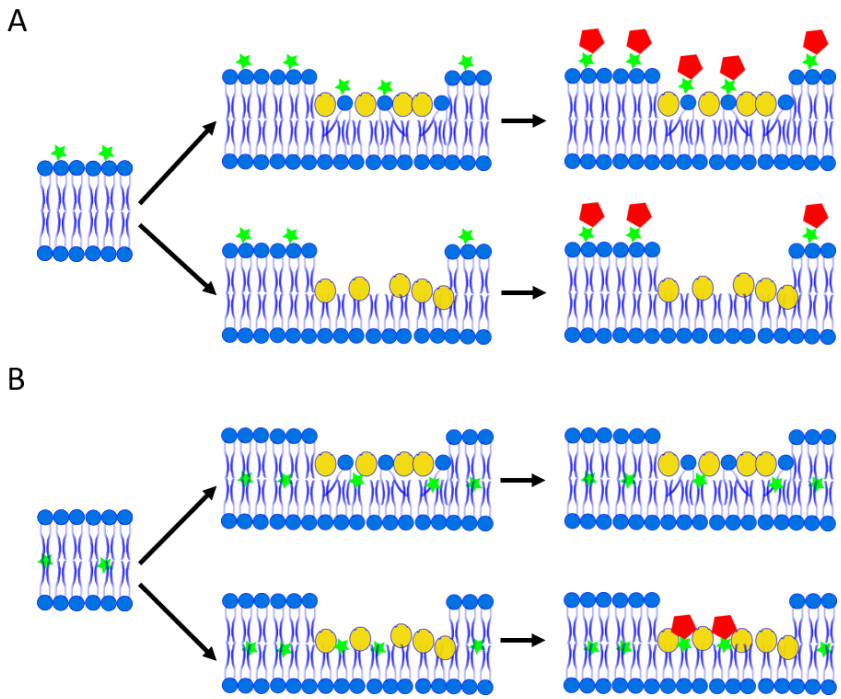

Figure 7.8. Schematic of the streptavidin-biotin assay. An SLB doped with biotinylated lipid heads (A) and tails (B) is treated with an AMP known to induce localised membrane thinning. Streptavidin is then added to the system, providing an AFM-visible marker for the exposed biotin and by extension, for the exposed phospholipid head or tail groups. Yellow circles (peptide), green stars (biotin) red pentagons (streptavidin).

If streptavidin is observed in the thinned domains when biotinylated tail groups are used, this will indicate exposed phospholipid tails are present i.e. the domain is a lipid monolayer. If no streptavidin is observed in the thinned domains for either experiment, this will indicate no exposed phospholipid tails or heads are present, and that the domains are entirely covered by AMP. Our proposed method cannot determine whether a domain entirely covered in AMP features an underlying thinned bilayer or a lipid monolayer, although in the AMP-coverage scenario, a lipid monolayer appears more plausible given that the membrane thickness is reduced in spite of additional coverage by AMPs.

7.2.2.2 Preparation of biotinylated SLBs and addition of reagents

For experiments with biotinylated lipid heads, 0.75 mg POPC, 0.25 mg POPG and 0.01 mg 18:1 biotinyl cap PE were combined in chloroform, dried under N_2 to form a lipid film and rehydrated to a final lipid concentration of 1 mg / mL. For experiments with biotinylated lipid tails, 0.75 mg POPC, 0.25 mg POPG and 0.01 mg 18:1-12:0 biotin PC were combined in chloroform, dried under N_2 to form a lipid film and rehydrated to a final lipid concentration of 1 mg / mL. Subsequent formation of SUVs and SLBs was performed in the usual way, as described in the main methods section of the thesis. The resulting SLBs consists of POPC:POPG (3:1 molar ratio) with ~ 1% biotinylated phospholipid. Epidermicin NI01 was used as the test AMP throughout, as it provides a reproducible and controlled system in which to compare the surface of three clear levels: transmembrane defects, thinned domains, and full bilayers. Peptide was manually injected to the SLB in all experiments (2.5 µL of 2.5 µM, final concentration ~ 62.5 nM). Streptavidin was also manually injected to the SLB in all experiments (10 µL of 0.01 mg / mL, final concentration ~ 1µg / mL). Following streptavidin addition, at least 5 min was given to enable binding before imaging.

7.2.3 Results

7.2.3.1 SLBs doped with biotinylated phospholipid heads

Figure 7.9A confirms that addition of 1% 18:1 biotinyl cap PE does not interfere with NI01's membrane disruption: SLBs doped with biotinylated phospholipid heads and treated with NI01 showed the expected disruption of networking patches of membrane thinning and transmembrane channels. Figure 7.9B shows the effect of adding streptavidin to the system. Whilst the added streptavidin is clearly present at the membrane surface, it is poorly resolved. Topography imaging became challenging, with streaking effects and unstable imaging. This may be expected; the bilayer surface contains many exposed biotins each of which will bind streptavidin and, as the SLB is fluid with each lipid is diffusing at ~ 2 $\mu m^2 s^{-1}$ [37], individual streptavidin will be moving faster than the AFM tip is scanning. Furthermore, if the tip becomes contaminated with biotinylated lipid, strong, uncontrolled interactions will occur between the tip and the sample, resulting in unstable imaging and streaking effects such as those observed here.

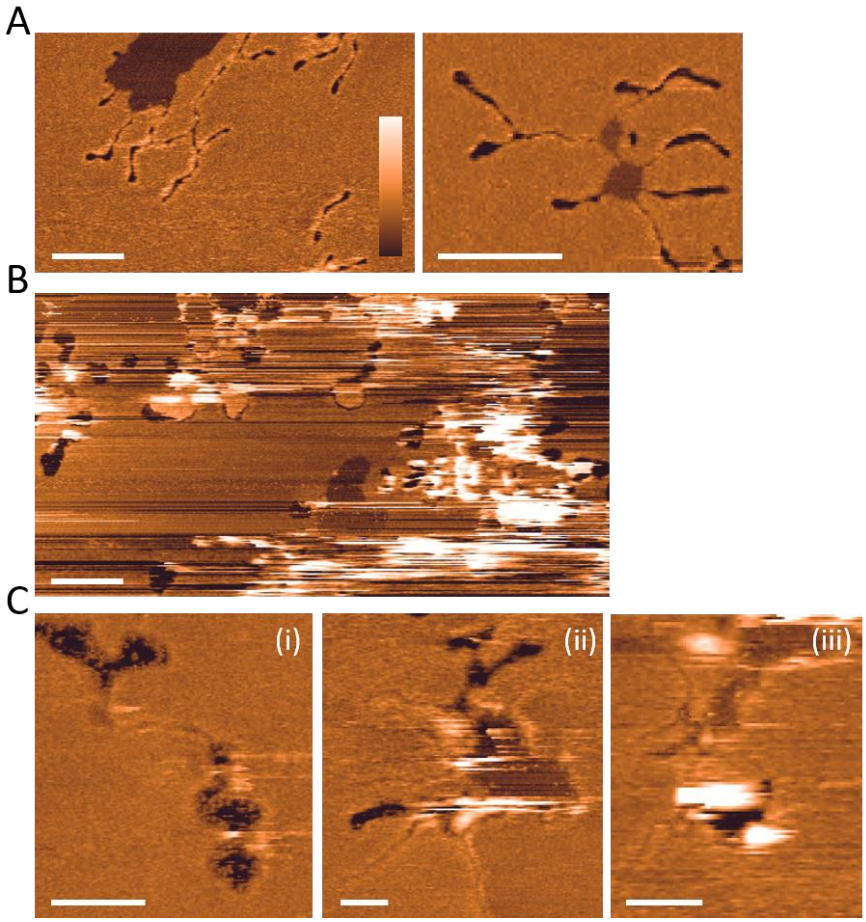

Figure 7.9. AFM topography images of POPC:POPG (3:1 molar ratio) SLBs doped with 1% biotin-functionalised lipid heads. (A) Treated with epidermicin NI01; (B-C) Treated with epidermicin NI01 and streptavidin: (B) The AFM images show a lot of poorly resolved protrusions and streaky features aligned to the fast scan direction, indicative of loosely bound and mobile material at the surface; (C) cleaner imaging showing non-specific streptavidin binding in transmembrane defects (i) and possible streptavidin observed in patches of membrane thinning (ii,iii). Scale bars are (A, B) 500 nm and (C) 200 nm. Colour scale is 18 nm in all images.

A small number of cleaner images were obtained (Fig 7.9C). Features consistent in size with streptavidin can be observed in transmembrane channels, indicating non-specific binding to the underlying mica surface (Fig 7.9C(i)).[285] Furthermore, some features consistent with streptavidin can be observed in the patches of membrane thinning (Fig 7.9C(ii)), indicating the presence of exposed phospholipid head groups. Whilst the poor imaging quality prevents definite conclusions, the data in Figure 7.9 does demonstrate the viability of the assay. The observed protrusions and streaky features confirm that streptavidin is binding to the membrane surface, verifying our hypothesis that streptavidin labelling can be used to identify exposed lipid domains at the membrane surface during peptide treatment.

7.2.3.2 SLBs doped with biotinylated phospholipid tails

Figure 7.10A provides confirmation that addition of 1% 18:1-12:0 biotin PC does not interfere with NI01's membrane disruption. Figure 7.10B shows the effect of adding streptavidin to the

system. In contrast to SLBs doped with biotinylated heads, topographical imaging remained clean and stable. Furthermore, features consistent in size with streptavidin appeared only in the transmembrane channels (i.e. streptavidin adsorbed to the underlying mica). Taken together, these results indicate that the thinned domains induced by epidermicin NI01 do not contain exposed phospholipid tails, and as such, do not represent an exposed lipid monolayer.

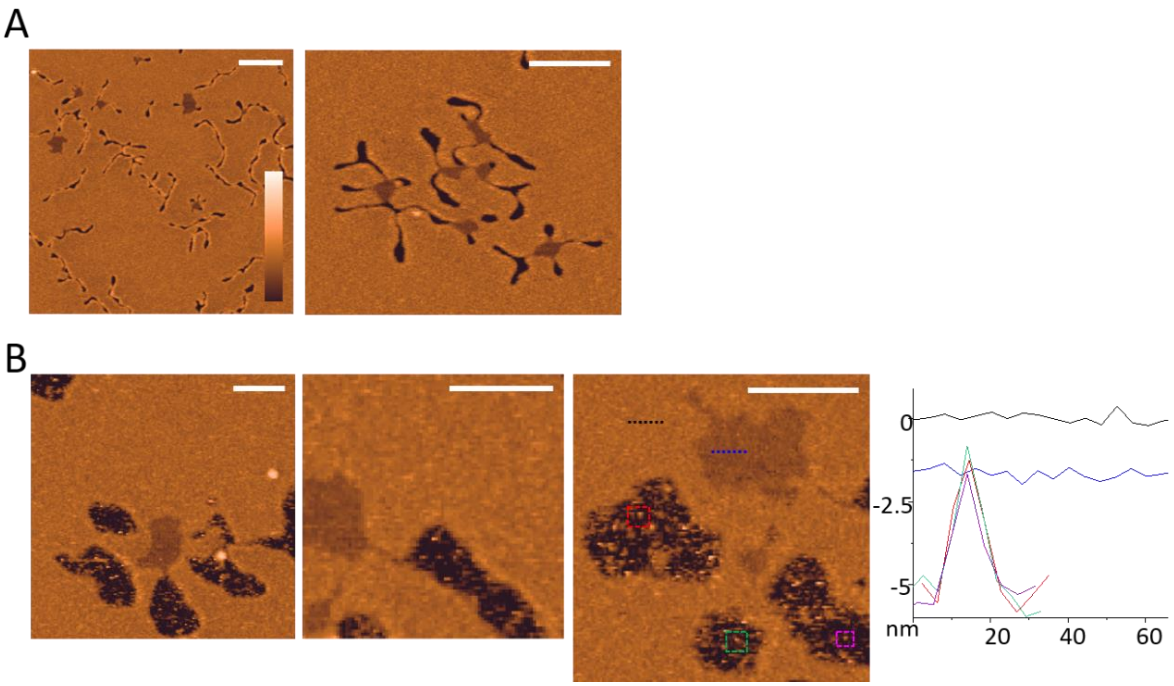

Figure 7.10. AFM topography images of POPC:POPG (3:1 molar ratio) SLBs doped with 1% biotin-functionalised lipid tails. (A) Treated with epidermicin NI01; (B) Treated with epidermicin NI01 and streptavidin. Topography images show particles only appear in the transmembrane channels. Corresponding line profiles for the right hand image are provided. Scale bars are (A) 500 nm and (B) 200 nm. Colour scale is 18 nm in all images.

7.2.3.3 Improving the experimental design by reducing lipid fluidity

To improve on the experimental design, we hypothesised that using gel-state (S_o) SLBs, with much lower lateral diffusion of lipids, would make bound streptavidin easier to resolve. Therefore, control experiments were run to confirm the compatibility of NI01's membrane disruption with S_o SLBs. The lipid mixture DPPC:DPPG (3:1 molar ratio) was chosen as it has a T_m of 41 °C and exists in the gel-state at room temperature. SLBs were formed in the usual way, but vesicle incubation and adsorption were performed at 51 °C. This allows initial formation of a L_d SLB, which is then cooled to room temperature, producing a homogenous S_o SLB (Fig 7.11A (i)). However, addition of NI01 to the S_o SLB caused no observable change over 30 mins of imaging (Fig 7.11A (ii, iii)). For comparison, the archetypal AMP magainin 2 was also tested. Like NI01, the peptide caused no observable change at the concentration required for disruption of L_d SLBs (Fig 7.11B (i,ii)). To assess whether S_o SLBs simply require a higher quantity of peptide to induce disruption, a 6-fold increase in concentration was added (Fig

7.10B (iii)). Although areas of bilayer were removed from the surface, the effect appeared mechanical rather than peptide induced, with the remaining bilayer homogenous and defect free. Collectively, Figure 7.11 shows that neither NI01 or magainin 2 are able to penetrate into and re-arrange the packing of S_o SLBs.

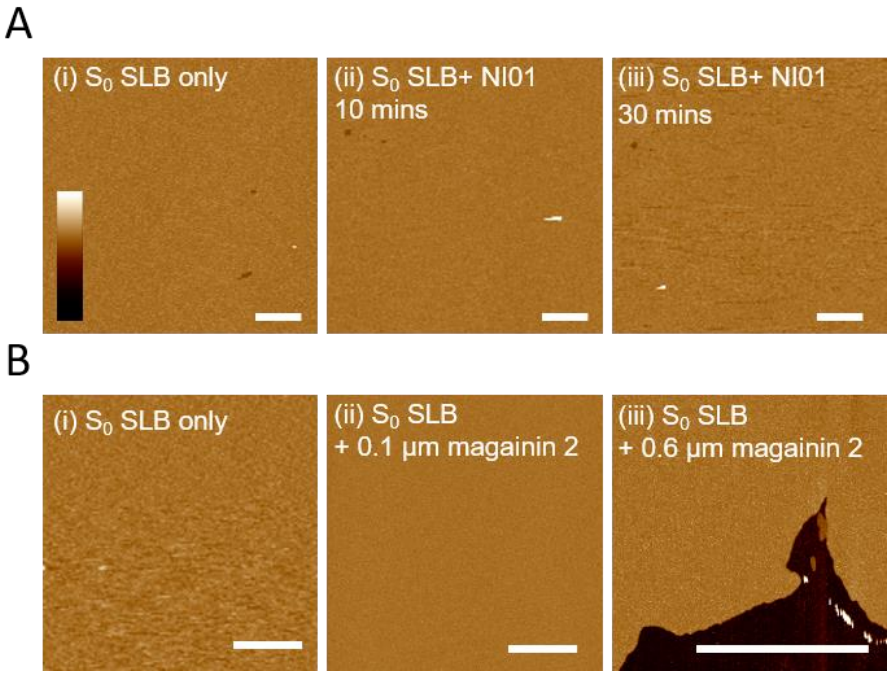

Figure 7.11. AFM topography images of AMP treated gel-state SLBs. (A) DPPC:DPPG (3:1 molar ratio) imaged at room temperature before (i) and after (ii,iii) addition of 0.25 µM epidermicin NI01 (10 and 30 mins respectively). (B) DPPC:DPPG (3:1 molar ratio) imaged at room temperature before (i) and after (ii,iii) addition of magainin 2 (0.1 µM and 0.6µM respectively). Scale bars: 500 nm. Colour bar: 18 nm.

To attempt to circumvent this problem, AMP was added to the L_d SLB before cooling to a S_o state. Figure 7.12A shows a DPPC:DPPG (3:1 molar ratio) SLB imaged at 51 °C before peptide addition. As expected, a continuous defect-free bilayer was observed. Figure 7.12B shows the SLB imaged at 51 °C after addition of magainin 2. Domain separation is observed, despite the temperature remaining above the T_m of the lipids. The lower domains (consistent with a L_d phase) appear porated, whilst the higher domains (consistent with S_o domains) appear defect free, providing further evidence that the AMP is not able to penetrate into S_o domains. The sample was then cooled to room temperature and re-imaged (Fig 7.12C (iii)). Despite the initial bilayer containing peptide-stabilised pores, cooling below the fluid-gel transition did not solidify these defects as expected. Instead, significant lipid rearrangement occurred, with only small domains of defect-free S_o SLB remaining on the surface.

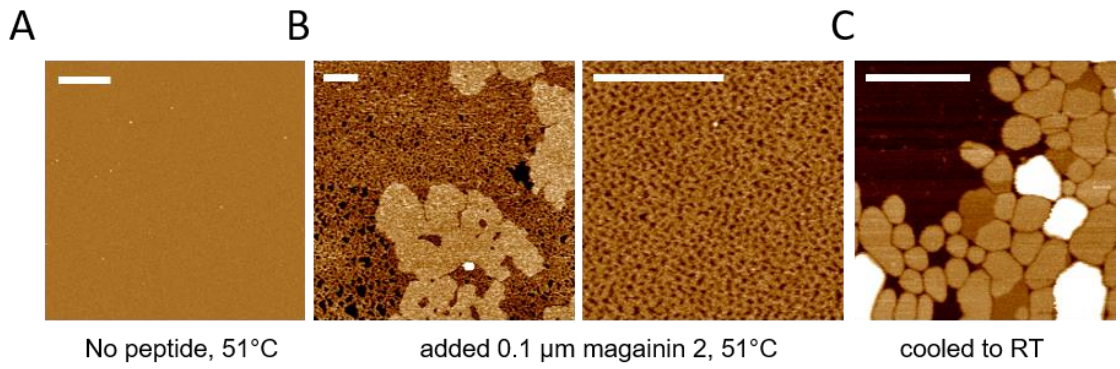

Figure 7.12. AFM topography images of an AMP treated SLB above and below the lipid transition temperature. DPPC:DPPG (3:1 molar ratio) is imaged at 51°C (A) before and (B) after addition of 0.1 µM magainin 2. Phase separation is observed with high regions of continuous SLB and low regions of porated SLB (shown at higher magnification in the right-hand image); (C) The sample is then cooled to room temperature and re-imaged. Poration is no longer observed. Scale bars: 1000 nm (A) and 200 nm (B,C). Colour bar: 18 nm.

7.2.4 Discussion

In this section, we have demonstrated through biotin-streptavidin binding that patches of membrane thinning induced by epidermicin NI01 are unlikely to contain exposed phospholipid tail groups. However, our approach was unable to give a definite conclusion as to the nature of these domains. Imaging fluid SLBs doped with biotinylated lipid head groups did not provide clean or stable conditions and reducing lipid fluidity did not provide the anticipated improvement, due to the inability of the AMPs tested to disrupt S_o SLBs. This resistance of S_o SLBs to AMP disruption is itself notable. Although native biological membranes are fluid, much of the eukaryotic membrane exists in a highly ordered, L_o state.[81] Although there is emerging evidence that L_o domains can form in bacterial membranes, the lack of high quantities of L_o-promoting lipids and hydrophobic molecules (such as cholesterol and sphingomyelin) means it is generally considered to be more disordered.[36] Our findings support the hypothesis that this difference in lipid order contributes to the selectivity of antimicrobial peptides for bacterial cells, with increased rigidity providing protection for eukaryotic cells against peptide induced disruption (see, e.g.[136]).

Looking ahead, a better approach may be to functionalise an AFM tip with streptavidin, and take multiple force measurements across the surface. Silicon nitride tips can be functionalised by first coating the tip with biotinylated bovine serum albumin via overnight submersion in a biotinylated bovine serum albumin solution, and then coupling streptavidin via 5 min submersion in streptavidin solution.[286],[287] With this tip, adhesion forces to a biotinylated surface could be measured. A significant difference in binding energy will occur when the streptavidin-functionalised tip is interacting with a biotin tag to when it is not, and this may give a cleaner and more quantitative indication of the distribution of exposed biotin tags across the surface.

8 Summary and outlook

It is widely accepted that antimicrobial peptides can act by targeting the lipid bilayer assemblies of microbial membranes, disrupting the lipid packing, leading to permeabilisation and cell death. Due to their multifunctional nature however, native sequences are likely not optimized for microbial membrane disruption. Indeed, most AMPs lack sufficient potency for direct clinical use. Therefore, there is a requirement to redesign AMPs or to create sequences *de novo*.

If the relationships between peptide sequence, mode of lipid disruption and biological activity were better understood, detailed guidelines on how to design more promising sequences could be developed. However, resolving modes of lipid disruption remains challenging. Peptide-lipid interactions are dynamic, localised, and adapt to different environments, meaning different biophysical techniques can give conflicting information.[30] The high temporal and spatial resolution of in-liquid AFM make it a powerful tool for directly observing dynamic and localised membrane disruption, and over the past decade, in-liquid AFM has gained popularity for resolving peptide-lipid interactions. Throughout this thesis, we have used this technique to directly address the challenge of relating antimicrobial motifs to the modes of lipid disruption induced. Our results have revealed novel sequence-function relationships that can now be used for further AMP development.

Starting with a simplified antimicrobial peptide template that conserved the core biophysical properties of animal-derived AMPs, we demonstrated that highly simplified sequences down to 9 amino acids in length can maintain comparable membrane disruption modes and biological activity to native sequences. This validates the hypothesis that native peptides have a large degree of sequence redundancy, and supports the development of simpler designs. Indeed, we showed that the specific membrane interactions of peptide sequences can be controlled at the single amino acid level. A mutation from alanine to lysine in the hydrophobic face of an amphipathic α- helix triggered a switch from conventional transmembrane, circular defects, to a disruption mechanism restricted to the upper leaflet of the bilayer with fractal-like morphology. We showed that these distinct pathways of lipid disruption translated into distinct antimicrobial activity and selectivity, with the conversion to upper-leaflet defects in model membranes correlating with a loss of haemolytic activity. Interestingly, a similar finding was observed in Chapter 5. The central subcomponent of epidermicin NI01, H2, was the only subcomponent showing no haemolytic activity, and the only subcomponent to only induce defects in the upper leaflet of lipid bilayers. A possible explanation for this observation could be that mammalian membranes resist this mode of disruption better than microbial membranes. If this is the case, adjusting sequences to favour upper-leaflet interactions may lead to improved therapeutic index. The general applicability now requires further research, but this represents a promising avenue for designing and optimising sequences for clinical use.

Having assessed a model system that maintained the archetypal properties of a native antimicrobial α-helix, we next demonstrated that the basic design rules for such systems can be expanded. The presence of a T/S rich face, in combination with a hydrophobic and cationic face, triggered additional membrane interactions compared to archetypal amphipathic AMPs. The construct interacted with both anionic and zwitterionic lipids via distinct pathways, whilst exerting antimicrobial behaviour but no toxicity. As such, it fulfilled the criteria for a *de-novo* AMP whilst also possessing additional ALPS-like properties. The biological implications of such auxiliary lipid interactions require further investigation. However, as ALPS-like motifs enable peptides and proteins to sense membrane curvature and membrane defects, we hypothesise that combining this with conventional AMP-motifs the design may be particularly useful as an anticancer sequence. Malignant transformation can lead both to increased exposure of anionic phospholipid, and to increased variability in the curvature and architecture of the membrane. A peptide sequence that is sensitive both to charge and to lipid packing arrangements may be able to better target such membranes. The anticancer activity of triAMP has been confirmed,[119] but the contribution of the faces to this activity requires further work.

Moving on from a single α-helix system, we then confirmed the hypothesis that the multi-helix peptide epidermicin NI01 supports a more complex multimodal mechanism. Subcomponents of the sequence induce discrete modes of this disruption, with the full peptide combining these modes into a synergistic and selective mechanism and the mechanism is conserved in another member of the bacteriocin family, aureocin A53. It seems likely that a multimodal mechanism will confer biological advantage and in support of this, NI01 has more potent activity than many AMPs. Such increased potency can be explained by our proposed model, whereby the initial formation of thinned membrane creates domain boundaries in the bilayer which can then actively recruit more peptide to reach a poration threshold more quickly. Therefore, the work presented in Chapter 5 highlights multi-helix peptides as an exciting route to develop more potent peptide sequences.

Following on in increasing levels of complexity, we then characterised the membrane interactions of a supramolecular system. As well as demonstrating that force-spectroscopy based imaging can be a useful tool to resolve the mechanical and topographical properties of peptide capsules under near-native conditions, we showed that self-assembled systems can induce membrane disruption both more rapidly and on a more prolonged timescale than monomeric AMPs. These results support the development of self-assembled peptide systems as therapeutic targets.[252]

Finally, we explored methodological enhancements to overcome the general limitation of AFM imaging: its inability to provide chemical information. Firstly, we demonstrated that correlative charge-mapping of a biological system in aqueous solution can be achieved using OLEPM. We mapped the topography and potential of an SLB, before during and after treatment with AMP,

and showed that the surface potential of the bilayer becomes more positive following peptide treatment, indicating that surface bound cationic peptide can be detected. Secondly, we demonstrated that the distribution of exposed phospholipid head or tail groups during peptide treatment can be resolved via chemical tagging. With this approach, we showed that thinned domains induced by NI01 likely do not contain exposed phospholipid tail groups, excluding the possibility that such domains represent an uncovered lipid monolayer and therefore improving on the current model. Our results confirm that both charge-mapping and chemical tagging are promising avenues to more specifically resolve AMPs and their interaction with lipids. The continued improvement to the chemical resolution of AFM methodologies is an important area of the field, as it will undoubtedly lead to a better appreciation of the processes occurring at the bilayer surface. In turn, this will enable better optimisation and design of peptide sequences for translational application.

A. Appendix

Figures A.1- A.8 show the "quality control" (QC) of the peptides synthesised in this thesis. MALDI-ToF MS spectra and analytical RP-HPLC traces are shown. Calculated and found values of m/z are provided. Next, captions for Video A.1 and A.2 (electronic attachment) are given. Finally, Table A.1 provides the abbreviations (3-letter and 1-letter) for canonical amino acids.

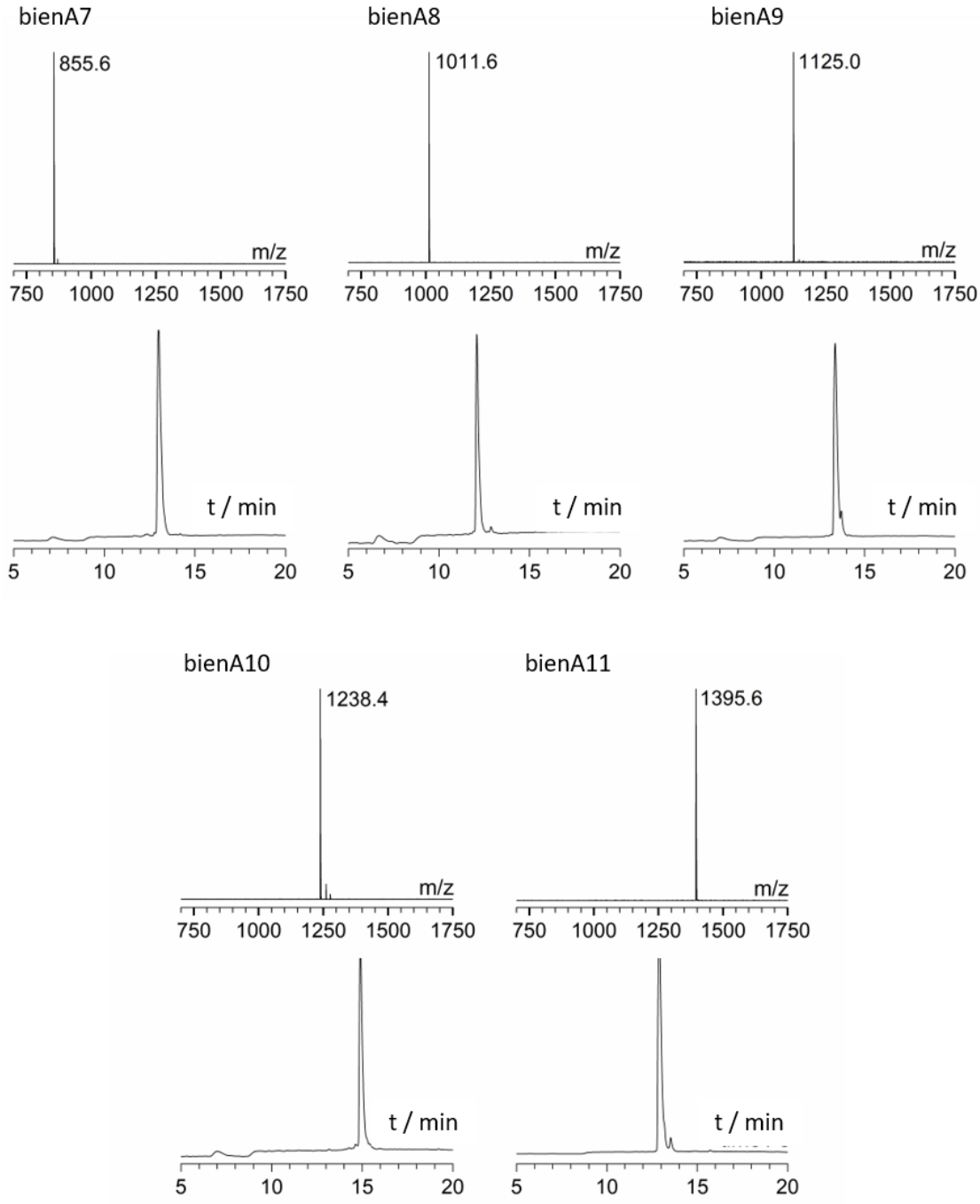

Figure A.1. QC bienA7 – A11. MS [M + H]+: bienA7, m/z 854.11 (calc), 855.6 (found); bienA8, m/z 1010.3 (calc), 1011.6 (found); bienA9, m/z 1123.46 (calc), 1125.0 (found); bienA10, m/z 1236.61 (calc), 1238.4 (found); bienA11, m/z 1392.8 (calc), 1395.6 (found).

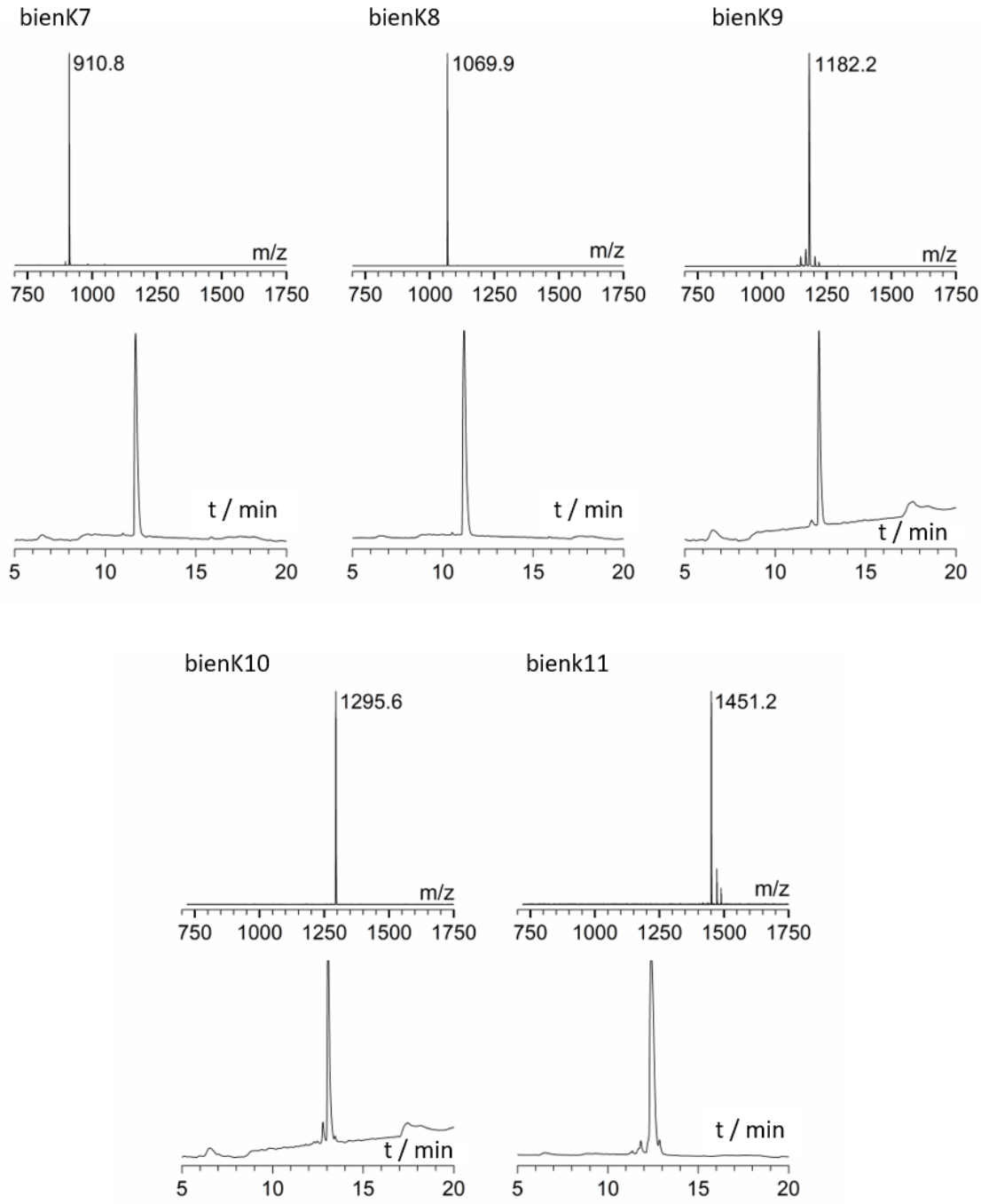

Figure A.2. QC bienK7 – A11. MS [M + H]+: bienK7, m/z 911.21 (calc), 910.8 (found); bienK8, m/z 1067.39 (calc), 1069.9 (found); bienK9, m/z 1180.55 (calc), 1182.2 (found); bienK10, m/z 1293.71 (calc), 1295.6 (found); bienK11, m/z 1449.89 (calc), 1451.2 (found).

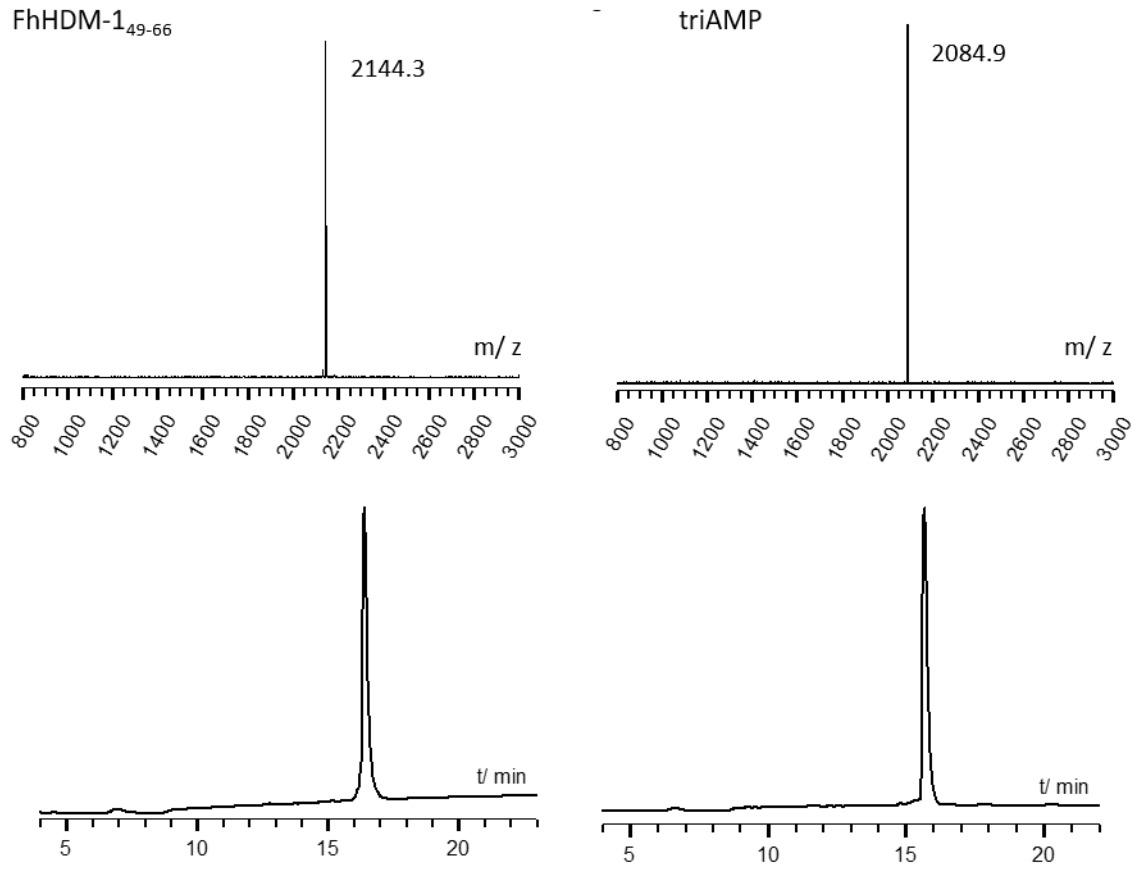

Figure A.3. QC FhHDM-1$_{49-66}$ and triAMP. MS [M + H]+: FhHDM-1$_{49-66}$, m/z 2141.52 (calc), 2144.3 (found); triAMP, m/z 2083.62 (calc), 2084.9 (found).

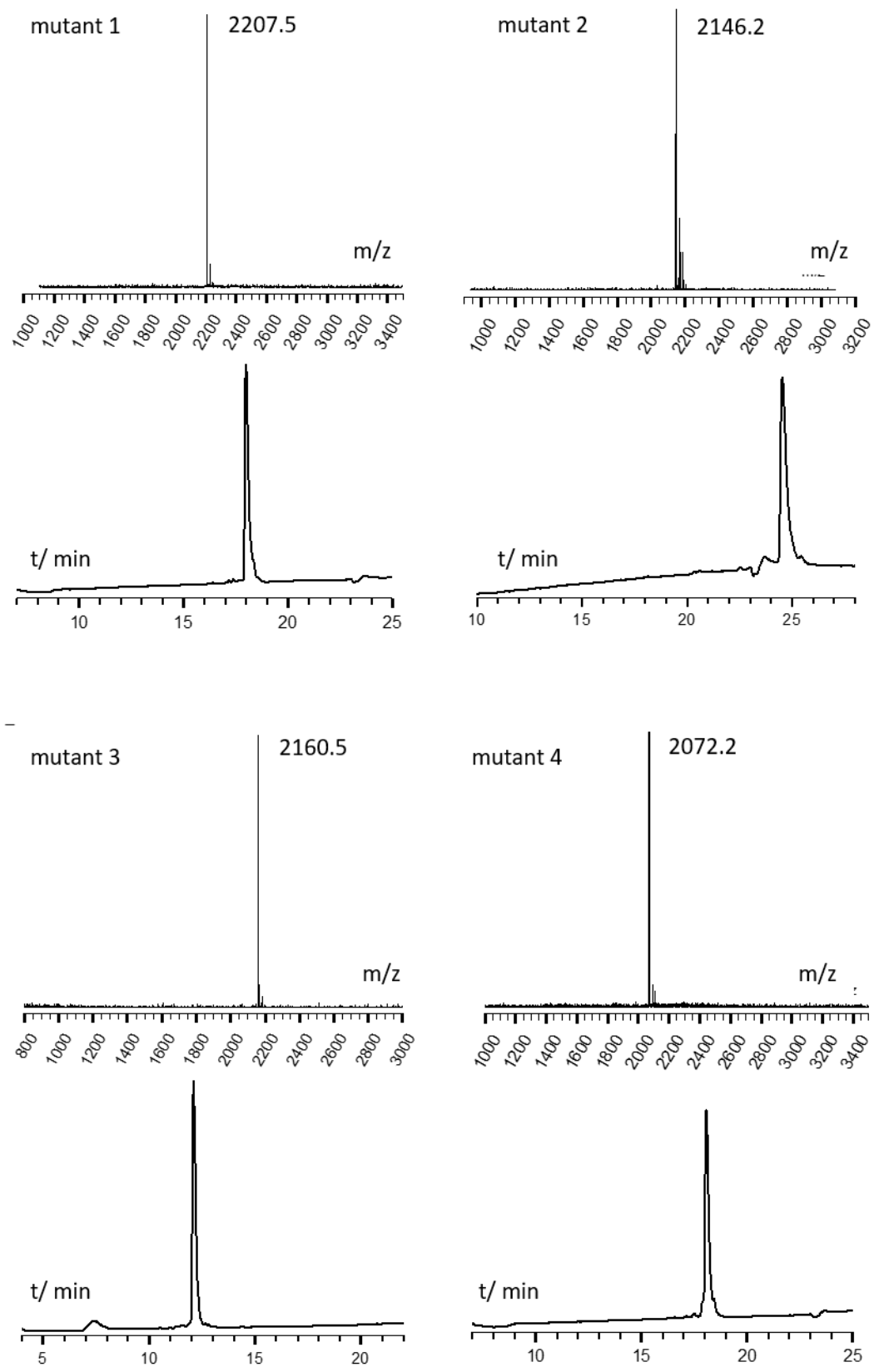

Figure A.4. QC HDM mutants 1 – 4. MS [M + H]+: mutant 1, m/z 2205.75 (calc), 2207.5 (found); mutant 2, m/z 2145.86 (calc), 2146.2 (found); mutant 3, m/z 2157.52 (calc), 2160.5 (found); mutant 4, m/z 2069.59 (calc), 2072.2 (found)

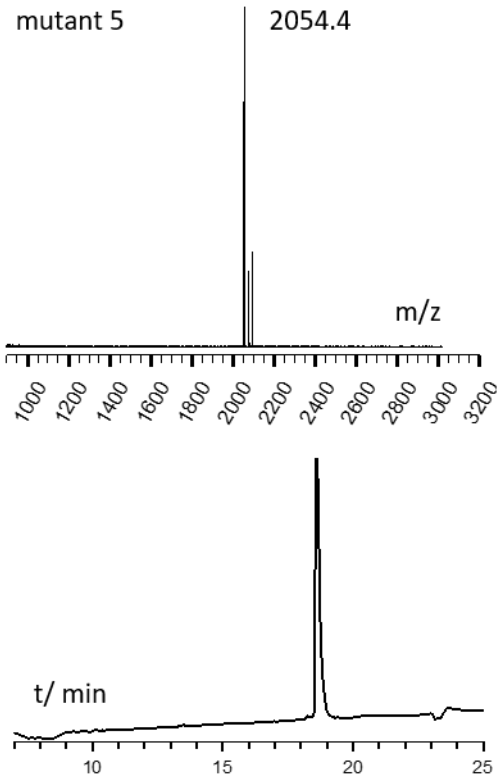

Figure A.5. QC HDM mutant 5. MS [M + H]+: 2053.39 m/z (calc), 2054.4 m/z (found).

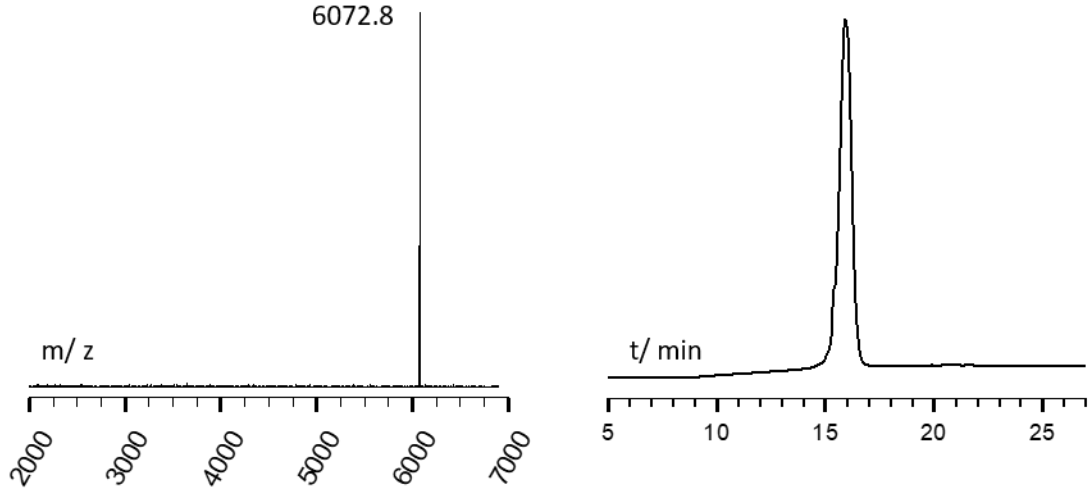

Figure A.6. QC epidermicin NI01. MS [M + H]+: 6073.3 m/z (calc), 6072.8 m/z (found).

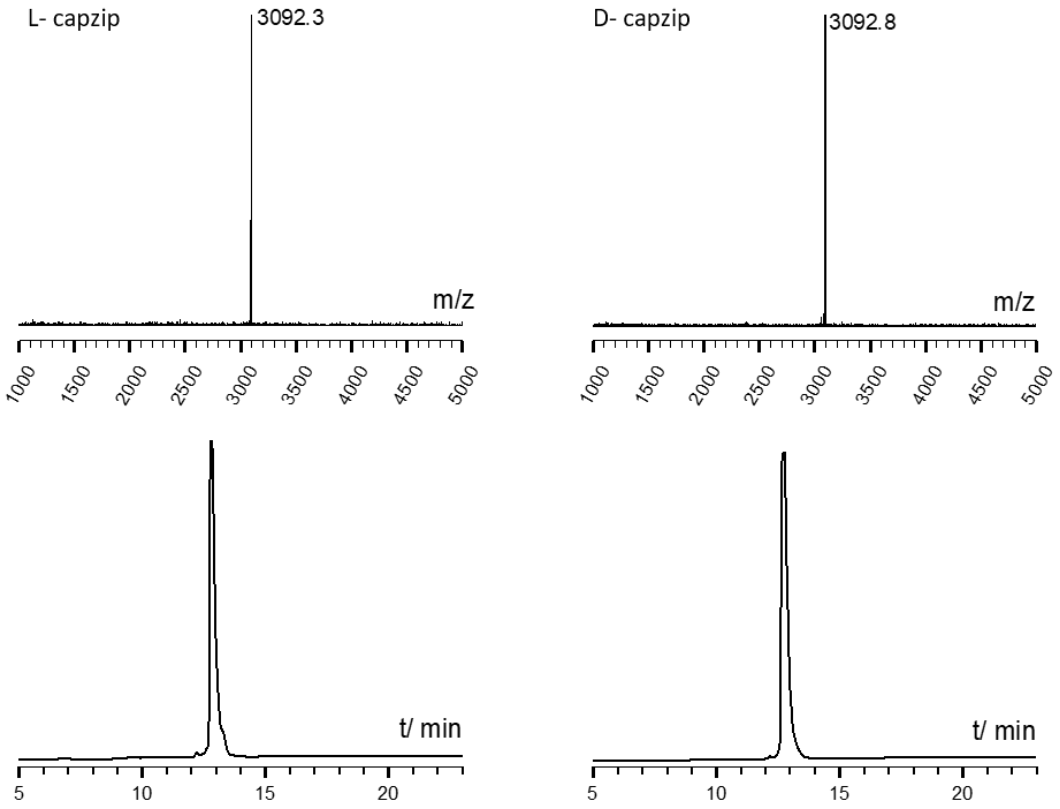

Figure A.7. QC L- and D- capzip. MS [M + H]+: L-capzip, m/z 3090.5 (calc), 3092.3 (found); D- capzip, m/z 3090.5 (calc), 3092.8 m/z (found).

Video A.1. Anionic SLB (POPC:POPG (3:1 molar ratio)) treated with 0.375 µM epidermicin NI01. The video shows consecutive scans from 3 min prior to peptide injection, to 30 min after peptide injection. The images were taken on a Cypher ES, with an AC40 cantilever, in tapping mode, at a line rate of 20 Hz and therefore 25.6 seconds per frame. Scan size is 4 µm.

Video A.2. Anionic SLB (POPC:POPG (3:1 molar ratio)) treated with 0.75 µM epidermicin NI01. The video shows consecutive scans from 1 min prior to peptide injection, to 6 min after peptide injection. The images were taken on a Cypher ES, with an AC40 cantilever, in tapping mode, at a line rate of 20 Hz and therefore 25.6 seconds per frame. Scan size is 4 µm.

Table A.1 Abbreviations (3-letter and 1-letter) for canonical amino acids

Amino acid	3 letter abbreviation	1 letter abbreviation
Alanine	Ala	A
Arginine	Arg	R
Asparagine	Asn	N
Aspartic acid	Asp	D
Cysteine	Cys	C
Glutamine	Gln	Q
Glutamic acid	Glu	E
Glycine	Gly	G
Histidine	His	H
Isoleucine	Ile	I
Leucine	Leu	L
Lysine	Lys	K
Methionine	Met	M

Phenylalanine	Phe	F
Proline	Pro	P
Serine	Ser	S
Threonine	Thr	T
Tryptophan	Trp	W
Tyrosine	Tyr	Y
Valine	Val	V

B. Bibliography

(1) Mookherjee, N.; Anderson, M. A.; Haagsman, H. P.; Davidson, D. J. Antimicrobial Host Defence Peptides: Functions and Clinical Potential. *Nat. Rev. Drug Discov.* **2020**, *19* (5), 311–332.

(2) Wang, G.; Li, X.; Wang, Z. APD3: The Antimicrobial Peptide Database as a Tool for Research and Education. *Nucleic Acids Res.* **2016**, *44* (D1), D1087–D1093.

(3) Gallo, R. L.; Hooper, L. V. Epithelial Antimicrobial Defence of the Skin and Intestine. *Nat. Rev. Immunol.* **2012**, *12* (7), 503–516.

(4) Faurschou, M.; Borregaard, N. Neutrophil Granules and Secretory Vesicles in Inflammation. *Microbes Infect.* **2003**, *5* (14), 1317–1327.

(5) Nguyen, L. T.; Haney, E. F.; Vogel, H. J. The Expanding Scope of Antimicrobial Peptide Structures and Their Modes of Action. *Trends Biotechnol.* **2011**, *29* (9), 464–472.

(6) Magana, M.; Pushpanathan, M.; Santos, A. L.; Leanse, L.; Fernandez, M.; Ioannidis, A.; Giulianotti, M. A.; Apidianakis, Y.; Bradfute, S.; Ferguson, A. L.; Cherkasov, A.; Seleem, M. N.; Pinilla, C.; de la Fuente-Nunez, C.; Lazaridis, T.; Dai, T.; Houghten, R. A.; Hancock, R. E. W.; Tegos, G. P. The Value of Antimicrobial Peptides in the Age of Resistance. *Lancet Infect. Dis.* **2020**, *20* (9), e216–e230.

(7) Joo, H.-S.; Fu, C.-I.; Otto, M. Bacterial Strategies of Resistance to Antimicrobial Peptides. *Philos. Trans. R. Soc. B Biol. Sci.* **2016**, *371* (1695), 20150292.

(8) Lee, T.-H.; Hofferek, V.; Separovic, F.; Reid, G. E.; Aguilar, M.-I. The Role of Bacterial Lipid Diversity and Membrane Properties in Modulating Antimicrobial Peptide Activity and Drug Resistance. *Curr. Opin. Chem. Biol.* **2019**, *52*, 85–92.

(9) Juhas, M. Horizontal Gene Transfer in Human Pathogens. *Crit. Rev. Microbiol.* **2015**, *41* (1), 101–108.

(10) Baltz, R. H. Daptomycin: Mechanisms of Action and Resistance, and Biosynthetic Engineering. *Curr. Opin. Chem. Biol.* **2009**, *13* (2), 144–151.

(11) Vriens, K.; Cammue, B.; Thevissen, K. Antifungal Plant Defensins: Mechanisms of Action and Production. *Molecules* **2014**, *19* (8), 12280–12303.

(12) Delattin, N.; De Brucker, K.; De Cremer, K.; P.A. Cammue, B.; Thevissen, K. Antimicrobial Peptides as a Strategy to Combat Fungal Biofilms. *Curr. Top. Med. Chem.*

2016, *17* (5), 604–612.

(13) Ordonez, S. R.; Amarullah, I. H.; Wubbolts, R. W.; Veldhuizen, E. J. A.; Haagsman, H. P. Fungicidal Mechanisms of Cathelicidins LL-37 and CATH-2 Revealed by Live-Cell Imaging. *Antimicrob. Agents Chemother.* **2014**, *58* (4), 2240–2248.

(14) Deslouches, B.; Di, Y. P. Antimicrobial Peptides with Selective Antitumor Mechanisms: Prospect for Anticancer Applications. *Oncotarget* **2017**, *8* (28), 46635–46651.

(15) Felício, M. R.; Silva, O. N.; Gonçalves, S.; Santos, N. C.; Franco, O. L. Peptides with Dual Antimicrobial and Anticancer Activities. *Front. Chem.* **2017**, *5*, 5.

(16) Roudi, R.; Syn, N. L.; Roudbary, M. Antimicrobial Peptides As Biologic and Immunotherapeutic Agents against Cancer: A Comprehensive Overview. *Front. Immunol.* **2017**, *8*, 1320.

(17) Torrent, M.; Pulido, D.; Rivas, L.; Andreu, D. Antimicrobial Peptide Action on Parasites. *Curr. Drug Targets* **2012**, *13* (9), 1138–1147.

(18) Vizioli, J.; Salzet, M. Antimicrobial Peptides versus Parasitic Infections? *Trends Parasitol.* **2002**, *18* (11), 475–476.

(19) Vale, N.; Aguiar, L.; Gomes, P. Antimicrobial Peptides: A New Class of Antimalarial Drugs? *Front. Pharmacol.* **2014**, *5*, 275.

(20) Batoni, G.; Maisetta, G.; Brancatisano, F. L.; Esin, S.; Campa, M. Use of Antimicrobial Peptides Against Microbial Biofilms: Advantages and Limits. *Curr. Med. Chem.* **2011**, *18* (2), 256–279.

(21) Dean, R. E.; O'Brien, L. M.; Thwaite, J. E.; Fox, M. A.; Atkins, H.; Ulaeto, D. O. A Carpet-Based Mechanism for Direct Antimicrobial Peptide Activity against Vaccinia Virus Membranes. *Peptides* **2010**, *31* (11), 1966–1972.

(22) Brice, D. C.; Toth, Z.; Diamond, G. LL-37 Disrupts the Kaposi's Sarcoma-Associated Herpesvirus Envelope and Inhibits Infection in Oral Epithelial Cells. *Antiviral Res.* **2018**, *158*, 25–33.

(23) Barlow, P. G.; Svoboda, P.; Mackellar, A.; Nash, A. A.; York, I. A.; Pohl, J.; Davidson, D. J.; Donis, R. O. Antiviral Activity and Increased Host Defense against Influenza Infection Elicited by the Human Cathelicidin LL-37. *PLoS One* **2011**, *6* (10), e25333.

(24) Howell, M. D.; Jones, J. F.; Kisich, K. O.; Streib, J. E.; Gallo, R. L.; Leung, D. Y. M. Selective Killing of Vaccinia Virus by LL-37: Implications for Eczema Vaccinatum. *J. Immunol.* **2004**, *172* (3), 1763–1767.

(25) Wiens, M. E.; Smith, J. G. α-Defensin HD5 Inhibits Human Papillomavirus 16 Infection via Capsid Stabilization and Redirection to the Lysosome. *MBio* **2017**, *8* (1), e02304-16.

(26) Nguyen, E. K.; Nemerow, G. R.; Smith, J. G. Direct Evidence from Single-Cell Analysis That Human α-Defensins Block Adenovirus Uncoating To Neutralize Infection. *J. Virol.* **2010**, *84* (8), 4041–4049.

(27) Le, C.-F.; Fang, C.-M.; Sekaran, S. D. Intracellular Targeting Mechanisms by Antimicrobial Peptides. *Antimicrob. Agents Chemother.* **2017**, *61* (4), e02340-16.

(28) Lai, Y.; Gallo, R. L. AMPed up Immunity: How Antimicrobial Peptides Have Multiple Roles in Immune Defense. *Trends Immunol.* **2009**, *30* (3), 131–141.

(29) Honigmann, A.; Pralle, A. Compartmentalization of the Cell Membrane. *J. Mol. Biol.* **2016**, *428* (24), 4739–4748.

(30) Guha, S.; Ghimire, J.; Wu, E.; Wimley, W. C. Mechanistic Landscape of Membrane-Permeabilizing Peptides. *Chem. Rev.* **2019**, *119* (9), 6040–6085.

(31) Harayama, T.; Riezman, H. Understanding the Diversity of Membrane Lipid Composition. *Nat. Rev. Mol. Cell Biol.* **2018**, *19* (5), 281–296.

(32) Teixeira, V.; Feio, M. J.; Bastos, M. Role of Lipids in the Interaction of Antimicrobial Peptides with Membranes. *Prog. Lipid Res.* **2012**, *51* (2), 149–177.

(33) Koehbach, J.; Craik, D. J. The Vast Structural Diversity of Antimicrobial Peptides. *Trends Pharmacol. Sci.* **2019**, *40* (7), 517–528.

(34) Sani, M.-A.; Separovic, F. How Membrane-Active Peptides Get into Lipid Membranes. *Acc. Chem. Res.* **2016**, *49* (6), 1130–1138.

(35) Huang, H. W. Action of Antimicrobial Peptides: Two-State Model. *Biochemistry* **2000**, *39* (29), 8347–8352.

(36) Strahl, H.; Errington, J. Bacterial Membranes: Structure, Domains, and Function. *Annu. Rev. Microbiol.* **2017**, *71* (1), 519–538.

(37) van Meer, G.; Voelker, D. R.; Feigenson, G. W. Membrane Lipids: Where They Are and How They Behave. *Nat. Rev. Mol. Cell Biol.* **2008**, *9* (2), 112–124.

(38) Ran, S.; Downes, A.; Thorpe, P. E. Increased Exposure of Anionic Phospholipids on the Surface of Tumor Blood Vessels. *Cancer Res.* **2002**, *62* (21), 6132–6140.

(39) Wang, C.; Chen, Y.-W.; Zhang, L.; Gong, X.-G.; Zhou, Y.; Shang, D.-J. Melanoma Cell

Surface-Expressed Phosphatidylserine as a Therapeutic Target for Cationic Anticancer Peptide, Temporin-1CEa. *J. Drug Target.* **2016**, *24* (6), 548–556.

(40) Li, J.; Koh, J.-J.; Liu, S.; Lakshminarayanan, R.; Verma, C. S.; Beuerman, R. W. Membrane Active Antimicrobial Peptides: Translating Mechanistic Insights to Design. *Front. Neurosci.* **2017**, *11*, 73.

(41) Faust, J. E.; Yang, P.-Y.; Huang, H. W. Action of Antimicrobial Peptides on Bacterial and Lipid Membranes: A Direct Comparison. *Biophys. J.* **2017**, *112* (8), 1663–1672.

(42) Islam, M. Z.; Alam, J. M.; Tamba, Y.; Karal, M. A. S.; Yamazaki, M. The Single GUV Method for Revealing the Functions of Antimicrobial, Pore-Forming Toxin, and Cell-Penetrating Peptides or Proteins. *Phys. Chem. Chem. Phys.* **2014**, *16* (30), 15752–15767.

(43) Kristensen, K.; Henriksen, J. R.; Andresen, T. L. Quantification of Leakage from Large Unilamellar Lipid Vesicles by Fluorescence Correlation Spectroscopy. *Biochim. Biophys. Acta - Biomembr.* **2014**, *1838* (12), 2994–3002.

(44) Haney, E. F.; Vogel, H. J. NMR of Antimicrobial Peptides. In *Annual Reports on NMR Spectroscopy*; Academic Press, 2009; pp 1–51.

(45) Porcelli, F.; Ramamoorthy, A.; Barany, G.; Veglia, G. On the Role of NMR Spectroscopy for Characterization of Antimicrobial Peptides. *Methods Mol. Biol.* **2013**, *1063*, 159–180.

(46) Bechinger, B.; Salnikov, E. S. The Membrane Interactions of Antimicrobial Peptides Revealed by Solid-State NMR Spectroscopy. *Chem. Phys. Lipids* **2012**, *165* (3), 282–301.

(47) Naito, A.; Matsumori, N.; Ramamoorthy, A. Dynamic Membrane Interactions of Antibacterial and Antifungal Biomolecules, and Amyloid Peptides, Revealed by Solid-State NMR Spectroscopy. *Biochim. Biophys. Acta - Gen. Subj.* **2018**, *1862* (2), 307–323.

(48) Avitabile, C.; D'Andrea, L. D.; Romanelli, A. Circular Dichroism Studies on the Interactions of Antimicrobial Peptides with Bacterial Cells. *Sci. Rep.* **2014**, *4*, 4293.

(49) Bürck, J.; Wadhwani, P.; Fanghänel, S.; Ulrich, A. S. Oriented Circular Dichroism: A Method to Characterize Membrane-Active Peptides in Oriented Lipid Bilayers. *Acc. Chem. Res.* **2016**, *49* (2), 184–192.

(50) Nielsen, J. E.; Bjørnestad, V. A.; Lund, R. Resolving the Structural Interactions between Antimicrobial Peptides and Lipid Membranes Using Small-Angle Scattering Methods: The Case of Indolicidin. *Soft Matter* **2018**, *14* (43), 8750–8763.

(51) Clifton, L. A.; Hall, S. C. L.; Mahmoudi, N.; Knowles, T. J.; Heinrich, F.; Lakey, J. H.

Structural Investigations of Protein–Lipid Complexes Using Neutron Scattering. In *Lipid-Protein Interactions. Methods in Molecular Biology*; Kleinschmidt, J. H., Ed.; Humana, New York, NY, 2019; Vol. 2003, pp 201–251.

(52) He, K.; Ludtke, S. J.; Huang, H. W.; Worcester, D. L. Antimicrobial Peptide Pores in Membranes Detected by Neutron In-Plane Scattering. *Biochemistry* **1995**, *34* (48), 15614–15618.

(53) Qian, S.; Heller, W. T. Peptide-Induced Asymmetric Distribution of Charged Lipids in a Vesicle Bilayer Revealed by Small-Angle Neutron Scattering. *J. Phys. Chem. B* **2011**, *115* (32), 9831–9837.

(54) Lipkin, R.; Lazaridis, T. Computational Studies of Peptide-Induced Membrane Pore Formation. *Philos. Trans. R. Soc. B Biol. Sci.* **2017**, *372* (1726), 20160219.

(55) Velasco-Bolom, J.-L.; Corzo, G.; Garduño-Juárez, R. Molecular Dynamics Simulation of the Membrane Binding and Disruption Mechanisms by Antimicrobial Scorpion Venom-Derived Peptides. *J. Biomol. Struct. Dyn.* **2018**, *36* (8), 2070–2084.

(56) Zhao, L.; Cao, Z.; Bian, Y.; Hu, G.; Wang, J.; Zhou, Y. Molecular Dynamics Simulations of Human Antimicrobial Peptide LL-37 in Model POPC and POPG Lipid Bilayers. *Int. J. Mol. Sci.* **2018**, *19* (4), 1186.

(57) Petkov, P.; Lilkova, E.; Ilieva, N.; Litov, L. Self-Association of Antimicrobial Peptides: A Molecular Dynamics Simulation Study on Bombinin. *Int. J. Mol. Sci.* **2019**, *20* (21), 5450.

(58) Lai, P.-K.; Kaznessis, Y. N. Insights into Membrane Translocation of Protegrin Antimicrobial Peptides by Multistep Molecular Dynamics Simulations. *ACS Omega* **2018**, *3* (6), 6056–6065.

(59) Ehrenstein, G.; Lecar, H. Electrically Gated Ionic Channels in Lipid Bilayers. *Q. Rev. Biophys.* **1977**, *10* (1), 1–34.

(60) Ludtke, S. J.; He, K.; Heller, W. T.; Harroun, T. A.; Yang, L.; Huang, H. W. Membrane Pores Induced by Magainin. *Biochemistry* **1996**, *35* (43), 13723–13728.

(61) Matsuzaki, K.; Murase, O.; Nobutaka, F.; Miyajima, K. An Antimicrobial Peptide, Magainin 2, Induced Rapid Flip-Flop of Phospholipids Coupled with Pore Formation and Peptide Translocation. *Biochemistry* **1996**, *35* (35), 11361–11368.

(62) Pouny, Y.; Rapaport, D.; Mor, A.; Nicolas, P.; Shai, Y. Interaction of Antimicrobial Dermaseptin and Its Fluorescently Labeled Analogs with Phospholipid Membranes. *Biochemistry* **1992**, *31* (49), 12416–12423.

(63) Epand, R. M.; Epand, R. F. Lipid Domains in Bacterial Membranes and the Action of Antimicrobial Agents. *Biochim. Biophys. Acta - Biomembr.* **2009**, *1788* (1), 289–294.

(64) Sharma, V. K.; Qian, S. Effect of an Antimicrobial Peptide on Lateral Segregation of Lipids: A Structure and Dynamics Study by Neutron Scattering. *Langmuir* **2019**, *35* (11), 4152–4160.

(65) Salvador-Gallego, R.; Mund, M.; Cosentino, K.; Schneider, J.; Unsay, J.; Schraermeyer, U.; Engelhardt, J.; Ries, J.; García-Sáez, A. J. Bax Assembly into Rings and Arcs in Apoptotic Mitochondria Is Linked to Membrane Pores. *EMBO J.* **2016**, *35* (4), 389–401.

(66) Yilmaz, N.; Kobayashi, T. Assemblies of Pore-Forming Toxins Visualized by Atomic Force Microscopy. *Biochim. Biophys. Acta - Biomembr.* **2016**, *1858* (3), 500–511.

(67) Mulvihill, E.; Sborgi, L.; Mari, S. A.; Pfreundschuh, M.; Hiller, S.; Müller, D. J. Mechanism of Membrane Pore Formation by Human Gasdermin-D. *EMBO J.* **2018**, *37* (14), e98321.

(68) Parsons, E. S.; Stanley, G. J.; Pyne, A. L. B.; Hodel, A. W.; Nievergelt, A. P.; Menny, A.; Yon, A. R.; Rowley, A.; Richter, R. P.; Fantner, G. E.; Bubeck, D.; Hoogenboom, B. W. Single-Molecule Kinetics of Pore Assembly by the Membrane Attack Complex. *Nat. Commun.* **2019**, *10* (1), 2066.

(69) Hodel, A. W.; Leung, C.; Dudkina, N. V; Saibil, H. R.; Hoogenboom, B. W. Atomic Force Microscopy of Membrane Pore Formation by Cholesterol Dependent Cytolysins. *Curr. Opin. Struct. Biol.* **2016**, *39*, 8–15.

(70) Rudd-Schmidt, J. A.; Hodel, A. W.; Noori, T.; Lopez, J. A.; Cho, H.-J.; Verschoor, S.; Ciccone, A.; Trapani, J. A.; Hoogenboom, B. W.; Voskoboinik, I. Lipid Order and Charge Protect Killer T Cells from Accidental Death. *Nat. Commun.* **2019**, *10* (1), 5396.

(71) Wimley, W. C. How Does Melittin Permeabilize Membranes? *Biophys. J.* **2018**, *114* (2), 251–253.

(72) Dufrêne, Y. F.; Ando, T.; Garcia, R.; Alsteens, D.; Martinez-Martin, D.; Engel, A.; Gerber, C.; Müller, D. J. Imaging Modes of Atomic Force Microscopy for Application in Molecular and Cell Biology. *Nat. Nanotechnol.* **2017**, *12* (4), 295–307.

(73) Ulman, A. *An Introduction to Ultrathin Organic Films: From Langmuir-Blodgett to Self-Assembly*; Academic Press, 1991.

(74) Brian, A. A.; McConnell, H. M. Allogeneic Stimulation of Cytotoxic T Cells by Supported Planar Membranes. *Proc. Natl. Acad. Sci.* **1984**, *81* (19), 6159–6163.

(75) McConnell, H. M.; Watts, T. H.; Weis, R. M.; Brian, A. A. Supported Planar

Membranes in Studies of Cell-Cell Recognition in the Immune System. *Biochim. Biophys. Acta - Rev. Biomembr.* **1986**, *864* (1), 95–106.

(76) Richter, R. P.; Bérat, R.; Brisson, A. R. Formation of Solid-Supported Lipid Bilayers: An Integrated View. *Langmuir* **2006**, *22* (8), 3497–3505.

(77) Morandat, S.; Azouzi, S.; Beauvais, E.; Mastouri, A.; El Kirat, K. Atomic Force Microscopy of Model Lipid Membranes. *Anal. Bioanal. Chem.* **2013**, *405* (5), 1445–1461.

(78) Norlén, L. Skin Barrier Structure and Function: The Single Gel Phase Model. *J. Invest. Dermatol.* **2001**, *117* (4), 830–836.

(79) Singer, S. J.; Nicolson, G. L. The Fluid Mosaic Model of the Structure of Cell Membranes. *Science* **1972**, *175* (4023), 720–731.

(80) Mouritsen, O. G.; Zuckermann, M. J. What's so Special about Cholesterol? *Lipids* **2004**, *39* (11), 1101–1113.

(81) Owen, D. M.; Williamson, D. J.; Magenau, A.; Gaus, K. Sub-Resolution Lipid Domains Exist in the Plasma Membrane and Regulate Protein Diffusion and Distribution. *Nat. Commun.* **2012**, *3* (1), 1256.

(82) Matsumoto, K.; Kusaka, J.; Nishibori, A.; Hara, H. Lipid Domains in Bacterial Membranes. *Mol. Microbiol.* **2006**, *61* (5), 1110–1117.

(83) Jia, Z.; O'Mara, M. L.; Zuegg, J.; Cooper, M. A.; Mark, A. E. The Effect of Environment on the Recognition and Binding of Vancomycin to Native and Resistant Forms of Lipid II. *Biophys. J.* **2011**, *101* (11), 2684–2692.

(84) Sáenz, J. P.; Grosser, D.; Bradley, A. S.; Lagny, T. J.; Lavrynenko, O.; Broda, M.; Simons, K. Hopanoids as Functional Analogues of Cholesterol in Bacterial Membranes. *Proc. Natl. Acad. Sci.* **2015**, *112* (38), 11971–11976.

(85) Mileykovskaya, E.; Dowhan, W. Visualization of Phospholipid Domains in Escherichia Coli by Using the Cardiolipin-Specific Fluorescent Dye 10-N-Nonyl Acridine Orange. *J. Bacteriol.* **2000**, *182* (4), 1172–1175.

(86) Asakawa, H.; Yoshioka, S.; Nishimura, K.; Fukuma, T. Spatial Distribution of Lipid Headgroups and Water Molecules at Membrane/Water Interfaces Visualized by Three-Dimensional Scanning Force Microscopy. *ACS Nano* **2012**, *6* (10), 9013–9020.

(87) Zwang, T. J.; Fletcher, W. R.; Lane, T. J.; Johal, M. S. Quantification of the Layer of Hydration of a Supported Lipid Bilayer. *Langmuir* **2010**, *26* (7), 4598–4601.

(88) Guo, L.; Har, J. Y.; Sankaran, J.; Hong, Y.; Kannan, B.; Wohland, T. Molecular Diffusion Measurement in Lipid Bilayers over Wide Concentration Ranges: A Comparative Study. *ChemPhysChem* **2008**, *9* (5), 721–728.

(89) Tero, R. Substrate Effects on the Formation Process, Structure and Physicochemical Properties of Supported Lipid Bilayers. *Materials* **2012**, *5* (12), 2658–2680.

(90) Tanaka, M.; Sackmann, E. Polymer-Supported Membranes as Models of the Cell Surface. *Nature* **2005**, *437* (7059), 656–663.

(91) Andersson, J.; Köper, I. Tethered and Polymer Supported Bilayer Lipid Membranes: Structure and Function. *Membranes* **2016**, *6* (2), 30.

(92) Clifton, L. A.; Paracini, N.; Hughes, A. V.; Lakey, J. H.; Steinke, N.-J.; Cooper, J. F. K.; Gavutis, M.; Skoda, M. W. A. Self-Assembled Fluid Phase Floating Membranes with Tunable Water Interlayers. *Langmuir* **2019**, *35* (42), 13735–13744.

(93) Janshoff, A.; Steinem, C. Mechanics of Lipid Bilayers: What Do We Learn from Pore-Spanning Membranes? *Biochim. Biophys. Acta - Mol. Cell Res.* **2015**, *1853* (11), 2977–2983.

(94) Rakshit, T.; Senapati, S.; Parmar, V. M.; Sahu, B.; Maeda, A.; Park, P. S.-H. Adaptations in Rod Outer Segment Disc Membranes in Response to Environmental Lighting Conditions. *Biochim. Biophys. acta. Mol. cell Res.* **2017**, *1864* (10), 1691–1702.

(95) Müller, D. J.; Schabert, F. A.; Büldt, G.; Engel, A. Imaging Purple Membranes in Aqueous Solutions at Sub-Nanometer Resolution by Atomic Force Microscopy. *Biophys. J.* **1995**, *68* (5), 1681–1686.

(96) Kumar, S.; Cartron, M. L.; Mullin, N.; Qian, P.; Leggett, G. J.; Hunter, C. N.; Hobbs, J. K. Direct Imaging of Protein Organization in an Intact Bacterial Organelle Using High-Resolution Atomic Force Microscopy. *ACS Nano* **2017**, *11* (1), 126–133.

(97) Liou, J.-W.; Hung, Y.-J.; Yang, C.-H.; Chen, Y.-C. The Antimicrobial Activity of Gramicidin A Is Associated with Hydroxyl Radical Formation. *PLoS One* **2015**, *10* (1), e0117065.

(98) Torcato, I. M.; Huang, Y.-H.; Franquelim, H. G.; Gaspar, D.; Craik, D. J.; Castanho, M. A. R. B.; Troeira Henriques, S. Design and Characterization of Novel Antimicrobial Peptides, R-BP100 and RW-BP100, with Activity against Gram-Negative and Gram-Positive Bacteria. *Biochim. Biophys. Acta - Biomembr.* **2013**, *1828* (3), 944–955.

(99) Alves, C. S.; Melo, M. N.; Franquelim, H. G.; Ferre, R.; Planas, M.; Feliu, L.; Bardají,

E.; Kowalczyk, W.; Andreu, D.; Santos, N. C.; Fernandes, M. X.; Castanho, M. A. R. B. Escherichia Coli Cell Surface Perturbation and Disruption Induced by Antimicrobial Peptides BP100 and PepR. *J. Biol. Chem.* **2010**, *285* (36), 27536–27544.

(100) Su, H.-N.; Chen, Z.-H.; Song, X.-Y.; Chen, X.-L.; Shi, M.; Zhou, B.-C.; Zhao, X.; Zhang, Y.-Z. Antimicrobial Peptide Trichokonin VI-Induced Alterations in the Morphological and Nanomechanical Properties of Bacillus Subtilis. *PLoS One* **2012**, *7* (9), e45818.

(101) Li, A.; Lee, P. Y.; Ho, B.; Ding, J. L.; Lim, C. T. Atomic Force Microscopy Study of the Antimicrobial Action of Sushi Peptides on Gram Negative Bacteria. *Biochim. Biophys. Acta - Biomembr.* **2007**, *1768* (3), 411–418.

(102) Zdybicka-Barabas, A.; Stączek, S.; Pawlikowska-Pawlęga, B.; Mak, P.; Luchowski, R.; Skrzypiec, K.; Mendyk, E.; Wydrych, J.; Gruszecki, W. I.; Cytryńska, M. Studies on the Interactions of Neutral Galleria Mellonella Cecropin D with Living Bacterial Cells. *Amino Acids* **2019**, *51* (2), 175–191.

(103) Dias, S. A.; Freire, J. M.; Pérez-Peinado, C.; Domingues, M. M.; Gaspar, D.; Vale, N.; Gomes, P.; Andreu, D.; Henriques, S. T.; Castanho, M. A. R. B.; Veiga, A. S. New Potent Membrane-Targeting Antibacterial Peptides from Viral Capsid Proteins. *Front. Microbiol.* **2017**, *8*, 775.

(104) Oliveira, M.; Gomes-Alves, A. G.; Sousa, C.; Mirta Marani, M.; Plácido, A.; Vale, N.; Delerue-Matos, C.; Gameiro, P.; Kückelhaus, S. A. S.; Tomas, A. M.; S. A. Leite, J. R.; Eaton, P. Ocellatin-PT Antimicrobial Peptides: High-Resolution Microscopy Studies in Antileishmania Models and Interactions with Mimetic Membrane Systems. *Biopolymers* **2016**, *105* (12), 873–886.

(105) Domingues, M. M.; Silva, P. M.; Franquelim, H. G.; Carvalho, F. A.; Castanho, M. A. R. B.; Santos, N. C. Antimicrobial Protein RBPI21-Induced Surface Changes on Gram-Negative and Gram-Positive Bacteria. *Nanomedicine Nanotechnology, Biol. Med.* **2014**, *10* (3), 543–551.

(106) Overton, K.; Greer, H.; Ferguson, M. A.; Spain, E. M.; Elmore, D. E.; Nunez, M. E.; Volle, C. Qualitative and Quantitative Changes to E. Coli During Treatment with Magainin 2 Observed in Native Conditions by Atomic Force Microscopy. *Langmuir* **2020**, *36* (2), 650–659.

(107) Mularski, A.; Wilksch, J. J.; Hanssen, E.; Strugnell, R. A.; Separovic, F. Atomic Force Microscopy of Bacteria Reveals the Mechanobiology of Pore Forming Peptide Action. *Biochim. Biophys. Acta - Biomembr.* **2016**, *1858* (6), 1091–1098.

(108) Mortensen, N. P.; Fowlkes, J. D.; Sullivan, C. J.; Allison, D. P.; Larsen, N. B.; Molin, S.; Doktycz, M. J. Effects of Colistin on Surface Ultrastructure and Nanomechanics of Pseudomonas Aeruginosa Cells. *Langmuir* **2009**, *25* (6), 3728–3733.

(109) Mikuláss, K. R.; Nagy, K.; Bogos, B.; Szegletes, Z.; Kovács, E.; Farkas, A.; Váró, G.; Kondorosi, É.; Kereszt, A. Antimicrobial Nodule-Specific Cysteine-Rich Peptides Disturb the Integrity of Bacterial Outer and Inner Membranes and Cause Loss of Membrane Potential. *Ann. Clin. Microbiol. Antimicrob.* **2016**, *15* (1), 43.

(110) Wang, C.; Zolotarskaya, O. Y.; Nair, S. S.; Ehrhardt, C. J.; Ohman, D. E.; Wynne, K. J.; Yadavalli, V. K. Real-Time Observation of Antimicrobial Polycation Effects on Escherichia Coli : Adapting the Carpet Model for Membrane Disruption to Quaternary Copolyoxetanes. *Langmuir* **2016**, *32* (12), 2975–2984.

(111) Pérez-Peinado, C.; Dias, S. A.; Domingues, M. M.; Benfield, A. H.; Freire, J. M.; Rádis-Baptista, G.; Gaspar, D.; Castanho, M. A. R. B.; Craik, D. J.; Henriques, S. T.; Veiga, A. S.; Andreu, D. Mechanisms of Bacterial Membrane Permeabilization by Crotalicidin (Ctn) and Its Fragment Ctn(15–34), Antimicrobial Peptides from Rattlesnake Venom. *J. Biol. Chem.* **2018**, *293* (5), 1536–1549.

(112) Nagy, K.; Mikuláss, K. R.; Végh, A. G.; Kereszt, A.; Kondorosi, É.; Váró, G.; Szegletes, Z. Interaction of Cysteine-Rich Cationic Antimicrobial Peptides with Intact Bacteria and Model Membranes. *Gen. Physiol. Biophys.* **2015**, *34* (2), 135–144.

(113) Fantner, G. E.; Barbero, R. J.; Gray, D. S.; Belcher, A. M. Kinetics of Antimicrobial Peptide Activity Measured on Individual Bacterial Cells Using High-Speed Atomic Force Microscopy. *Nat. Nanotechnol.* **2010**, *5* (4), 280–285.

(114) Benn, G.; Pyne, A. L. B.; Ryadnov, M. G.; Hoogenboom, B. W. Imaging Live Bacteria at the Nanoscale: Comparison of Immobilisation Strategies. *Analyst* **2019**, *144* (23), 6944–6952.

(115) Heesterbeek, D. A.; Bardoel, B. W.; Parsons, E. S.; Bennett, I.; Ruyken, M.; Doorduijn, D. J.; Gorham, R. D.; Berends, E. T.; Pyne, A. L.; Hoogenboom, B. W.; Rooijakkers, S. H. Bacterial Killing by Complement Requires Membrane Attack Complex Formation via Surface-bound C5 Convertases. *EMBO J.* **2019**, *38* (4), e99852.

(116) Abbasi, F.; Leitch, J. J.; Su, Z. F.; Szymanski, G.; Lipkowski, J. Direct Visualization of Alamethicin Ion Pores Formed in a Floating Phospholipid Membrane Supported on a Gold Electrode Surface. *Electrochim. Acta* **2018**, *267*, 195–205.

(117) Abbasi, F.; Alvarez-Malmagro, J.; Su, Z. F.; Leitch, J. J.; Lipkowski, J. Pore Forming Properties of Alamethicin in Negatively Charged Floating Bilayer Lipid Membranes

Supported on Gold Electrodes. *Langmuir* **2018**, *34* (45), 13754–13765.

(118) Pfeil, M.-P.; Pyne, A. L. B.; Losasso, V.; Ravi, J.; Lamarre, B.; Faruqui, N.; Alkassem, H.; Hammond, K.; Judge, P. J.; Winn, M.; Martyna, G. J.; Crain, J.; Watts, A.; Hoogenboom, B. W.; Ryadnov, M. G. Tuneable Poration: Host Defense Peptides as Sequence Probes for Antimicrobial Mechanisms. *Sci. Rep.* **2018**, *8* (1), 14926.

(119) Hammond, K.; Lewis, H.; Faruqui, N.; Russell, C.; Hoogenboom, B. W.; Ryadnov, M. G. Helminth Defense Molecules as Design Templates for Membrane Active Antibiotics. *ACS Infect. Dis.* **2019**, *5* (8), 1471–1479.

(120) Henderson, J. M.; Waring, A. J.; Separovic, F.; Lee, K. Y. C. Antimicrobial Peptides Share a Common Interaction Driven by Membrane Line Tension Reduction. *Biophys. J.* **2016**, *111* (10), 2176–2189.

(121) Hall, K.; Lee, T.-H.; Mechler, A. I.; Swann, M. J.; Aguilar, M.-I. Real-Time Measurement of Membrane Conformational States Induced by Antimicrobial Peptides: Balance Between Recovery and Lysis. *Sci. Rep.* **2015**, *4* (1), 5479.

(122) Harrison, P. L.; Heath, G. R.; Johnson, B. R. G.; Abdel-Rahman, M. A.; Strong, P. N.; Evans, S. D.; Miller, K. Phospholipid Dependent Mechanism of Smp24, an α-Helical Antimicrobial Peptide from Scorpion Venom. *Biochim. Biophys. Acta - Biomembr.* **2016**, *1858* (11), 2737–2744.

(123) Khadka, N. K.; Aryal, C. M.; Pan, J. Lipopolysaccharide-Dependent Membrane Permeation and Lipid Clustering Caused by Cyclic Lipopeptide Colistin. *ACS Omega* **2018**, *3* (12), 17828–17834.

(124) Mecke, A.; Lee, D.-K.; Ramamoorthy, A.; Orr, B. G.; Banaszak Holl, M. M. Membrane Thinning Due to Antimicrobial Peptide Binding: An Atomic Force Microscopy Study of MSI-78 in Lipid Bilayers. *Biophys. J.* **2005**, *89* (6), 4043–4050.

(125) Pyne, A.; Pfeil, M. P.; Bennett, I.; Ravi, J.; Iavicoli, P.; Lamarre, B.; Roethke, A.; Ray, S.; Jiang, H.; Bella, A.; Reisinger, B.; Yin, D.; Little, B.; Muñoz-García, J. C.; Cerasoli, E.; Judge, P. J.; Faruqui, N.; Calzolai, L.; Henrion, A.; Martyna, G. J.; Grovenor, C. R. M.; Crain, J.; Hoogenboom, B. W.; Watts, A.; Ryadnov, M. G. Engineering Monolayer Poration for Rapid Exfoliation of Microbial Membranes. *Chem. Sci.* **2017**, *8* (2), 1105–1115.

(126) Oliva, R.; Del Vecchio, P.; Grimaldi, A.; Notomista, E.; Cafaro, V.; Pane, K.; Schuabb, V.; Winter, R.; Petraccone, L. Membrane Disintegration by the Antimicrobial Peptide (P)GKY20: Lipid Segregation and Domain Formation. *Phys. Chem. Chem. Phys.* **2019**, *21* (7), 3989–3998.

(127) Heath, G. R.; Harrison, P. L.; Strong, P. N.; Evans, S. D.; Miller, K. Visualization of Diffusion Limited Antimicrobial Peptide Attack on Supported Lipid Membranes. *Soft Matter* **2018**, *14* (29), 6146–6154.

(128) Mihajlovic, M.; Lazaridis, T. Charge Distribution and Imperfect Amphipathicity Affect Pore Formation by Antimicrobial Peptides. *Biochim. Biophys. Acta - Biomembr.* **2012**, *1818* (5), 1274–1283.

(129) Lee, T.-H.; Hall, K.; Aguilar, M.-I. The Effect of Charge on Melittin-Induced Changes in Membrane Structure and Morphology. *Aust. J. Chem.* **2020**, *73* (3), 195.

(130) Pan, J.; Khadka, N. K. Kinetic Defects Induced by Melittin in Model Lipid Membranes: A Solution Atomic Force Microscopy Study. *J. Phys. Chem. B* **2016**, *120* (20), 4625–4634.

(131) García-Sáez, A. J.; Chiantia, S.; Salgado, J.; Schwille, P. Pore Formation by a Bax-Derived Peptide: Effect on the Line Tension of the Membrane Probed by AFM. *Biophys. J.* **2007**, *93* (1), 103–112.

(132) Rakowska, P. D.; Jiang, H.; Ray, S.; Pyne, A.; Lamarre, B.; Carr, M.; Judge, P. J.; Ravi, J.; Gerling, U. I. M.; Koksch, B.; Martyna, G. J.; Hoogenboom, B. W.; Watts, A.; Crain, J.; Grovenor, C. R. M.; Ryadnov, M. G. Nanoscale Imaging Reveals Laterally Expanding Antimicrobial Pores in Lipid Bilayers. *Proc. Natl. Acad. Sci.* **2013**, *110* (22), 8918–8923.

(133) De Santis, E.; Alkassem, H.; Lamarre, B.; Faruqui, N.; Bella, A.; Noble, J. E.; Micale, N.; Ray, S.; Burns, J. R.; Yon, A. R.; Hoogenboom, B. W.; Ryadnov, M. G. Antimicrobial Peptide Capsids of de Novo Design. *Nat. Commun.* **2017**, *8* (1), 2263.

(134) Kim, S. Y.; Pittman, A. E.; Zapata-Mercado, E.; King, G. M.; Wimley, W. C.; Hristova, K. Mechanism of Action of Peptides That Cause the PH-Triggered Macromolecular Poration of Lipid Bilayers. *J. Am. Chem. Soc.* **2019**, *141* (16), 6706–6718.

(135) Lee, T.-H.; N. Hall, K.; Aguilar, M.-I. Antimicrobial Peptide Structure and Mechanism of Action: A Focus on the Role of Membrane Structure. *Curr. Top. Med. Chem.* **2015**, *16* (1), 25–39.

(136) Henderson, J. M.; Iyengar, N. S.; Lam, K. L. H.; Maldonado, E.; Suwatthee, T.; Roy, I.; Waring, A. J.; Lee, K. Y. C. Beyond Electrostatics: Antimicrobial Peptide Selectivity and the Influence of Cholesterol-Mediated Fluidity and Lipid Chain Length on Protegrin-1 Activity. *Biochim. Biophys. Acta - Biomembr.* **2019**, *1861* (10), 182977.

(137) Bodescu, M. A.; Rosenkötter, F.; Fritz, J. Time Lapse AFM on Vesicle Formation from

Mixed Lipid Bilayers Induced by the Membrane–Active Peptide Melittin. *Soft Matter* **2017**, *13* (38), 6845–6851.

(138) Lei, H.-Z.; Tian, T.; Du, Q.; Hu, J.; Zhang, Y. Sequence-Dependent Interactions between Model Peptides and Lipid Bilayers. *Nucl. Sci. Tech.* **2017**, *28* (9), 124.

(139) Pan, J.; Dalzini, A.; Khadka, N. K.; Aryal, C. M.; Song, L. Lipid Extraction by α-Synuclein Generates Semi-Transmembrane Defects and Lipoprotein Nanoparticles. *ACS omega* **2018**, *3* (8), 9586–9597.

(140) Pan, J.; Dalzini, A.; Song, L. Cholesterol and Phosphatidylethanolamine Lipids Exert Opposite Effects on Membrane Modulations Caused by the M2 Amphipathic Helix. *Biochim. Biophys. Acta - Biomembr.* **2019**, *1861* (1), 201–209.

(141) Leite, N. B.; Aufderhorst-Roberts, A.; Palma, M. S.; Connell, S. D.; Neto, J. R.; Beales, P. A. PE and PS Lipids Synergistically Enhance Membrane Poration by a Peptide with Anticancer Properties. *Biophys. J.* **2015**, *109* (5), 936–947.

(142) Pittman, A. E.; Marsh, B. P.; King, G. M. Conformations and Dynamic Transitions of a Melittin Derivative That Forms Macromolecule-Sized Pores in Lipid Bilayers. *Langmuir* **2018**, *34* (28), 8393–8399.

(143) Lam, K. L. H.; Wang, H.; Siaw, T. A.; Chapman, M. R.; Waring, A. J.; Kindt, J. T.; Lee, K. Y. C. Mechanism of Structural Transformations Induced by Antimicrobial Peptides in Lipid Membranes. *Biochim. Biophys. Acta - Biomembr.* **2012**, *1818* (2), 194–204.

(144) Krauson, A. J.; He, J.; Wimley, W. C. Gain-of-Function Analogues of the Pore-Forming Peptide Melittin Selected by Orthogonal High-Throughput Screening. *J. Am. Chem. Soc.* **2012**, *134* (30), 12732–12741.

(145) Li, S.; Kim, S. Y.; Pittman, A. E.; King, G. M.; Wimley, W. C.; Hristova, K. Potent Macromolecule-Sized Poration of Lipid Bilayers by the Macrolittins, A Synthetically Evolved Family of Pore-Forming Peptides. *J. Am. Chem. Soc.* **2018**, *140* (20), 6441–6447.

(146) Badosa, E.; Moiset, G.; Montesinos, L.; Talleda, M.; Bardají, E.; Feliu, L.; Planas, M.; Montesinos, E. Derivatives of the Antimicrobial Peptide BP100 for Expression in Plant Systems. *PLoS One* **2013**, *8* (12).

(147) Kim, S.; Jeon, T.-J.; Oberai, A.; Yang, D.; Schmidt, J. J.; Bowie, J. U. Transmembrane Glycine Zippers: Physiological and Pathological Roles in Membrane Proteins. *Proc. Natl. Acad. Sci.* **2005**, *102* (40), 14278–14283.

(148) Senes, A.; Engel, D. E.; DeGrado, W. F. Folding of Helical Membrane Proteins: The

Role of Polar, GxxxG-like and Proline Motifs. *Curr. Opin. Struct. Biol.* **2004**, *14* (4), 465–479.

(149) Lupas, A. N.; Bassler, J. Coiled Coils - A Model System for the 21st Century. *Trends Biochem. Sci.* **2017**, *42* (2), 130–140.

(150) Merrifield, R. B. Solid Phase Peptide Synthesis. I. The Synthesis of a Tetrapeptide. *J. Am. Chem. Soc.* **1963**, *85* (14), 2149–2154.

(151) Mäde, V.; Els-Heindl, S.; Beck-Sickinger, A. G. Automated Solid-Phase Peptide Synthesis to Obtain Therapeutic Peptides. *Beilstein J. Org. Chem.* **2014**, *10* (1), 1197–1212.

(152) Montalbetti, C. A. G. N.; Falque, V. Amide Bond Formation and Peptide Coupling. *Tetrahedron* **2005**, *61* (46), 10827–10852.

(153) Atherton, E.; Fox, H.; Harkiss, D.; Logan, C. J.; Sheppard, R. C.; Williams, B. J. A Mild Procedure for Solid Phase Peptide Synthesis: Use of Fluorenylmethoxycarbonylamino-Acids. *J. Chem. Soc. Chem. Commun.* **1978**, No. 13, 537–539.

(154) Chang, C. D.; Meienhofer, J. Solid-Phase Peptide Synthesis Using Mild Base Cleavage of N Alpha-Fluorenylmethyloxycarbonylamino Acids, Exemplified by a Synthesis of Dihydrosomatostatin. *Int. J. Pept. Protein Res.* **1978**, *11* (3), 246–249.

(155) Jaradat, D. M. M. Thirteen Decades of Peptide Synthesis: Key Developments in Solid Phase Peptide Synthesis and Amide Bond Formation Utilized in Peptide Ligation. *Amino Acids* **2018**, *50* (1), 39–68.

(156) Vaino, A. R.; Janda, K. D. Solid-Phase Organic Synthesis: A Critical Understanding of the Resin. *J. Comb. Chem.* **2000**, *2* (6), 579–596.

(157) García-Martín, F.; Quintanar-Audelo, M.; García-Ramos, Y.; Cruz, L. J.; Gravel, C.; Furic, R.; Côté, S.; Tulla-Puche, J.; Albericio, F. ChemMatrix, a Poly(Ethylene Glycol)-Based Support for the Solid-Phase Synthesis of Complex Peptides. *J. Comb. Chem.* **2006**, *8* (2), 213–220.

(158) Alsina, J.; Albericio, F. Solid-Phase Synthesis of C-Terminal Modified Peptides. *Biopolymers* **2003**, *71* (4), 454–477.

(159) Petrou, C.; Sarigiannis, Y. Peptide Synthesis: Methods, Trends, and Challenges. In *Peptide Applications in Biomedicine, Biotechnology and Bioengineering*; Koutsopoulos, S., Ed.; Woodhead Publishing, 2018; pp 1–21.

(160) Bodanszky, M. Techniques for the Facilitation of Peptide Synthesis. In *Principles of*

Peptide Synthesis; Springer Berlin Heidelberg, 1993; pp 249–271.

(161) Fekete, S.; Veuthey, J.-L.; Guillarme, D. New Trends in Reversed-Phase Liquid Chromatographic Separations of Therapeutic Peptides and Proteins: Theory and Applications. *J. Pharm. Biomed. Anal.* **2012**, *69*, 9–27.

(162) Schaiberger, A. M.; Moss, J. A. Optimized Sample Preparation for MALDI Mass Spectrometry Analysis of Protected Synthetic Peptides. *J. Am. Soc. Mass Spectrom.* **2008**, *19* (4), 614–619.

(163) Gill, S. C.; von Hippel, P. H. Calculation of Protein Extinction Coefficients from Amino Acid Sequence Data. *Anal. Biochem.* **1989**, *182* (2), 319–326.

(164) Kuipers, B. J. H.; Gruppen, H. Prediction of Molar Extinction Coefficients of Proteins and Peptides Using UV Absorption of the Constituent Amino Acids at 214 Nm To Enable Quantitative Reverse Phase High-Performance Liquid Chromatography−Mass Spectrometry Analysis. *J. Agric. Food Chem.* **2007**, *55* (14), 5445–5451.

(165) Kelly, S.; Price, N. The Use of Circular Dichroism in the Investigation of Protein Structure and Function. *Curr. Protein Pept. Sci.* **2000**, *1* (4), 349–384.

(166) Moffitt, W. Optical Rotatory Dispersion of Helical Polymers. *J. Chem. Phys.* **1956**, *25* (3), 467–478.

(167) Sreerama, N.; Woody, R. W. Computation and Analysis of Protein Circular Dichroism Spectra. *Methods Enzymol.* **2004**, *383*, 318–351.

(168) Greenfield, N. J.; Fasman, G. D. Computed Circular Dichroism Spectra for the Evaluation of Protein Conformation. *Biochemistry* **1969**, *8* (10), 4108–4116.

(169) Greenfield, N. J. Using Circular Dichroism Spectra to Estimate Protein Secondary Structure. *Nat. Protoc.* **2006**, *1* (6), 2876–2890.

(170) Pelton, J. T.; McLean, L. R. Spectroscopic Methods for Analysis of Protein Secondary Structure. *Anal. Biochem.* **2000**, *277* (2), 167–176.

(171) Morrisett, J. D.; Jackson, R. L.; Gotto, A. M. Lipid-Protein Interactions in the Plasma Lipoproteins. *Biochim. Biophys. Acta - Rev. Biomembr.* **1977**, *472* (2), 93–133.

(172) Roccatano, D.; Colombo, G.; Fioroni, M.; Mark, A. E. Mechanism by Which 2,2,2-Trifluoroethanol/Water Mixtures Stabilize Secondary-Structure Formation in Peptides: A Molecular Dynamics Study. *Proc. Natl. Acad. Sci.* **2002**, *99* (19), 12179–12184.

(173) Hope, M. J.; Bally, M. B.; Webb, G.; Cullis, P. R. Production of Large Unilamellar Vesicles by a Rapid Extrusion Procedure. Characterization of Size Distribution, Trapped

Volume and Ability to Maintain a Membrane Potential. *Biochim. Biophys. Acta - Biomembr.* **1985**, *812* (1), 55–65.

(174) Kelly, S. M.; Price, N. C. The Application of Circular Dichroism to Studies of Protein Folding and Unfolding. *Biochim. Biophys. Acta - Protein Struct. Mol. Enzymol.* **1997**, *1338* (2), 161–185.

(175) Miles, A. J.; Wallace, B. A. Circular Dichroism Spectroscopy of Membrane Proteins. *Chem. Soc. Rev.* **2016**, *45* (18), 4859–4872.

(176) Ranjbar, B.; Gill, P. Circular Dichroism Techniques: Biomolecular and Nanostructural Analyses- A Review. *Chem. Biol. Drug Des.* **2009**, *74* (2), 101–120.

(177) Kirwan, J. P.; Hodges, R. S. Transmission of Stability Information through the N-Domain of Tropomyosin Is Interrupted by a Stabilizing Mutation (A109L) in the Hydrophobic Core of the Stability Control Region (Residues 97-118). *J. Biol. Chem.* **2014**, *289* (7), 4356–4366.

(178) Henry, D. C. The Cataphoresis of Suspended Particles. Part I.—The Equation of Cataphoresis. *Proc. R. Soc. London. Ser. A* **1931**, *133* (821), 106–129.

(179) Meyer, G.; Amer, N. M. Novel Optical Approach to Atomic Force Microscopy. *Appl. Phys. Lett.* **1988**, *53* (12), 1045–1047.

(180) Hoogenboom, B. W. AFM in Liquids. In *Encyclopedia of Nanotechnology*; Bhushan, B., Ed.; Springer Netherlands: Dordrecht, 2012; pp 83–89.

(181) Ando, T.; Uchihashi, T.; Scheuring, S. Filming Biomolecular Processes by High-Speed Atomic Force Microscopy. *Chem. Rev.* **2014**, *114* (6), 3120–3188.

(182) Hansma, P. K.; Cleveland, J. P.; Radmacher, M.; Walters, D. A.; Hillner, P. E.; Bezanilla, M.; Fritz, M.; Vie, D.; Hansma, H. G.; Prater, C. B.; Massie, J.; Fukunaga, L.; Gurley, J.; Elings, V. Tapping Mode Atomic Force Microscopy in Liquids. *Appl. Phys. Lett.* **1994**, *64* (13), 1738–1740.

(183) Kiracofe, D.; Kobayashi, K.; Labuda, A.; Raman, A.; Yamada, H. High Efficiency Laser Photothermal Excitation of Microcantilever Vibrations in Air and Liquids. *Rev. Sci. Instrum.* **2011**, *82* (1), 013702.

(184) Han, W.; Lindsay, S. M.; Jing, T. A Magnetically Driven Oscillating Probe Microscope for Operation in Liquids. *Appl. Phys. Lett.* **1996**, *69* (26), 4111–4113.

(185) Umeda, K.; Oyabu, N.; Kobayashi, K.; Hirata, Y.; Matsushige, K.; Yamada, H. High-Resolution Frequency-Modulation Atomic Force Microscopy in Liquids Using

Electrostatic Excitation Method. *Appl. Phys. Express* **2010**, *3* (6), 065205.

(186) Labuda, A.; Hohlbauch, S.; Kocun, M.; Limpoco, F. T.; Kirchhofer, N.; Ohler, B.; Hurley, D. Tapping Mode AFM Imaging in Liquids with BlueDrive Photothermal Excitation. *Micros. Today* **2018**, *26* (6), 12–17.

(187) Krieg, M.; Fläschner, G.; Alsteens, D.; Gaub, B. M.; Roos, W. H.; Wuite, G. J. L.; Gaub, H. E.; Gerber, C.; Dufrêne, Y. F.; Müller, D. J. Atomic Force Microscopy-Based Mechanobiology. *Nat. Rev. Phys.* **2019**, *1* (1), 41–57.

(188) Pittenger, B.; Erina, N.; Su, C. Quantitative Mechanical Property Mapping at the Nanoscale with PeakForce QNM http://www.bruker.com/fileadmin/user_upload/8-PDF-Docs/SurfaceAnalysis/AFM/ApplicationNotes/AN128-RevB0-Quantitative_Mechanical_Property_Mapping_at_the_Nanoscale_with_PeakForceQNM-AppNote.pdf (accessed Oct 22, 2020).

(189) Derjaguin, B. V; Muller, V. M.; Toporov, Y. P. Effect of Contact Deformations on the Adhesion of Particles. *J. Colloid Interface Sci.* **1975**, *53* (2), 314–326.

(190) Habibullah, H. 30 Years of Atomic Force Microscopy: Creep, Hysteresis, Cross-Coupling, and Vibration Problems of Piezoelectric Tube Scanners. *Measurement* **2020**, *159*, 107776.

(191) Redondo-Morata, L.; Giannotti, M. I.; Sanz, F. Stability of Lipid Bilayers as Model Membranes: Atomic Force Microscopy and Spectroscopy Approach. In *Atomic Force Microscopy in Liquid*; Baró, A. M., Reifenberger, R. G., Eds.; Wiley-VCH: Weinheim, Germany, 2012; pp 259–284.

(192) Richter, R. P.; Brisson, A. R. Following the Formation of Supported Lipid Bilayers on Mica: A Study Combining AFM, QCM-D, and Ellipsometry. *Biophys. J.* **2005**, *88* (5), 3422–3433.

(193) Victorov, A. V.; Janes, N.; Taraschi, T. F.; Hoek, J. B. Packing Constraints and Electrostatic Surface Potentials Determine Transmembrane Asymmetry of Phosphatidylethanol. *Biophys. J.* **1997**, *72* (6), 2588–2598.

(194) Richter, R. P.; Maury, N.; Brisson, A. R. On the Effect of the Solid Support on the Interleaflet Distribution of Lipids in Supported Lipid Bilayers. *Langmuir* **2005**, *21* (1), 299–304.

(195) Haug, T.; Kjuul, A. K.; Stensvåg, K.; Sandsdalen, E.; Styrvold, O. B. Antibacterial Activity in Four Marine Crustacean Decapods. *Fish Shellfish Immunol.* **2002**, *12* (5), 371–385.

(196) Pace, C. N.; Scholtz, J. M. A Helix Propensity Scale Based on Experimental Studies of Peptides and Proteins. *Biophys. J.* **1998**, *75* (1), 422–427.

(197) Li, L.; Vorobyov, I.; Allen, T. W. The Different Interactions of Lysine and Arginine Side Chains with Lipid Membranes. *J. Phys. Chem. B* **2013**, *117* (40), 11906–11920.

(198) Cunningham, B.; Wells, J. High-Resolution Epitope Mapping of HGH-Receptor Interactions by Alanine-Scanning Mutagenesis. *Science* **1989**, *244* (4908), 1081–1085.

(199) Cipcigan, F.; Carrieri, A. P.; Pyzer-Knapp, E. O.; Krishna, R.; Hsiao, Y.-W.; Winn, M.; Ryadnov, M. G.; Edge, C.; Martyna, G.; Crain, J. Accelerating Molecular Discovery through Data and Physical Sciences: Applications to Peptide-Membrane Interactions. *J. Chem. Phys.* **2018**, *148* (24), 241744.

(200) Hawrani, A.; Howe, R. A.; Walsh, T. R.; Dempsey, C. E. Origin of Low Mammalian Cell Toxicity in a Class of Highly Active Antimicrobial Amphipathic Helical Peptides. *J. Biol. Chem.* **2008**, *283* (27), 18636–18645.

(201) Derjaguin, B. V. *Theory of Stability of Colloids and Thin Films*; Springer US: New York, 1989.

(202) Brochard-Wyart, F.; de Gennes, P. G.; Sandre, O. Transient Pores in Stretched Vesicles: Role of Leak-Out. *Phys. A Stat. Mech. its Appl.* **2000**, *278* (1–2), 32–51.

(203) Huang, H. W.; Chen, F.-Y.; Lee, M.-T. Molecular Mechanism of Peptide-Induced Pores in Membranes. *Phys. Rev. Lett.* **2004**, *92* (19), 198304.

(204) Gözen, I.; Dommersnes, P.; Czolkos, I.; Jesorka, A.; Lobovkina, T.; Orwar, O. Fractal Avalanche Ruptures in Biological Membranes. *Nat. Mater.* **2010**, *9* (11), 908–912.

(205) Homsy, G. M. Viscous Fingering in Porous Media. *Annu. Rev. Fluid Mech.* **1987**, *19* (1), 271–311.

(206) Wilkinson, D.; Willemsen, J. F. Invasion Percolation: A New Form of Percolation Theory. *J. Phys. A. Math. Gen.* **1983**, *16* (14), 3365–3376.

(207) Hu, J.; Chen, C.; Zhang, S.; Zhao, X.; Xu, H.; Zhao, X.; Lu, J. R. Designed Antimicrobial and Antitumor Peptides with High Selectivity. *Biomacromolecules* **2011**, *12* (11), 3839–3843.

(208) Bamford, R. A.; Smith, A.; Metz, J.; Glover, G.; Titball, R. W.; Pagliara, S. Investigating the Physiology of Viable but Non-Culturable Bacteria by Microfluidics and Time-Lapse Microscopy. *BMC Biol.* **2017**, *15* (1), 121.

(209) Robinson, M. W.; Menon, R.; Donnelly, S. M.; Dalton, J. P.; Ranganathan, S. An

Integrated Transcriptomics and Proteomics Analysis of the Secretome of the Helminth Pathogen Fasciola Hepatica. *Mol. Cell. Proteomics* **2009**, *8* (8), 1891–1907.

(210) Harnett, W.; Harnett, M. M. Helminth-Derived Immunomodulators: Can Understanding the Worm Produce the Pill? *Nat. Rev. Immunol.* **2010**, *10* (4), 278–284.

(211) Robinson, M. W.; Donnelly, S.; Hutchinson, A. T.; To, J.; Taylor, N. L.; Norton, R. S.; Perugini, M. A.; Dalton, J. P. A Family of Helminth Molecules That Modulate Innate Cell Responses via Molecular Mimicry of Host Antimicrobial Peptides. *PLoS Pathog.* **2011**, *7* (5), e1002042.

(212) Alvarado, R.; To, J.; Lund, M. E.; Pinar, A.; Mansell, A.; Robinson, M. W.; O'Brien, B. A.; Dalton, J. P.; Donnelly, S. The Immune Modulatory Peptide FhHDM-1 Secreted by the Helminth Fasciola Hepatica Prevents NLRP3 Inflammasome Activation by Inhibiting Endolysosomal Acidification in Macrophages. *FASEB J.* **2017**, *31* (1), 85–95.

(213) Alvarado, R.; O'Brien, B.; Tanaka, A.; Dalton, J. P.; Donnelly, S. A Parasitic Helminth-Derived Peptide That Targets the Macrophage Lysosome Is a Novel Therapeutic Option for Autoimmune Disease. *Immunobiology* **2015**, *220* (2), 262–269.

(214) Zelezetsky, I.; Tossi, A. Alpha-Helical Antimicrobial Peptides—Using a Sequence Template to Guide Structure–Activity Relationship Studies. *Biochim. Biophys. Acta - Biomembr.* **2006**, *1758* (9), 1436–1449.

(215) Thivierge, K.; Cotton, S.; Schaefer, D. A.; Riggs, M. W.; To, J.; Lund, M. E.; Robinson, M. W.; Dalton, J. P.; Donnelly, S. M. Cathelicidin-like Helminth Defence Molecules (HDMs): Absence of Cytotoxic, Anti-Microbial and Anti-Protozoan Activities Imply a Specific Adaptation to Immune Modulation. *PLoS Negl. Trop. Dis.* **2013**, *7* (7), e2307.

(216) Eliseev, I. E.; Terterov, I. N.; Yudenko, A. N.; Shamova, O. V. Linking Sequence Patterns and Functionality of Alpha-Helical Antimicrobial Peptides. *Bioinformatics* **2019**, *35* (16), 2713–2717.

(217) Wang, G.; Li, X.; Wang, Z. APD2: The Updated Antimicrobial Peptide Database and Its Application in Peptide Design. *Nucleic Acids Res.* **2009**, *37* (suppl_1), D933–D937.

(218) Vanni, S.; Vamparys, L.; Gautier, R.; Drin, G.; Etchebest, C.; Fuchs, P. F. J.; Antonny, B. Amphipathic Lipid Packing Sensor Motifs: Probing Bilayer Defects with Hydrophobic Residues. *Biophys. J.* **2013**, *104* (3), 575–584.

(219) Drin, G.; Casella, J.-F.; Gautier, R.; Boehmer, T.; Schwartz, T. U.; Antonny, B. A General Amphipathic α-Helical Motif for Sensing Membrane Curvature. *Nat. Struct. Mol. Biol.* **2007**, *14* (2), 138–146.

(220) Robinson, M. W.; Alvarado, R.; To, J.; Hutchinson, A. T.; Dowdell, S. N.; Lund, M.; Turnbull, L.; Whitchurch, C. B.; O'Brien, B. A.; Dalton, J. P.; Donnelly, S. A Helminth Cathelicidin-like Protein Suppresses Antigen Processing and Presentation in Macrophages via Inhibition of Lysosomal VATPase. *FASEB J.* **2012**, *26* (11), 4614–4627.

(221) He, Y.; Lazaridis, T. Activity Determinants of Helical Antimicrobial Peptides: A Large-Scale Computational Study. *PLoS One* **2013**, *8* (6), e66440.

(222) Mihajlovic, M.; Lazaridis, T. Antimicrobial Peptides Bind More Strongly to Membrane Pores. *Biochim. Biophys. Acta - Biomembr.* **2010**, *1798* (8), 1494–1502.

(223) Kyte, J.; Doolittle, R. F. A Simple Method for Displaying the Hydropathic Character of a Protein. *J. Mol. Biol.* **1982**, *157* (1), 105–132.

(224) Heng, N. C. K.; Tagg, J. R. What's in a Name? Class Distinction for Bacteriocins. *Nat. Rev. Microbiol.* **2006**, *4* (2), 160.

(225) Acedo, J. Z.; Chiorean, S.; Vederas, J. C.; van Belkum, M. J. The Expanding Structural Variety among Bacteriocins from Gram-Positive Bacteria. *FEMS Microbiol. Rev.* **2018**, *42* (6), 805–828.

(226) Towle, K. M.; Vederas, J. C. Structural Features of Many Circular and Leaderless Bacteriocins Are Similar to Those in Saposins and Saposin-like Peptides. *Medchemcomm* **2017**, *8* (2), 276–285.

(227) Perez, R. H.; Zendo, T.; Sonomoto, K. Circular and Leaderless Bacteriocins: Biosynthesis, Mode of Action, Applications, and Prospects. *Front. Microbiol.* **2018**, *9*, 2085.

(228) Netz, D. J. A.; Bastos, M. do C. de F.; Sahl, H.-G. Mode of Action of the Antimicrobial Peptide Aureocin A53 from Staphylococcus Aureus. *Appl. Environ. Microbiol.* **2002**, *68* (11), 5274–5280.

(229) Yoneyama, F.; Imura, Y.; Ichimasa, S.; Fujita, K.; Zendo, T.; Nakayama, J.; Matsuzaki, K.; Sonomoto, K. Lacticin Q, a Lactococcal Bacteriocin, Causes High-Level Membrane Permeability in the Absence of Specific Receptors. *Appl. Environ. Microbiol.* **2009**, *75* (2), 538–541.

(230) Yoneyama, F.; Imura, Y.; Ohno, K.; Zendo, T.; Nakayama, J.; Matsuzaki, K.; Sonomoto, K. Peptide-Lipid Huge Toroidal Pore, a New Antimicrobial Mechanism Mediated by a Lactococcal Bacteriocin, Lacticin Q. *Antimicrob. Agents Chemother.* **2009**, *53* (8), 3211–3217.

(231) Bruhn, H. A Short Guided Tour through Functional and Structural Features of Saposin-like Proteins. *Biochem. J.* **2005**, *389* (2), 249–257.

(232) Pieta, P.; Majewska, M.; Su, Z.; Grossutti, M.; Wladyka, B.; Piejko, M.; Lipkowski, J.; Mak, P. Physicochemical Studies on Orientation and Conformation of a New Bacteriocin BacSp222 in a Planar Phospholipid Bilayer. *Langmuir* **2016**, *32* (22), 5653–5662.

(233) Sandiford, S.; Upton, M. Identification, Characterization, and Recombinant Expression of Epidermicin NI01, a Novel Unmodified Bacteriocin Produced by Staphylococcus Epidermidis That Displays Potent Activity against Staphylococci. *Antimicrob. Agents Chemother.* **2012**, *56* (3), 1539–1547.

(234) Gibreel, T. M.; Upton, M. Synthetic Epidermicin NI01 Can Protect Galleria Mellonella Larvae from Infection with Staphylococcus Aureus. *J. Antimicrob. Chemother.* **2013**, *68* (10), 2269–2273.

(235) Halliwell, S.; Warn, P.; Sattar, A.; Derrick, J. P.; Upton, M. A Single Dose of Epidermicin NI01 Is Sufficient to Eradicate MRSA from the Nares of Cotton Rats. *J. Antimicrob. Chemother.* **2017**, *72* (3), 778–781.

(236) Hammond, K.; Lewis, H.; Halliwell, S.; Desriac, F.; Nardone, B.; Ravi, J.; Hoogenboom, B. W.; Upton, M.; Derrick, J. P.; Ryadnov, M. G. Flowering Poration—A Synergistic Multi-Mode Antibacterial Mechanism by a Bacteriocin Fold. *iScience* **2020**, *23* (8), 101423.

(237) Kwok, S. C.; Hodges, R. S. Stabilizing and Destabilizing Clusters in the Hydrophobic Core of Long Two-Stranded α-Helical Coiled-Coils. *J. Biol. Chem.* **2004**, *279* (20), 21576–21588.

(238) Lau, S. Y.; Taneja, A. K.; Hodges, R. S. Synthesis of a Model Protein of Defined Secondary and Quaternary Structure. Effect of Chain Length on the Stabilization and Formation of Two-Stranded Alpha-Helical Coiled-Coils. *J. Biol. Chem.* **1984**, *259* (21), 13252–13261.

(239) Zhou, N. E.; Kay, C. M.; Hodges, R. S. Synthetic Model Proteins. Positional Effects of Interchain Hydrophobic Interactions on Stability of Two-Stranded Alpha-Helical Coiled-Coils. *J. Biol. Chem.* **1992**, *267* (4), 2664–2670.

(240) Barlič, A.; Gutiérrez-Aguirre, I.; Caaveiro, J. M. M.; Cruz, A.; Ruiz-Argüello, M.-B.; Pérez-Gil, J.; González-Mañas, J. M. Lipid Phase Coexistence Favors Membrane Insertion of Equinatoxin-II, a Pore-Forming Toxin from Actinia Equina. *J. Biol. Chem.* **2004**, *279* (33), 34209–34216.

(241) Schön, P.; García-Sáez, A. J.; Malovrh, P.; Bacia, K.; Anderluh, G.; Schwille, P.

Equinatoxin II Permeabilizing Activity Depends on the Presence of Sphingomyelin and Lipid Phase Coexistence. *Biophys. J.* **2008**, *95* (2), 691–698.

(242) Gonzalez, C.; Langdon, G. M.; Bruix, M.; Galvez, A.; Valdivia, E.; Maqueda, M.; Rico, M. Bacteriocin AS-48, a Microbial Cyclic Polypeptide Structurally and Functionally Related to Mammalian NK-Lysin. *Proc. Natl. Acad. Sci.* **2000**, *97* (21), 11221–11226.

(243) Michalek, M.; Sönnichsen, F. D.; Wechselberger, R.; Dingley, A. J.; Hung, C.-W.; Kopp, A.; Wienk, H.; Simanski, M.; Herbst, R.; Lorenzen, I.; Marciano-Cabral, F.; Gelhaus, C.; Gutsmann, T.; Tholey, A.; Grötzinger, J.; Leippe, M. Structure and Function of a Unique Pore-Forming Protein from a Pathogenic Acanthamoeba. *Nat. Chem. Biol.* **2013**, *9* (1), 37–42.

(244) Cerasoli, E.; Ravi, J.; Gregor, C.; Hussain, R.; Siligardi, G.; Martyna, G.; Crain, J.; Ryadnov, M. G. Membrane Mediated Regulation in Free Peptides of HIV-1 Gp41: Minimal Modulation of the Hemifusion Phase. *Phys. Chem. Chem. Phys.* **2012**, *14* (3), 1277–1285.

(245) Oh, D.; Shin, S. Y.; Lee, S.; Kang, J. H.; Kim, S. D.; Ryu, P. D.; Hahm, K.-S.; Kim, Y. Role of the Hinge Region and the Tryptophan Residue in the Synthetic Antimicrobial Peptides, Cecropin A(1−8)−Magainin 2(1−12) and Its Analogues, on Their Antibiotic Activities and Structures. *Biochemistry* **2000**, *39* (39), 11855–11864.

(246) Chan, D. I.; Prenner, E. J.; Vogel, H. J. Tryptophan- and Arginine-Rich Antimicrobial Peptides: Structures and Mechanisms of Action. *Biochim. Biophys. Acta - Biomembr.* **2006**, *1758* (9), 1184–1202.

(247) Vukomanović, M.; Žunič, V.; Kunej, Š.; Jančar, B.; Jeverica, S.; Podlipec, R.; Suvorov, D. Nano-Engineering the Antimicrobial Spectrum of Lantibiotics: Activity of Nisin against Gram Negative Bacteria. *Sci. Rep.* **2017**, *7* (1), 4324.

(248) Prudêncio, C. V.; dos Santos, M. T.; Vanetti, M. C. D. Strategies for the Use of Bacteriocins in Gram-Negative Bacteria: Relevance in Food Microbiology. *J. Food Sci. Technol.* **2015**, *52* (9), 5408–5417.

(249) Ebbensgaard, A.; Mordhorst, H.; Aarestrup, F. M.; Hansen, E. B. The Role of Outer Membrane Proteins and Lipopolysaccharides for the Sensitivity of Escherichia Coli to Antimicrobial Peptides. *Front. Microbiol.* **2018**, *9*, 2153.

(250) Acedo, J. Z.; van Belkum, M. J.; Lohans, C. T.; Towle, K. M.; Miskolzie, M.; Vederas, J. C. Nuclear Magnetic Resonance Solution Structures of Lacticin Q and Aureocin A53 Reveal a Structural Motif Conserved among Leaderless Bacteriocins with Broad-Spectrum Activity. *Biochemistry* **2016**, *55* (4), 733–742.

(251) De Santis, E.; Ryadnov, M. G. Self-Assembling Peptide Motifs for Nanostructure Design and Applications. In *Amino Acids, Peptides and Proteins*; Ryadnov, M. G., Hudekz, F., Eds.; The Royal Society of Chemistry, 2016; Vol. 40, pp 199–238.

(252) Lombardi, L.; Falanga, A.; Del Genio, V.; Galdiero, S. A New Hope: Self-Assembling Peptides with Antimicrobial Activity. *Pharmaceutics* **2019**, *11* (4), 166.

(253) Liu, L.; Xu, K.; Wang, H.; Jeremy Tan, P. K.; Fan, W.; Venkatraman, S. S.; Li, L.; Yang, Y.-Y. Self-Assembled Cationic Peptide Nanoparticles as an Efficient Antimicrobial Agent. *Nat. Nanotechnol.* **2009**, *4* (7), 457–463.

(254) Wang, H.; Xu, K.; Liu, L.; Tan, J. P. K.; Chen, Y.; Li, Y.; Fan, W.; Wei, Z.; Sheng, J.; Yang, Y.-Y.; Li, L. The Efficacy of Self-Assembled Cationic Antimicrobial Peptide Nanoparticles against Cryptococcus Neoformans for the Treatment of Meningitis. *Biomaterials* **2010**, *31* (10), 2874–2881.

(255) Debnath, S.; Shome, A.; Das, D.; Das, P. K. Hydrogelation Through Self-Assembly of Fmoc-Peptide Functionalized Cationic Amphiphiles: Potent Antibacterial Agent. *J. Phys. Chem. B* **2010**, *114* (13), 4407–4415.

(256) Chen, W.; Yang, S.; Li, S.; Lang, J. C.; Mao, C.; Kroll, P.; Tang, L.; Dong, H. Self-Assembled Peptide Nanofibers Display Natural Antimicrobial Peptides to Selectively Kill Bacteria without Compromising Cytocompatibility. *ACS Appl. Mater. Interfaces* **2019**, *11* (32), 28681–28689.

(257) Matsuura, K. Synthetic Approaches to Construct Viral Capsid-like Spherical Nanomaterials. *Chem. Commun.* **2018**, *54* (65), 8944–8959.

(258) Fotin, A.; Cheng, Y.; Sliz, P.; Grigorieff, N.; Harrison, S. C.; Kirchhausen, T.; Walz, T. Molecular Model for a Complete Clathrin Lattice from Electron Cryomicroscopy. *Nature* **2004**, *432* (7017), 573–579.

(259) Castelletto, V.; de Santis, E.; Alkassem, H.; Lamarre, B.; Noble, J. E.; Ray, S.; Bella, A.; Burns, J. R.; Hoogenboom, B. W.; Ryadnov, M. G. Structurally Plastic Peptide Capsules for Synthetic Antimicrobial Viruses. *Chem. Sci.* **2016**, *7* (3), 1707–1711.

(260) Schibli, D. J.; Hwang, P. M.; Vogel, H. J. The Structure of the Antimicrobial Active Center of Lactoferricin B Bound to Sodium Dodecyl Sulfate Micelles. *FEBS Lett.* **1999**, *446* (2–3), 213–217.

(261) Cochran, A. G.; Skelton, N. J.; Starovasnik, M. A. Tryptophan Zippers: Stable, Monomeric β-Hairpins. *Proc. Natl. Acad. Sci.* **2001**, *98* (10), 5578–5583.

(262) Kepiro, I. E.; Marzuoli, I.; Hammond, K.; Ba, X.; Lewis, H.; Shaw, M.; Gunnoo, S. B.;

De Santis, E.; Łapińska, U.; Pagliara, S.; Holmes, M. A.; Lorenz, C. D.; Hoogenboom, B. W.; Fraternali, F.; Ryadnov, M. G. Engineering Chirally Blind Protein Pseudocapsids into Antibacterial Persisters. *ACS Nano* **2020**, *14* (2), 1609–1622.

(263) Crowther, R. A.; Pinch, J. T.; Pearse, B. M. F. On the Structure of Coated Vesicles. *J. Mol. Biol.* **1976**, *103* (4), 785–798.

(264) Musacchio, A.; Smith, C. J.; Roseman, A. M.; Harrison, S. C.; Kirchhausen, T.; Pearse, B. M. . Functional Organization of Clathrin in Coats. *Mol. Cell* **1999**, *3* (6), 761–770.

(265) Uppalapati, M.; Lee, D. J.; Mandal, K.; Li, H.; Miranda, L. P.; Lowitz, J.; Kenney, J.; Adams, J. J.; Ault-Riché, D.; Kent, S. B. H.; Sidhu, S. S. A Potent D-Protein Antagonist of VEGF-A Is Nonimmunogenic, Metabolically Stable, and Longer-Circulating in Vivo. *ACS Chem. Biol.* **2016**, *11* (4), 1058–1065.

(266) Arranz-Gibert, P.; Ciudad, S.; Seco, J.; García, J.; Giralt, E.; Teixidó, M. Immunosilencing Peptides by Stereochemical Inversion and Sequence Reversal: Retro-D-Peptides. *Sci. Rep.* **2018**, *8* (1), 6446.

(267) Olsen, J. V; Ong, S.-E.; Mann, M. Trypsin Cleaves Exclusively C-Terminal to Arginine and Lysine Residues. *Mol. Cell. Proteomics* **2004**, *3* (6), 608–614.

(268) Migliore, M.; Bonvicini, A.; Tognetti, V.; Guilhaudis, L.; Baaden, M.; Oulyadi, H.; Joubert, L.; Ségalas-Milazzo, I. Characterization of β-Turns by Electronic Circular Dichroism Spectroscopy: A Coupled Molecular Dynamics and Time-Dependent Density Functional Theory Computational Study. *Phys. Chem. Chem. Phys.* **2020**, *22* (3), 1611–1623.

(269) Perczel, A.; Hollosi, M.; Foxman, B. M.; Fasman, G. D. Conformational Analysis of Pseudocyclic Hexapeptides Based on Quantitative Circular Dichroism (CD), NOE, and x-Ray Data. The Pure CD Spectra of Type I and Type II .Beta.-Turns. *J. Am. Chem. Soc.* **1991**, *113* (26), 9772–9784.

(270) Pyne, A.; Thompson, R.; Leung, C.; Roy, D.; Hoogenboom, B. W. Single-Molecule Reconstruction of Oligonucleotide Secondary Structure by Atomic Force Microscopy. *Small* **2014**, *10* (16), 3257–3261.

(271) Medrano, M.; Fuertes, M. Á.; Valbuena, A.; Carrillo, P. J. P.; Rodríguez-Huete, A.; Mateu, M. G. Imaging and Quantitation of a Succession of Transient Intermediates Reveal the Reversible Self-Assembly Pathway of a Simple Icosahedral Virus Capsid. *J. Am. Chem. Soc.* **2016**, *138* (47), 15385–15396.

(272) Haney, E. F.; Mansour, S. C.; Hancock, R. E. W. Antimicrobial Peptides: An

Introduction. In *Antimicrobial Peptides. Methods in Molecular Biology.*; Hansen, P. R., Ed.; Humana Press, New York, NY, 2017; Vol. 1548, pp 3–22.

(273) Jin, M.; Lu, F.; Belkin, M. A. High-Sensitivity Infrared Vibrational Nanospectroscopy in Water. *Light Sci. Appl.* **2017**, *6* (7), e17096.

(274) Xiao, L.; Schultz, Z. D. Spectroscopic Imaging at the Nanoscale: Technologies and Recent Applications. *Anal. Chem.* **2018**, *90* (1), 440–458.

(275) Melitz, W.; Shen, J.; Kummel, A. C.; Lee, S. Kelvin Probe Force Microscopy and Its Application. *Surf. Sci. Rep.* **2011**, *66* (1), 1–27.

(276) Collins, L.; Kilpatrick, J. I.; Kalinin, S. V; Rodriguez, B. J. Towards Nanoscale Electrical Measurements in Liquid by Advanced KPFM Techniques: A Review. *Reports Prog. Phys.* **2018**, *81* (8), 086101.

(277) Kobayashi, N.; Asakawa, H.; Fukuma, T. Nanoscale Potential Measurements in Liquid by Frequency Modulation Atomic Force Microscopy. *Rev. Sci. Instrum.* **2010**, *81* (12), 123705.

(278) Kobayashi, N.; Asakawa, H.; Fukuma, T. Dual Frequency Open-Loop Electric Potential Microscopy for Local Potential Measurements in Electrolyte Solution with High Ionic Strength. *Rev. Sci. Instrum.* **2012**, *83* (3), 033709.

(279) Hirata, K.; Kitagawa, T.; Miyazawa, K.; Okamoto, T.; Fukunaga, A.; Takatoh, C.; Fukuma, T. Visualizing Charges Accumulated in an Electric Double Layer by Three-Dimensional Open-Loop Electric Potential Microscopy. *Nanoscale* **2018**, *10* (30), 14736–14746.

(280) Nagamachi, S.; Yamakage, Y.; Maruno, H.; Ueda, M.; Sugimoto, S.; Asari, M.; Ishikawa, J. Focused Ion Beam Direct Deposition of Gold. *Appl. Phys. Lett.* **1993**, *62* (17), 2143–2145.

(281) Nuzzo, R. G.; Allara, D. L. Adsorption of Bifunctional Organic Disulfides on Gold Surfaces. *J. Am. Chem. Soc.* **1983**, *105* (13), 4481–4483.

(282) Ekeroth, J.; Konradsson, P.; Höök, F. Bivalent-Ion-Mediated Vesicle Adsorption and Controlled Supported Phospholipid Bilayer Formation on Molecular Phosphate and Sulfate Layers on Gold. *Langmuir* **2002**, *18* (21), 7923–7929.

(283) Ip, S.; Li, J. K.; Walker, G. C. Phase Segregation of Untethered Zwitterionic Model Lipid Bilayers Observed on Mercaptoundecanoic-Acid-Modified Gold by AFM Imaging and Force Mapping. *Langmuir* **2010**, *26* (13), 11060–11070.

(284) Green, N. M. Avidin and Streptavidin. In *Methods in Enzymology*; Wilchek, M., Bayer,

E. A., Eds.; Academic Press, 1990; Vol. 184, pp 51–67.

(285) Neish, C. S.; Martin, I. L.; Henderson, R. M.; Edwardson, J. M. Direct Visualization of Ligand-Protein Interactions Using Atomic Force Microscopy. *Br. J. Pharmacol.* **2002**, *135* (8), 1943–1950.

(286) Barattin, R.; Voyer, N. Chemical Modifications of AFM Tips for the Study of Molecular Recognition Events. *Chem. Commun.* **2008**, No. 13, 1513.

(287) Florin, E.; Moy, V.; Gaub, H. Adhesion Forces between Individual Ligand-Receptor Pairs. *Science* **1994**, *264* (5157), 415–417.